Fault-hosted geothermal systems in southeastern British Columbia

by

Theron Finley

A thesis submitted in partial fulfillment of the requirements for the degree of

Master of Science

Department of Earth and Atmospheric Sciences
University of Alberta

Abstract

Geothermal energy is a low-carbon, base-load, renewable energy resource that should form part of the future global energy portfolio as we seek to reduce carbon emissions and mitigate climate change. In Canada, geothermal resources are underdeveloped and require further investigation to facilitate their development. This thesis applies structural geology, petrology, and geophysics to investigate potential geothermal resources in southeastern British Columbia with a focus on thermal springs. These resources are spatially coincident with major fault systems – the Southern Rocky Mountain Trench (SRMT) fault, Purcell Trench fault, and Columbia River fault – that likely allow for the deep circulation and heating of meteoric water in the crust.

Field investigations and structural analyses presented in Chapter 2 reveal a previously undocumented post-Eocene phase of right-lateral strike-slip accommodated across multiple fault structures in southeastern British Columbia. These kinematics are consistent with earthquake focal mechanisms and maximum stress directions in the region, which suggests that neotectonic strain plays an important role in controlling the location of thermal springs. When viewed in this context, it is apparent that thermal springs are localized by zones of stress concentration such as fault tips, intersections, and step-overs. On a broader scale, thermal springs are spatially associated with clusters of seismicity. Thus, structural geology and seismology may allow for predictive mapping of hidden geothermal systems elsewhere in the Canadian Cordillera.

Structural cross-sections and petrographic analyses presented in Chapter 3 reveal strong structural and microstructural anisotropy in rocks near the Valemount geothermal prospect, which is located along the SRMT fault. Understanding the structural anisotropy is key to interpreting magnetotelluric (MT) surveys conducted in the area. At map scale (over tens of kilometers), several subparallel brittle and ductile fault structures represent numerous phases of deformation from the Jurassic to late Cenozoic. Some of these faults may act as permeable conduits for thermal fluid. At microscopic scale (microns to millimeters), highly metamorphosed rocks of the Yellowjacket Gneiss contain conductive minerals including graphite

and sulfides, which are aligned and partially connected along cleavage planes. Observations at both scales indicate that anisotropic MT inversions are more appropriate for geothermal exploration in highly deformed regions.

Preface

Chapter 1 describes the motivation behind this thesis and provides a broad introduction to geothermal energy resources around the world. Geothermal resources are highly diverse, and it is important to place the resources in Canada within the context of global geothermal resources. This chapter benefited greatly from the lessons learned on my international travels as a Hugh C. Morris Fellow in 2018 and 2019.

Chapter 2 is the main body of work I conducted as part of my MSc research. With the guidance of my supervisors I led the design of this project, including the plans for fieldwork, scientific objectives, and interpretation of results. I conducted two seasons of fieldwork in southeastern British Columbia collecting structural data in the fault zones that are associated with possible geothermal resources in the region. An early version of this chapter was published in the proceedings of the 2020 World Geothermal Congress in Reykjavik, Iceland (postponed to May 2021 due to COVID-19), which is the preeminent conference for geothermal energy research. A similar version was published in the Geoscience BC 2019 annual report on activities. A final, more thorough version is being prepared for submission to the Journal of Structural Geology or similar publication. I will be first author on this manuscript, with Stephen Johnston, Martyn Unsworth, Dinu Pana, and Jonathan Banks as co-authors.

Chapter 3 describes work I conducted in collaboration with Benjamin Lee, a PhD student in Martyn Unsworth's research group. I drafted geological maps and cross sections of the Valemount area based on preexisting GSC mapping and my own fieldwork in the area. I collected samples of suspected graphitic schist in the field and arranged the XRD and SEM analyses. Unfortunately, some final analyses were interrupted by the COVID-19 pandemic and are therefore not included here. This work is currently being integrated into a manuscript led by Benjamin Lee, for which I am contributing to the discussion and interpretation of results.

Chapter 4 provides a summary of my results and contributions, and highlights the most significant results. Some suggestions for future work are also provided.

During my degree, several months were spent attempting to use multi-component aqueous geothermometry to refine previous estimates of reservoir temperatures and circulation depths of thermal spring systems in the Canadian Cordillera. This research was not successful due to high charge balance errors and the absence of Aluminum ion concentrations in the dataset from Grasby et al., (2000), and is consequently not included in this thesis. Future efforts to resample the thermal springs may resolve these issues.

Acknowledgements

This thesis has relied on the support, guidance, and kindness of many people, and I hope to acknowledge them all here. Any omissions are due to my forgetfulness rather than lack of appreciation.

First and foremost, enormous thanks go to my three supervisors Martyn Unsworth, Stephen Johnston, and Jonathan Banks. Thank you for believing in my project from the beginning, allowing the freedom to pursue questions that interested me, providing guidance when I went down the wrong paths and encouragement to continue along the right ones.

Samuel Johnson and Noah Van Camp are thanked for their dedicated efforts as field assistants during the summer of 2018. Dinu Pana is owed considerable thanks for introducing me to the field area and sharing with me some of his favourite outcrops. Michael Hesketh generously contributed his time to helping me with setting up tablet computers for field mapping.

Walter Harley and Mark Labbe are thanked for preparing excellent thin sections of samples from Canoe Reach. Nathan Gerein and Guibin Ma are thanked for their help operating the SEM and interpreting results. Rebecca Funk is thanked for her rapid XRD analyses.

This project was primarily funded as part of the geothermal theme of the Future Energy Systems program, a Canada First Research Excellence Fund initiative at the University of Alberta. I received additional monetary support through an NSERC Canada Graduate Scholarship – Masters, and a Geoscience BC scholarship. I was also awarded a Hugh C. Morris Fellowship in 2018, which allowed for international travel to bolster my understanding of geothermal systems. Special thanks to Kimberley Foundation chairwoman Ms. Sue Roppel, who provided direct support during my tenure as a Hugh Morris Fellow. Though too numerous to list here, thanks are owed to the many researchers whom I met with during my world travels.

Thanks also go to my fantastic colleagues at the University of Alberta – especially those in the MT lab: Ben Lee, Brandon Chase, Cedar Hanneson, Darcy Cordell, Enci Wang, Sean Bettac, and Zoe Vestrum – for their moral support and friendship throughout during my time in Edmonton.

Finally, sincere thanks go to my friends, family, and especially my amazing partner Kathryn, for their ongoing love, patience, and encouragement as I tackled this challenge.

Table of Contents

List of Figures

SW population at high angles to the valleys. b) Unidirectional equal-distance quadrant histogram of the dips of all fault planes measured in this study. The majority are steeper than 60°. c) Unidirectional equal-distance circular histogram showing rake of slickenlines on fault planes using the standard convention of hanging-wall motion relative to the foot-wall, such that 0° = sinistral, +90° = normal, 180° = dextral, and -90° = reverse. The largest populations are normal and dextral. d) Kinematics of large fault planes with observable damage/fracture zones, and/or gouge layers greater than 1cm in width. These large faults are dominantly north-south striking, steeply-dipping, and dextral.

Figure 2.9. Photos from the Valemount/Canoe Reach area. See Figure 2.2 for photo locations and directions. Beachballs show kinematics for each fault plane. a) View south from the north end of the Kinbasket hydroelectric reservoir near Valemount, captured at low water level in May 2018. Red dot shows the location of the Canoe River thermal spring. b) Vestiges of dextral slickenlines in basal Neoproterozoic Windermere Supergroup on the northeast side of the lake (lat. 52.5691°N, long. 118.8420°W). Fault is oriented 168°/63°, slickenlines (red arrow) are oriented 19°→192°. c) Large, oxidized, fault plane in basal Windermere Supergroup on northeast side of lake (lat. 52.6202°N, long. 118.9424°W). Fault is oriented 170°/54°, dextral slickenlines (not pictured) are oriented 15°→333°. d) Dextral slickenlines in Paleoproterozoic Bulldog Gneiss on the northeast side of the lake (lat. 52.6412°N, long. 118.9759°W). Fault is oriented 139°/84°, slickenlines (red arrow) are oriented 15°→143°.

Figure 2.10. Photos from the southern segment of the SRMT, from the US border to southern Kinbasket Lake. See Figure 2.4 for photo locations. Beachballs show kinematics for each fault plane. Concentric circles indicate movement out of the page, circles containing an ‘x’ indicate movement into the page. a) Looking east at a dextral fault plane oriented 304°/86° within the Redwall fault zone near Radium Hot Springs (lat. 50.6356°N, long. 116.0372°W). Red arrow shows slickenline orientation (30°→119°). b) Oblique view from the southeast of dextral fault plane (200°/88°) with shallowly north-plunging corrugations (red arrow: 14°→016°) and shallowly south-plunging dextral slickenlines (not visible: 25°→217°) near the south end of the Lussier River fault (lat. 49.7175°N, long. 115.5458°W). c) Looking east at a large fault plane (162°/76°) with abundant dextral slickenlines (01°→160°) near the south end of Kinbasket Lake (51.6376°N, 117.4191°W).

Figure 2.11. Photos from the Purcell Trench. See Figures 2.5 and 2.6 for photo locations. Beachballs show kinematics for each fault plane. Concentric circles indicate movement out of the page, circles containing an ‘x’ indicate movement into the page. a) Breccia and gouge zone at outcrop of the Adit fault near Beaton (lat. 50.7025°N, long. 117.7095°W). Dextral slickenlines (14°→150°) are present on a subvertical, limonitic fault plane (345°/85°). Rock hammer for scale. b) One of numerous dextral slickenlines (03°→003°) observed on vertical fault zone (184°/78°) along Duncan Lake (lat. 50.4164°N, long. 116.9591°W). c) Dextral slickenlines (12°→347°) on a limonitic subvertical fault plane (145°/81°) located 10 km north of Duncan Lake (lat. 50.6958°N, long. 117.1007°W). d) Dextral fault zone (005°/63°) on the western shore of Kootenay Lake near Kaslo (lat. 49.8524°N, long. 116.9032°W). e) Faint dextral slickenlines (01°→005°) on the fault wall shown in e). f) A dextral fault (024°/89°) cross-cutting a normal fault (331°/68°) on the west side of the Purcell Trench along Highway 3 (lat. 49.1392°N, long. 116.6420°W).

Figure 2.12. Photos from the Columbia River fault. See Figures 2.3 and 2.6 for photo locations. Beachballs show kinematics for each fault plane. Concentric circles indicate movement out of the page, circles containing an 'x' indicate movement into the page. a) View northeast at outcrop on Highway 23 above the southeastern abutment of the Revelstoke Dam (lat. 51.0486°N, long. 118.1901°W). A splay of the main Columbia River fault is exposed here and is reinforced with rebar and shotcrete. Dextral slickenlines (44°→248°) are present on the footwall of the splay fault (240°/88°). b) A set of SW-NE striking normal faults (fault: 235°/41°; slickenlines: 41°→329°) exposed near Mica Dam (lat. 52.0710°N, long. 118.5590°W). Person circled for scale. c) A wide (1.2 m) gouge zone exposed along Highway 23 near Halcyon Hot Springs (lat. 50.5217°N, long. 117.8998°W). Dextral slickenlines (10°→221°) are present on the fault walls (218°/65°). d) Fault originally mapped as a normal fault by Thompson et al. (2004b), reinterpreted as a reverse fault based on folded footwall and reverse slickenlines on the hanging wall. This fault occurs in a possible restraining bend of the dextral Columbia River fault (lat. 50.3406°N, long. 118.0394°W). Rock hammer for scale. e) Broad zone of breccia and gouge striking west (280°/34°) at the north end of Slocan Lake (lat. 50.0983°N, long. 117.4586°W), possibly related to north south shortening in the restraining bend of the Slocan-Columbia River fault system. A tufa deposit occurs where the fault intersects the pre-roadcut ground surface. f) Subvertical fault plane.

Figure 2.13. Photos from the Slocan Lake area. See Figure 2.6 for photo locations. Beachballs show kinematics for each fault plane. Concentric circles indicate movement out of the page, circles containing an 'x' indicate movement into the page. a) View east at outcrop on Highway 6 north of New Denver (lat. 50.0555°N, long. 117.4323°W). Small, 20 cm wavelength, south-vergent folds are observed in felsic sills intruded parallel to the S1 cleavage (oriented 278°/51°) of the Slocan phyllite. Circle is approximately 1.5 m wide. b) View south at outcrop on Highway 6 south of New Denver (lat. 49.8189°N, long. 117.4549°W). A 2 m wide subvertical brittle dextral fault oriented 172°/74° cuts across shallowly east-dipping (008°/31°) ductile fabric of the Slocan Lake fault/Valkyr shear zone. White encircled dot and "x" indicate motion towards and away from the viewer, respectively.

Figure 2.14. a) Grey dots illustrate all seismicity (Mag. 2-7) in the Canadian Cordillera adapted from Ristau et al (2007) from 1984 to 2004. Red dots are hot springs, which are concentrated in regions of moderate seismicity. b) Focal mechanisms for earthquakes of M 4 and greater from Ristau et al (2007). Note that earthquakes in southeast BC are strike-slip, and likely dextral if a NNW-SSE nodal plane is selected.

Figure 2.15. a) Strain ellipse for approximate S_{Hmax} orientation in southeastern BC (Ristau et al., 2007), and corresponding predicted modes of brittle deformation on faults and fractures. Average orientations of the SRMT fault, Purcell Trench fault, Columbia River fault, and Slocan Lake fault, are shown for reference. b) Schematic map of fault kinematics in this study. Stereoplot shows density contours for P-axes for all dextral faults oriented parallel to the trend of the valleys (N=236).

Figure 2.16. Structural settings especially conducive to hydrothermal fluid upwellings adapted from Curewitz and Karson (1997). Orange shaded polygons are "breakdown" regions where stress is concentrated and fracture density is enhanced. a) Fault tip permeability, a possible control on the location of the warm springs at the southern tip of the Columbia River fault. b) Fault

Chapter 1: Geothermal Energy in Canada and Around the World

Abstract

Geothermal energy is a low-emission, baseload power source which, if developed, could aid in Canada's efforts to combat anthropogenic climate change. One of the largest obstacles to further development of geothermal energy in Canada is a lack of geological understanding of the controls on the location of geothermal systems. Geoscientists therefore have a crucial role to play in advancing geothermal energy development. This chapter provides an overview of the diversity of geothermal systems around the world and how they compare to those in Canada. The geothermal resources of southeastern BC – the focus of this thesis – are placed in a global context.

1.1 Motivation

1.1.1 Addressing climate change

Combatting anthropogenic climate change is a grand challenge of the 21st century. The rapid increase of anthropogenic CO_2 (and other greenhouse gases) being introduced to the atmosphere over the past two centuries largely via fossil fuel combustion, has caused a warming trend observable around the world (Figure 1.1; IPCC, 2013). The consequences of rising global temperatures for human health are numerous, but among the most severe are: desertification of large swaths of previously arable land, substantial sea level rise and land-loss due to deglaciation, a decrease in oceanic productivity due to warming and acidification, and an increase in hazardous weather events (IPCC, 2014a). Many of these outcomes will have a tremendous effect on the habitability of particular regions of the globe and will likely be accompanied by humanitarian crises. It is therefore imperative that measures are taken to dramatically reduce carbon emissions to slow climate change.

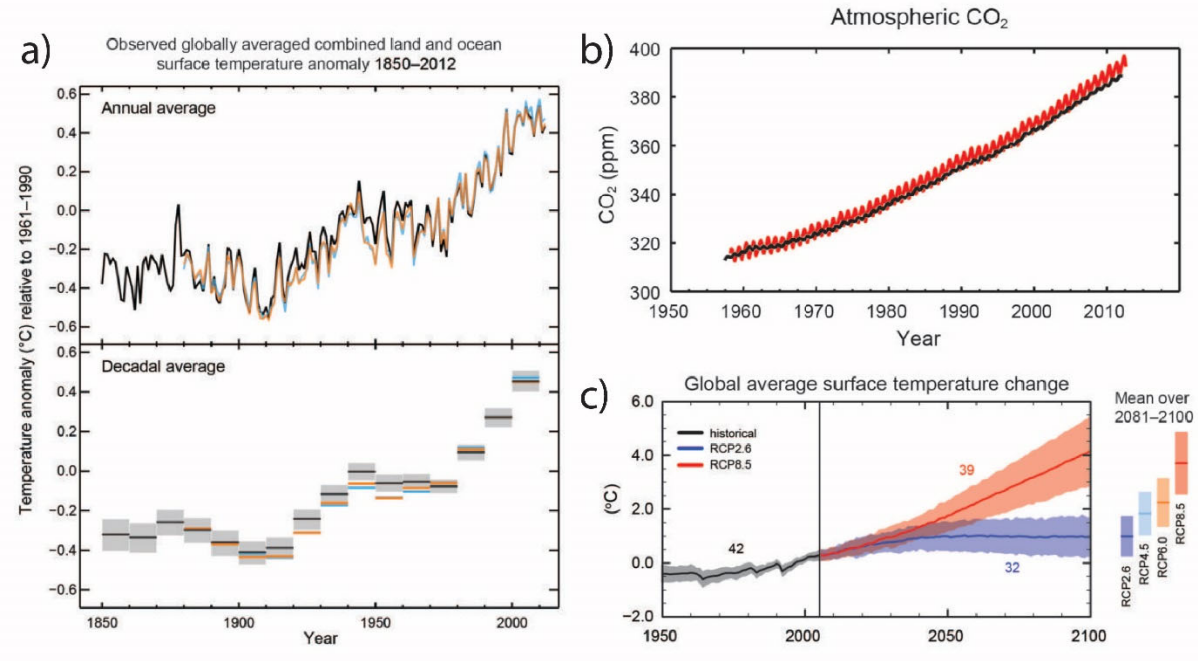

Figure 1.1. a) Observed global temperature anomaly trend from 1850 to present, measured relative to the average temperature from 1961-1990. b) Observed global atmospheric CO_2 concentrations. c) Projected global temperature trends over the next century based on several Representative Concentration Pathways (RCP's). Source of all figures: (IPCC, 2013).

There are many facets to reducing carbon emissions including social and behavioral change, progressive policy development, and technical innovation. An important aspect of these changes is the transition to energy sources with low carbon footprints (IPCC, 2014b). There are a wide variety of sources of renewable energy, all with their own benefits and drawbacks. The energy portfolio of the future will likely include a diverse range of energy sources, tailored to and based on the local availability of wind, sun, hydraulic head, and geothermal heat.

Furthermore, as the world's population grows and simultaneously becomes more industrialized, the demand for electricity is growing (IEA, 2019). New renewable energy sources must therefore not only replace existing fossil fuel combustion, but also keep pace with the increasing demand. Exploration of all possible renewable energy sources is necessary if countries are to meet the ambitious emissions targets they have committed to (ECCC, 2016).

1.1.2 The role of geothermal energy

Geothermal energy is heat produced within Earth's interior. The two main sources of this heat are: i) radioactive decay of potassium, thorium, and uranium, most of which is sequestered in the Earth's crust, and ii) remnant primordial heat from Earth's initial accretion (Dye, 2012). The thermal energy moves

from the interior of the Earth to the exterior following a geothermal gradient. In Earth's shallow crust (upper 5 km), the geothermal gradient (global average of 25-30 ˚C/km) is augmented by processes such as magma emplacement, crustal thinning, and hydrothermal convection, which create shallow thermal anomalies that are economically mineable from the surface. Hydrothermal fluid (typically water or steam) is necessary to transfer heat from the subsurface to the surface, where it is used directly for industrial processes and heating buildings, or to generate electricity by driving turbines.

The Earth produces a tremendous amount of geothermal power (47,000 GW; Davies and Davies, 2010). However, worldwide, only ~16 GWe of geothermal electricity and 107 GWt of direct-use geothermal heat is utilized (Huttrer, 2020; Lund and Toth, 2020), together representing far less than 1% of Earth's total geothermal heat flux. It is estimated that 160 GWe of geothermal electricity will be produced in 2050 (Goldstein et al., 2011), which is still two orders of magnitude smaller than the Earth's total heat flux. Therefore, while the amount of geothermal energy contained in the Earth is theoretically finite, it is unlikely we will ever exhaust this resource, and it is therefore classified as renewable so long as individual reservoirs are sustainably managed (Stefansson, 2000).

A major limitation of most renewable energy sources (e.g., wind, solar, hydro) is their intermittency. This intermittency is commonly expressed as the capacity factor, a ratio between the amount of energy produced over a given period of time and the maximum amount they could theoretically have produced during that time. Whereas many renewable energy sources have low capacity factors, geothermal energy operates with a high capacity factor and can contribute "baseload" power to an electrical grid (Figure 1.2; EIA, 2020). Current electrical grids are not designed to handle the fluctuations inherent to most renewable energy sources and require that energy is either: a) produced at levels well above the average demand, or b) stored between periods of peak production and demand (Yekini Suberu et al., 2014). Because of its high capacity factor, geothermal energy has the potential to be a critical part of the future energy portfolio.

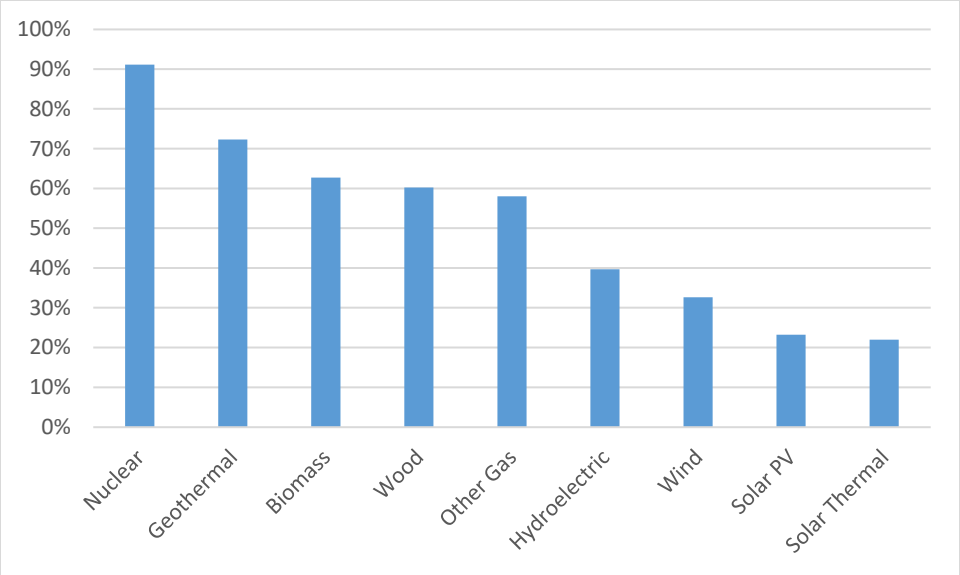

Figure 1.2. Average Capacity Factor of renewable energy sources in the US from 2010 to 2019. Geothermal power is second only to nuclear power in terms of its intermittency. Wind, solar, and even hydroelectric power have very low capacity factors (i.e., they are more intermittent). Data source (EIA, 2020).

Geothermal energy production and utilization creates minor carbon emissions. Geothermal power plants do not require the construction of major infrastructure nor the mining and transport of combustible fuel. Heat is "mined" in situ and no combustion occurs in the conversion to electricity. The only emissions of a power plant is CO_2 and other gases released from steam, the volume of which are much less than the emissions produced via fossil fuels combustion (Kristmannsdóttir and Ármannsson, 2003). When lifecycle emissions are accounted for, geothermal energy produces an order of magnitude less greenhouse gas than other baseload energy sources such as gas plants or hydroelectric dams, and similar low emissions as other forms of renewable energy (Figure 1.3; IPCC, 2014b).

Additionally, the levelized cost of electricity per megawatt hour produced at geothermal power plants is much lower than other renewable energy sources, and is competitive with fossil fuel resources (Figure 1.3; IPCC, 2014a). This should in theory make geothermal energy attractive to investors, but significant geological uncertainty remains and the upfront exploration risks are high (e.g., Witter et al., 2019).

Direct use of geothermal energy for heating can also significantly contribute to the reduction of fossil fuel combustion and has been shown to displace six times the amount of fossil fuel combustion compared to geothermal electricity production (Lavigne et al., 2020). Furthermore, geothermal heating has been shown to be cost-competitive when compared to fossil fuel burning (Hofmann et al., 2014; Majorowicz and Moore, 2014). This is especially true in cold climates where space heating is required for large portions of

the year. Much of Canada is therefore well positioned to benefit from both electrical and direct uses of geothermal energy.

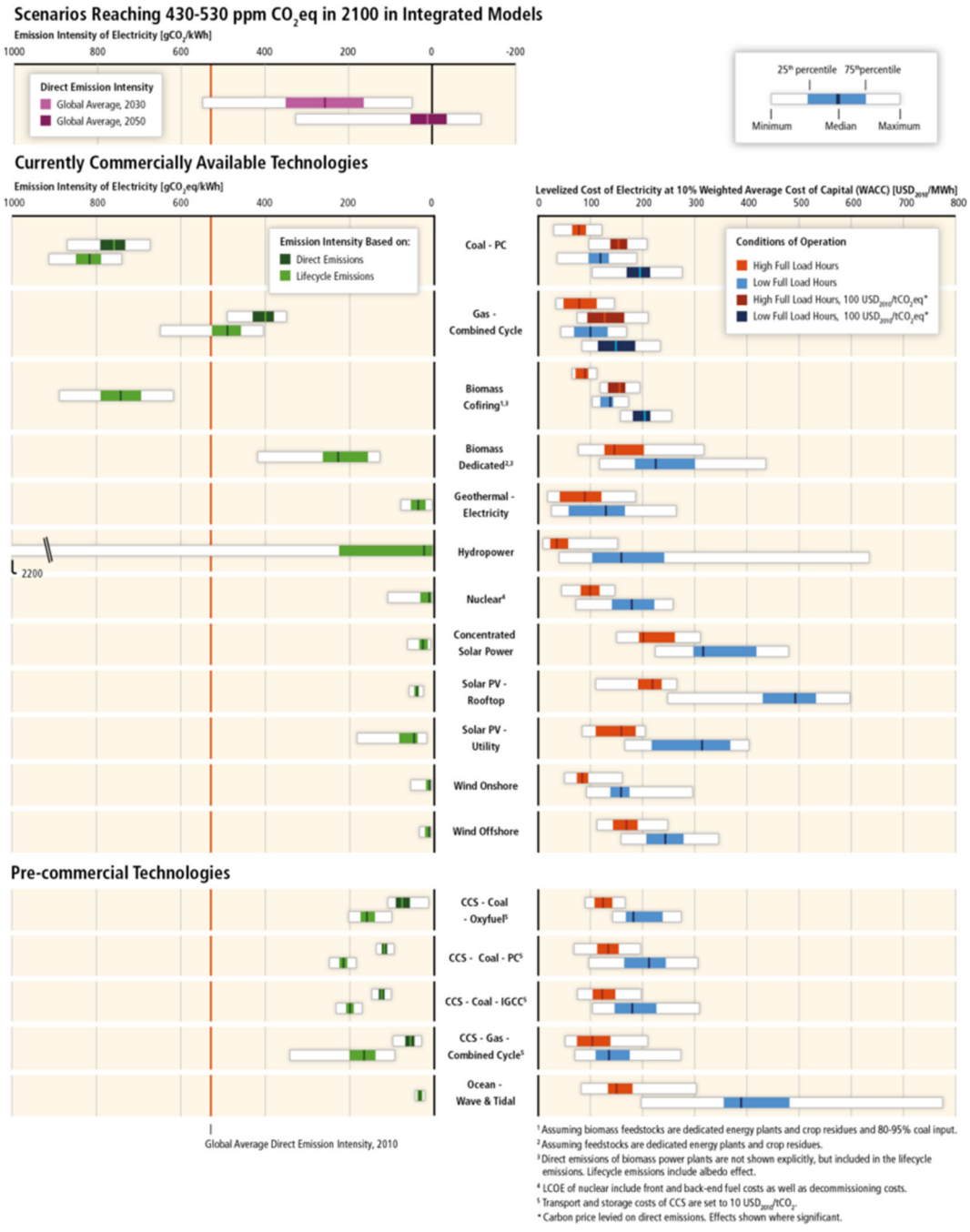

Figure 1.3. Lifecycle Emission Intensity and Levelized Cost of Electricity for several commercially available electricity generation technologies. Geothermal electricity produces very minor emissions (less than 75 gCO_2eq/kWh) as compared to other baseload power sources. Geothermal electricity is, on average, cheaper than other renewable energy sources, and competitive with electrical generation with fossil fuels. Figure adapted from IPCC (2014b).

1.1.3 The role of geoscientists

Geoscientists can aid in the transition to renewable energy and a low carbon future. In addition to playing a role in locating the minerals used in batteries for electronics and electric cars, and generating the geologic knowledge required for Carbon Capture and Storage installations, many of the skills and methods developed for exploration of minerals and fossil fuels can be transferred to exploration for geothermal energy. A limitation to broader adoption of geothermal energy is the lack of geological understanding of the subsurface (Barbier, 2002; Taylor, 2007); it is difficult to predict where geothermal reservoirs exist, and this presents a risk to investors. Geological and geophysical techniques still need to be better adapted to target reservoirs of geothermal fluids, in order to make predictions about the amount of thermal energy contained within them. Furthermore, historically, geothermal fields were identified based on surface expressions such as hot springs and fumaroles, but it has become clear that many geothermal systems may be hidden from the surface (e.g., Dobson, 2016). New predictive exploration techniques therefore need to be partially independent of surface geothermal expressions.

This thesis is focused on the application of structural geology and geophysics to geothermal exploration in southeastern BC. Geological structures, especially faults, play a critical role in controlling the dynamics of geothermal systems around the world. Faults introduce strong heterogeneity to the permeability structure of the crust, and allow for the deep circulation of hydrothermal fluids, creating positive temperature anomalies in the shallow crust. Understanding the orientations of faults and the stresses that act on them can allow for predictive mapping of geothermal systems (e.g., Faulds and Hinz, 2015). Several geophysical methods can complement structural analyses. Electromagnetic surveys can identify geothermal fluid present along fault planes, and seismology can provide constraints on the kinematics and crustal stress that together control the fault permeability. These methods have been successfully applied in geothermal exploration around the world but are there are challenges unique to working in the Canadian Cordillera including difficulty of access, sparse data coverage, dense vegetation, and thick glacial overburden.

1.2 Types of geothermal resources

Categorization of geothermal resources is helpful for understanding how best to approach exploration, and for conducting comparative geothermal resource assessments. Given the diversity of geothermal resource types, it is important that appropriate analogs are considered when assessing resources for their potential. Here, I distinguish geothermal resources based on five categorization schemes: (1) heat source, (2) temperature and enthalpy, (3) heat transport, (4) permeability, and (5) geologic/tectonic setting. Geothermal resources around the world can be described by a unique combination of these categorizations.

1.2.1 Heat source

Geothermal resources can be categorized based upon their source of heat, or more specifically, the mechanism by which sufficient heat is transferred to the shallow crust where it can be accessed economically by drilling from the surface. The average geothermal gradient of the Earth is 25-30 °C/km which means that in most places, subsurface temperatures above 100°C are found below 3 km depth. Drilling to such depths can be prohibitively expensive. so ideal geothermal targets are those where the geothermal gradient is steeper than average. The three main mechanisms that create positive temperature anomalies are: active upper crustal magmatism, radioactivity in crustal rocks, and crustal thinning. In active volcanic regions, molten rock is emplaced near the surface due to the introduction of volatiles (e.g., arc volcanoes), decompression melting (e.g., rifting), and anomalous heating (e.g., mantle hot spots). Radiogenic heat is associated with felsic plutonic suites with high proportions of Uranium, Thorium, and Potassium (Reed and Miller, 1980; Lewis et al., 1992) although other rock types, such as felsic gneiss and sedimentary rock, can also produce significant heat (e.g., Bachu, 1993). Crustal thinning steepens the geothermal gradient, bringing the heat of Earth's interior within economic reach of the surface. There are circumstances where a geothermal resource has more than one heat source; for example, on New Zealand's North Island, overlapping arc magmatism and continental rifting combine to create very high temperature geothermal resources in the near surface.

1.2.2 Temperature and enthalpy

Categorizing geothermal resources based on temperature is useful when assessing the appropriate technology for harnessing the heat. There is no standardized classification scale, and the choice of scale is dependent on the region and intended use. For example, what is considered a low temperature in Iceland, might be considered medium or high temperature elsewhere. For simplicity, I divide geothermal resources into 3 groups based on the temperature of fluid when entering the power station: high (>200°C), medium (100-200°C), and low (<100°C). High temperature geothermal resources are most well-suited to steam-driven electrical turbines (dry-steam and flash-steam plants). Medium temperature geothermal resources are well-suited to binary cycle (e.g., Organic Rankine Cycle) electrical plants, in which heat from the geothermal fluid is exchanged with a secondary working fluid with a lower boiling point, which is subsequently "flashed" through a turbine (Zarrouk and Moon, 2014; DiPippo, 2015). Low temperature geothermal resources are generally unsuitable for electrical generation, although electricity has been generated from geothermal fluids as cool as 73°C using a binary cycle plant (e.g., Holdmann, 2007). In most cases, fluids that are below 100°C are used for direct heating, either for individual buildings, entire municipal districts, or industrial processes (Lund and Toth, 2020). There are other factors that dictate which type of installation is most appropriate. Reservoir pressure and volume contribute to the enthalpy

of the system, which better describes the energy of a geothermal resource (DiPippo, 2015). Flow rate, ambient air temperatures, and the saturation index of the geothermal fluid (i.e., its potential for scaling or corrosion) are also important considerations when deciding on the correct power generation method. However, the temperature of the fluid provides a rough constraint on its utility.

1.2.3 Heat transport

All geothermal resources require a fluid, typically water, to carry heat from depth to the (near) surface, as heat itself cannot be directly extracted from rock for use. Geothermal systems are classified as either convective or conductive, depending on whether fluid moves naturally through the system, or whether it needs to be injected or pumped through the system (Moeck, 2014). In convective systems, cool groundwater percolates down to the heat source (e.g., a magma body or pluton) where it gains heat and becomes positively buoyant, rising to commercially accessible depths or to the surface as a hot spring. In conductive systems, groundwater in deep aquifers is heated in situ and does not rise to the surface naturally. Accessing conductive systems requires deep drilling and the expenditure of a significant amount of energy pumping fluid to the surface. In some cases, hot rocks exist in the subsurface, but do not possess the necessary permeability to facilitate the exchange of heat with groundwater; hydraulic stimulation can create fractures promoting heat exchange prior to pumping of the fluid to the surface. Such systems are called Enhanced Geothermal Systems or Hot Dry Rock and are considered conductive because the hydraulic circulation is not naturally driven.

1.2.4 Permeability

Permeability is required to allow the contact of fluid with hot rock, and to permit the movement of fluid to the near surface. Rock permeability can be primary (e.g., intergranular pore space) or secondary (e.g., faults, fractures, and karst features). Fractures control permeability in volcanic and plutonic systems, which are composed of otherwise impermeable igneous rocks. Major fault structures can allow the circulation of fluids to great depths such that a shallow temperature anomaly (magma or radioactivity) is not necessary. In sedimentary basins, pore space or karst cavities provide space for a high volume of geothermal fluid.

1.2.5 Geologic setting

Geothermal resources can be categorized according to their geologic setting. Each geologic setting has a characteristic heat source, temperature range, and fluid transport mechanism.

- Active volcanic provinces include oceanic and continental volcanic arcs, mid-ocean ridges, and mantle hot spots, and are some of the most prolific geothermal regions. Volcanic geothermal resources are typically high enthalpy. Fluid is heated in proximity to molten magma bodies and

convects along fractures that develop during active deformation of the volcanic system. Examples of well-known volcanic geothermal systems include those in Iceland (hot spot and spreading ridge), Central America (continental arc), and the Philippines (oceanic arc).

- Plutonic belts, the crystalline roots of old volcanoes, host a number of geothermal systems around the world. These systems have a wide range of temperatures, from low to high. Young, recently crystallized plutons contain residual magmatic heat, while older plutons continue to produce radioactive heat for 10's of millions of years. Fluid is heated in proximity to crystalline plutons and typically ascends to the surface along faults and fractures. In some cases, because crystalline rock is not highly permeable, hydraulic fracturing is required to create the necessary permeability (Enhanced Geothermal Systems). Many geothermal systems in central Alaska are plutonic, the heat source for the Geysers geothermal field in California is a young (~1Ma), shallow pluton (Dalrymple et al., 1999), and the Milford FORGE project in Utah will frack an impermeable pluton to exploit its heat (Allis et al., 2016).
- Extensional settings include back-arcs, mid-ocean ridges, and continental rifts, and are host to several highly productive geothermal fields around the world. In many cases, there is overlap between extensional and volcanic systems. These are mid to high enthalpy systems, and fluids are heated by deep circulation along faults, or by proximity to shallow molten magma that occurs due to decompression melting. Ongoing crustal extension leads to a steep geothermal gradient, and fluid does not need to circulate as deeply as in regions with average geothermal gradients. Furthermore, active extensional faults are excellent pathways for fluid. Examples include the numerous geothermal fields in the Basin and Range of Nevada and Utah, the Taupo Rift (which overlaps with the Taupo volcanic arc) in New Zealand, the East Africa continental rift, and the Rhine Graben in Germany. Geothermal resources in extensional settings are sometimes referred to as "fault hosted" systems due to the fact that significant transport of heat energy occurs via fluid flow along permeable fault zones. This definition can, however, be more broadly applied to any geothermal systems where fault zones permit the deep circulation of fluid. These settings are often seismically active, as strain is necessary to maintain fault permeability over time.
- Sedimentary basins, especially deep Foreland basins near mountain ranges, host low enthalpy geothermal resources in deep permeable aquifers (e.g., Banks and Harris, 2018). Fluids are commonly heated by radioactivity in basement rocks or surrounding sedimentary rocks (Bachu, 1993), or simply due to their great burial depth. Sedimentary rocks have low thermal conductivities, and act to insulate deep aquifers, allowing for the build-up of heat in the subsurface. Deep drilling is required to access these resources. These resources produce less power than those in other geologic settings and have not been as widely developed. European

countries such as Germany and Switzerland, have invested heavily in sedimentary basin geothermal systems, particularly in the Molasse Basin (Weber et al., 2015). Because sedimentary basins are typically highly developed for oil and gas exploration, there is extensive data on the subsurface, which decreases the risk of geothermal projects in these regions.

- Active orogenic belts host unconventional geothermal resources that are as yet unproven commercially. Only one such resource has been investigated in detail on the South Island of New Zealand. There, the active uplift of the Southern Alps along the eastern hanging-wall of the Alpine Fault has outpaced the cooling rate of the rocks as they are exhumed. As a result, there is a significant temperature anomaly in the hanging-wall of the fault (Sutherland et al., 2017). It is not yet known whether similar resources exist elsewhere in the world.

1.3 Canada's geothermal resources in a global context

1.3.1 Geothermal energy in Canada

Canada has no installed geothermal capacity despite having tremendous potential, especially in the western provinces and territories (Grasby et al., 2012). Over the past four decades several attempts have been made to develop geothermal energy in Canada, but none have attained commercial success. An overview of the history of Canadian geothermal energy research and development in Canada is provided by Grasby et al. (2012). A major wave of research and exploration occurred in the late 1970's and early 1980's in response to rising oil prices. Of particular note are the attempts to harness geothermal energy at Mount Meager, a volcano 150 km north of Vancouver, temperature gradient wells drilled in the Eocene Coryell Syenite and Cretaceous Raft Batholith of south-central BC in 1978, and a direct-use production well drilled to reservoirs at 2 km depth in the sedimentary formations beneath the University of Regina in 1979.

Canadian geothermal energy exploration was limited between the 1980's and the 2000's. In the past decade however, there have been renewed attempts to develop geothermal energy: University of Alberta researchers have conducted feasibility studies for the use of geothermal energy in oil-sands processing (e.g., Majorowicz et al., 2013), Borealis Geopower Inc. has embarked on exploration programs near the towns of Valemount, Terrace, and Fort Liard (Huang et al., 2018), DEEP Earth Energy Production Corp. has commenced drilling for a 5 MW power plant in southern Saskatchewan, the Yukon government has undertaken several studies of geothermal potential in the territory (Fraser et al., 2018), private companies (Eavor Technologies, Terrapin Geothermics, Razor Energy Corp) have pilot projects to utilize geothermal energy in Alberta, and a new research campaign is ongoing at Mount Meager (Grasby et al., 2020).

It is useful to compare Canada's geothermal resources to those that have been developed around the world. Canada is host to a wide variety of geological settings conducive to geothermal energy extraction, including active volcanic arcs, plutonic belts, and sedimentary basins.

1.3.2 Sedimentary basins

The Western Canada Sedimentary Basin (WCSB), which underlies much of Alberta, Saskatchewan, and western Northwest Territories, is prospective for geothermal energy development. The basin consists of carbonate rocks deposited on the ancient North American passive margin in the Paleozoic, overlain by clastic rocks formed from sediments shed from the Cordilleran Orogen between the Jurassic and Paleocene (Cant and Stockmal, 1989). It has a wedge-shaped geometry, with the Precambrian basement dipping west-southwest to a maximum of 4 km under the foothills of the Canadian Rocky Mountains (Figure 1.4; Bachu and Burwash, 1991; Hofmann et al., 2014). Data from decades of petroleum exploration provides excellent control on the distribution of thermal aquifers that may be prospective to geothermal energy production (Majorowicz and Grasby, 2010). In the deepest part of the basin, temperatures in aquifers may reach 180°C (Hofmann et al., 2014), although the largest fraction of thermal reservoirs are between 70 and 90 °C (Banks, 2016).

The geothermal resources in the WCSB are generally low enthalpy. While some reservoirs would be suitable for power generation using binary-cycle plants, most would only be suitable for direct-use applications. All geothermal resources in the WCSB are considered conductive, as there is no active circulation of thermal fluid. Geothermal wells would require pumping to bring the thermal fluid to the surface. The cold climate and consequent high space heating demand in this region make direct-use geothermal an appealing and cost-effective way to reduce emissions caused by heating with fossil fuels (Majorowicz and Moore, 2014; Lavigne et al., 2020). Furthermore, coproduced fluids from oil and gas wells contain significant thermal energy, and may serve to offset emissions of the oil and gas sector (Ferguson and Ufondu, 2017; Leitch et al., 2019).

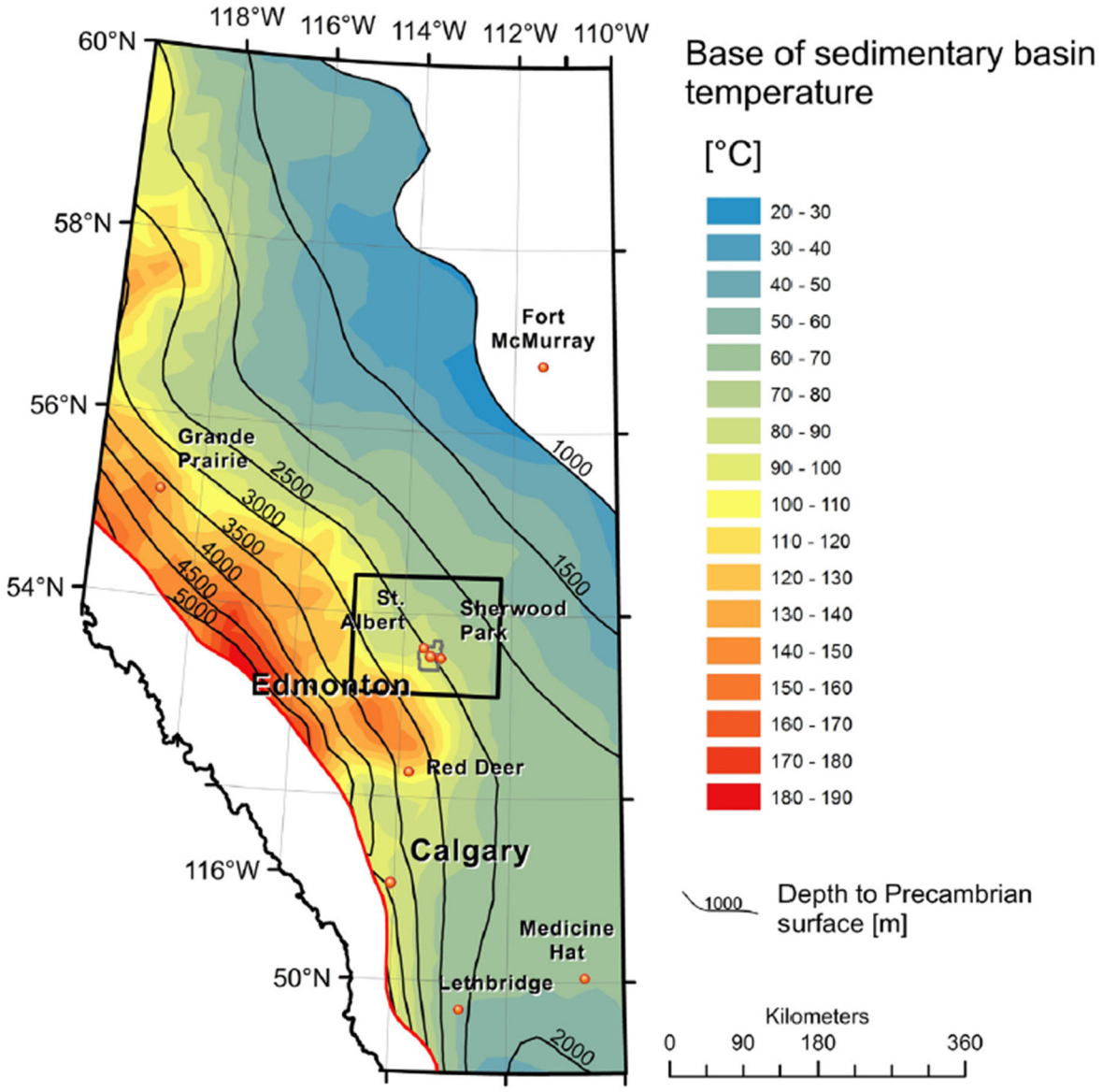

Figure 1.4. Map of temperatures at the basement unconformity of the Western Canada Sedimentary Basin. Temperatures increase from northeast to southwest as the basement unconformity is more deeply buried. Temperatures exceed 180°C near Hinton, AB. Source: (Hofmann et al., 2014)

1.3.3 Volcanic systems

The majority of active and recent volcanism in Canada occurs within British Columbia and Yukon (Edwards and Russell, 2000). Quaternary and Neogene volcanic zones can be divided into five distinct belts: the Garibaldi, Wells Gray-Clearwater, Anahim, Northern Cordilleran, and the Wrangell (Figure 1.5). Many of the central and northern volcanic regions are considered too distant from the existing electrical grid to be of economic interest; the required installation of transmission lines makes these regions uneconomical for geothermal energy production (Grasby et al., 2012). The main volcanic systems

of interest lie in the Garibaldi volcanic belt (GVB), a component of the Cascadia magmatic arc which is attributable to subduction of the Juan de Fuca plate beneath North America (Green et al., 1988).

Mount Meager is the most well-investigated volcanic system in the GVB in terms of its geothermal potential. Extensive research was conducted by the Geological Survey and BC Hydro in the 1970's and 1980's. Exploratory wells drilled between 1974 and 1984 revealed the presence of geothermal reservoirs with temperatures exceeding 250°C. A demonstration power plant was installed for a period of two years before the research project was cancelled in part due to falling oil prices. At the time, it was also concluded that the rocks underlying Mt. Meager were insufficiently permeable for the high flow volumes required for geothermal energy production. Witter (2019) reviewed data from early exploration attempts at Mount Meager and found that sufficient permeability may in fact exist. As a result, a new research campaign is ongoing at Mount Meager (Grasby et al., 2020). Other major volcanic centers in the GVB include Mount Cayley and Mount Garibaldi, both of which are near to the town of Squamish and could host geothermal energy resources of their own (Grasby et al., 2012).

The geothermal resources at Mount Meager are high enthalpy and are prospective for geothermal electricity production. The resource is similar to existing volcanic geothermal fields around the world, including those in the continental volcanic arcs of the western U.S., Japan, and New Zealand. Exploration strategies for such resources are mature and could be applied to Mount Meager.

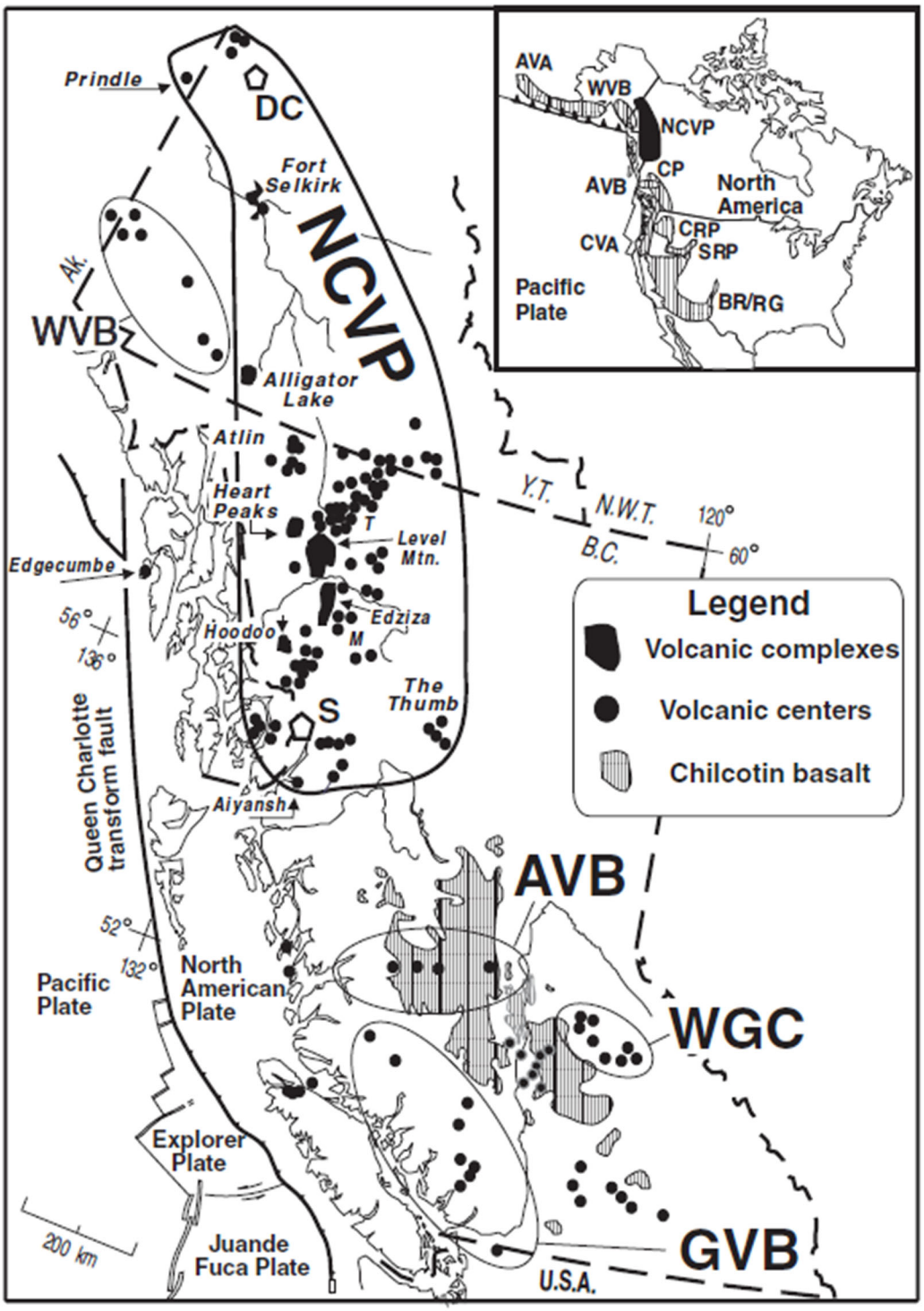

Figure 1.5. Location of Quaternary and Neogene volcanic centers in the Canadian Cordillera from Edwards and Russell (2000). GVB – Garibaldi volcanic belt, WGC – Wells Gray-Clearwater volcanic field, AVB – Anaheim volcanic belt, WVB – Wrangell volcanic belt, NCVP – northern Cordillera volcanic province.

1.3.4 Plutonic systems

Mesozoic and Cenozoic intrusive rocks occur throughout the Canadian Cordillera of western Canada. Jurassic and Cretaceous plutons represent the roots of volcanic arcs developed at paleo-subduction zones, while the Cenozoic plutons are the result of crustal extension (Armstrong, 1988). Lewis et al. (1992) measured radiogenic heat generation in many of these plutons and found the Cenozoic and Cretaceous plutons of southeastern BC to be high (4-5 $\mu W/m^3$; Figure 1.6). Consequently, this region has been recognized as having high potential for the development of Enhanced Geothermal Systems, for which the necessary permeability is created via hydraulic stimulation (Grasby et al., 2012).

Plutonic geothermal systems are not widely developed globally. A close analog to those in the Canadian Cordillera can be found in the Central Alaskan Hot Spring Belt, where numerous thermal springs occur in close association with highly radioactive plutons (Kolker, 2008). At least one of these hot springs have been exploited for both electricity generation and direct-use (Chena hot springs; Holdmann, 2007), while others are exclusively direct-use (East, 1982). In both cases, thermal fluid is thought to ascend to the surface along pre-existing faults and fractures in the plutons (Kolker, 2008). Elsewhere, such as the Milford FORGE project in Utah, plutonic systems are targets for Enhanced Geothermal System development.

Plutonic geothermal systems rely on fault and fracture permeability to allow the circulation of fluids and exchange of heat. If those fractures are natural and pre-existing, it is critical that their orientation and kinematics are known, as they will introduce strong directionality to the fluid circulation pathways. If no permeable fractures exist, then it is critical that the state of stress in the crust is known, to facilitate development of Enhanced Geothermal Systems.

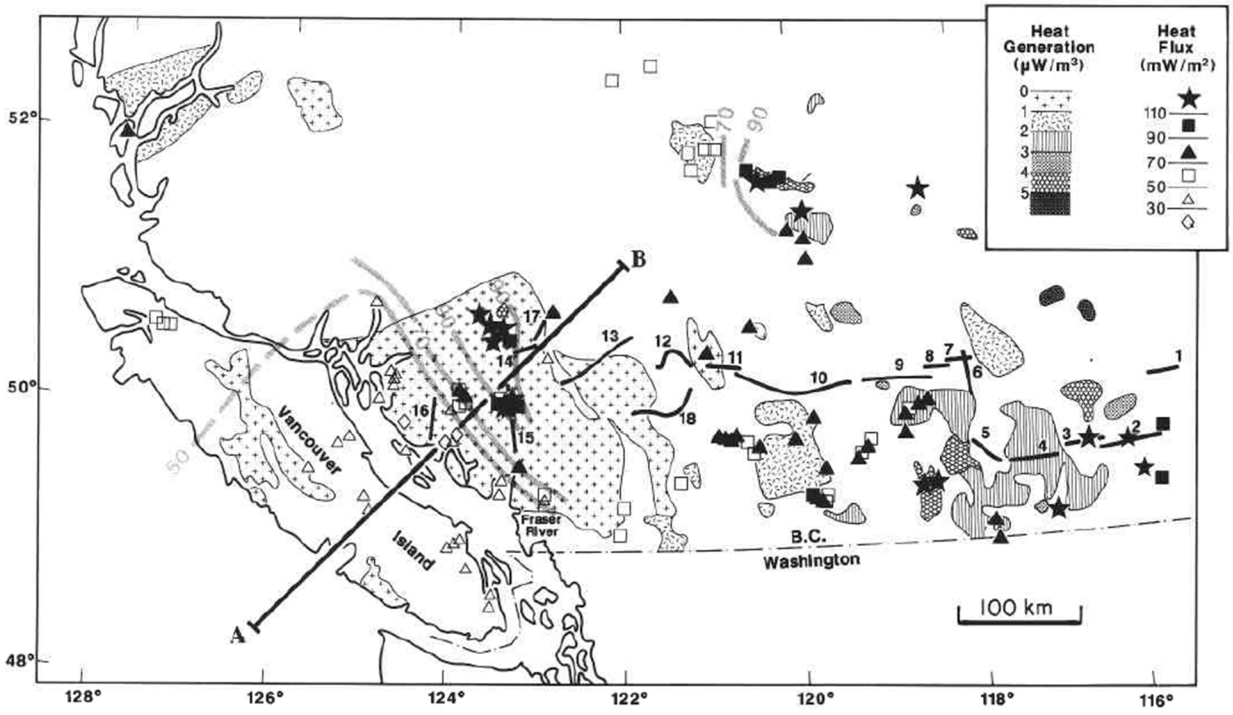

Figure 1.6. Heat generation from and heat flow near Mesozoic and Cenozoic Plutons in the southern Canadian Cordillera along the Lithoprobe transect (Lewis et al., 1992). Heat generation is generally higher in Mesozoic and Cenozoic plutons in the eastern part of the map.

1.4 Geothermal Research at the University of Alberta

The research described in this thesis was carried out in the geothermal energy research group at the University of Alberta. This group is part of the Future Energy Systems program and is one of the most active geothermal energy research groups in Canada. The goal of this research program is to undertake multidisciplinary research that will enable geothermal energy as a key part of Canada's transition to a low-carbon economy. Critically, it is recognized by researchers of this group that, in addition to technological innovation, the social and economic aspects of this transition must be considered.

This thesis focusses on important geological details that will guide geothermal energy development in fault-hosted systems in the Canadian Cordillera. However, this research can be placed in broader context by considering the multiple barriers that geothermal energy development faces in Canada, and which are being addressed through projects conducted by Future Energy Systems researchers:

1. Insufficient regulatory environments in some jurisdictions. Well-defined regulations concerning royalties, tax-incentives, resource ownership, and environmental protection are necessary for companies seeking to evaluate the economic potential of a natural resource. However, because

geothermal energy is not widely developed in Canada, many jurisdictions have not yet developed comprehensive regulations specific to geothermal projects. For example, the province of Alberta has not established a regulatory framework for geothermal wells, and this introduces uncertainty that makes investors hesitant to enter the market (Martin, 2018). Lobbying by advocacy groups (e.g., Canadian Geothermal Energy Association) as well as public pressure may prompt governments to develop or expand geothermal regulations. Public pressure will only occur if sufficient outreach efforts are made to inform the public of the benefits of geothermal energy. Regulations specific to geothermal energy project should be developed in consultation with economic researchers who have studied the successes and failures of geothermal regulations around the world.

2. Unfavourable market conditions that prevent geothermal energy from being cost-competitive: In jurisdictions with inexpensive electricity and heat, there may not be sufficient economic impetus to adopt new forms of energy. Furthermore, in energy markets already dominated by renewable energy, the public perception is that less effort should be spent exploring for new energy sources. In British Columbia for example, the electricity market is dominated by large-scale hydroelectric installations that contribute ample inexpensive, renewable, baseload power to the electrical grid. Additionally, many homes in BC are heated with natural gas, which is relatively inexpensive and perceived by many to be an acceptably low-carbon energy source. Consequently, there is little desire in BC to diversify the energy portfolio for electricity or heating, though this may change in the future, especially as electricity demand continues to rise (BC Hydro, 2019). A notable exception in BC is the Clarke Lake geothermal field near Fort Nelson: this remote First Nation community relies on electricity and heat generated via fossil fuel combustion, so there is increased incentive to transition to geothermal as compared to other parts of the province.
3. The need to obtain approval and social license from local people, particularly Indigenous groups: Many geothermal resources in western Canada are associated with thermal springs that have significant cultural value, both as recreational destinations, and as spiritual places for Indigenous People. To obtain social license from the public, geothermal development needs to respect these valuable cultural assets. Furthermore, geothermal developers are bound by law to engage and consult with Indigenous people at all stages of project. Many geothermal resources occur in proximity to First Nation communities, and while these communities could stand to benefit from the development of geothermal resources (e.g., replacement of aging diesel electrical generators), it is important that geothermal exploration programs respect their rights and wishes.
4. Inadequate technology to harness the low-temperature systems found in Canada: Most of Canada's geothermal resources are considered low-enthalpy, with lower thermal and potential

energy than conventional geothermal systems around the world. It is therefore important that existing technologies be optimized for this lower temperature range. In Alberta for example, most geothermal reservoirs have temperatures in the range of 70-90°C and require new technological innovation to be used to efficiently generate electricity (Banks, 2016). Technologies such as the Organic Rankine Cycle engines used at Chena Hot Springs in Alaska (Holdmann, 2007) could provide solutions for these low temperature resources. Alternatively, researchers at the University of Alberta are developing Stirling Engines optimized for geothermal resources in Canada (e.g., Stumpf, 2019).

5. Geological uncertainty about the location and nature of geothermal resources. There is significant uncertainty about the location, subsurface geometry, and thermodynamic properties of geothermal resources in Canada, largely due to sparse data coverage inherent to the vast Canadian landscape. More geological, geophysical, and geochemical data are required to understand the locations of geothermal resources on a regional scale, and their specific characteristics on a local scale.

This thesis addresses this last point by using geological and geophysical methods to image and characterize fault systems in southeastern BC that may provide the necessary pathways for geothermal fluids to reach the surface. Most known geothermal systems in southeastern BC are expressed at the surface by hot springs, which commonly occur along major fault zones. One of the largest outstanding questions is the role that these faults play in controlling the location and geometry of geothermal systems. An improved understanding of the structural and tectonic controls on spring location will aid in targeting future exploratory drilling and may also allow for the discovery of previously unknown geothermal systems. Southeastern BC is sparsely populated with the five largest population centers being Cranbrook (pop. 18,761), Trail-Fruitvale (pop. 12,643), Nelson (pop. 10,664), Castlegar (pop. 8039), and Revelstoke (pop. 7547), according to the 2016 Canadian census (Statistics Canada, 2017). While this region has been suggested to have potential for direct and electrical use of geothermal energy (Geoscience BC, 2015; Tuya Terra Geo Corp, 2016), many of the known geothermal systems are a considerable distance from population centers. Electrical transmission lines and direct-use geothermal pipelines both suffer from heat losses that cause a reduction of efficiency proportional to the distance from the power plant or geothermal well. Therefore, finding new resources closer to these population centers is essential if they are to be a viable heat or power source for these communities.

1.5 Conclusion

This thesis is focused on geothermal resources in southeastern British Columbia, some of which manifest at the surface as thermal springs. It is speculated that the heat source for these geothermal systems is in part the anomalous radioactivity in Cretaceous and Eocene plutons throughout the region (Lewis et al.,

1992; Grasby et al., 2012). Additionally, the crust is thin in this region (Hyndman and Currie, 2011), heat flow is high (Majorowicz and Grasby, 2010), and the geothermal gradient is relatively steep (Allen et al., 2006). There are no active volcanic systems within hundreds of kilometers of these geothermal resources, so molten magma is an unlikely heat source. The geothermal resources in this region are considered to be convective; meteoric water is believed to percolate down to depths of at least 2 km where it becomes buoyant and ascends to the surface along permeable fault structures (Grasby et al., 2000; Grasby and Hutcheon, 2001). The hydraulic head differential between mountain massifs and adjacent valleys likely contributes to the development of hydrothermal convection cells (Grasby and Hutcheon, 2001). Most of the geothermal resources in southeastern BC are likely low or medium temperature, and suitable for direct-use heating or possibly electricity generation via binary cycle power plant (Geoscience BC, 2015; Tuya Terra Geo Corp, 2016).

It is plausible that geothermal systems without surface manifestations (blind geothermal systems) exist in southeastern BC and have gone undiscovered due to thick vegetation and glacial overburden, as well as a low degree of exploration relative to prolific geothermal fields. Blind geothermal systems would actually be desirable development targets because the rare ecosystems surrounding hot springs (e.g., Grasby and Lepitzki, 2002) would not be disturbed, nor would there be a concern of damaging natural hot springs enjoyed by the public.

Several techniques in geology and geophysics can be used to search for blind geothermal systems. In geothermal systems where faults play a dominant role, structural geology can be used to predict the location of geothermal upwellings (e.g., Faulds and Hinz, 2015). Additionally, geophysical methods sensitive to the presence of fluids in the subsurface (e.g., magnetotellurics), can be used to image geothermal reservoirs at depth (Heise et al., 2008). In Chapter 2 of this thesis, fault kinematics and crustal stress state in southeastern BC are investigated in an effort to better understand the structural controls on geothermal systems in this region. In Chapter 3, geophysical and geological techniques are used to investigate fault architecture and subsurface fluid flow of a specific geothermal play near Valemount, BC.

Chapter 2: Cenozoic fault kinematics and crustal stress in southeastern BC: controls on the distribution of thermal springs and potential geothermal resources.

2.1 Abstract

Thermal springs in southeastern BC occur in association with several major fault zones, which may permit deep circulation of fluid through fractured reservoirs to depths greater than 2 km. Both the current stress field and the most recent kinematics of these faults likely play a strong role in localizing hydrothermal systems but are poorly resolved. In this chapter new data is presented from structural mapping along the Columbia River, Slocan Lake, Purcell Trench, Southern Rocky Mountain Trench (SRMT), and Redwall faults. The datasets of fault plane and slickenline orientations suggest a previously unidentified, post-Eocene phase of dextral strike-slip kinematics on reactivated Eocene normal faults. The NNE-SSW stress field required for these kinematics is similar to the present-day stress field derived from crustal earthquake focal mechanisms. There is a positive correlation between the location of springs and a broad region of low-level seismicity in southeastern BC. At smaller scales, geothermal upwellings may be localized by local zones of enhanced permeability including fault intersections and strain transfer zones.

2.2 Introduction

There has long been interest in developing geothermal energy in western Canada (Jessop et al., 1991; Grasby et al., 2012), but as yet, there are no operating geothermal power plants or direct heating systems (excluding shallow geo-exchange). Part of the problem is that there is limited geological understanding of the regions where geothermal potential is highest, particularly in the complexly deformed Canadian Cordillera of British Columbia (BC) and Yukon. Crustal heat flow in the Cordillera is relatively high (80–100 milliwatts per square meter [mW/m2]; Davis and Lewis, 1984), and the occurrence of more than 130 thermal springs (Figure 2.1a) has attracted the interest of geothermal developers. However, data constraining the subsurface are limited, which discourages investment.

Most geothermal systems occur in magmatically and tectonically active areas (e.g., western United States, Japan, New Zealand, Iceland). This is due in part to the elevated enthalpy in the crust, but also to the enhanced permeability of brittle faults, which act as conduits for circulating hydrothermal fluids. Several characteristics of fault zones influence their structure, including age and amount of seismic activity (e.g., Curewitz and Karson, 1997), kinematics (e.g., Meixner et al., 2016) and subsurface geometry (e.g., Moreno et al., 2018). Understanding these parameters is key to understanding the geothermal systems that fault zones may host.

Hydrothermal systems (i.e., thermal springs) in the Canadian Cordillera are broadly associated with major fault zones (Grasby and Hutcheon, 2001). However, the specific factors that localize thermal springs in the Cordillera are poorly resolved, and the location of potential blind systems (e.g., Faulds et al., 2015) is difficult to predict. This chapter focuses on the hydrogeologically-significant properties (kinematics, geometry, age and activity) of three major fault zones in southeastern BC — the Southern Rocky Mountain Trench (SRMT) fault, the Purcell Trench fault, and the Columbia River fault — all of which are spatially associated with hydrothermal systems. Herein are presented new structural data that allow us to identify a previously undocumented phase of post-Eocene dextral strike-slip faulting. The data suggest that the post-Eocene reactivation of pre-existing Cordilleran structures provides a primary constraint on the localization of potential geothermal systems in southeastern BC.

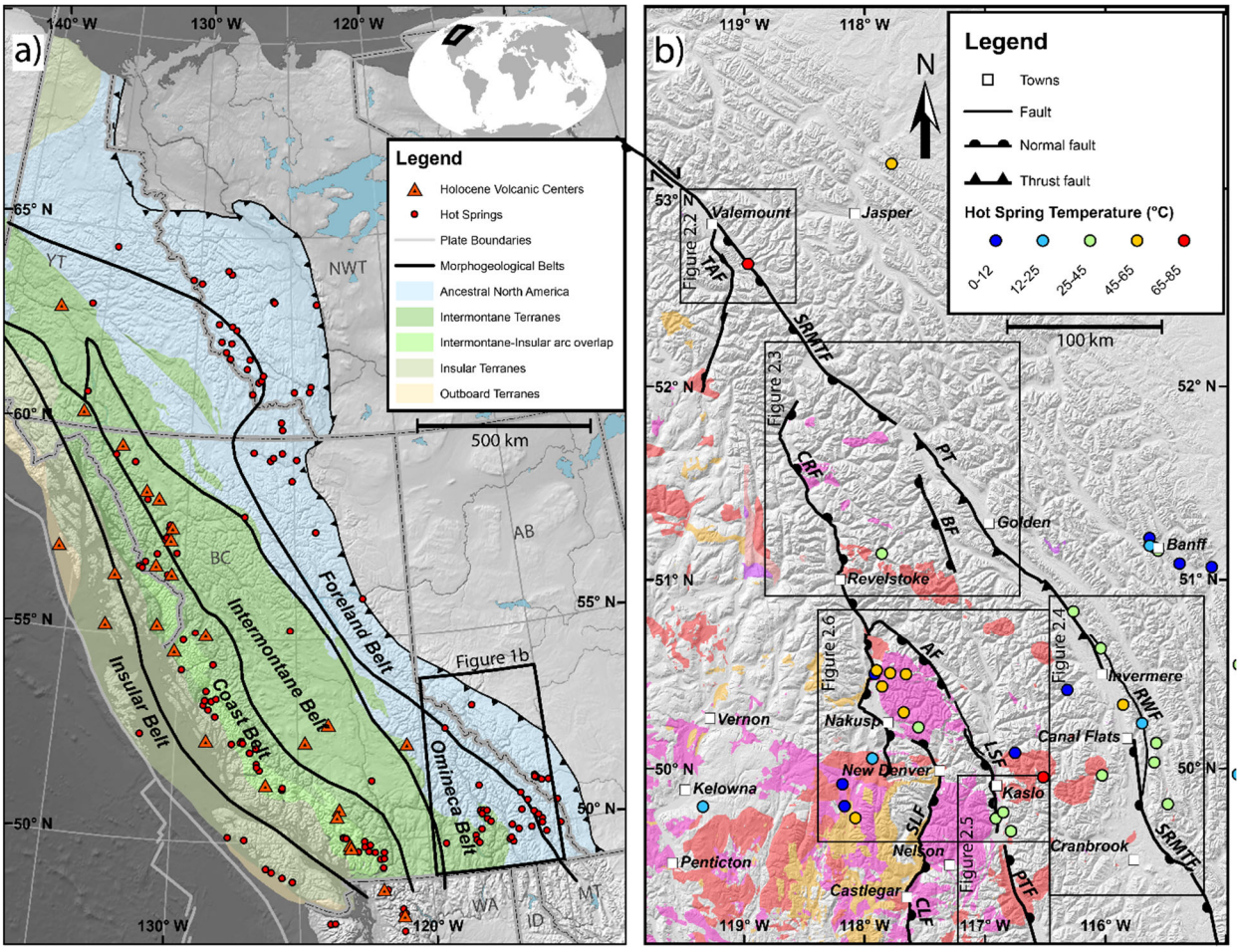

Figure 2.1. a) Regional geological setting of the Canadian Cordillera. Morphogeological belts are after Gabrielse et al. (1991), and the boundaries of ancestral North America and autochthonous superterranes (Intermontane, Insular, and Outboard) are after Colpron and Nelson (2011). Volcanoes active in the

Holocene (American Geological Institute, 2003) occur predominantly within the Coast Belt. Concentrations of thermal springs occur along the axis of the Coast Belt, in the northern Omineca and Foreland belts, and in the southern Omineca and Foreland belts (Woodsworth and Woodsworth, 2014). Note that the latter two clusters do not correspond to regions of active volcanism but do correspond to significant (>100 milliwatts per square meter [mW/m2]) heat-flow anomalies (see Majorowicz and Grasby, 2010). The region considered in this study lies within the southern Omineca and Foreland belts. b) Major faults in southeastern BC considered in this study. Abbreviations: AF, Adit fault; BF, Beaver River fault; CLF, Champion Lakes fault; CRF, Columbia River fault; LSF, Lakeshore fault; PT, Purcell Thrust; PTF, Purcell Trench fault; SRMTF, Southern Rocky Mountain Trench fault; RWF, Redwall fault; SLF, Slocan Lake fault; TAF, Thompson Albreda fault. Jurassic plutons are shown in pink, Cretaceous plutons in red, and Cenozoic plutons in orange after Cui et al. (2017). Black rectangles show regions considered in further detail in subsequent figures.

2.3 Background

2.3.1 Regional Geology

The Canadian Cordillera is an ~800 km wide orogen that stretches from the Arctic Ocean to the United States border, mostly within the Northwest Territories, Yukon, British Columbia, and Alberta. Its elevated topography, rugged relief and complex geology reflect a protracted and ongoing interaction between various oceanic plates, accreted terranes, and continental North America (Gabrielse and Yorath, 1991). For simplicity, the Cordillera can be divided into five major morphogeological belts (Figure 2.1a; Gabrielse et al., 1991). The easternmost Foreland Belt is composed of folded and thrusted—but largely unmetamorphosed—carbonate and siliciclastic rocks of an ancestral passive margin and a subsequent foreland basin. Adjacent and to the west is the Omineca Belt, which is dominantly composed of metamorphosed sedimentary rocks coeval with those in the Foreland Belt and deformed during the same mountain-building events. The Omineca Belt has been intruded by numerous Jurassic and Cretaceous continental arc–type plutonic suites (Armstrong, 1988), and tectonic windows expose metamorphosed crystalline rocks, interpreted as cratonic basement exhumed during Eocene extension (Parrish et al., 1988). Contractional deformation of the Omineca and Foreland belts is associated with Jurassic and younger accretionary and collisional events, including accretion of oceanic arc terranes that make up the more westerly Intermontane Belt (Evenchick et al., 2007). West of the Intermontane Belt lies the Coast Belt, which is largely composed of intrusive and metamorphic rocks associated with the Cretaceous to Eocene accretion of the westernmost Insular Belt that underlies Vancouver Island, Haida Gwaii and the Alaska Panhandle (Evenchick et al., 2007). Young and active continental arc volcanoes are being constructed atop the Coast Belt as a result of ongoing subduction of the Juan de Fuca Plate and other micro-plates off the western margin of the continent (Green et al., 1988). Active hydrothermal systems

occur in all five morphogeological belts of the Canadian Cordillera; this study is focused on those situated in the southern Omineca Belt, between 49 – 53°N (Figure 2.1b).

2.3.2 Sources and Expressions of Heat Flow in the Canadian Cordillera

The Cordillera is one of the most promising regions in Canada for geothermal energy development due to its high heat flow and elevated geothermal gradients (Grasby et al., 2012). Whereas much of eastern and central Canada is underlain by old and cold cratonic lithosphere and ancient orogenic belts, the Cordillera is geologically young and is subject to ongoing tectonic and magmatic processes that are conducive to the development of geothermal systems. Asthenospheric convection induced by the release of water from the subducting Juan de Fuca slab is thought to keep the Cordilleran lithosphere hot and elevated without the need for a thick continental root (Hyndman et al., 2005); the Cordilleran crust is only 30-35 km thick compared to the adjacent 40-45 km thick cratonic crust despite being significantly higher in elevation (Hyndman and Currie, 2011). Seismic tomography has revealed an east to west contrast in lithospheric thickness on the order of 150 km that roughly corresponds to the western edge of the Canadian Rockies (Bao et al., 2014; Chen et al., 2019). As a result of the thin crust and lithosphere, the heat flow is high and the geothermal gradient elevated within the Cordillera.

The presence of more than 130 thermal springs throughout the Cordillera (Figure 2.1a) provides a first-order indication that heat flow might be sufficient for geothermal energy extraction. Outlet temperatures of these springs range from 20 to 80°C (Woodsworth and Woodsworth, 2014). Chemical geothermometers, which estimate reservoir temperature based on solute concentrations and ratios at the spring outlets, indicate that the maximum temperatures reached by some of these systems exceeds 180°C, implying maximum circulation depths in the range of 2–5 km (Grasby and Hutcheon, 2001; Allen et al., 2006; Caron et al., 2007). Although thermal springs are not necessarily the best indicator of geothermal prospectivity (Ferguson and Grasby, 2011), they do provide a basic indication of geothermal resource potential, in a subsurface environment that is otherwise poorly constrained by data.

The geothermal gradient of the Cordillera ranges from 20 to 50°C/km (Hitchon, 1984; Lewis et al., 1992; Grasby and Hutcheon, 2001). These values, though lower than most conventional (high enthalpy) geothermal energy resources, are similar to gradients measured in low enthalpy systems being explored and developed for electricity generation in Europe and New Zealand (Agemar et al., 2014; Reyes, 2015; Farquharson et al., 2016). Crustal heat flow in the Cordillera ranges from ~40 to 130 mW/m^2 (Hyndman and Lewis, 1995; Blackwell and Richards, 2004; Majorowicz and Grasby, 2010). Heat flow is locally very high (>200 mW/m^2) near active volcanoes in the Garibaldi volcanic belt in southwestern BC (e.g., Mount Meager), but these values do not reflect the bulk thermal conditions in the Cordillera. In several

broad regions heat flow exceeds 100 mW/m^2 (see Majorowicz and Grasby, 2010), which is comparable to geothermal energy–producing regions such as Nevada and Utah (Blackwell and Richards, 2004).

Interestingly, one of these regions of elevated heat-flow, the southern Omineca Belt (Columbia Mountains) of southeastern BC, does not contain any active or recently active volcanoes, which suggests that in addition to the regionally thin crust and steepened geothermal gradient (Hyndman and Currie, 2011) the anomalous heat might come from radiogenic sources in crustal granitic intrusions. Indeed, radioactive heat generation measured in Cretaceous and Paleogene intrusive suites is high in the Omineca Belt (Figure 2.1b; Lewis et al., 1992). These intrusive suites are pervasive throughout the Omineca Belt and many occur in close association with large scale faults that cut through the region.

2.3.3 Fault Zones and their Relation to Hydrothermal Systems

Fault zones typically have an anisotropic permeability structure, dependent on the relative percentages of clay fault gouge and fractured wall rock (Caine et al., 1996). Typically, cross-fault flow is impeded by the impermeable (clay rich) core material, while along-fault flow is facilitated by the permeable damaged (fractured) zone. Grasby and Hutcheon (2001) presented a conceptual model for hydrothermal convection cells in the Canadian Cordillera in which meteoric water percolates vertically down through the crust until it encounters a shallowly dipping fault plane, and is then forced back up to the surface via the damaged zone conduit. Because faults typically crop out in valleys due to accelerated erosion of comminuted fault rock, there is a natural topographic drive to such systems, with recharge occurring in mountainous highlands.

Grasby and Hutcheon (2001) compared several parameters, including heat flow, permeability, topography/relief, infiltration rate, and the presence of fault zones, with regards to their influence on the location of thermal springs in the southern Canadian Cordillera. Ultimately they determined that—with the exception of springs near the Pliocene to recent Mount Meager volcanic complex (Read, 1990)—fault zones act as a primary control on the position of thermal springs in the Canadian Cordillera, whereas the other factors have a negligible influence. From east to west, the significant fault zones in the southeastern Cordillera identified by Grasby and Hutcheon (2001) as hydrogeologically significant are (see Figure 2.1b): SRMT fault, Purcell Trench fault, Columbia River fault, Okanagan fault, Harrison Lake fault, and West Coast fault. We are primarily concerned with the easternmost three faults. These three structures have been interpreted as steep- to shallow-dipping Eocene normal faults with variable amounts of displacement that record post-compressive extension of the Cordillera (Lane, 1984; Parrish et al., 1988; van der Velden and Cook, 1996; Doughty and Price, 2000).

What remains unanswered is why thermal springs cluster in certain regions of the Cordillera, why some faults host thermal springs while others do not, and why thermal springs are distributed unevenly along these fault zones. Variations in crustal heat flow, precipitation/infiltration rate, and topographic relief occur on wavelengths of hundreds of kilometers, which are too broad to explain the pattern of hot spring occurrence (Grasby and Hutcheon, 2001; Ferguson and Grasby, 2011). It is therefore likely that inter- and intra-fault variations in geometry, kinematics, and permeability structure are critical controls on the localization of thermal springs. In addition to improving understanding of known hydrothermal systems, answering these questions may help identify hidden geothermal resources, also known as "blind" geothermal systems.

It has been shown in other structurally-controlled geothermal systems that the current stress state of the crust and resulting fault kinematics can predict which fault segments are the most permeable; faults oriented parallel or oblique to S_{Hmax} (maximum horizontal compression) are more likely to be permeable because of their tendency to dilate or slip, respectively, whereas those oriented perpendicular to S_{Hmax} are more likely to remain sealed (Barton et al., 1995; Meixner et al., 2016). Furthermore, there is a positive correlation between strain rate and fault permeability and seismic activity has been shown to maintain fault permeability via episodic refracturing of minerals precipitating within the fault zone (Curewitz and Karson, 1997). Within seismically active regions with favourably-oriented faults, specific structural settings have been shown to be especially favourable to hydrothermal upwelling. Sibson (1996) showed that in fault-fracture "meshes" high structural permeability develops parallel to fault-fracture intersections (often parallel to σ_2, the intermediate stress axis). Curewitz and Karson (1997) reviewed 25 hydrothermal fields around the world and suggested that stress concentration at fault tips, fault interaction zones (releasing and restraining bends), and fault intersections promoted long-lived fracture permeability and therefore hydrothermal upwelling. In the highly structurally-controlled geothermal fields of the Great Basin in Nevada, Faulds and Hinz (2015) categorized the structural settings of 426 geothermal systems and found that zones of greater structural complexity (e.g., relay ramps, step-overs, fault terminations, fault intersections, etc.) host the majority of geothermal systems due to enhanced permeability across multiple fractures. Based on this work, the locations of previously unidentified blind geothermal systems have been successfully predicted via detailed mapping and identification of favourable structural settings (e.g., Craig et al., 2017). A similar approach may be appropriate for the amagmatic, fault-associated hydrothermal systems in British Columbia.

Given that recent fault activity exerts the strongest control on fault permeability, it is important to understand the most recent tectonic history of the Canadian Cordillera. Following the Jurassic to Paleocene contractional phase of deformation that built the Canadian Cordilleran orogen, it is widely

believed that a reduction in marginal compressive stress and resultant gravitational collapse of the orogen (Armstrong, 1982; Coney and Harms, 1984; Parrish et al., 1988; Vanderhaeghe and Teyssier, 1997) led to the development of an array of normal faults in the Eocene, particularly in the southeastern Cordillera. These structures are among those that appear to localize thermal spring outlets (Grasby and Hutcheon, 2001). Below, the fault zones considered in this study and the active hydrothermal systems they host, are summarized.

2.4 Study Areas

2.4.1 The SRMT fault and related structures

The SRMT constitutes the southern segment of a nearly 3000 km long topographic lineament that stretches from northwestern Montana, through eastern British Columbia, across the Yukon Territory, ultimately terminating north of Fairbanks, Alaska. The segments of this lineament in northern BC and Yukon are known as the Northern Rocky Mountain Trench and Tintina Trench, respectively, and these are known to host major Eocene dextral faults (Roddick, 1967; Gabrielse, 1985; Pope and Sears, 1997; McMechan, 2000). The SRMT is instead occupied by a steeply west-dipping normal fault—the SRMT fault—for much of its length. A shallowly west-dipping Cretaceous thrust fault, the Purcell Thrust crops out along the west wall of the SRMT, and it is worth noting here that this structure is unrelated to the similarly named Purcell Trench fault.

Evidence for extensional displacement is documented near the town of Valemount, BC; McDonough and Simony (1988) noted a “crush zone” with west-side-down dip-slip slickenlines on the northeast shore of Kinbasket Lake and estimated that it offsets the Paleoproterozoic gneisses of the Malton Gneiss Complex by less than 2 km (Figure 2.2). 100 km to the south, between the Solitude and Adamant ranges, Gal and Ghent (1990) proposed 2 km of west-side-down displacement to explain the apparently undisturbed metamorphic isograds; southwest-side-up movement on the post-metamorphic Purcell Thrust would have truncated the isograds, but normal dip-slip on the SRMT fault may have restored them to their approximate original positions.

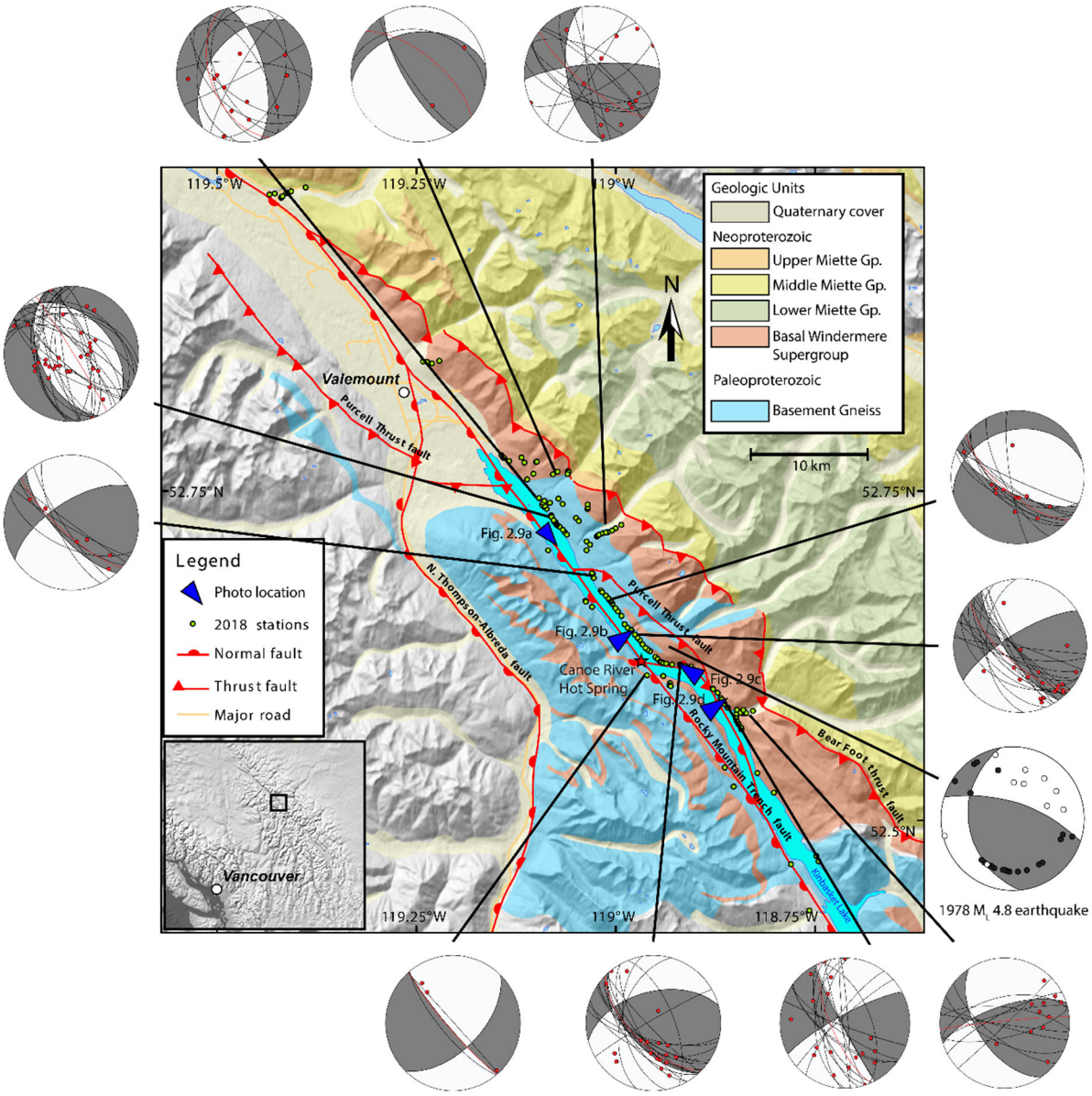

Figure 2.2. Geology of the Valemount and northern Kinbasket Lake (Canoe Reach) area, after Murphy (2007). Green dots are sites that were examined in the field. Lower-hemisphere stereonets ('beachball' plots) show fault plane (black great circles) and slickenline orientations (red dots) for subsets of data collected as part of this research. White compressional (P) and grey dilational (T) quadrants represent the average kinematics for each subset. The focal mechanism determined from P-wave first motion polarities (black dot = up, white dot = down) for the 1978 Richter magnitude (ML) 4.8 McNaughton Lake earthquake (Rogers et al., 1980) is provided for comparison (second lowest on right). Blue triangles point in direction of photos shown in Figure 2.9.

At the south end of Kinbasket Lake the SRMT widens considerably (Figure 2.3), and mapping has failed to identify any normal faults for a 150 km interval to the south. Instead, the Purcell Thrust, which places metamorphosed rocks from the west over unmetamorphosed rocks to the east (Kubli and Simony, 1994), is the main fault occupying the valley floor. At the south end of Kinbasket Lake the Beaver River normal fault diverges from the SRMT fault at a ~20° angle to the west (Figure 2.3; Poulton and Simony, 1980), occupying the floor of the northernmost Purcell Trench (see Section 2.4.2 below). An alternative suggestion is that the SRMT fault (variably mapped as the Chancellor fault, e.g., Gal and Ghent (1990)) diverges ~15° to the east, ultimately merging with the "White River Break" (Figure 2.4) of Henderson (1954) and North and Henderson (1954a, 1954b), which has variably been interpreted as a thrust fault, or dextral shear zone (Charlesworth, 1959).

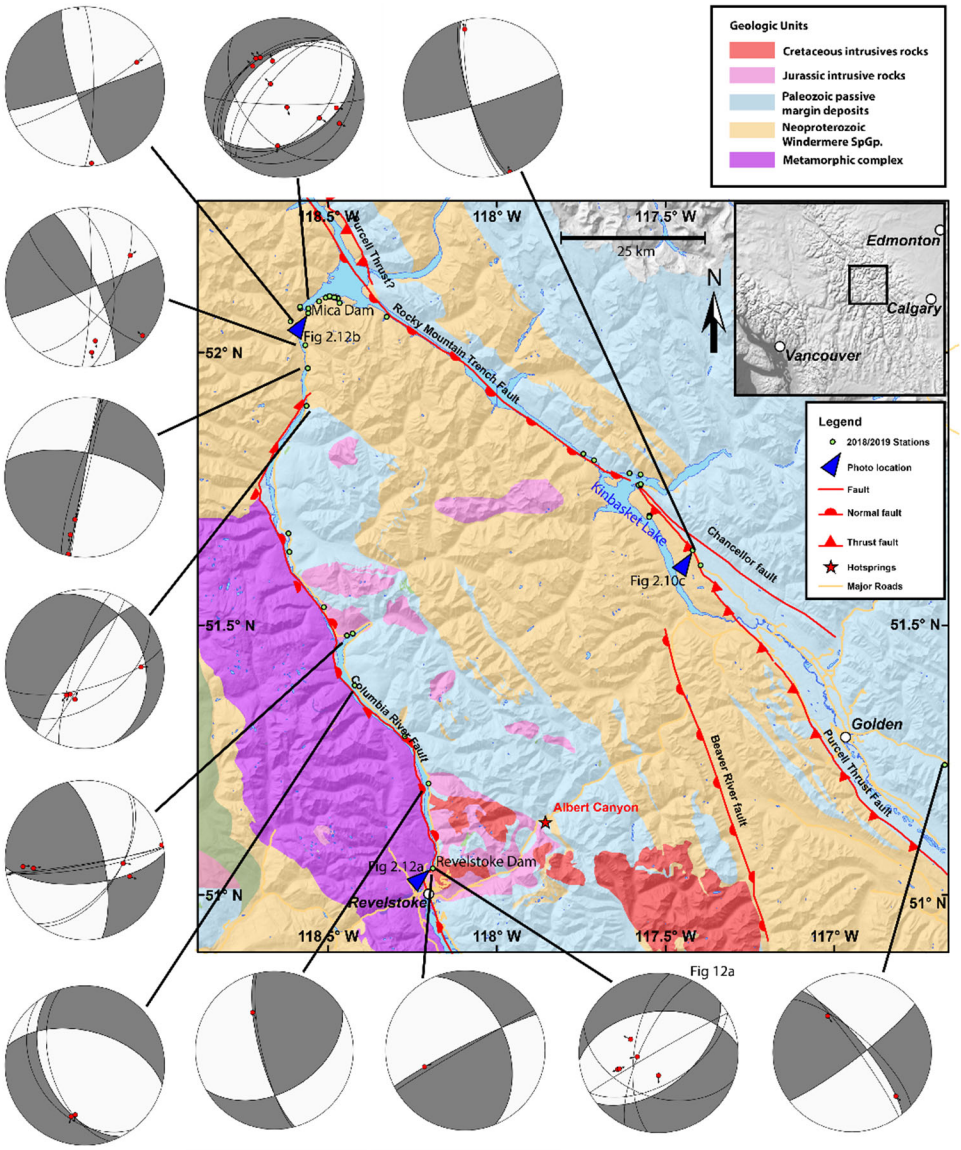

Figure 2.3. Geology of the Big Bend area, north of Golden and Revelstoke, after Cui et al. (2017). Lower-hemisphere stereoplots ('beachballs') show fault plane (black great circles) and slickenline (red dots) orientations for subsets of data collected as part of this research. P (white) and T (grey) quadrants represent the average kinematics for each subset. Blue triangles point in direction of photos shown in Figures 2.10 and 2.12.

In the southernmost part of the trench near Cranbrook, the distribution of Miocene sediments suggests that extensional block faulting occurred along the SRMT from the Eocene to Pliocene or younger (Clague, 1974). Seismic reflection profiles and balanced cross sections at this latitude (49-54 °N) indicate at least 10 km of dip-slip offset across the SRMT fault (Höy et al., 1993; van der Velden and Cook, 1996).

Eight thermal springs occur in the vicinity of the SRMT. Thirty kilometers south of Valemount, the Canoe River spring discharges on the southwestern shore of Kinbasket Lake (Figure 2.2) near the intersection of a splay and the main strand of the SRMT fault (McDonough and Morrison, 1990). South of Canoe River there is a 270 km segment of the trench where no springs occur. This gap roughly corresponds to the segment of the trench where the valley floor is occupied by the Purcell Thrust. At the south end of this gap, the Wolfenden warm spring occurs along the floor of the trench near the town of Spillimacheen. Farther south, the Radium and Red Rock springs are closely associated with the Redwall fault, while the Lussier, Ram Creek, and Wildhorse springs occur along the Lussier River fault. Both of these faults lie parallel to and 10-20 km to the east of the SRMT. The Fairmont spring occurs along the main trench valley, and although no faults are mapped at its location, the SRMT fault and Hall Lake fault both project underneath thick Quaternary cover towards its location.

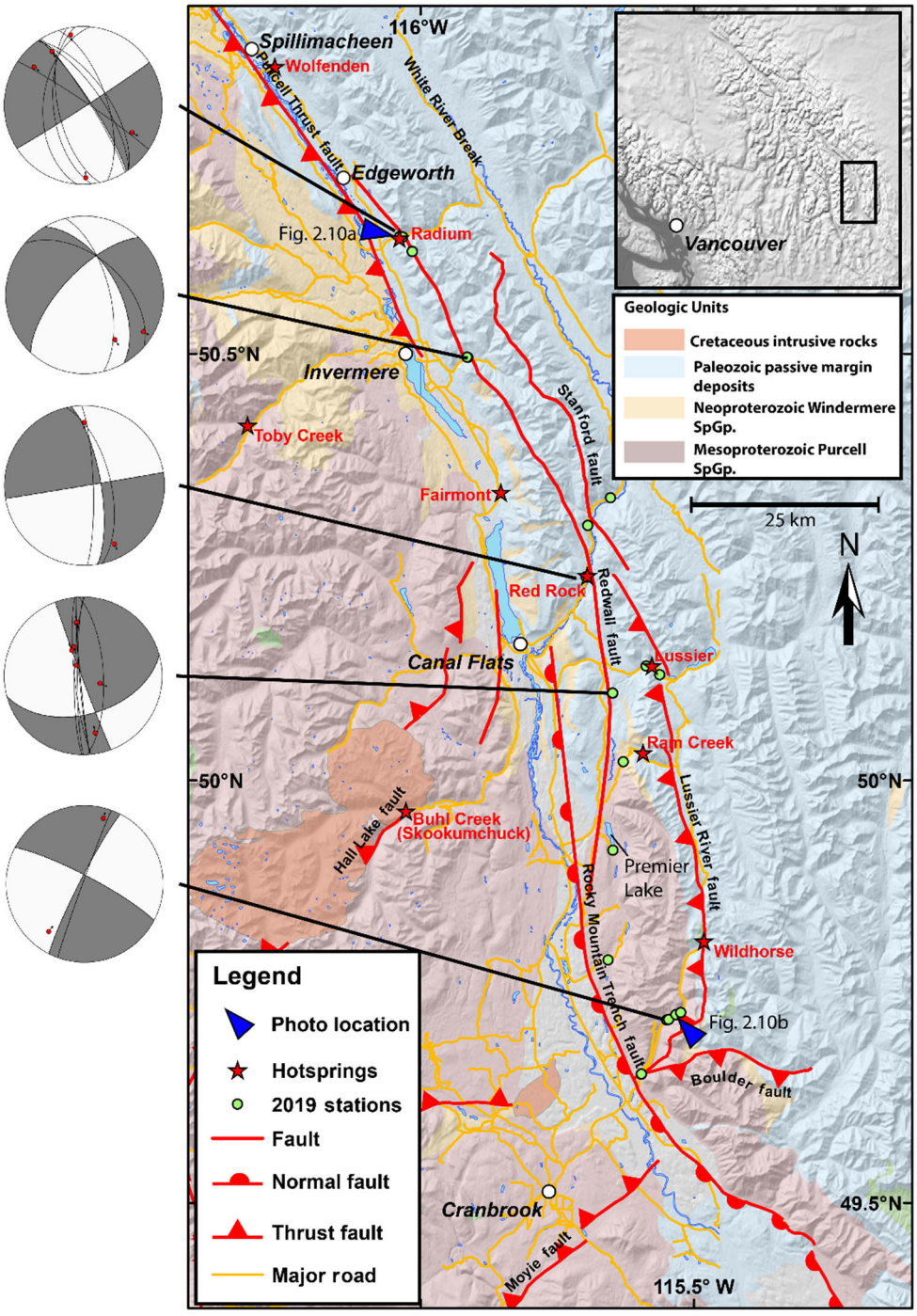

Figure 2.4 Geology of the SRMT from Radium to Cranbrook, after Cui et al. (2017). Lower-hemisphere stereoplots ('beachballs') show fault plane (black great circles) and slickenline (red dots) orientations for subsets of data collected as part of this research. P (white) and T (grey) quadrants represent the average kinematics for each subset. Blue triangles point in direction of photos shown in Figure 2.10.

The Redwall fault is an enigmatic structure that has not been investigated in great detail since it was first mapped by Henderson (1954). Its surface trace extends from the hamlet of Edgeworth, passing east of

Radium Hot Springs. It continues south along the Stanford Range, intersecting the Kootenay River at the Red Rock warm springs, before its surface trace is lost near Premier Lake. It has been suggested that it merges with the Lussier River fault to the south (Foo, 1979), which also hosts several thermal springs. The fault is subvertical for its entire length, leading several authors to conclude that it originated as a strike-slip fault characterized by either sinistral (Henderson, 1954) or dextral (Charlesworth, 1959) motion. Alternatively, Foo (1979) considered the Redwall fault to be a back-rotated thrust fault.

The Redwall fault is so-named due to the striking red colour of the fault zone, caused by hematite oxidation. The fault zone occurs in conjunction with a zone of subangular to subrounded, matrix-supported pebble to boulder conglomerate. This texture was originally interpreted to represent a zone of Cretaceous fault breccia (Henderson, 1954), but subsequent investigations have suggested that most of the breccia may be due to pre-Cretaceous evaporite-solution collapse (e.g., Stanton, 1966), a theory supported by the proximity of extensive gypsum deposits (Henderson, 1954). Stratigraphic offsets, and evidence of shearing within the solution-collapse breccia, indicate that it has subsequently been reworked by faulting (of hitherto uncertain kinematics), with strain concentration possibly occurring in the rheologically-weak evaporites.

2.4.2 The Purcell Trench fault

The Purcell Trench is a major north-trending valley that begins in northern Idaho and merges northward with the SRMT at 51°N. It is occupied for much of its length by Kootenay Lake. A sharp east-west contrast in metamorphic grade across the southern trench has led some to map an east-side-down normal fault—the Purcell Trench fault—along its southern segment (Figure 2.5; Doughty and Price, 1999, 2000). Note that the Purcell Trench fault is confusingly not the same as the Purcell Thrust, which lies in the SRMT to the east. The Purcell Trench fault is mapped from northern Idaho as far north as Crawford Bay (Doughty and Price, 2000; Brown and MacLeod, 2011; Cui et al., 2017). Along the central and northern reaches of Kootenay Lake, several west-dipping normal faults (Gallagher, Josephine, and Lakeshore-Schroeder faults) on the western shore may be genetically related to the Purcell Trench Fault (Moynihan and Pattison, 2008). North of Kaslo, the valley bifurcates into the NNW-trending Trout Lake valley and the north-trending Duncan Lake valley. The Lakeshore-Schroeder fault parallels the western edge of the Trout Lake valley, and may merge with the east-side-down Adit fault (Thompson and Dhesi, 2009; Kraft et al., 2011). No extensional structures are mapped in the southern Duncan Lake valley for ~75 km northward. In the northern-most segment of this valley, the east-dipping Beaver River normal fault, which truncates the western boundary of the Dogtooth duplex near Golden, was mapped by Poulton and Simony (1980) and Kubli and Simony (1994).

The Purcell Trench hosts one major hot spring, located at Ainsworth. It discharges from calc-silicate rocks in the immediate footwall of the Eocene Lakeshore fault on the western side of central Kootenay Lake. On the east side of the lake, warm water discharges in the subsurface of the Bluebell Mine at Riondel (Desrochers, 1992), and there is rumoured to be a warm spring east of Crawford Bay (Woodsworth and Woodsworth, 2014).

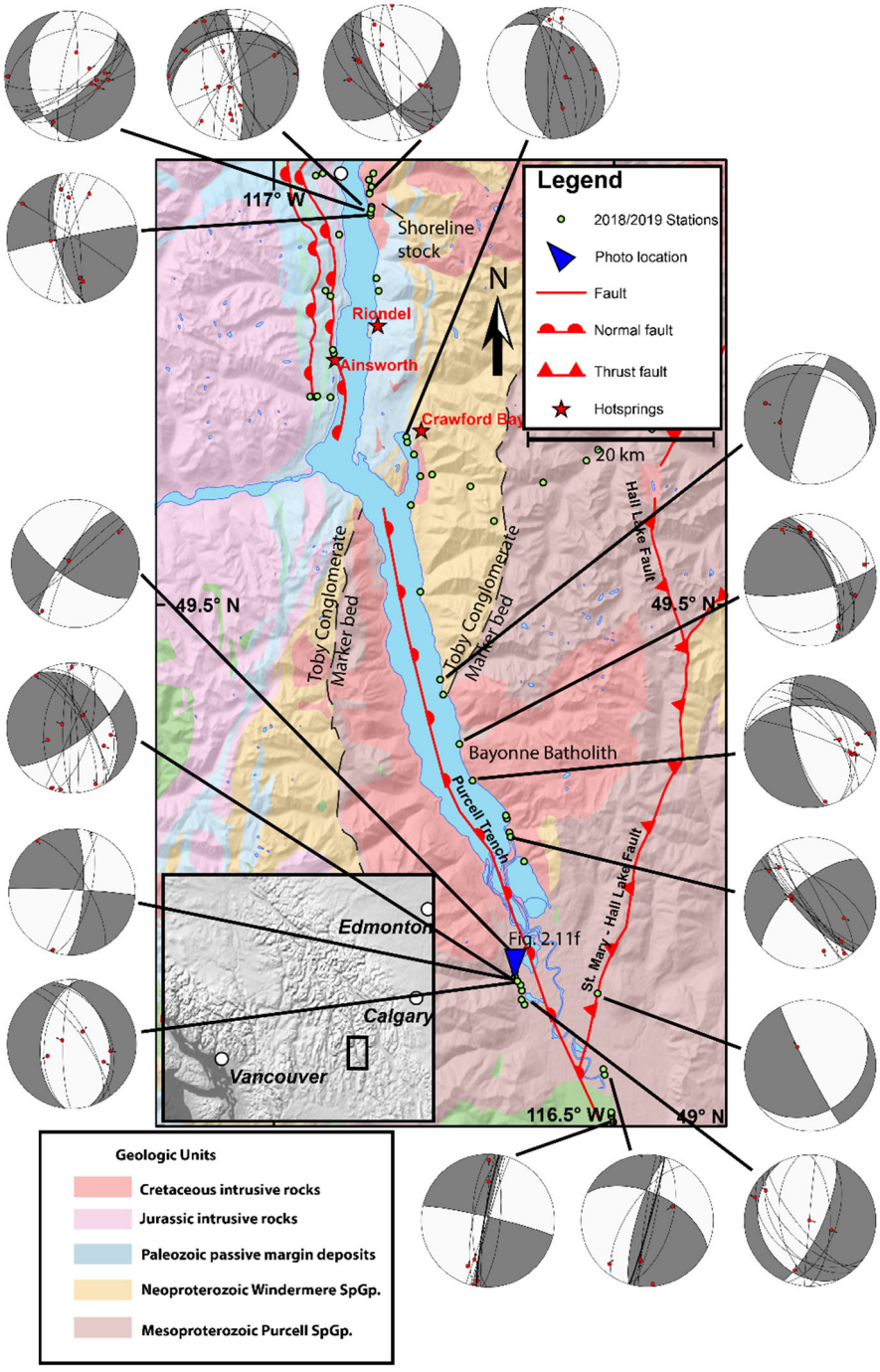

Figure 2.5. Geology of the southern Purcell Trench after Cui et al. (2017). Lower-hemisphere stereoplots ('beachballs') show fault plane (black great circles) and slickenline (red dots) orientations for subsets of data collected as part of this research. P (white) and T (grey) quadrants represent the average kinematics for each subset. Blue triangles point in direction of photos shown in Figure 2.11. The Toby Conglomerate marker bed provides a constraint on the magnitude of dextral separation across the Purcell Trench.

2.4.3 The Columbia River fault and Slocan Lake-Champion Lake fault system

The Columbia River fault and Slocan Lake fault system approximately follow the eastern boundary of the amphibolite- to granulite-grade Shuswap composite metamorphic complex (specifically the Monashee and Valhalla complexes). For much of their length the brittle exposures of the Columbia River fault and Slocan Lake-Champion Lake faults are coincident with and overprint the surface traces of broad zones of ductile shear: the Monashee Décollement and Valkyr shear zone, respectively, which arch over the metamorphic complexes to the west (Read and Brown, 1981; Lane, 1984; Carr et al., 1987).

The Columbia River fault extends ~225 km southward from the Mica hydroelectric dam (52°N) to the hamlet of Burton on Lower Arrow Lake (50°N). Dip-slip displacements estimated on the basis of offset metamorphic isograds range between <1 km (Lemieux et al., 2003), 1–10 km (Lane, 1984), 15–80 km (Read and Brown, 1981) and 30 km (Parrish et al., 1988). Excavations during the construction of the Revelstoke hydroelectric dam in the late 1970s provided the opportunity for detailed structural analysis of the brittle Columbia River fault; Lane (1984) measured the orientation of kinematic indicators at the dam site and at several sites along Highway 23 to the north of the dam. He concluded that primary displacement was extensional dip-slip, with a later phase of dextral strike-slip motion that was deemed insignificant. He also speculated that the right-hand step in the trace of the fault at the dam site might be associated with vertical axis rotation during dextral transpression. South of Revelstoke, the fault is parallel to Upper Arrow Lake, and a segment is mapped onshore on the east side of the lake immediately south of the Galena Bay ferry terminal (Kraft et al., 2011). Near Halcyon Hot Spring, the fault swings southwest across the lake, and then trends parallel to the west side of Saddle Mountain before terminating at the hamlet of Burton (Figure 2.6).

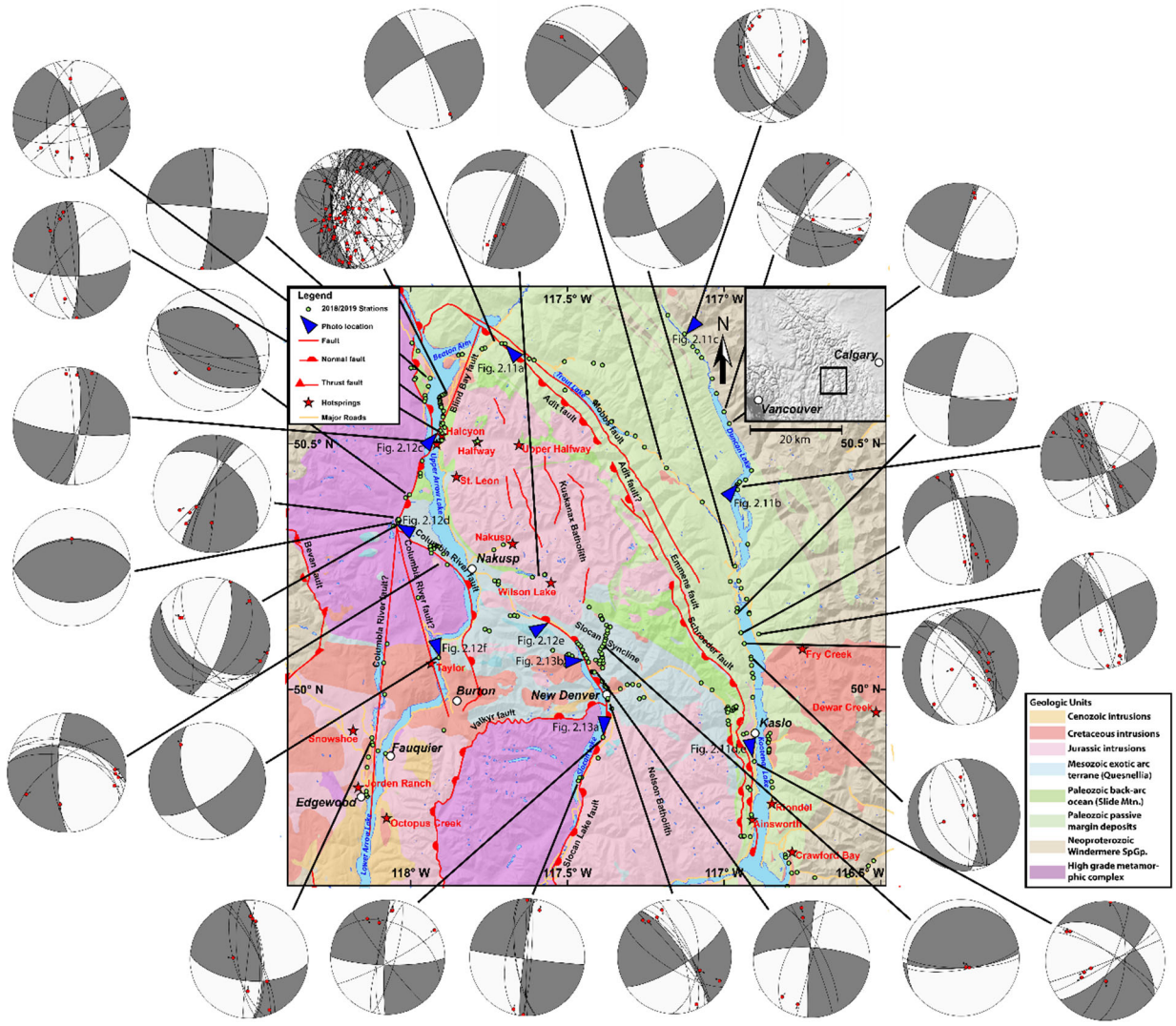

Figure 2.6. Geology of the Purcell Trench, Slocan Lake fault, and southern Columbia River fault, after Cui et al. (2017). Lower-hemisphere stereoplots ('beachballs') show fault plane (black great circles) and slickenline (red dots) orientations for subsets of data collected as part of this research. P (white) and T (grey) quadrants represent the average kinematics for each subset. Blue triangles point in direction of photos shown in Figures 2.11, 2.12, and 2.13.

The Slocan Lake-Champion Lake fault system extends ~140 km from Summit Lake along Highway 6 between Nakusp and New Denver, south along Slocan Lake, through Castlegar, ending near Montrose. Ductile and brittle normal shear in the central segment of the fault is thought to amount to at least 10 km (Parrish, 1981; Carr, 1986). Interpreted deep seismic reflection profiles suggest that the fault zone dips shallowly east, penetrating the Moho (Cook et al., 1992). South of Castlegar, the Champion Lake segment is mapped as a moderate to steeply (40–80°) east-dipping normal fault with a minimum of 1–2 km of offset (Corbett and Simony, 1984).

Many of the springs associated with the Columbia River fault occur in the vicinity of Nakusp. The commercially developed Halcyon spring discharges on the east shore of Upper Arrow Lake, along the mapped trace of the Columbia River fault (Kraft et al., 2011). Several springs—Upper and Lower Halfway, St. Leon, Nakusp (commercially developed), and Wilson Lake—issue from within or adjacent to the Jurassic Kuskanax batholith, which underlies most of the mountain range to the northeast of Nakusp (Parrish and Wheeler, 1983; Thompson et al., 2009b). Several warm springs—Snowshoe, Jorden Ranch, Octopus Creek, and Taylor—occur along the shores of Lower Arrow Lake south of Nakusp, along lineaments possibly connected to the Columbia River fault. No identified warm springs occur along the Slocan Lake-Champion Lake fault, however several mineral seeps are present along Highway 6 southeast of Nakusp. The Slocan Lake-Champion Lake fault is included in this study because of its likely kinematic link to the Columbia River fault system.

2.4.4 Summary

In summary, faults within the SRMT, Purcell Trench, and Columbia River valley, are all known to have accommodated Eocene ductile and brittle extension. Estimates of offset on individual structures vary widely between 1-80 km. In most cases, the magnitude and kinematics of slip has been estimated by recognizing offset strata and metamorphic zones rather than through detailed kinematic analysis of the fault zones themselves. While many of the Eocene normal faults in southeastern BC are steeply dipping and brittle, a few have very shallow dips, and ductile kinematic indicators (e.g., Columbia River and Slocan Lake faults). Little attention has been paid to the post-Eocene kinematics and activity of these faults, which is arguably the most consequential time period when considering structural permeability. Eocene extension is generally held to be the most recent phase of kinematics, but the results presented herein demonstrate otherwise.

2.5 Methods

Detailed structural fieldwork was conducted in the summers of 2018 and 2019 over nine weeks in the triangular region between Valemount, Castlegar, and Cranbrook (Figure 2.1b). Special attention was paid to the structure in the vicinity of Valemount, Nakusp, and Kaslo due to the commercial interest and demonstrated potential for geothermal development in these areas (Desrochers, 1992; Ghomshei, 2007; Kimball, 2010; Geoscience BC, 2015). Exposures of previously studied brittle faults were specifically targeted and many newly documented outcrops and fault exposures were visited. Work focused on road- and highway-side outcrops, and on lake shorelines where kinematic indicators were most likely to be exposed on fresh surfaces. Representative measurements were made of all observable phases of kinematic indicators. Cross-cutting relationships were documented in order to constrain the relative timing of deformation (see Appendix A). Nearly 700 orientation measurements of fault planes, slickenlines, and

other kinematic indicators were collected (see Appendix B for the full data set). Simultaneous dip and dip-direction measurements were collected with a Brunton Geo Pocket Transit compass. Care was taken to avoid mistaking Riedel shears – which provide an ambiguous sense of slip – for the more diagnostic mineral (quartz and/or calcite) growths on the lee side of fault plane asperities (Petit, 1987). Slickenlines were ranked on a relativistic confidence scale of 1-3, where 1 indicated an ambiguous sense of slip, 2 indicated a preferred, but not certain, sense of slip and 3 indicated an unequivocal sense of slip. Those with rankings of 1 were excluded from kinematic analyses but included in statistics of fault dips and slickenline plunges. Data were collected using ArcGIS collector on a GPS-enabled iPad Pro, which allowed for efficient, spatially accurate collection of hundreds of structural data points, along with real-time annotation of photographs. Georeferenced geological maps were used to locate exposures of faults mapped by previous workers.

Due to the scatter inherent to structural orientations collected over such a large geographic scale, the measurements were subdivided based on geographic location, orientation, and kinematics, to more clearly illustrate the trends and clusters. Data were divided into local clusters collected within a radius of at most 10 km to display local variation within fault zones. On a regional scale, data for each fault zone—the Columbia River, Slocan Lake, Purcell Trench, and SRMT faults—were separated to show any variation in kinematics between each major structure. All groups of orientations were plotted on equal-area lower-hemisphere stereoplots using Orient software (Vollmer, 2019). Angular misfits between the measured fault plane and slickenline pairs provided an indication of data quality, and those with misfits greater than 20° were discarded. Misfits were not artificially corrected by rotating the slickenline into parallel with the fault plane, as this procedure did not significantly affect the results of the subsequent kinematic analysis and doing so would obscure real error in the data. Beachball plots and accompanying P, M, and T axes were calculated from the average kinematics of each set of structural measurements. On these plots, the black great circles illustrate the strike and dip of fault planes, and the red great circle shows the average fault plane within the data cluster. The red dots show the trend and plunge of slickenlines, and arrows attached to the red dots show the direction of hanging wall movement. The white and grey quadrants of the beachballs indicate the average orientation of P (compressional) and T (tensional) axes respectively. These are determined based on the assumption that the P axis will be 45° to the fault plane, which is a poor approximation for singular fault planes, but reasonable when combining many measurements. Beachball plots for data clusters of local kinematics within fault zones accompany maps in Figure 2.2 to Figure 2.6, and clusters corresponding to entire fault zones are shown in Figure 2.7. The kinematics for each measurement were further categorized according to slickenline rake (sinistral=0°, dextral=180°, normal=-90°, reverse=+90°), and plotted on a rose diagram (circular histogram) to represent the relative proportions of each group (Figure 2.8).

Measurements in each fault zone were filtered based on the regional trend of each fault-occupied valley. Because each valley is already known to host a major fault, it is reasonable to assume that most significant fault planes parallel the valley trend regardless of their kinematics; this assumption is supported by the fact that the majority of the planes and kinematic indicators collected in this study record valley-parallel strike-slip and valley normal dip-slip. A threshold value of 30° to the average valley trend was used so as to capture most fault strands that fall within the possible range of R and P shears (which would ideally be oriented 15° to the main fault occupying the valley; Dresen, 1991), and to exclude any potential antithetic R' and P' shears (which would ideally be oriented 75° to the valley). The valley-parallel filtered data were then divided into groups based on their kinematics. The unfiltered and filtered datasets are shown in Figure 2.7.

2.6 New Results & Observations

Our dataset of brittle fault kinematic indicators provides evidence for widespread dextral strike-slip on the three major fault systems in southeastern BC. Of the 662 fault-slickenline pairs we collected, 42.6% indicate dextral and dextral-oblique slip, 24.9% indicate pure normal slip, 21.5% indicate sinistral and sinistral-oblique slip, 6.6% indicate reverse, and the remainder are ambiguous. A full table of kinematic indicators is provided in Appendix A. When plotted according to rake (Figure 2.8c), two distinct populations emerge: dextral and normal. Most fault planes measured in the field were minor and did not have broad damage zones or mature clay gouge, which suggests that they represent minor splays of larger faults assumed to be beneath lakes and glacial overburden in valley bottoms. Where large fault zones with broad zones of breccia and gouge were observed, they were most commonly dextral (Figure 2.8d). Of the sinistral fault planes, 54.9% strike at high angles (>30°) to the strike of the fault-occupied valleys in which they lie, suggesting that they may be antithetic bookshelf faults (Mandl, 1987) related to broader dextral shearing. Among the faults oriented at low angles (<30°) to the strike of the valleys, distinct populations of normal and dextral kinematic indicators emerge (Figure 2.7). The mean orientation of the dextral fault population is subparallel to the mean orientation of the normal fault population (Figure 2.7), suggesting that one phase may reactivate the other. While many of these fault zones have previously been interpreted to have undergone Eocene normal displacement on planes with dips ranging from steep to shallow (Parrish et al., 1988), our observations indicated that these kinematic indicators occur predominantly on subvertical to vertical fault planes: 71% of the fault planes observed dip steeper than 60° (Figure 2.8b). Kinematics of local structural domains are shown in Figures 2.2 and 2.6, and below, we review the observations from key sites in the study area.

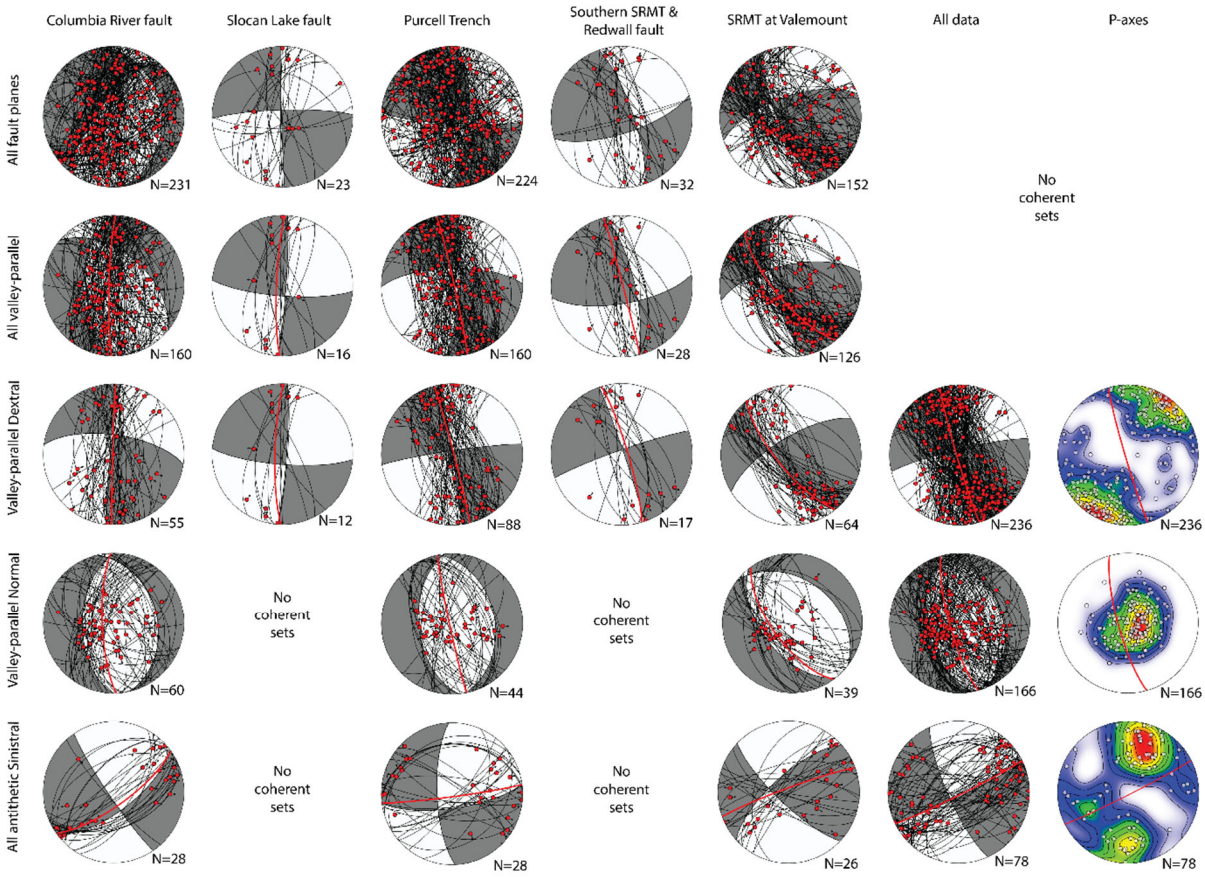

Figure 2.7. Equal angle lower-hemisphere beachball plots showing distinct subdomains of structural measurements collected in each major fault zone (columns 1-5), and for the entire dataset (columns 6). Column 7 shows contoured P-axes for the three largest kinematic populations; red indicates the densest cluster of P-axes. Row 1 shows all unfiltered fault planes, row 2 shows all valley-parallel (<30° to the regional trend) fault planes, rows 3 and 4 show all valley-parallel dextral and normal faults respectively. Row 5 shows all sinistral faults oriented at high angles (>30°) to the valley, representing possible R' shears.

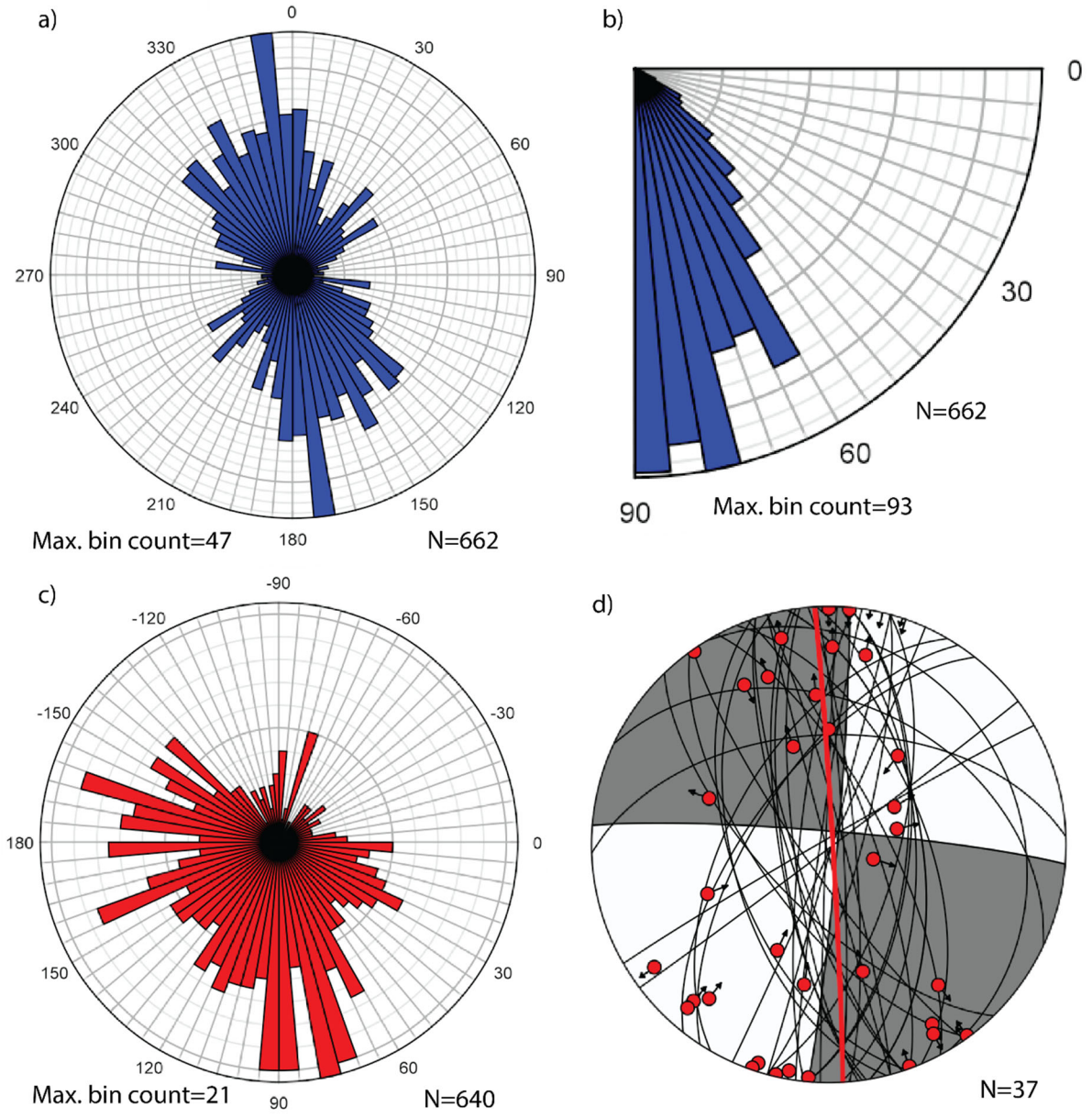

Figure 2.8. a) Bidirectional equal-distance circular histogram of the strikes of all 662 fault planes measured in this study. The strong NNW-SSE population is apparent, as is the subsidiary NE-SW population at high angles to the valleys. b) Unidirectional equal-distance quadrant histogram of the dips of all fault planes measured in this study. The majority are steeper than 60°. c) Unidirectional equal-distance circular histogram showing rake of slickenlines on fault planes using the standard convention of hanging-wall motion relative to the foot-wall, such that 0° = sinistral, +90° = normal, 180° = dextral, and -90° = reverse. The largest populations are normal and dextral. d) Kinematics of large fault planes with observable damage/fracture zones, and/or gouge layers greater than 1cm in width. These large faults are dominantly north-south striking, steeply-dipping, and dextral.

2.6.1 The SRMT fault and adjacent structures

Detailed fieldwork in the Valemount area in 2018 (Figure 2.2) revealed abundant brittle dextral kinematic indicators on subvertical fault planes (Figure 2.9b-d) along Canoe Reach, the northern segment of Kinbasket Lake. Note that these kinematic indicators are slickenlines, and are distinct from the Mesozoic mylonites documented along Kinbasket Lake by Murphy (1990) and the orogen parallel L-tectonites that define the Valemount Strain Zone immediately northeast of the SRMT (McDonough and Simony, 1989). The west-side-down "crush zone" at the north end of the lake documented by McDonough and Simony (1988) was observed, but these kinematics were not found to characterize other outcrops further south along the lake. As shown in column 5 of Figure 2.7, of the 152 fault planes and kinematic indicators measured in the Valemount area, 126 (83%) are subparallel (<30°) to the valley trend, and 64 (51%) of those indicate dextral slip while only 39 (31%) indicate normal slip. The remaining 23 (18%) valley-parallel fault planes (not shown in figure) host a mix of sinistral, reverse, and ambiguous kinematics. A total of 26 fault planes occur at high angles to the valley, and 19 (73%) of these are sinistral. Note that P-axes predicted by both the valley-parallel dextral faults and high-angle sinistral faults are similar, suggesting these populations are genetically related conjugate sets.

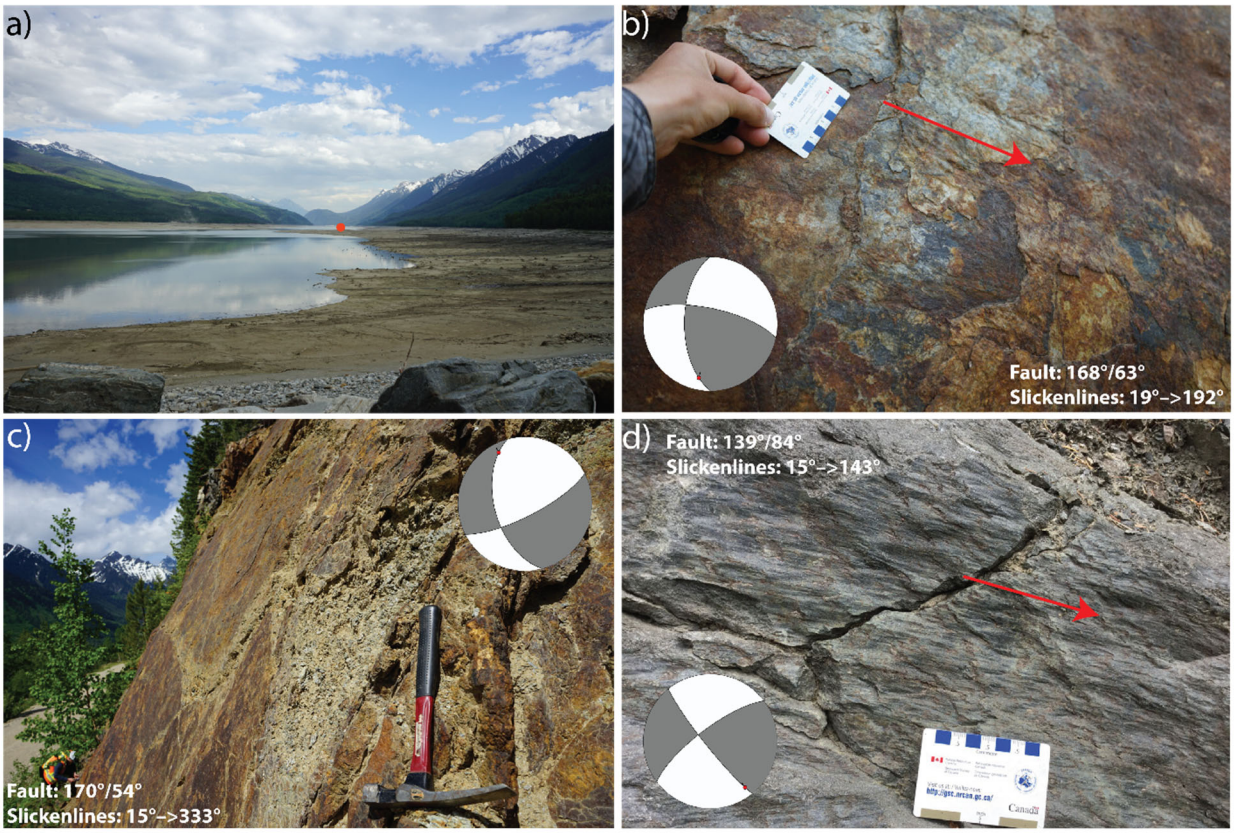

Figure 2.9. Photos from the Valemount/Canoe Reach area. See Figure 2.2 for photo locations and directions. Beachballs show kinematics for each fault plane. a) View south from the north end of the Kinbasket hydroelectric reservoir near Valemount, captured at low water level in May 2018. Red dot shows the location of the Canoe River thermal spring. b) Vestiges of dextral slickenlines in basal Neoproterozoic Windermere Supergroup on the northeast side of the lake (lat. 52.5691°N, long. 118.8420°W). Fault is oriented 168°/63°, slickenlines (red arrow) are oriented 19°→192°. c) Large, oxidized, fault plane in basal Windermere Supergroup on northeast side of lake (lat. 52.6202°N, long. 118.9424°W). Fault is oriented 170°/54°, dextral slickenlines (not pictured) are oriented 15°→333°. d) Dextral slickenlines in Paleoproterozoic Bulldog Gneiss on the northeast side of the lake (lat. 52.6412°N, long. 118.9759°W). Fault is oriented 139°/84°, slickenlines (red arrow) are oriented 15°→143°.

Two hundred kilometers south of Valemount (50 km north of Golden) near the southern end of Kinbasket Lake (Figure 2.3), an outcrop of Cambrian McKay Group in the immediate footwall of the Purcell Thrust fault displays abundant dextral slickenlines on vertical fault planes (Figure 2.10c). Notably, these dextral kinematic indicators are nearly 200 km farther south than had previously been documented in the SRMT by Murphy (1990) and McMechan (2000). Dextral kinematic indicators were also observed at exposures of the Redwall fault immediately east of Radium Hot Springs (Figure 2.10a), along the Westroc mine road east of Invermere, and at the Red Rock warm springs on the Kootenay River forest service road. An outcrop on a forest service road southwest of Lussier Hot Springs displays red- and orange-stained microbreccia and abundant slickenlines characteristic of the Redwall fault, which is not traditionally mapped this far south. Dextral kinematics were also observed on a fault plane assumed to be a splay of the Lussier River fault (Figure 2.10b), indicating that dextral shear is distributed throughout the eastern side of the SRMT. As shown in column 4 of Figure 2.7, of the 32 fault planes measured along the southern portions of the trench, 28 (88%) are within 30° of the valley trend, and 17 (61%) of these demonstrate clear dextral slip while the remainder host a mix of normal, sinistral, and ambiguous kinematics. Only 4 fault planes were measured at high angles to the valley and they are a mix of dextral and reverse.

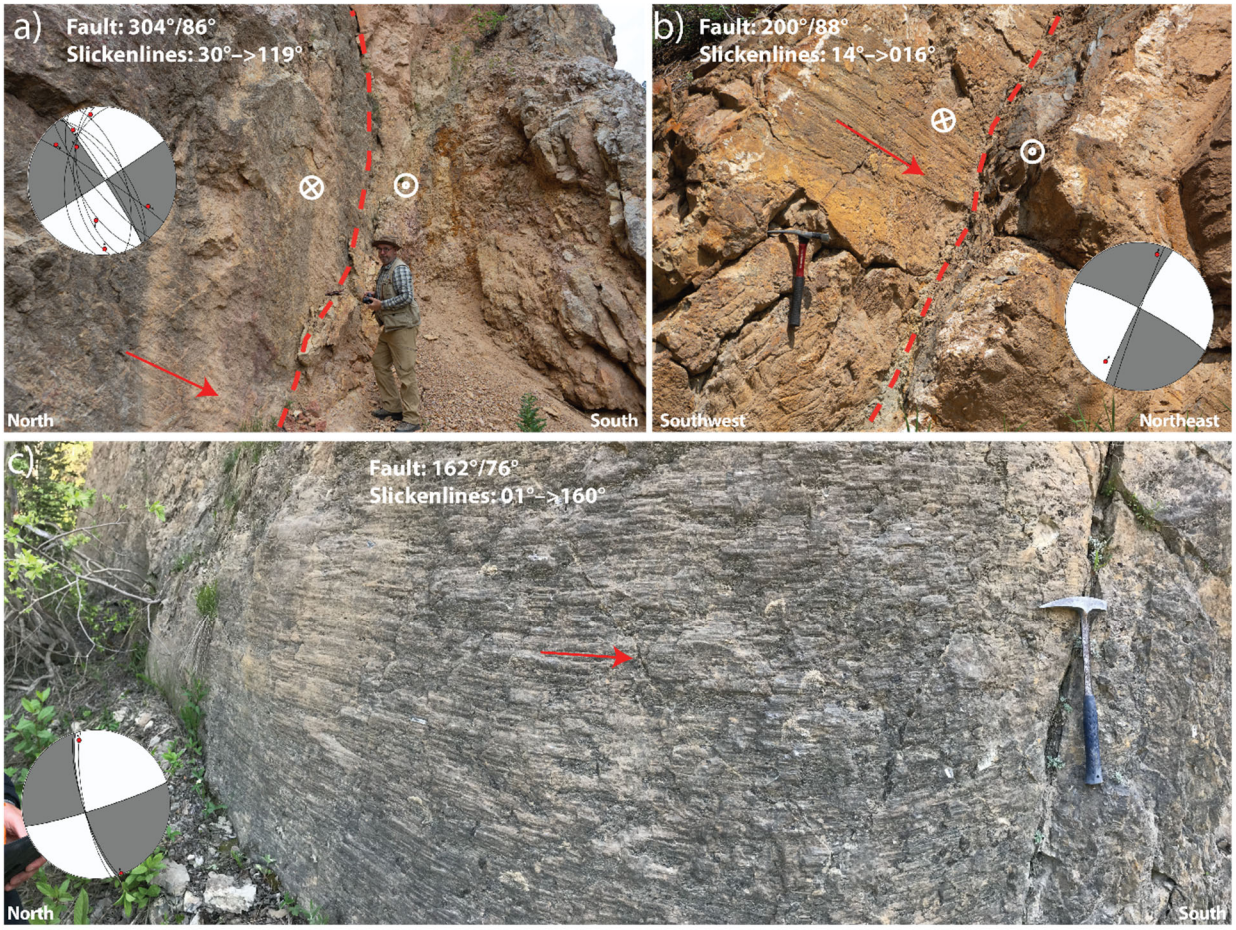

Figure 2.10. Photos from the southern segment of the SRMT, from the US border to southern Kinbasket Lake. See Figure 2.4 for photo locations. Beachballs show kinematics for each fault plane. Concentric circles indicate movement out of the page, circles containing an 'x' indicate movement into the page. a) Looking east at a dextral fault plane oriented 304°/86° within the Redwall fault zone near Radium Hot Springs (lat. 50.6356°N, long. 116.0372°W). Red arrow shows slickenline orientation (30°→119°). b) Oblique view from the southeast of dextral fault plane (200°/88°) with shallowly north-plunging corrugations (red arrow: 14°→016°) and shallowly south-plunging dextral slickenlines (not visible: 25°→217°) near the south end of the Lussier River fault (lat. 49.7175°N, long. 115.5458°W). c) Looking east at a large fault plane (162°/76°) with abundant dextral slickenlines (01°→160°) near the south end of Kinbasket Lake (51.6376°N, 117.4191°W).

2.6.2 The Purcell Trench

Detailed fieldwork in 2018 and 2019 revealed abundant brittle dextral kinematic indicators on subvertical fault planes along much of the Purcell Trench, Duncan River, and Lardeau River (Figures 2.5 and 2.6). Five kilometers southeast of Beaton Arm on Upper Arrow Lake, an outcrop coincident with the mapped trace of the Adit fault – mapped as a west-side-down normal fault by Kraft et al. (2011) – hosts a 60 cm-wide vertical zone of oxidized breccia and gouge material (Figure 2.11a). Unambiguous dextral

slickenlines occur on the fault walls and cleavage appears to be locally dragged into parallel with the fault plane. Farther south along the Trout Lake/Lardeau River valley, several outcrops host faint dextral slickenlines and mineral growths on vertical planar surfaces. No fault has been mapped along the Lardeau River; the Adit fault diverges from the valley and is mapped in the mountains to the southwest. However, slickenlines are consistently exposed at outcrops along the floor of this valley. At the south end of Duncan Lake, well developed dextral slickenlines are present on a large fault plane in Cambrian Badshot Formation marble.

North along Duncan Lake and Duncan River, several outcrops display dextral slickenlines (Figure 2.11b and c). This topographic lineament continues northward into the Beaver River valley, which merges with the Rocky Mountain Trench at 51.5°N. The steeply-west-dipping Beaver River normal fault is mapped in the northern end of this valley (Poulton and Simony, 1980; Kubli and Simony, 1994). It is possible that a through-going fault structure with a history of both normal and dextral slip exists in this valley.

Several locations within the Cretaceous Shoreline Stock and late Cretaceous Mount Skelly pluton on the east side of Kootenay lake display vertical brittle fractures with dextral kinematics. On the west side of Kootenay Lake, just south of Kaslo, a large limonitic fault plane with faint dextral slickenlines cuts obliquely through a highway outcrop (Figure 2.11d and e). On the west side of the Purcell Trench along Highway 3, Brown et al. (1994) documented a brittle fault zone which they interpreted to be a footwall splay of the Purcell Trench fault. We revisited this location and found dextral slickenlines on a notable vertical fault plane striking at a low angle to the main trench axis. Critically, this dextral fault appears to cross-cut and offset a normal fault in the same outcrop (Figure 2.11f), which suggests dextral faulting post-dates normal faulting.

As shown in column 3 of Figure 2.7, of the 224 fault planes measured within the Purcell Trench (including within the Duncan and Trout lake valleys), 160 (71%) are within 30° of the valley trend. Of those, 88 (55%) exhibit dextral kinematics, 44 (28%) are normal, and the remainder (17%) are a mix of sinistral, reverse, and ambiguous kinematics. Of the 65 fault planes that are oriented at high angle, 28 (43%) are sinistral, 22 (34%) are dextral, 14 (22%) are normal, and one is ambiguous. Note that the high-angle sinistral faults share the same P-axis orientation as the valley-parallel dextral faults, suggesting these populations are genetically related conjugate sets.

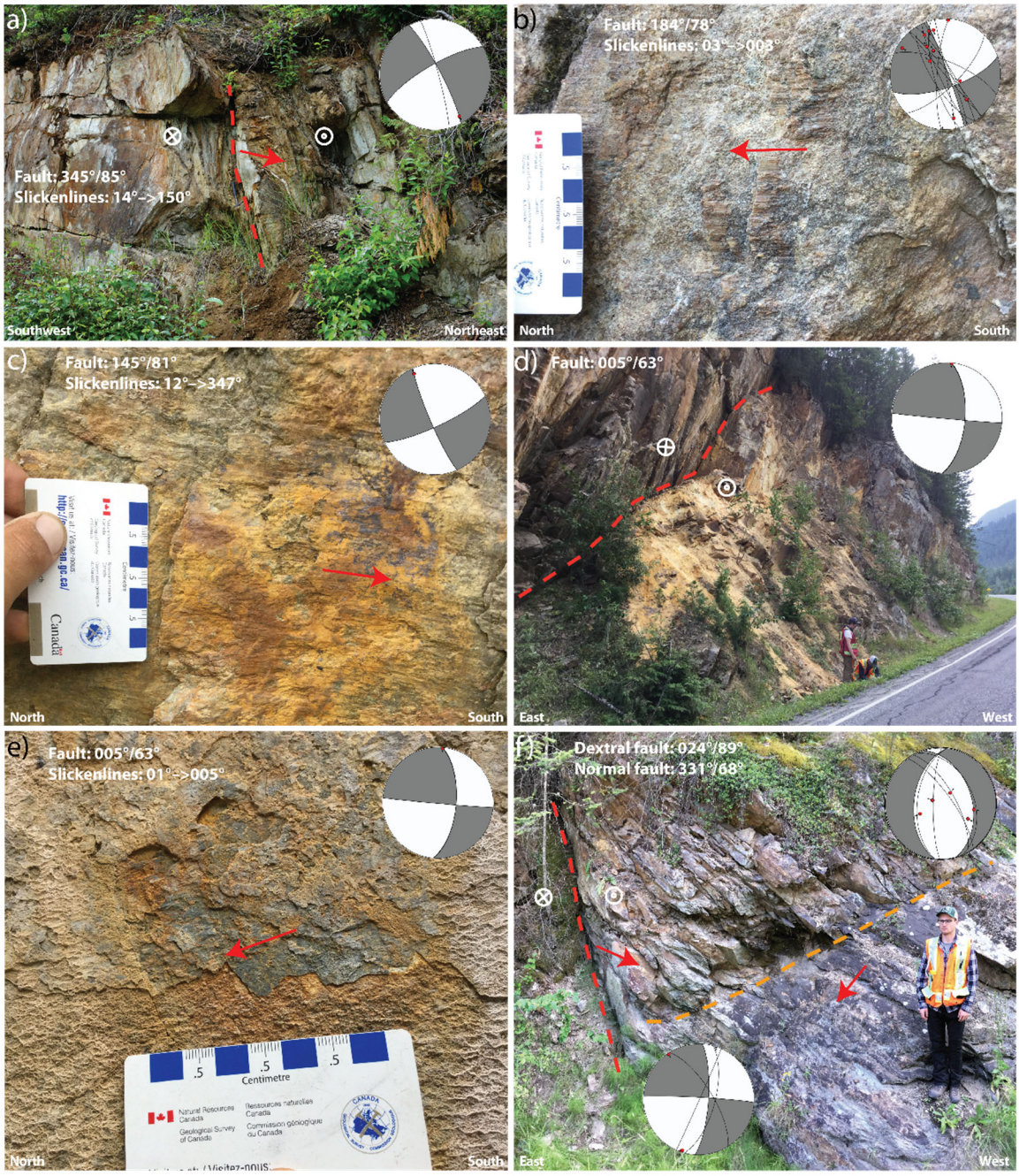

Figure 2.11. Photos from the Purcell Trench. See Figures 2.5 and 2.6 for photo locations. Beachballs show kinematics for each fault plane. Concentric circles indicate movement out of the page, circles containing an 'x' indicate movement into the page. a) Breccia and gouge zone at outcrop of the Adit fault near Beaton (lat. 50.7025°N, long. 117.7095°W). Dextral slickenlines (14°→150°) are present on a subvertical, limonitic fault plane (345°/85°). Rock hammer for scale. b) One of numerous dextral slickenlines (03°→003°) observed on vertical fault zone (184°/78°) along Duncan Lake (lat. 50.4164°N, long. 116.9591°W). c) Dextral slickenlines (12°→347°) on a limonitic subvertical fault plane (145°/81°) located 10 km north of Duncan Lake (lat. 50.6958°N, long. 117.1007°W). d) Dextral fault zone (005°/63°) on the western shore of Kootenay Lake near

Kaslo (lat. 49.8524°N, long. 116.9032°W). e) Faint dextral slickenlines (01°→005°) on the fault wall shown in e). f) A dextral fault (024°/89°) cross-cutting a normal fault (331°/68°) on the west side of the Purcell Trench along Highway 3 (lat. 49.1392°N, long. 116.6420°W).

2.6.3 The Columbia River fault and Slocan Lake-Champion Lake fault systems

Detailed fieldwork in 2018 and 2019 revealed abundant brittle dextral kinematic indicators on subvertical fault planes along much of the Columbia River fault and Slocan Lake-Champion Lake faults (Figure 2.6). At the eastern abutment of the Revelstoke Dam along Highway 23 (Figure 2.3), both normal dip-slip and dextral strike-slip kinematic indicators were observed in a broad zone of gouge and fault breccia believed to be a hanging-wall splay of the main Columbia River Fault zone now buried beneath the dam (Figure 2.12a). Fault planes here mostly dip steeply (>60°) to the east and southeast, and slickenlines trend from south to southwest. These measurements are consistent with those of Lane (1984) at this site, who concluded that the dextral motion post-dated the Eocene dip-slip component. Other exposures (Hathaway Ck. and Carnes Ck.) documented by Lane (1984) were revisited, but few diagnostic slickenlines were observed. Further north along the Columbia River valley, near Mica Creek, low-confidence sinistral and dextral strike-slip kinematic indicators are observed on several minor subvertical fault planes. Immediately south of the Mica Dam, a consistent set of north-northwest dipping normal faults (Figure 2.12b) is exposed where the valley makes an abrupt change to a northwest-southeast trend, perhaps marking a releasing bend in a dextral-system.

Forty kilometers south of Revelstoke, near Beaton Arm on Upper Arrow Lake (Figure 2.6), a near-vertical, north-striking, 50 cm wide fault gouge zone cuts through granodiorite of the Upper Jurassic (~160 Ma; Parrish et al., 1988) Galena Bay stock. Horizontal slickenlines with ambiguous slip sense were observed on the fault walls, but potential Riedel shears oriented ~15° to the main fault plane are consistent with dextral slip.

Thirty kilometers north of Nakusp, Highway 23 appears to follow the trace of a NNW striking fault plane with dextral and sinistral slickenlines on vertical planar surfaces on either side of the road. Another fault, with a 1-2 m wide gouge zone cuts across the outcrop towards the NE (Figure 2.12c). Dextral slickenlines are present on its walls. This fault zone appears to be aligned with the Blind Bay fault mapped by Kraft (2013), which was not included in the GSC map publications by Kraft et al. (2011). The 60° angle between these two faults suggests they may be a conjugate pair.

West across Upper Arrow Lake from Nakusp an outcrop was visited of fault gouge originally interpreted as an exposure of the locally northwestward-striking Columbia River fault by Lemieux et al. (2003). The main schistose fabric of the footwall rock was observed to strike west, and is folded into small-amplitude south-vergent folds. Such deformation is consistent with reverse faulting during north-south shortening

within a dextral restraining bend, rather than east-west extension as postulated by Lemieux et al. (2003). We made a similar reinterpretation at a nearby outcrop (Figure 2.12d) 10 km WNW near Arrow Park Lake originally mapped as a normal fault by (Thompson et al., 2004b).

The southern tip of the Columbia River fault is commonly mapped as being east of the hamlet of Burton. However, the strong north-south topographic lineaments of Lower Arrow Lake (illustrated in Figure 2.6) suggest that this fault zone may continue southward on separate splays from the left-step in the Columbia River fault near Arrow Park Lake. One such lineament follows the Mosquito Creek valley to Lower Arrow Lake. An outcrop aligned with this lineament on the east side of Lower Arrow Lake hosts dextral slickenlines on a steeply-dipping fault plane (Figure 2.12f). These slickenlines were observed by Hyndman (1968) but their regional significance was not recognized at the time. The second lineament follows the Whatshan River valley and Whatshan Lake towards the hamlet of Fauquier. Dextral slickenlines were observed on fault planes in the Cretaceous (77-79 Ma; Thompson et al., 2004a, 2009a) Whatshan Lake batholith.

The Jurassic Kuskanax batholith, from which several thermal springs issue, has several north-south-striking faults mapped through its core, which appear to be subvertical based on their intersection with topography (Figure 2.6). Thompson et al. (2009b) mapped these faults as dextrally offsetting roof pendants of Paleozoic metavolcanic rocks as well as the surrounding Jurassic quartz monzonite. We documented vertical fault planes with dextral slickenlines in exposures of the Kuskanax Batholith along the Halfway River (near Lower Halfway hot spring), and along Kuskanax Creek, 5 km west of Nakusp hot spring. It seems likely that these faults arose from the same transpression that caused dextral motion on the Columbia River fault and may provide the permeability allowing hot springs to reach the surface within the batholith.

As shown in column 1 of Figure 2.7, of the 231 fault planes measured along the Columbia River valley from the Mica Dam to Edgewood, 160 (69%) are within 30° of the valley trend. Of these, 55 (34%) are dextral, while 60 (38%) are normal, while the remainder (28%) are a mix of sinistral (32), reverse (5), and ambiguous (8). Notably, a large portion of the valley-parallel sinistral and normal faults were from the Albert Point area, south of the Galena Bay ferry terminal. The kinematics in this region are highly variable, and not as coherent as other segments of the valley. If kinematics from Albert Point are excluded from the analysis, valley-parallel fault kinematics are comprised 42% dextral, 31% normal, 17% sinistral, 4% reverse, and 6% ambiguous). Of the 71 faults measured at high angle to the Columbia River valley, 28 (39%) were sinistral, 18 (25%) dextral, 16 (23%) normal, 8 (13%) reverse, and one ambiguous. Note that the high-angle sinistral faults share a similar P-axis orientation as the valley-parallel dextral faults, suggesting these populations are genetically related as conjugate sets.

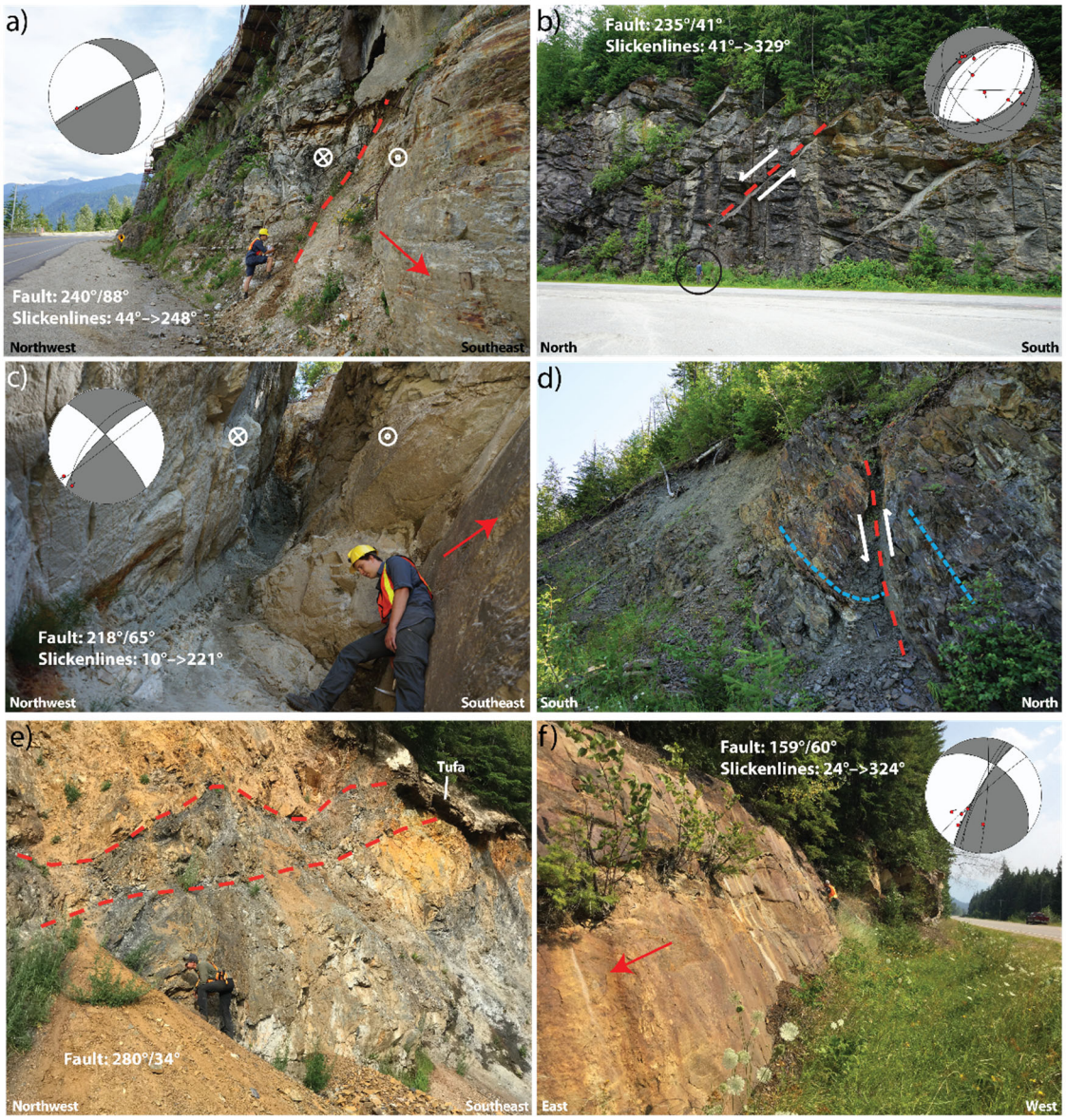

Figure 2.12. Photos from the Columbia River fault. See Figures 2.3 and 2.6 for photo locations. Beachballs show kinematics for each fault plane. Concentric circles indicate movement out of the page, circles containing an 'x' indicate movement into the page. a) View northeast at outcrop on Highway 23 above the southeastern abutment of the Revelstoke Dam (lat. 51.0486°N, long. 118.1901°W). A splay of the main Columbia River fault is exposed here and is reinforced with rebar and shotcrete. Dextral slickenlines (44°→248°) are present on the footwall of the splay fault (240°/88°). b) A set of SW-NE striking normal faults (fault: 235°/41°; slickenlines: 41°→329°) exposed near Mica Dam (lat. 52.0710°N, long. 118.5590°W). Person circled for scale. c) A wide (1.2 m) gouge zone exposed along Highway 23 near Halcyon Hot Springs (lat. 50.5217°N, long. 117.8998°W). Dextral slickenlines (10°→221°) are present on the fault walls (218°/65°). d) Fault originally mapped as a normal fault by Thompson et al. (2004b), reinterpreted as a reverse fault based on folded footwall and reverse slickenlines on the hanging wall. This fault occurs in a possible restraining bend of the

dextral Columbia River fault (lat. 50.3406°N, long. 118.0394°W). Rock hammer for scale. e) Broad zone of breccia and gouge striking west (280°/34°) at the north end of Slocan Lake (lat. 50.0983°N, long. 117.4586°W), possibly related to north south shortening in the restraining bend of the Slocan-Columbia River fault system. A tufa deposit occurs where the fault intersects the pre-roadcut ground surface. f) Subvertical fault plane.

In the region between southern Upper Arrow Lake and northern Slocan Lake, a belt of east-west-trending faults and folds (the Slocan Syncline; Ross and Kellerhals, 1968) occurs at a high angle to the regional strike (Figure 2.6). Cretaceous and Cenozoic intrusions are affected by this deformation: brittle faults are observed on the margins of plutons, and felsic sills that intruded along the primary cleavage planes are folded, forming south-verging folds (Figure 2.13a). Age constraints on these intrusions are sparse, so it is difficult to confirm the timing of this deformation, but it is at least post-Cretaceous, if not post-Eocene. This suggests that the region between the northern tip of the Slocan Lake fault and the southern tip of the Columbia River fault could be a restraining bend in a dextral system. Parrish, (1981) recognized this east-west striking zone of south-verging folds and faults but associated them with Jurassic orogenesis.

At two locations along the east side of Slocan Lake, where the Slocan Lake fault crosses Highway 6, subhorizontal dextral slickenlines were observed on subvertical fault planes, in one case on a brittle fault that cuts through the Eocene-aged Ladybird granite (Carr, 1992), and on another that cuts at a high angle (Figure 2.13b) across the Eocene-aged ductile fabric of the Valkyr shear zone (Carr et al., 1987). The Ladybird granite and Valkyr shear zone are well studied, and their ages well constrained to the Eocene. Thus, these cross-cutting relationships provide a critical lower age constraint on our post-Eocene strike-slip faulting.

As shown in column 2 of Figure 2.7, of the 23 fault planes measured along the Slocan Lake valley, 16 are valley parallel, and 12 of those are dextral. Of the remaining 7 at high angles to the valley, 3 are sinistral, 2 are dextral, and 2 are reverse.

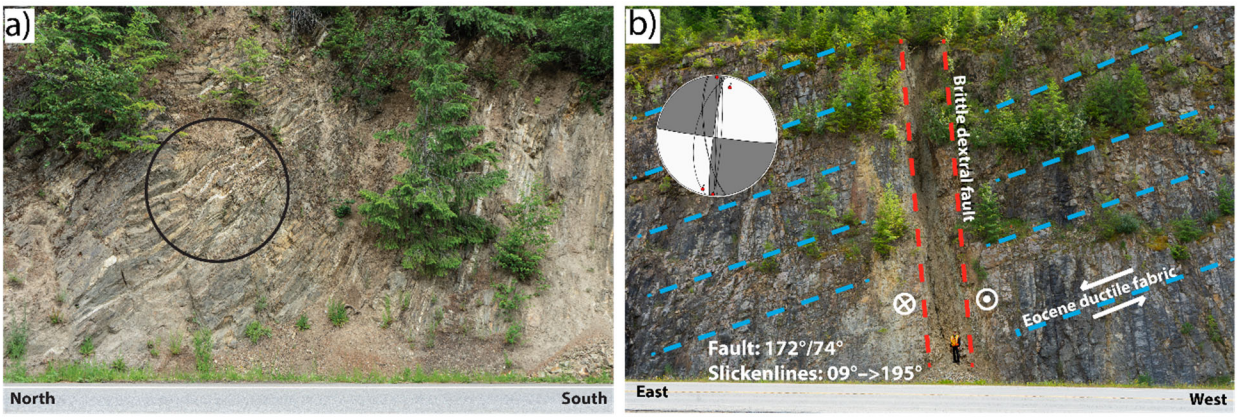

Figure 2.13. Photos from the Slocan Lake area. See Figure 2.6 for photo locations. Beachballs show kinematics for each fault plane. Concentric circles indicate movement out of the page, circles containing an 'x' indicate movement into the page. a) View east at outcrop on Highway 6 north of New Denver (lat. 50.0555°N, long. 117.4323°W). Small, 20 cm wavelength, south-vergent folds are observed in felsic sills intruded parallel to the S1 cleavage (oriented 278°/51°) of the Slocan phyllite. Circle is approximately 1.5 m wide. b) View south at outcrop on Highway 6 south of New Denver (lat. 49.8189°N, long. 117.4549°W). A 2 m wide subvertical brittle dextral fault oriented 172°/74° cuts across shallowly east-dipping (008°/31°) ductile fabric of the Slocan Lake fault/Valkyr shear zone. White encircled dot and "x" indicate motion towards and away from the viewer, respectively.

2.7 Discussion

2.7.1 Fault Kinematics and Age

Our data demonstrate that dextral faulting is the dominant mode of kinematics present along the three major fault zones of the southeastern Canadian Cordillera, and for the following reasons, it is likely that this phase of slip is the most recent and overprints other phases:

1. Dextral kinematic indicators observed on valley-parallel fault planes represent the largest population of all kinematic indicators (34%). We make the assumption that older slip surfaces are more likely to have been overprinted and thus are less well represented in the data.
2. In several places, brittle dextral kinematic indicators occur near or overprint zones of late Cretaceous to Eocene ductile deformation (e.g., mylonites in the Columbia River fault and Slocan Lake fault, SRMT fault near Valemount). Mylonites record shear strain from deeper structural levels below the brittle-plastic transition at ~15 km depth, whereas slickenlines develop in brittle crust (Fossen and Cavalcante, 2017). Therefore, slickenlines co-occurring with mylonites are likely the younger phase.
3. In several places, dextral kinematic indicators occur within Cretaceous plutons, and in one case within an Eocene pluton (Ladybird Granite), and therefore must postdate these intrusions by several million years, allowing for their cooling and exhumation.
4. The regional stress orientations calculated from modern earthquake focal mechanisms (Ristau et al., 2007; Heidbach et al., 2016) are consistent with the average orientation of P-axes determined for dextral fault plane-slickenline pairs in our study area, suggesting that this state of stress persists into the present day.
5. Brittle normal faults represent the second largest percentage of all kinematic indicators observed in the study area, and the majority of these faults share a similar strike and dip to the dextral

faults. This suggests they are oriented favourably for dextral-reactivation in the post-Eocene stress regime defined by Ristau et al. (2007).

Furthermore, a notable population of sinistral faults oriented approximately 60° to the main population of dextral faults is likely a genetically related conjugate set, and is consistent with the NNE-SSW P-axes predicted by the dominant dextral phase.

2.7.2 Estimates of the Magnitude of Offset

The amount of dextral offset across these multiple structures is difficult to estimate but is likely on the order of tens of kilometers based on the evidence below. Larger estimates of displacement on the order of hundreds of kilometers would ignore numerous cross-fault stratigraphic and magmatic (plutonic) correlations. Here, we discuss the constraints on offsets across each major fault zone:

Along the SRMT near Valemount, McDonough and Simony (1988) asserted that the textural, structural, and metamorphic similarities between the Malton Gneiss to the west and Yellowjacket and Bulldog Gneisses to the east precludes major dextral offset as suggested by (Chamberlain et al., 1985); it would be fortuitous for such similar packages of rock to end up adjacent to one another given that no other similar lithologies are cross cut by the SRMT fault to the north or south. Murphy (1990), referring to the dextral mylonites he observed along Kinbasket Lake, suggested that 55 km of late Mesozoic dextral displacement was possible based on the offset of the Purcell Thrust fault and the staurolite-kyanite isograd. We agree with this maximum estimate of offset but argue that at least part of that offset was achieved during post-Eocene dextral slip. Farther south along the SRMT there are few stratigraphic horizons or identifiable structural boundaries to act as reliable piercing points. The trench lies parallel to the structural grain of the Foreland Belt, bounding the Proterozoic Purcell and Windermere Supergroups to the west and the Cambrian McKay Group the east. A block of Purcell rocks outcrop on the east side of the trench northeast of Cranbrook, but these could plausibly be restored to any position along the Purcell Anticlinorium for hundreds of kilometers northward along the trench (Figure 2.4).

Along the Purcell Trench north of Creston, the Late Cretaceous Bayonne batholith is mapped on both sides of the valley (Figure 2.5). Its north-south extent on the west side of the valley is nearly double that of the east side, allowing for the possibility of ~25 km of dextral displacement (Figure 2.5). Notably, K/Ar ages reported by Archibald et al. (1983) (also see: “Canadian Geochronology Knowledgebase,” 2013) within the Bayonne Batholith on the west side of the valley are consistently 20 Myr younger (Early Paleogene) than those on the east side of the lake (Late Cretaceous), suggesting that the two plutonic bodies may not be genetically related and thus provide no constraint on displacement at all. On the northern margin of the Bayonne Batholith, the distinctive conglomerates of the Neoproterozoic Toby

Formation (basal Windermere Supergroup) strike at 40° to the trench and are similarly dextrally offset by ~25 km (Figure 2.6). Farther north along Kootenay Lake there are no distinctive piercing points, and the highly lineated rocks of the Early Paleozoic Hamill and Lardeau groups that strike parallel to the valley effectively obscure any strike-parallel offsets.

At the southern end of the Columbia River fault, several en-echelon dextral offsets, each less than 2 km, are mapped across Jurassic and Cretaceous plutons. Based on similar truncated structural patterns Parrish (1981) suggested that there might be 15 km of dextral slip across the Rodd Creek fault (now known as the southern tip of the Columbia River fault) of Hyndman (1968) but did not favour this hypothesis because "the structure and metamorphic grade to the north of each of these areas are markedly different". To the north of Nakusp, small offsets of <250m are mapped across vertical faults within the Jurassic Kuskanax batholith. Farther north along the Columbia River valley, no distinctive piercing points exist.

The small magnitude of offset may in fact be a contributing factor to enhanced structural permeability in southeastern BC. As fault displacement increases so too does the width of the central gouge zone (Shipton et al., 2006), which is typically composed of impermeable clay rather than permeable fractures. Furthermore, as faults mature, strain becomes progressively more concentrated, transitioning from a diffuse fracture zone to a discrete through-going fault plane. As has been pointed out by several authors (e.g., Sibson, 1996; Curewitz and Karson, 1997; Faulds and Hinz, 2015), greater structural complexity and fracture density is more conducive to hydrothermal fluid flow. As faults become more mature, permeability is not maintained on the peripheral fractures, and structural complexity decreases.

2.7.3 Neotectonic Stress and Strain

In situ stress measurements in the southeastern Cordillera are sparse and those that do exist are derived from earthquake focal mechanisms (Heidbach et al., 2016). The southeastern Canadian Cordillera is characterized by a low level of seismicity as compared to the active convergent margin to the west, but at greater levels than the central intermontane region of British Columbia, and the stable foreland basin and craton to the east (Ristau et al., 2007). Strain rates estimated from geodetic GNSS instruments range between 4-16 nanostrain/year (Kreemer et al., 2014), though the instrument coverage is sparse east of the Cascade forearc and the sense (kinematics) of strain is not well resolved. Within the study area, ~25 earthquakes occur each year, and are between M_w 0-4 (Fig. 15a). Ristau et al. (2007) calculated moment tensor solutions for earthquakes of M 4 and greater for all of western Canada (moment tensor solutions are not possible for magnitudes less than 4). Only five earthquakes above the required threshold occurred in the study area since the beginning of the catalogue in 1984, but all are dominantly strike-slip, with dextral nodal planes aligned with the major fault zones of the Cordillera, and sinistral nodal planes oriented at high angles to the regional strike (Fig. 15b). Principal stress (σ_1) orientations estimated from

the Pressure (P) axes of these focal mechanisms are sub-horizontal and trend NNE-SSW. The earthquake focal mechanisms and associated σ_1 vectors are closely aligned with the kinematics and predicted stress orientation required to produce the widespread dextral kinematics described in this study. For example, in 1978, a M_w 4.8 earthquake occurred south of Valemount (Rogers et al., 1980), and was initially investigated due to concerns over the filling of the Kinbasket Lake reservoir (historically referred to as McNaughton Lake). The preferred focal mechanism for this earthquake was dominantly right lateral, with a reverse component, on a SSE striking fault plane. Ultimately it was concluded that the earthquake was not induced by the reservoir, but rather was attributed to "stresses associated with residual strain energy stored during the mountain building process" (Rogers et al., 1980). The orientation of the focal mechanism of the McNaughton Lake earthquake is similar to the orientation of fault planes and slickenlines observed in the area (Figure 4) and was therefore likely not due to "residual strain" but ongoing dextral transpression.

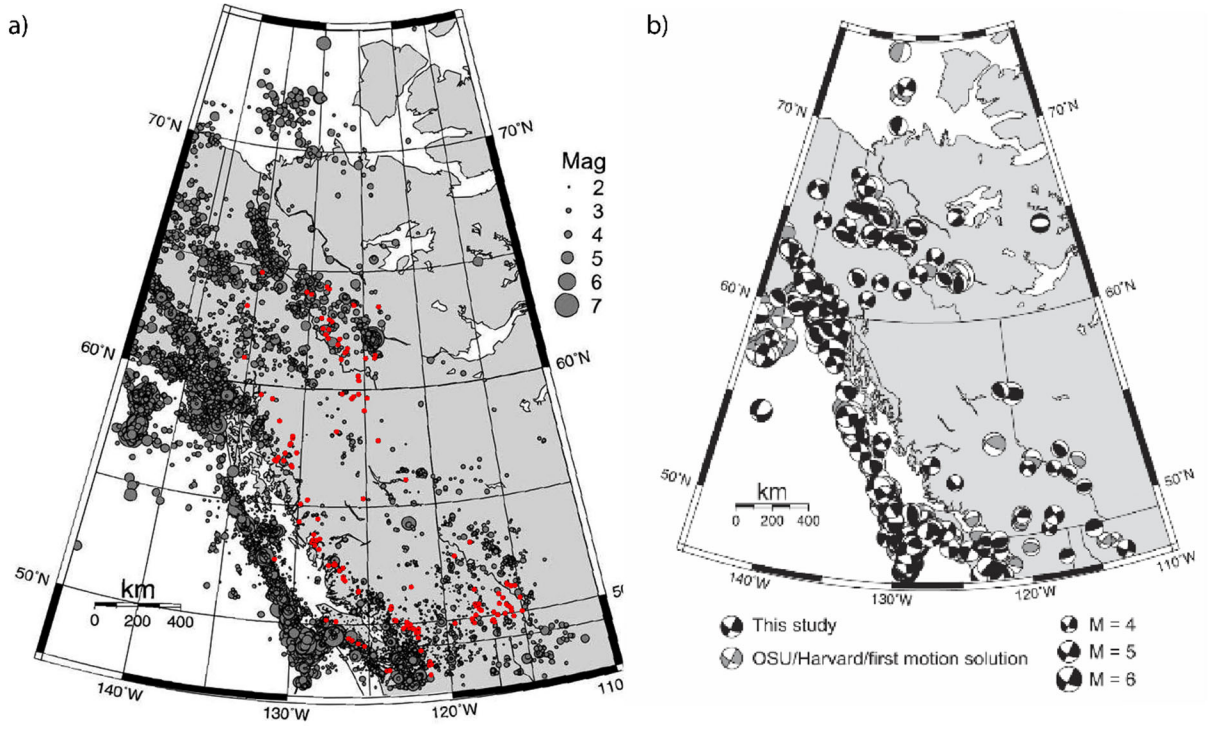

Figure 2.14. a) Grey dots illustrate all seismicity (Mag. 2-7) in the Canadian Cordillera adapted from Ristau et al (2007) from 1984 to 2004. Red dots are hot springs, which are concentrated in regions of moderate seismicity. b) Focal mechanisms for earthquakes of M 4 and greater from Ristau et al (2007). Note that earthquakes in southeast BC are strike-slip, and likely dextral if a NNW-SSE nodal plane is selected.

It is likely that the post-Eocene stress state is transpressional and that the dextral faults observed in this study are manifestations of the present low levels of seismicity in this region. Furthermore, this ongoing

seismicity may be important in maintaining fault permeability and allowing for the occurrence of thermal springs in the southeastern Cordillera.

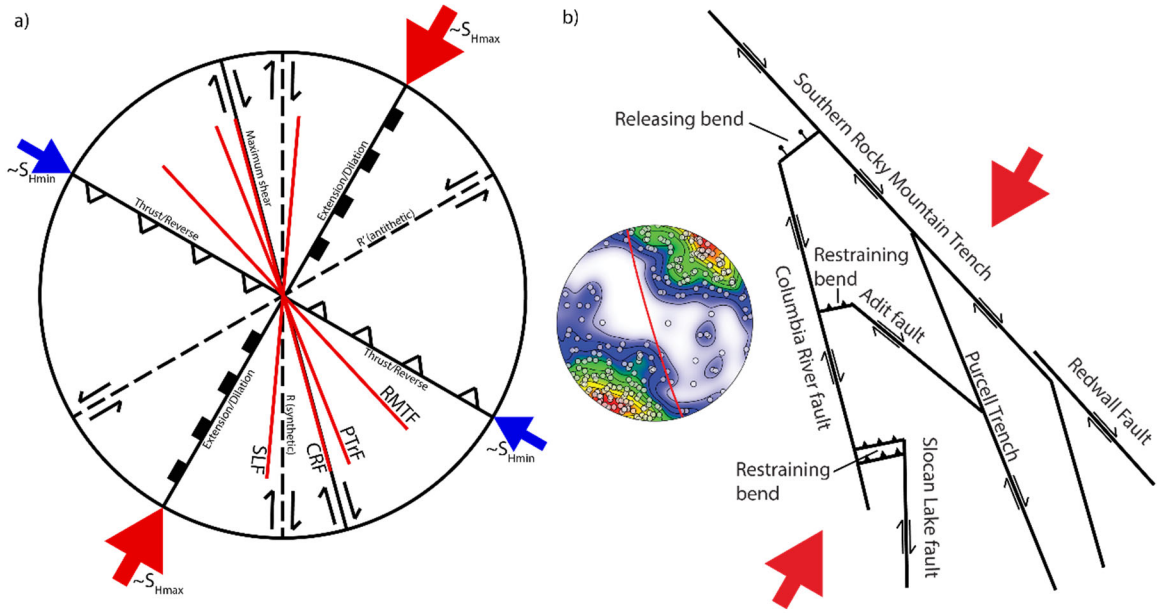

Figure 2.15. a) Strain ellipse for approximate S_{Hmax} orientation in southeastern BC (Ristau et al., 2007), and corresponding predicted modes of brittle deformation on faults and fractures. Average orientations of the SRMT fault, Purcell Trench fault, Columbia River fault, and Slocan Lake fault, are shown for reference. b) Schematic map of fault kinematics in this study. Stereoplot shows density contours for P-axes for all dextral faults oriented parallel to the trend of the valleys (N=236).

2.7.4 Fault Permeability and Spring Localization

At a regional scale, low levels of seismic activity in the southeastern Cordillera may be responsible for maintaining crustal fault permeability, thereby controlling the occurrence of thermal springs in the area. In the Cordillera, three main clusters of thermal springs—southeastern BC, coastal BC, and along the NWT/Yukon border—all correspond to regions of elevated seismicity as compared to central BC (Fig. 15a). Curewitz and Karson (1997) showed that active strain enhances structural permeability via episodic re-fracturing of fault zones and surrounding wall rock that would otherwise be clogged by hydrothermal mineral precipitation. Furthermore, faults and fractures that are critically stressed and oriented parallel to, or between 30-45° to, the maximum stress axis, will either dilate or slip, respectively, thus permitting the flow of fluid (Barton et al., 1995). In other geothermal fields, strain rate is considered a critical control on geothermal prospectivity (e.g., Faulds et al., 2015). While patterns of seismicity cannot be used to predict specific locations of thermal upwellings, they can explain regional distributions. Past efforts to characterize the fault and fracture permeability of the entire Cordillera with regard to geothermal

prospectivity (Kimball, 2010) did not consider the variable seismic activity, and weighted the permeability of all faults equally. In future efforts, patterns of seismicity should be considered.

At more local scales, specific structural settings appear to localize thermal spring outlets. Curewitz and Karson (1997) showed that stress concentration at fault tips, step-overs, and intersections promoted structural permeability. Faulds and Hinz (2015) showed that local regions of enhanced structural complexity (e.g., pull-aparts) are particularly favourable for hydrothermal upwelling. Sibson (1996) showed that in fractured rock meshes, fluid preferentially flows parallel to σ_2 along fault and fracture intersections. Therefore, according to the Andersonian model of faulting (Anderson, 1905), fluid flow in a strike-slip regime would be preferentially vertical. As we have shown in this study, recent kinematics of the southeastern Canadian Cordillera are predominately strike-slip, and therefore conducive to near-vertical fluid flow.

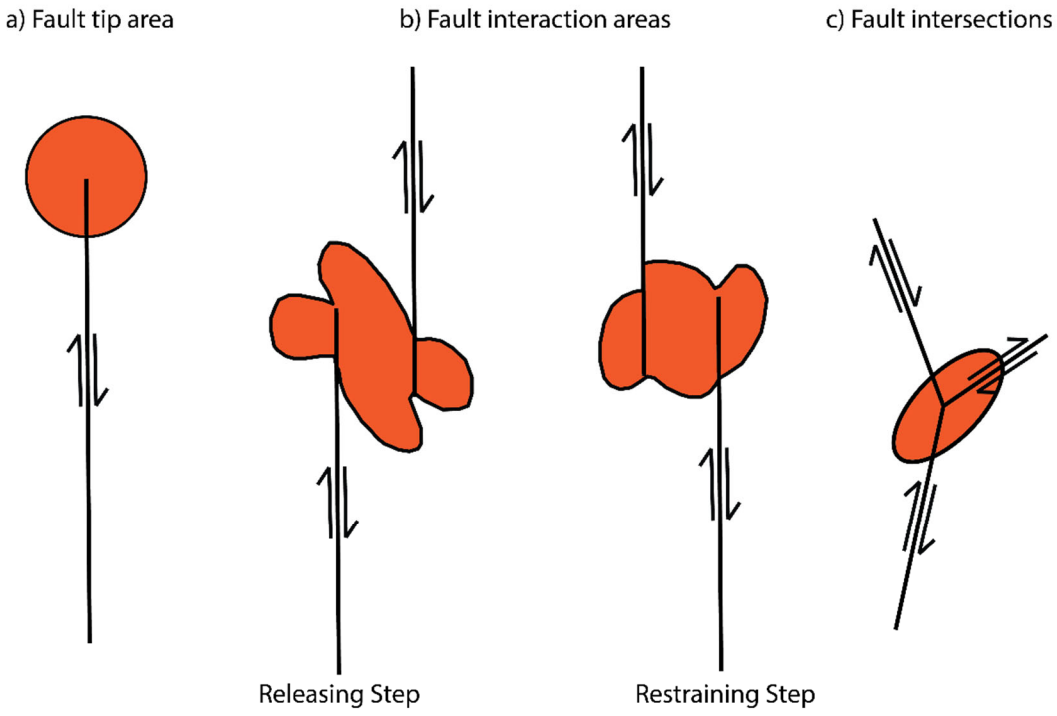

Figure 2.16. Structural settings especially conducive to hydrothermal fluid upwellings adapted from Curewitz and Karson (1997). Orange shaded polygons are "breakdown" regions where stress is concentrated and fracture density is enhanced. a) Fault tip permeability, a possible control on the location of the warm springs at the southern tip of the Columbia River fault. b) Fault interaction zones (releasing and restraining steps), a possible control on the location of the cluster of springs near Nakusp, and the cluster near Crawford Bay. c) Fault intersections, a possible control on the location of the Canoe River spring.

It is likely that a combination of these structural settings is required to explain the localization of thermal springs in the Canadian Cordillera within the broader pattern of active regional strain. In some cases, specific fault intersections can be identified: the Canoe Reach spring (Figure 2.2) occurs at the intersection of the main strand and a splay of the SRMT fault (McDonough and Morrison, 1990) and the Halcyon spring (Figure 2.6) occurs at the intersection of the Columbia River fault and the Blind Bay fault (Kraft, 2013). In other cases, intersections between smaller splays and Riedel shears not identified in regional mapping, but apparent in the angular variation of dextral fault plane strikes measured in this study, may provide the main control on geothermal springs. The cluster of thermal springs north of Nakusp (Figure 2.6) occurs north of the restraining bend between the Columbia River fault and Slocan Lake fault, and south of the restraining bend between the Columbia River fault and Adit fault, and therefore falls within a "fault interaction zone" as per Curewitz and Karson, (1997), where stress is concentrated, leading to increased fracture permeability. An example of this enhanced fracture density is found in the numerous small-offset dextral faults that cut the Kuskanax Batholith. The cluster of warm springs (Snowshoe, Jorden Ranch, and Octopus) south of Nakusp (Figure 2.6) may be due to stress concentration at the tip of a previously unrecognized splay of the Columbia River fault that follows the Whatshan Lake lineament. The Ainsworth spring and the two warm springs (Riondel and Crawford Bay) on the east side of the lake (Figure 2.6) occur in a potential zone of strain transfer between the steeply-west-dipping Lakeshore fault, and the steeply-east-dipping Purcell Trench fault. The springs along the Redwall fault (Figure 2.4) do not fit as readily into a zone of potential stress concentration. Instead, it is likely that the combination of primary permeability of the solution collapse breccia, and secondary permeability of Cenozoic fractures, is what makes this structure such a great host of thermal springs. The oxidation of conglomerate clasts and surrounding matrix material suggests that the Redwall fault has a protracted history of hydrothermal flow. For example, at Red Rock warm springs, a large, layered, tufa dome is situated at the top of the cliff on the north side of the Kootenay River. The dome is bisected by the cliff such that the interior is visible, and no thermal water presently flows. Another tufa deposit occurs a few kilometers to the east. It is evident that hydrothermal flow on the Redwall fault is ephemeral, and that thermal springs have migrated along it through time, which is also a prediction of the Curewitz and Karson (1997) model.

2.7.5 The Possibility of Blind Geothermal Systems

Convective geothermal systems with no modern surface manifestation (blind systems) are known to occur in active geothermal fields throughout the world. For example, blind systems constitute nearly 40% of known systems in Nevada, and it is likely that far more are yet to be discovered (Faulds and Hinz, 2015). Conceptual models for these inconspicuous geothermal resources vary, but typically an impermeable

layer blocks the ascent of fluids, or cold influx of shallow groundwater may dilute or divert a rising plume (Dobson, 2016). It is conceivable that similar blind systems exist in the Canadian Cordillera, masked by high infiltration rates of cold meteoric water. Precipitation rates are higher in the Canadian Cordillera than in the arid Great Basin of the southwestern United States, and thick glacial overburden may facilitate near-surface dispersion and dilution of any ascending plumes of geothermal brine. At least one blind geothermal system has been identified in the Canadian Cordillera, in the Bluebell mine at Riondel (Fig. 9); during mine operation in 1956, workers encountered water 20–30°C flowing from cracks at 90–1000 liters per second (L/sec) at a depth of ~300 m below ground (Desrochers, 1992). This thermal water did not flow to the surface, or, if it did, it had already cooled below detectable levels. It is a statistical likelihood that other blind systems remain undiscovered elsewhere in the Canadian Cordillera, particularly due to the low "degree-of-exploration" (Coolbaugh et al., 2006) in the area. A first-order prediction of their location may come from identifying where local zones of stress concentration may occur, given the orientation of faults in the current crustal stress field. A few possible locations in southeastern BC stand out as candidates for blind systems in our structural framework: the right-stepover (releasing bend) at the northernmost end of the Columbia River Fault near the Mica Dam (Figure 2.3), the right-stepover (releasing bend) in Duncan Lake (Figure 2.6), and the intersection of the Beaver River, RMT, and Chancellor faults, at the south end of Kinbasket Lake (Figure 2.3). However, these predictions are speculative and further investigation is required.

2.7.6 Broader Tectonic Implications

There is an extensive record of Cenozoic dextral shear partitioned between numerous structures across the Cordillera. The most prominent dextral structure in the Canadian Cordillera is the Northern Rocky Mountain Trench – Tintina Trench fault system. In the Yukon, Cretaceous geological units are offset by at least 400 km across the Tintina Trench fault zone (Roddick, 1967). Johnston (1999) argued that an additional 400 km of dextral displacement may be accommodated within synkinematic mid Cretaceous intrusions in the northern Cordillera. In northeastern BC, the Northern Rocky Mountain Trench fault and subsidiary parallel structures (Kutcho and Pinchi faults) are collectively thought to have accommodated up to 1000 km of displacement through the Cretaceous to the Eocene, based on offsets between geological units (Gabrielse, 1985).

Farther south, large dextral displacements are not as easily distinguished. Northeast of Prince George, the Northern Rocky Mountain Trench fault intersects with the SRMT fault, which extends a further ~850 km along the western edge of the Rocky Mountains to northwestern Montana. No significant dextral offsets have been observed along the SRMT fault, despite the fact that its strike deviates only 20° counterclockwise to the Northern Rocky Mountain Trench fault. McMechan (2000) showed that dextral

displacement of ~60 km occurs in the Walker Creek fault zone near the intersection of the northern and southern trench segments and suggested this deformation was late Cretaceous to Eocene in age. Even further south, McDonough and Simony (1989) documented the dextral oblique Valemount Strain Zone, but concluded it was related to the Jurassic(?) Bear Foot thrust. Murphy (1990) documented dextral mylonites at the northern end of Kinbasket Lake along the SRMT and estimated a maximum of 55 km of displacement occurred between 135 and 51 Ma.

No dextral kinematic indicators or displacements have previously been observed on the SRMT south of the Kinbasket Lake mylonites. Instead, the major faults of southeastern BC are considered by most authors to be part of an array of Eocene normal faults. Any dextral displacement south of ~53°N is thought to be partitioned between several en-echelon fault structures farther to the west. Several authors have argued that the Fraser – Straight Creek fault accommodates ~100 km of Late Cretaceous to Eocene dextral displacement (Kleinspehn, 1985; Coleman and Parrish, 1991). The Fraser – Straight Creek fault truncates the Yalakom fault at a low angle, which is believed to have accommodated an additional 100 km of dextral slip. Price and Carmichael (1986) fit a small circle to the Northern Rocky Mountain Trench, Tintina Trench, and Fraser – Straight Creek fault systems, concluding that the two structures were mechanically coupled, and that the Fraser – Straight Creek accommodated 100 km of the 450 km displacement on the Northern Rocky Mountain Trench and Tintina Trench faults – the remaining 350 km of displacement being accommodated through oblique convergence in the southern Canadian Rockies.

In the western parts of the Canadian Cordillera, brittle faults have been shown to be active post-Eocene. The Harrison Lake shear zone and associated structures (which are host to several thermal springs) are believed to have been active in the late Cretaceous through to the early Neogene (Journeay and Csontos, 1989; Journeay and van Ulden, 1998). The West Coast fault (which also hosts several springs), strikes northwest just offshore of Vancouver Island, and is thought to have been active in the late Jurassic to early Eocene (Muller et al., 1981). No neotectonic studies have been conducted on the West Coast fault, but it is likely to be active today given its position in the accretionary wedge of an active convergent margin. Along the axis of the Coast Belt, the Coast Shear Zone exhibits a complex history of motion, including dextral shear, between 65-55 Ma (Klepeis et al., 1998; Rusmore et al., 2001). In the Alaska Panhandle, the Chatham Straight and Border Ranges faults show evidence for significant dextral shear (150 km and 700 km respectively) in the late Cretaceous to Eocene (Hudson et al., 1980; Smart et al., 1996). South of the BC-Yukon border, the Chatham Strait fault and Coast Shear Zone merge with the Denali fault, which is known to be active from the Eocene to present on various segments (Lanphere, 1978; Bemis et al., 2015). Offshore of northern BC, the transpressional Queen Charlotte - Fairweather fault is active in the present day (Rohr et al., 2000; Cassidy et al., 2014).

The Cordillera, from California in the south to Alaska in the north, has been subject to widespread, diffuse dextral shear from the Jurassic to present. Margin-parallel tractions on the Pacific-North America plate boundary apparently affect the crustal strain far into the hinterland of the Cordillera. The NNE-SSW stress directions from earthquake focal mechanisms (and the dextral strain recorded on faults) likely reflect a transition from margin-parallel stress at the Cascadia margin, to orogen-normal stress in the foreland. In southeastern BC, Eocene extension is commonly thought to be the most recent phase of tectonism (e.g., Clague, 1974; Lane, 1984; Parrish et al., 1988; van der Velden and Cook, 1996), but the data presented in this chapter show that dextral shear is more recent.

2.7.7 Suggested future work

A critical conclusion of this work is that dextral kinematics observed on fault planes are related to the present-day stress and strain fields in the southeastern Cordillera. Unfortunately, instrumentation (e.g., seismographs and geodetic GNSS receivers) is sparse in this region. The seismic waveforms that are available possess high noise-to-signal ratios that prevent the determination of robust earthquake focal mechanisms, and consequently only those for earthquakes of M=4 and greater can be calculated (e.g., Ristau et al., 2007). A denser network of seismometers may rectify this issue, although Gilbert (pers. comm., 2020) indicated that even a dense network of stations deployed near Valemount was still unable to resolve focal mechanisms, possibly due to strong anisotropy in the crust. At the very least, a denser network of seismometers would allow for more accurate epicenter locations, in order to test whether earthquakes align along faults. In addition, a denser network of GNSS stations would allow for real-time estimates of crustal strain and displacement relative to stable North America. Current GNSS networks in western Canada are focused on understanding the active tectonic processes occurring in the forearc region of the Juan de Fuca subduction zone and only a handful of stations exist in the backarc. Obtaining seismic and geodetic data on a denser grid would provide a critical test of the predictions of this study.

2.8 Conclusions

Potential geothermal resources in southeastern BC are likely amagmatic and rely on the deep circulation of thermal fluids along permeable fracture pathways to bring heat close to the surface. Our regional-scale investigation of the structural settings of hydrothermal systems in southeastern BC has revealed a consistent pattern of dextral kinematics on brittle subvertical fault planes coincident with the surface traces of faults previously mapped as Eocene and Jura-Cretaceous in age; dextral kinematic indicators were identified along the Rocky Mountain Trench, Purcell Trench, Columbia River Valley, and Slocan Valley. The timing of this transpressional deformation is constrained to post-Eocene based on cross-cutting relationships observed in Eocene-aged rocks. The NNE-SSW maximum stress axis required for these kinematics is consistent with the focal mechanisms of several crustal earthquakes that have occurred

in the region, suggesting that transpressional strain has developed following the well-documented period of crustal extension in the Eocene. This NNE-SSW stress field in southeastern BC likely reflects a transition from the margin-parallel (NNW-SSE) maximum stress orientations within the Cascadia forearc to the orogen-normal (NE-SW) maximum stress orientations in the Cordilleran foreland. When placed in the context of the current stress field, two main controls on the location of thermal springs become apparent: on a regional scale, there is a positive correlation between seismicity across the entire Cordillera and the locations of thermal springs. On local scales, dextral fault tips, intersections, and interaction zones are shown to be favourable locations for hydrothermal upwelling.

Chapter 3: Linking subsurface conductivity anomalies to regional and microscopic structures near Valemount, BC.

3.1 Abstract

Magnetotelluric (MT) surveys south of Valemount, BC, have revealed several low resistivity features that could represent hydrothermal fluid or conductive mineral phases (e.g., graphite, sulfide) in the subsurface. There is commercial interest in developing geothermal resources in this area, and because hydrothermal fluids are critical components of geothermal resources whereas graphite and sulfides are not, it is crucial that the cause of these low resistivity anomalies be investigated (Cumming, 2009). In this chapter, detailed geological cross sections constrained by 1:50k bedrock maps constructed parallel to MT survey profiles are compared to 3D isotropic and anisotropic resistivity models derived from MT data. The isotropic resistivity model contains heterogeneous features that do not match well with mapped structures and lithological units, whereas features in the anisotropic resistivity model align better with structural and lithological boundaries in the cross-sections. To investigate the cause of these conductive anomalies, six representative hand samples from the Paleoproterozoic Yellowjacket Gneiss and Neoproterozoic Lower Miette Group were collected in the vicinity of the MT surveys. Samples were examined with petrographic and scanning electron microscopes, as well as an X-ray diffractometer, to determine morphology, connectivity, and modal percentage of potentially conductive mineral phases. In the Yellowjacket Gneiss, elongate, partially connected pyrite crystals were observed parallel to the primary foliation. Graphite was found filling brittle fractures parallel and at low angles to the primary foliation, as well as on grain boundaries in both the Yellowjacket Gneiss and Lower Miette Group. In some cases, graphite and sulfides are in contact, suggesting that both might contribute to the anisotropic resistivity of the rock. Although the modal percentages collectively comprise less than 5% of the rock volume, this may be sufficient to explain some conductivity anomalies observed in the MT models. The cross-sections and petrological analyses together allow for more informed interpretation of conductive features in the MT models, which will aid future geothermal exploration efforts.

3.2 Introduction

Western Canada is the most prospective region in the country for geothermal energy resource development (Grasby et al., 2012). The high heat flow, steep geothermal gradients, and occurrence of 130 thermal springs in the Canadian Cordillera are especially attractive, and the region has been investigated intermittently for decades. One area that has attracted commercial interest is the Canoe River hot spring, 30 km southeast of the town of Valemount, BC. As part of recent geothermal exploration efforts by

Borealis GeoPower Ltd., magnetotelluric (MT) surveys were conducted in the vicinity of the geothermal system in hopes of imaging thermal fluids in the subsurface (Lee, 2020).

MT surveys use naturally-occurring electromagnetic waves to image the resistivity (or its reciprocal, conductivity) of the subsurface and are commonly used to search for and characterize geothermal systems (Muñoz, 2014). Electromagnetic methods such as MT are especially sensitive to the location of magma bodies, hydrothermal brines, and alteration products such as smectite, all of which have low resistivities and can indicate potential targets for further geothermal development (Muñoz, 2014). Mineral phases such as graphite and sulfide (e.g., pyrite), which are not generally associated with active hydrothermal systems, can also be the cause of low resistivity anomalies (e.g., Nelson and Van Voorhis, 1983; Frost et al., 1989; Yoshino and Noritake, 2011). Interpreting a resistivity model derived from inverting MT data is an inherently non-unique task. This is because multiple geometries of electrical structures can be fit to the data, and because a single bulk resistivity value can be explained by many permutations of conductive fluids and minerals. Synthetic inversions can be used to test the robustness of particular subsurface geometries (Siripunvaraporn et al., 2005), and empirical relations based on laboratory studies can be used to estimate the amount of conductive fluid in pore space or melt-fraction based on the bulk conductivity (Archie, 1942; Pommier and Le-Trong, 2011). However, field-based geological constraints are also valuable in constraining and interpreting the results of MT inversions (Bedrosian, 2007).

In this chapter, geological constraints are used to improve the interpretation of resistivity models from Lee (2020) in the Valemount area. A critical uncertainty of the resistivity models is whether conductive bodies represent geothermal fluids flowing along permeable fractures, or other conductive phases such as graphite. Detailed geological cross sections are constructed to provide regional constraint on major structures and their subsurface geometry, while petrographic analyses provide constraint on the possible cause of conductivity at a microscopic scale.

3.3 Background

3.3.1 Valemount geography

The town of Valemount (pop. 1000) and the northern arm of Kinbasket Lake (known as Canoe Reach) lie in the northernmost segment of the Southern Rocky Mountain Trench (SRMT), a major fault-controlled valley system that extends southward from Valemount to northern Montana. The SRMT forms the geographic boundary between the Canadian Rocky Mountains to the east and the Columbia Mountains to the west. The Columbia Mountains are further subdivided into the Monashee Mountains to the southwest of Valemount, and the Cariboo Mountains to the northwest (Figure 3.1). North of Valemount, the

continuation of the SRMT topographic lineament is known as the Northern Rocky Mountain Trench in northeastern BC and the Tintina Trench in Yukon.

3.3.2 Stratigraphy and Lithology

The highly metamorphosed (amphibolite facies) Paleoproterozoic Malton Gneiss Complex is the dominant lithological package underlying the Canoe Reach area (Figure 3.1). The Malton Gneiss Complex is divided into three units: The Bulldog Gneiss and Yellowjacket Gneiss on the northeast side of the SRMT, and the Malton Gneiss on the southwest side. The Bulldog Gneiss is mostly quartzofeldspathic paragneiss with minor amphibolitic layers, and has been dated at 1870 Ma (McDonough and Parrish, 1991). The Yellowjacket Gneiss is a fairly homogeneous granodioritic orthogneiss also dated at 1870 Ma (McDonough and Parrish, 1991). The Malton Gneiss is a heterogeneous mix of quartzofeldspathic paragneiss, amphibolitic gneiss, and orthogneiss, and is slightly older than the Bulldog and Yellowjacket, at 1987 Ma (McDonough and Simony, 1988; McDonough and Parrish, 1991). All three gneiss packages are overlain unconformably by the Neoproterozoic lower Miette Group, characterized by a lower granule sandstone (grit) unit and overlying quartzite and calc-silicate pelites. The Miette Group is thin where it drapes the Malton Gneiss Complex, and considerably thicker to the east, west, and south, implying that the Malton Gneiss Complex formed a basement high during the deposition of the Miette Group in the Neoproterozoic.

3.3.3 Structural History

The rocks in the Valemount area record a complex and protracted history of deformation which is discussed in detail by McDonough and Simony, (1988). A brief overview of the tectonics of the Canadian Cordillera is also provided in Section 2.3.1 of this thesis. The age and nature of deformation on various structural features is relevant to understanding the geothermal systems that may exist in the region: young brittle faults often act as conduits for fluid flow and become less permeable with time as they are clogged with mineral precipitate; older fault zones exhumed from below the brittle-ductile transition do not possess permeable fractured damage zones, though they still may juxtapose rocks with significantly different hydrogeological properties. A summary of the structural history is provided below in chronological order. These structural relationships are key constraints on balanced cross sections presented in this chapter.

<u>The basement-cover detachment:</u> The contact between the Neoproterozoic metasediments of the Lower Miette Group and the Paleoproterozoic gneiss of the Malton Gneiss Complex is marked by thin mylonite zones interpreted as ductile detachments. The amount of slip along this detachment is believed to be relatively small due to the consistent occurrence of thin Miette Group where it overlies the Malton Gneiss

Complex, and thick Miette Group elsewhere (McDonough and Simony, 1988). Thin sections of the mylonitic zones revealed equant, strain-free quartz crystals, which indicates the mylonites developed before peak metamorphism in the area (McDonough and Simony, 1988). Any kinematic indicators (if originally present) were overprinted and annealed during subsequent metamorphism. The detachment is thought to have developed due to the strong rheological contrast between the crystalline basement and sedimentary cover during an early phase of tectonic compression (McDonough and Simony, 1988).

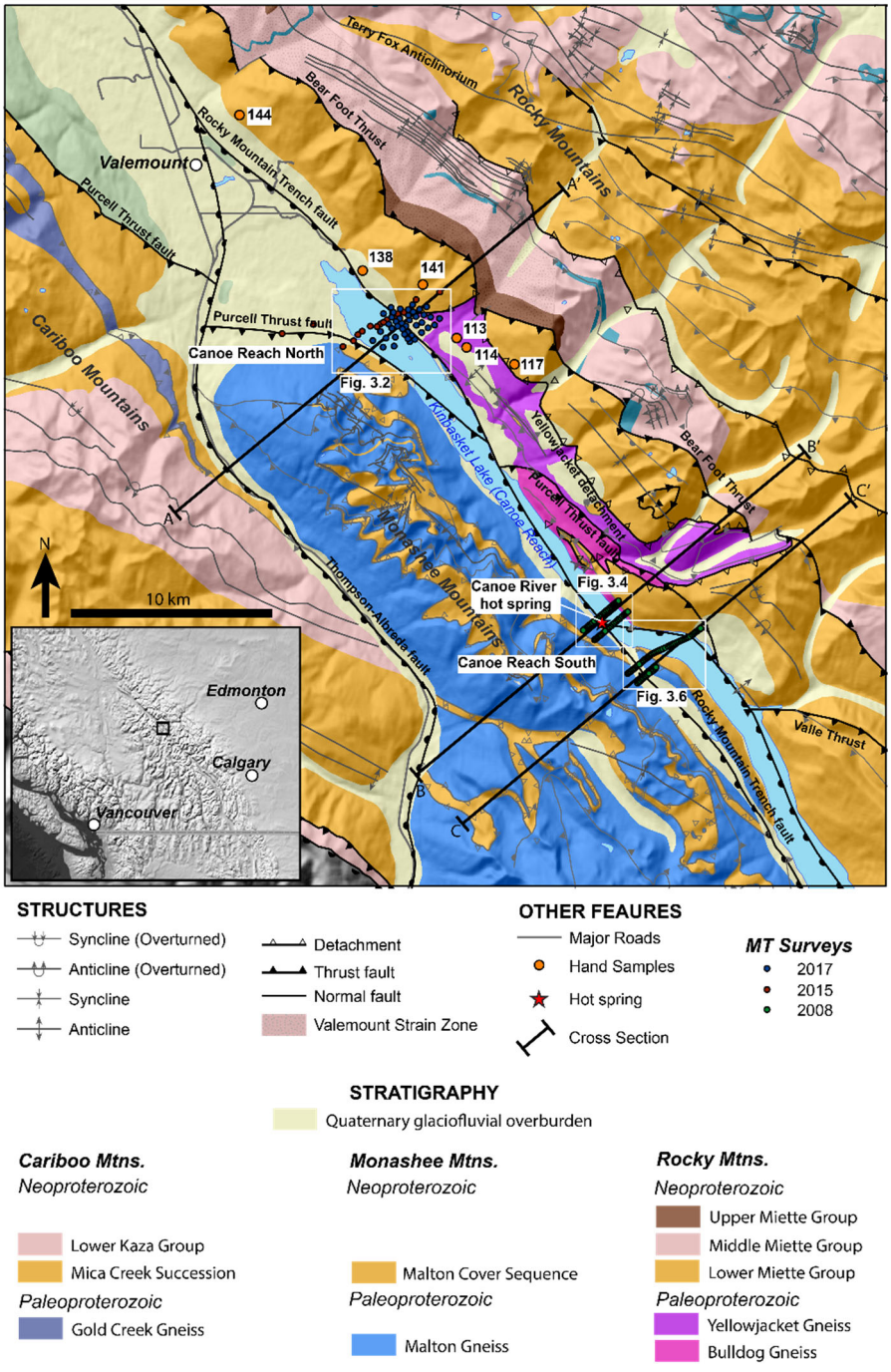

Figure 3.1. Geology map of the Valemount area. Corresponding cross sections (A-A', B-B', and C-C') are shown in Figures 3.3, 3.5, and 3.7. White rectangles indicate extent of MT models shown in Figures 3.2, 3.4, and 3.6. MT stations from Lee (2020) are shown. Samples described in this chapter are marked with orange dots.

The Bear Foot thrust: The Bear Foot thrust brings the Yellowjacket Gneiss and overlying Lower Miette Group overtop of the Middle Miette on the northeastern edge of the study area. Tight folds and a strong mylonitic fabric are observed in both the hanging wall and foot wall of the fault. Regional metamorphic isograds are not offset across the fault, which constrains motion to pre- or syn-peak metamorphism. Shortening across the fault is estimated to be a minimum of 20 km based on the geometry of deformation in the Yellowjacket Gneiss, and the offset between Lower Miette Group in the foot wall and hanging wall. Thin sections show S-C fabrics and rotated porphyroblasts that show both northeast directed reverse dip-slip, and northwest directed dextral strike slip shear sense. In the foot wall of the Bear Foot thrust, a zone of L-tectonites known as the Valemount Strain Zone (McDonough and Simony, 1989), is interpreted to have resulted from reverse-dextral transpression across the fault in the Mesozoic.

The Purcell thrust: The Purcell Thrust is a major "out-of-sequence" regional thrust fault that truncates earlier Rocky Mountain structures in its foot wall, including the Bear Foot thrust. A distinct contrast in metamorphic grade across the fault indicates it is post-metamorphic (McDonough and Simony, 1988). It has been mapped along the western edge of the SRMT for several 100 kilometers south of Valemount (e.g., Craw, 1978; Gal and Ghent, 1990). Both brittle and ductile kinematic features are observed in the fault zone.

Eocene extension (SRMT and Thompson Albreda faults): The SRMT fault, a steeply west-dipping Eocene normal fault, occupies the SRMT for much of its length, with offset estimated to be between 2-10 km (Clague, 1974; McDonough and Simony, 1988; van der Velden and Cook, 1996), although thick glacial overburden on the trench floor inhibits detailed investigation of this structure. In the Canoe Reach area, cataclasites with west-side down kinematic indicators were observed at one location along the lake by McDonough and Simony (1988). West of Valemount, the Thompson-Albreda fault also accommodated minor Eocene extension.

Post-Eocene dextral reactivation: As detailed in Chapter 2 of this thesis, an abundance of dextral slickenlines along the northeastern side of Canoe Reach represent a previously undocumented phase of kinematics. The close match between these kinematics and the focal mechanisms of local earthquakes suggests that this phase of dextral deformation is ongoing, and reactivates the Eocene extensional

structures. This phase of deformation is relevant to active hydrothermal systems in the area, as young or active faults are typically more permeable than old inactive ones.

3.3.4 Geothermal Exploration in Valemount

The Canoe Reach thermal spring south of Valemount, BC, has attracted commercial and scientific interest in geothermal energy resource development in the area for at least three decades (Fairbank and Faulkner, 1992; Piteau Associates Engineering Ltd., 1994; Ghomshei, 2007; Ghomshei et al., 2009; Sadlier-Brown and May, 2009; Geoscience BC, 2015; Tuya Terra Geo Corp, 2016). Most recently, Borealis GeoPower Ltd. has undertaken a geothermal exploration program in the area (Village of Valemount, 2012).

At 67 °C, the spring discharge is among the hottest of all hot springs in BC and aqueous geothermometers indicate that the thermal fluid may reach 129°C to 187°C via deep (3-5 km) circulation in the subsurface (Ghomshei, 2007). Previous investigations have suggested that the heat source for the geothermal resource may be related to: a) Quaternary volcanism observed 50 km to the southwest in the Wells Gray area, b) radiogenic heat produced by the Malton Gneiss, c) asthenospheric convection and elevated heat flow beneath the Cordillera, and/or d) deep circulation of meteoric water on permeable fault planes (Ghomshei et al., 2009). Depending on the volumetric flow rate of the Canoe River hydrothermal system, it may be possible for electricity to be generated at a binary cycle geothermal power plant near Valemount. At the very least, hot water could be used for direct heating (Tuya Terra Geo Corp, 2016).

3.3.5 MT Surveys

The MT method uses naturally occurring electromagnetic waves to image the conductivity structure of the earth over a range of depths (500 m to 50 km), which makes it useful for regional geothermal exploration (Muñoz, 2014). The two main sources of electromagnetic signals used for MT are lighting strikes—which generally produce signals with frequencies >1 Hz—and currents induced in the Earth's magnetosphere by variations in the solar wind—which generally have frequencies <1 Hz (Chave and Jones, 2012). When these signals encounter the surface of the Earth, the majority of the energy is reflected, while a small amount penetrates into the ground. The depth to which it penetrates is governed by the skin depth equation:

$$\delta = \sqrt{\frac{\rho}{\pi \mu f}}$$

in which the penetration depth (δ) is proportional to the Earth's resistivity (ρ), and inversely proportional to the Earth's magnetic permeability (μ) and the frequency (f) of the incident wave. Electric and

magnetic fields are measured at the surface of the Earth in the time-domain at MT stations for periods of days to weeks. The time series are converted to frequency domain, and the frequency-dependant impedance tensor is computed, which contains information about the Earth's resistivity. From the impedance tensor, two values, the apparent resistivity (ρ_a) and phase angle (Φ), can be calculated, both of which are also frequency-dependent, with higher frequencies sensitive to shallow depths and lower frequencies sensitive to deeper depths. The apparent resistivity describes the integrated resistivity of the earth to a specific depth, while the phase describes changes in resistivity with depth. MT impedance data (or, equivalently, ρ_a and Φ data) are inverted using a geophysical inversion algorithm (e.g., Kelbert et al., 2014) to solve for a three-dimensional model of the resistive and conductive features in the subsurface.

Broadband MT surveys in the Valemount area were conducted in 2008 by Quantec Geoscience Ltd as part of a geothermal exploration program (Sadlier-Brown and May, 2009) near the Canoe River spring outlet (hereafter referred to as Canoe Reach South). Additional surveys were conducted by Lee (2020) in 2015, 2016, and 2017, as part of ongoing geothermal exploration closer to Valemount (hereafter referred to as Canoe Reach North). The frequency range of the MT data (300-0.001 Hz for Lee, and 10000-0.001 Hz for Quantec) are sensitive to structures at > 50 km depth, but the short (< 5 km) profiles only allowed for imaging of the subsurface resistivity to depths of 2 km at Canoe Reach North and 1 km at Canoe Reach South. From both sets of data, Lee (2020) produced two series of 3D inversions, the first assuming electrical isotropy using the ModEM algorithm (Kelbert et al., 2014), and the second allowing for anisotropic conductivity using an algorithm developed by Kong et al. (2020). A limitation of the anisotropic inversion was that the anisotropic axes were aligned to N-S, E-W, and vertical directions, which may not align with the true anisotropic axes of the subsurface at Canoe Reach. Inversions with axes aligned to the local geologic strike (i.e., NW-SE instead of N-S) are currently in progress, and may reveal the full extent and true ratio of anisotropic resistivities, but are not expected to drastically change interpretations.

Electrical anisotropy in the subsurface can be due to a variety of structural features and petrological textures at a wide range of scales (μm to km). Fundamentally, the connectivity of conductive material (e.g., brine, magma, metal) must be different in at least 2 axes to allow for preferential current flow along planes or lines. Geologically, there are two main ways in which electrical anisotropy can be created: sedimentary deposition, and tectonic strain. Deposition of sediment creates planar layers that may have variable electrical properties with depth (e.g., Edwards et al., 1984); resistivities are typically equal in the two horizontal axes (ρ_x and ρ_y), and reduced in the vertical (ρ_z). Tectonic strain (extension, compression, and shear) can create both planar and linear features that preferentially conduct electricity. Non-penetrative brittle planar features (i.e., faults and fractures) can act as conduits or reservoirs for

conductive fluid (Caine et al., 1996; Curewitz and Karson, 1997; Peacock et al., 2013). Additionally, conductive minerals (e.g., graphite, sulfides) can become aligned along penetrative ductile fabrics such as cleavage planes and stretching lineations (Mathez et al., 1995; Yoshino and Noritake, 2011; Liddell et al., 2016). While the concentrations of conductive minerals in the original rock may not have been sufficient to produce a conductivity anomaly, the process of shearing may increase connectivity along one or more axes, as mineral grains are aligned and stretched. The discovery of possible electrical anisotropy at Canoe Reach by Lee (2020) prompted this investigation of its cause, specifically through improved mapping of brittle fault structures in the area, and the search for the presence of connected, conductive minerals such as graphite and sulfide.

3.4 Methods

Following collection and initial processing of the MT data by Lee (2020), geological investigations including field mapping, sampling, structural analysis, and microscopic analysis were conducted to provide better constraint on the MT models, and to identify the cause(s) of electrical anisotropy in the subsurface.

3.4.1 Field work

Two weeks of fieldwork were conducted in the Canoe Reach area in May of 2018. The focus of mapping was to investigate the Cenozoic fault kinematics in the region (see Chapter 2), but structural measurements of bedding and metamorphic foliations were also collected to augment existing structural measurements available in local 1:50k bedrock maps (McDonough and Morrison, 1990; McDonough and Mountjoy, 1990; McDonough et al., 1991; McDonough and Murphy, 1994). Samples were collected routinely both for reference purposes and for additional petrological analyses. At 6 locations along geologic strike from the Canoe Reach North MT array, outcrops of Miette Group and Yellowjacket Gneiss appeared graphitic, having a dark grey metallic luster, and leaving a distinct dark grey streak when rubbed. Samples were collected at each of these locations with the specific intention to determine graphite content due to the implications for conductivity of the rock.

3.4.2 Cross Section Construction

Following fieldwork, geologic cross sections were constructed parallel to the MT model profiles created by Lee (2020) at Canoe Reach North and Canoe Reach South. Existing cross sections accompanying 1:50k maps (McDonough and Morrison, 1990; McDonough and Mountjoy, 1990; McDonough et al., 1991; McDonough and Murphy, 1994) were inadequate for our purposes because they did not align with

the MT surveys. The structural relationships at Canoe Reach are variable along-strike and it is therefore important to have well-aligned cross sections to aid in the interpretation of MT inversion model features.

Geologic cross sections are semi-quantitative inverse models (Grose et al., 2019) based upon surface measurements of structural fabrics and observations of lithological changes. Like MT inversions the results of cross-section construction are non-unique and multiple subsurface geometries can explain the same surface outcrop pattern. Several fundamental principles help guide the construction of cross-sections in order to arrive at a plausible result:

- Lithological and structural features that are cross-cut by faults must match when fault displacement is restored (Dahlstrom, 1969).
- Lateral continuity can be assumed for rocks that are deposited (e.g., sedimentary and some volcanic rocks), but not necessarily for those that are intruded or explosively erupted (Steno, 1669).
- Penetrative and non-penetrative structural fabrics can be assumed to be relatively continuous along-strike, and somewhat continuous down-dip.
- Following Occam's razor, simple subsurface geometries that fit the surface data are generally regarded as more plausible than complex subsurface geometries.

Three geological cross sections were constructed independently of the geophysical models produced from the MT surveys. In other words, the MT inversion results were not used to guide the geometry of faults and other features. The most detailed geological maps from the area (1:50k scale) available as PDF's from the Geological Survey of Canada (McDonough and Morrison, 1990; McDonough and Mountjoy, 1990; McDonough et al., 1991; McDonough and Murphy, 1994) were georeferenced in ArcMap, and lithological and fault contacts were digitized. Orientations of bedding and cleavage presented on these maps were collated along with supplemental structural measurements collected during fieldwork in the summer of 2018. Topographic profiles for the cross sections were created from the ASTER Global Digital Elevation Model (NASA/METI/AIST/Japan Spacesystems and U.S./Japan ASTER Science Team, 2019). Structural measurements within 5-10 km of the profile were projected onto the profile plane under the assumption of some along-strike continuity of bedding and structural fabrics. Specific features and constraints for each cross section are discussed below.

Cross section A (Figure 3.3) was constructed parallel to MT profiles presented by Lee (2020) at Canoe Reach North. At this latitude, the Yellowjacket Gneiss outcrops on the northeast side of the trench in the hanging wall of the Bear Foot thrust. It is overlain by a thin slice of the Lower Miette group, separated by the mylonitic Yellowjacket Detachment, which is subhorizontal in this region as implied by its

intersection with topography in the geologic map. To the northeast of the Bear Foot thrust, is a thick, southwest-dipping succession of Lower, Middle and Upper Miette Group rocks. The dip of the Yellowjacket Gneiss is variable, but overall it appears to dip 45° to the southwest. If an offset of only 1-2 km is assumed for the SRMT fault (as per McDonough and Simony, 1988), it is necessary for Yellowjacket to exist under the SRMT and Malton Gneiss to the southwest, although no surface outcrops exist to confirm its presence there. The Malton Gneiss is thrust overtop of the Yellowjacket Gneiss on the Purcell Thrust, a late stage thrust fault. Ductile deformation of the Malton Gneiss is complex, and the folds shown on the cross section are only representative. West-side-down normal offset on the Thompson-Albreda fault is estimated to be 0.5-4.5 km by Murphy et al. (1991) and a median value of 2 km is chosen for the cross section.

Cross Section B (Figure 3.5) was constructed parallel to MT model profiles A and B at Canoe Reach South. At this latitude, both the Yellowjacket Gneiss and Bulldog Gneiss outcrop on the northeast side of the SRMT. The Yellowjacket Gneiss is thrust over a succession of the Lower and Middle Miette Group on the Bear Foot Thrust. A small wedge of the Lower Miette Group is present in the hanging wall of the Bear Foot Thrust, in contact with the Yellowjacket Gneiss along the arched Yellowjacket Detachment. Between Cross Section A and B, the surface trace of the Purcell Thrust crosses from the southwest to northeast side of the SRMT fault. The Purcell Thrust and an associated minor splay bring the Bulldog Gneiss overtop of the Yellowjacket Gneiss. This cross section implies that the Bear Foot thrust is offset vertically across the Purcell Thrust by a minimum of 6 km, though greater separation is possible and is unconstrained due to the absence of Yellowjacket Gneiss in the hanging wall. Assuming 2 km of offset on the SRMT fault implies that the Bulldog Gneiss underlies the Malton Gneiss southwest of the trench.

Cross section C (Figure 3.7) is constructed parallel to MT model profiles C and D at Canoe Reach South. At this latitude the Bear Foot Thrust places the Yellowjacket Gneiss overtop of a thick succession of the Lower Miette Group. A thin slice of the Lower Miette Group is present on top of the Yellowjacket Gneiss, separated by the Yellowjacket Detachment. The Purcell Thrust places the Bulldog Gneiss and Malton Gneiss overtop of the Yellowjacket Gneiss and Lower Miette Group. The Bulldog Gneiss does not outcrop along the profile but is inferred to exist based on the relationships shown in Cross Section B to the immediate northwest. At this latitude the SRMT fault splits into two splays, which are both inferred to have 1 km of normal offset. The Malton Gneiss at this latitude has several intercalated bands of Lower Miette Group rocks which may be duplicated by large nappe structures.

3.4.3 Microscopy

To investigate the cause of conductive features in MT models, six hand samples collected from outcrops of Yellowjacket Gneiss and Lower Miette Group near the northeastern end of the Canoe Reach North MT survey profile were prepared for examination with petrographic microscope, scanning electron microscope, and X-ray diffractometer. Of particular interest was the presence (or absence) of conductive mineral phases such as graphite and sulfide (e.g., pyrite). The combination of these three microscopic techniques allowed for quantitative (modal percentage) and qualitative (connectivity) characterization of these mineral phases where they existed.

Petrographic microscopy is useful for rapid identification of common mineral phases, as well as characterization of metamorphic textures (e.g., MacKenzie and Adams, 1994). A combination of plane polarized light (PPL), cross polarized light (XPL) can be used to identify translucent minerals, while reflected light (RL) can be used to identify opaque minerals such as pyrite and graphite. Thin sections (30 µm thick) oriented approximately perpendicular to the strike of the metamorphic foliation in each rock were prepared for examination with petrographic microscope. Photomicrographs were captured using a digital camera attached to a Zeiss Axioscope petrographic microscope, and processed using ZEN, a proprietary software of Zeiss.

Scanning Electron Microscopy (SEM) allows for definitive identification of elemental constituents of material at scales on the order of several microns (e.g., Goldstein et al., 2018). A focused beam of high-energy electrons is directed at the sample surface and the interaction of the beam with the material produces an array of emissions including x-rays. SEM instruments fitted with an Energy-Dispersive X-Ray Spectrometer (EDS), can distinguish the characteristic X-ray emissions of specific elements, which is useful in confirming mineral identities, particularly those at scales difficult to distinguish with petrographic microscopy. Additionally, SEM instruments fitted with Back-Scattered Electron (BSE) detectors can produce compositional maps based on the elastic interactions between the electrons and atoms in the sample material; atoms with higher atomic numbers produce higher BSE intensities.

The same thin sections observed with the petrographic microscope were observed with the SEM but it became apparent that the adhesive product used to impregnate and bind the thin sections was carbon bearing, and represented a potentially false-positive graphite signature. Epo-Thin Epoxy Resin was used to mount each sample to the glass microscope slide and Epo-Tek 301 epoxy was used to bind friable samples during polishing. These epoxy resins rely on the reaction of epichlorohydrin (C_3H_5ClO) with bisphenol A ($(CH_3)_2C(C_6H_4OH)_2$), to produce bisphenol A diglycidyl ether (BADGE). Because BADGE is an organic compound, the presence of carbon must be taken into consideration when searching for

graphite with analytical instruments. We found that epoxy contamination may be identified in EDS data by the presence of a trace of chlorine from the epichlorohydrin. Therefore, only carbon signatures without an accompanying chlorine peak were considered reliable indicators of graphite occurrence. That said, the presence of epoxy or graphite may not be mutually exclusive; in our samples, graphite commonly occupied recessive pockets and fractures, which may also preserve traces of epoxy during polishing of thin sections. It is also worth noting that past studies of graphite in metamorphic rocks have found chlorine in conjunction with the graphite and concluded the chlorine was naturally-occurring (e.g., Mathez et al., 1995). While this may be true, we chose to address the potential for contamination from epoxy by preparing thick sections (~5-10mm thick). These were cut from the same samples as the thin sections, and polished down by several millimeters to remove adhesive driven into fractures while under vacuum during the preparation process. These thick sections were analyzed with the SEM instrument, using both the EDS and BSE detectors. X-ray spectra were produced for specific targets on the polished samples surfaces, and element maps were produced based on the back scattered electrons. Targets on the thick sections measured with the EDS detector usually had little to no chlorine as compared to the thin sections, demonstrating that epoxy contamination in thin sections is valid concern that can be avoided by creating thick sections.

While petrographic microscopy and SEM analyses are useful for determining morphology and connectivity of possible conductive phases, they cannot easily provide a quantitative assessment of modal percentage of these phases. Petrographic microscopy relies on visual estimation, and many of these phases are difficult to discern. SEM analysis is limited by the width of the beam, and therefore would provide a different estimate depending on the scale at which the analysis is conducted. X-Ray Diffraction can provide a whole-rock estimation of mineral modal percentage (Bish and Post, 1989). X-rays are directed at a powdered sample, and the refracted X-rays are measured. Peaks in the refracted X-rays are characteristic of specific mineral crystal lattices. Such peaks occur due to constructive interference between the incident and refracted X-rays, which occurs only at specific incident angles determined by Bragg's Law:

$$2\delta \sin\theta = n\lambda$$

Where δ is the spacing between crystal lattice planes, θ is the incident angle of the X-ray beam, n is an integer, and λ is the wavelength of the X-ray beam. A Rietveld refinement can then be applied to the X-ray spectra to determine precise modal percentage (Rietveld, 1969).

One sample of Yellowjacket Gneiss—believed to have a particularly high percentage of graphite and pyrite—based visual inspection and SEM analysis, was prepared for X-Ray diffractometry. An agate

mortar and pestle followed by a McCrone mill were used to reduce the sample to a fine powder. The sample was scanned using a Rigaku Ultima IV XRD instrument. It was scanned from 5 to 80° at a rate of 1.2°/minute. Data interpretation was conducted using Jade 9.6 software. A Rietveld refinement was scheduled to further resolve modal percentages, but this was interrupted by COVID-19.

3.5 Results

3.5.1 Cross Section Comparison

3.5.1.1 Cross Section A (Canoe Reach North)

Cross Section A (Figure 3.3) corresponds to the MT survey conducted by Lee (2020) at Canoe Reach North, located approximately 15 km southeast of Valemount. Lee (2020) performed two inversions, one assuming isotropic resistivity, and another assuming anisotropic resistivity. Features in the anisotropic model closely align with the geological boundaries in maps and cross-sections (Figures 3.2 and 3.3), and the r.m.s. misfit was consistently smaller for the anisotropic inversion than the isotropic inversion at all frequencies (Figure 4.12 in Lee, 2020). The most notable features are discussed below; for a detailed discussion and interpretation of the individual features, see Chapter 4.5 of Lee (2020).

In general, boundaries of the anisotropic features (AF) align with the locations and strikes of mapped geological structures and lithological packages whereas the boundaries of isotropic conductors (IC) and isotropic resistors (IR) do not match the mapped geology. In particular, the sharp boundary between AF2 and AF3 matches very closely with the mapped location of the SRMT fault (Figure 3.2), and the wedge-shaped geometry of AF3 matches well with the subsurface geometry of the Yellowjacket Gneiss between the SRMT fault and Bear Foot Thrust (Figure 3.3). Furthermore, AF3 is conductive in the North-South (ρ_x) and East-West (ρ_y) directions, but resistive in the vertical direction (ρ_z). These orientations are consistent with the SSE strike and shallow-moderate dip of cleavage of the Yellowjacket Gneiss in this region, implying that conductive minerals may be aligned along cleavage planes, enhancing cleavage-parallel conduction and inhibiting cleavage-normal conduction. In contrast, features IC4 and IC5 in the isotropic model are not continuous along-strike, and instead plunge perpendicular to the dip of the Yellowjacket Gneiss measured in the field.

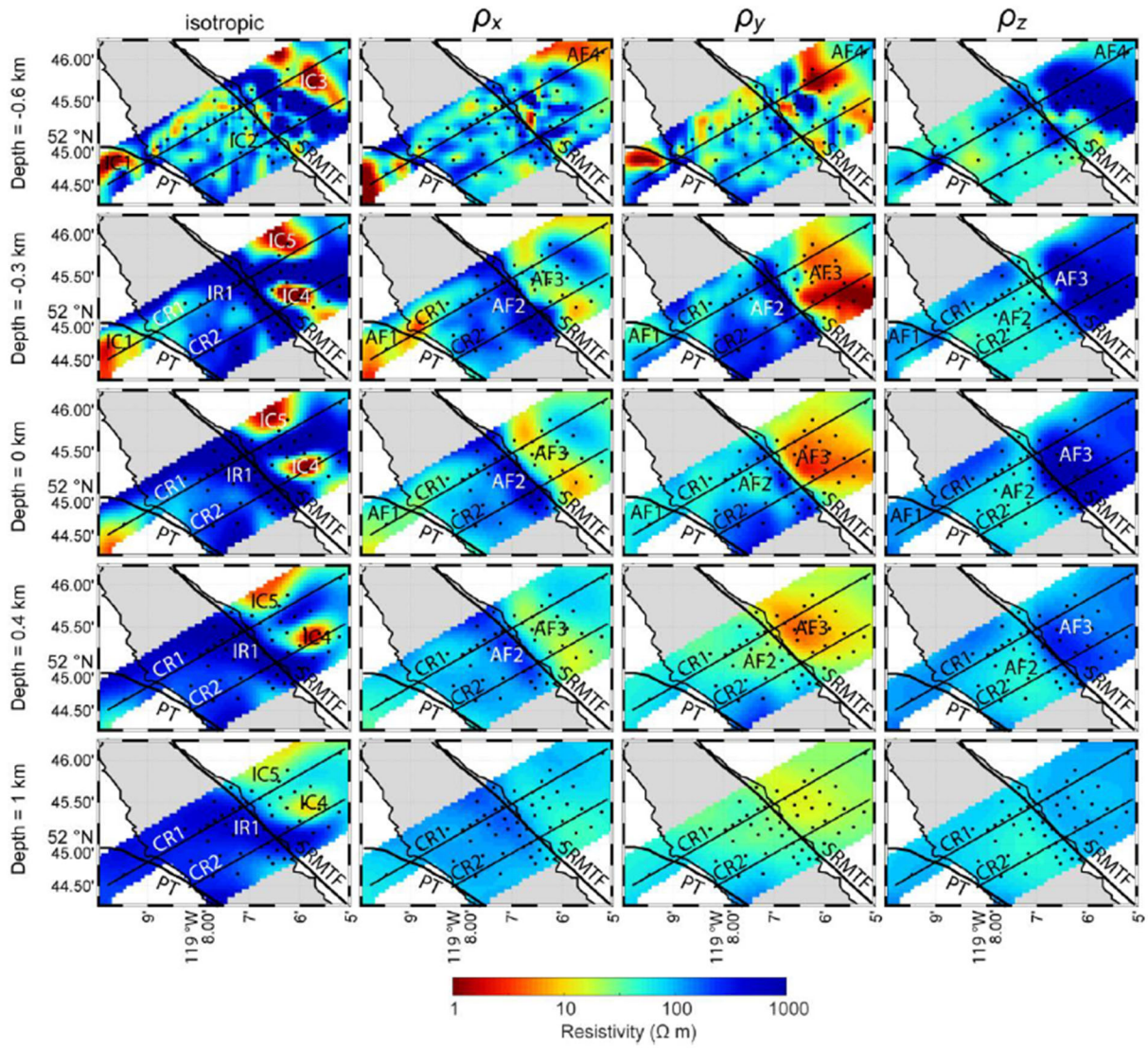

Figure 3.2. Map view of isotropic (column 1) and anisotropic (columns 2-4) resistivity models at five depth slices at Canoe Reach North from Lee (2020). Anisotropic resistivities are calculated in three axes: N-S (ρ_x), E-W ($\rho_{y)}$, and vertically (ρ_z). Black dots are MT stations. CR1 and CR2 correspond to the model sections in Figure 3.6. Major faults are labelled: SRMTF = Southern Rocky Mountain Trench Fault, PT = Purcell Thrust. Numbered isotropic conductors (IC), isotropic resistors (IR), and anisotropic features (AF) are discussed in the text.

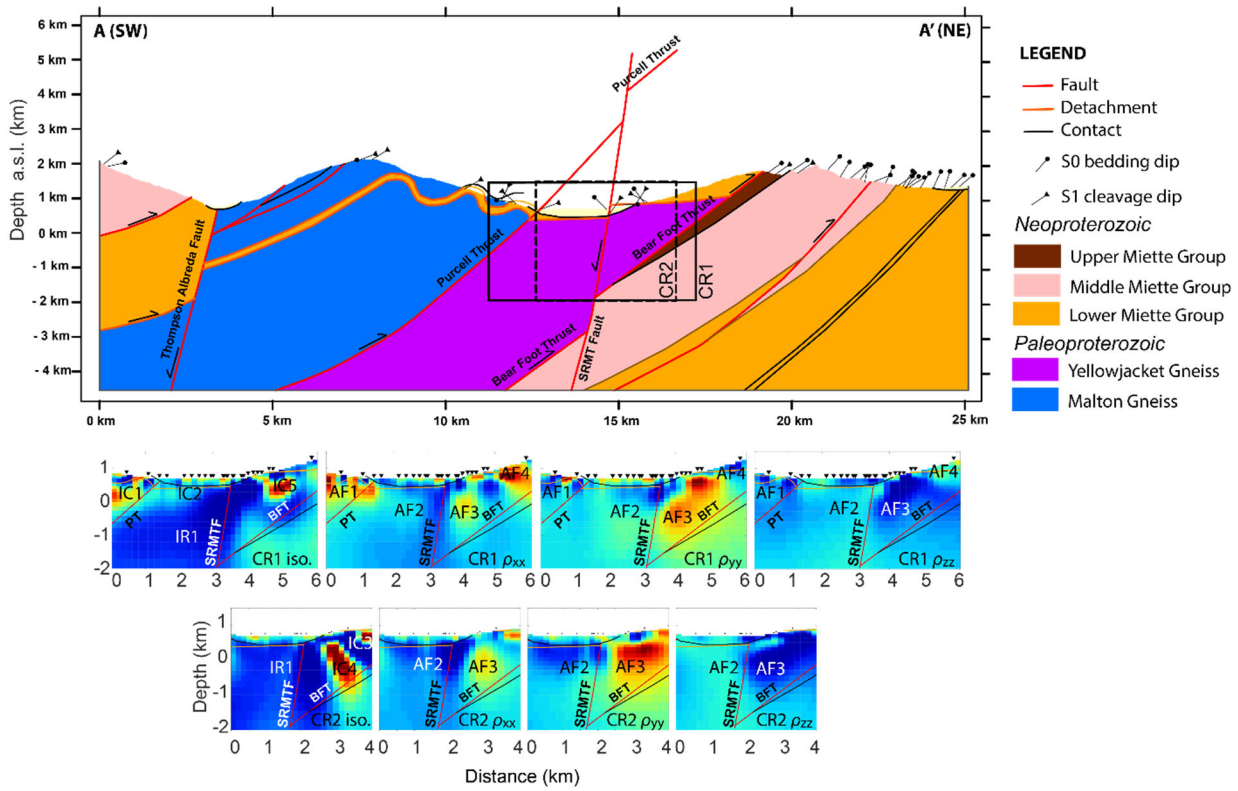

Figure 3.3. Cross Section A compared to isotropic (iso.) and anisotropic (ρ_x, ρ_y, and ρ_z) resistivity models at Canoe Reach North from Lee (2020). Black rectangles on the geologic cross-section indicate the alignment of model sections CR1 (northern profile) and CR2 (southern profile) with the geology.

3.5.1.2 Cross Section B (Canoe Reach South)

Cross Section B (Figure 3.5) corresponds to two of the four MT surveys (Line A and B; Lee 2020) conducted by Quantec Geoscience at Canoe Reach South, located approximately 30 km southeast of Valemount. Lee (2020) performed two inversions with this data, one assuming isotropic resistivity, and another assuming anisotropic resistivity. Both models contain features that correspond to geological boundaries in maps and cross sections (Figures 3.4 and 3.5), although the r.m.s. misfit was smaller for the anisotropic inversions at nearly all frequencies (Figure 4.12 in Lee 2020). The most notable features are discussed below; for a detailed discussion and interpretation of the individual features, see section 4.5 of Lee (2020).

The boundaries of the anisotropic features (AF) roughly align with the locations and strikes of mapped geological structures and lithological packages whereas the boundaries of isotropic conductors (IC) and isotropic resistors (IR) do not match the mapped geology. In particular, the sharp boundary between AF6/8/10 and AF9, matches closely with the mapped location of the SRMT fault. AF6 is a narrow,

subvertical feature that occurs underneath the outlet of the Canoe River hot spring, at the mapped intersection of the SRMT fault and a minor splay. This feature is most conductive in the vertical direction and may represent a vertical fluid conduit feeding the Canoe River thermal spring.

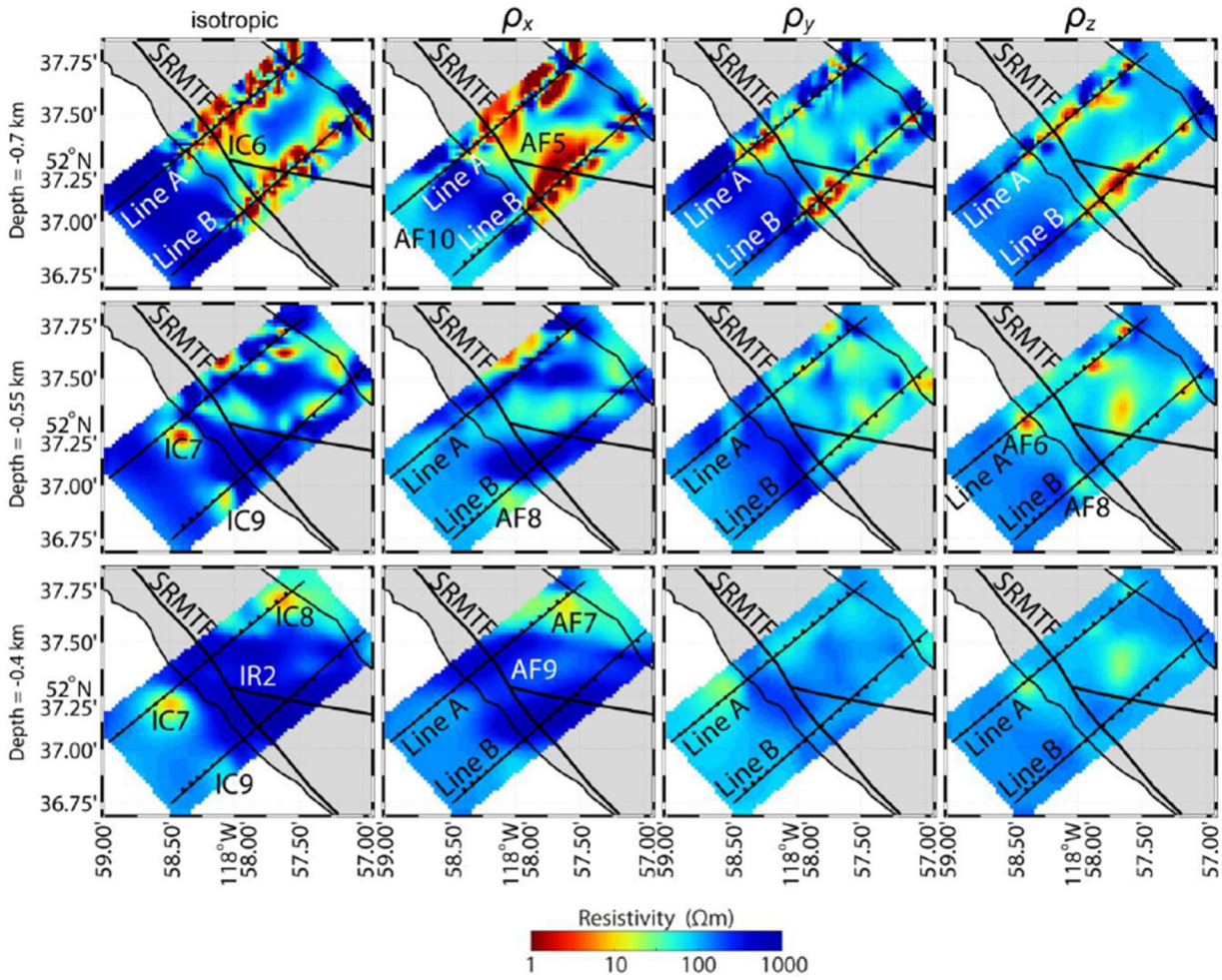

Figure 3.4. Map view of isotropic (column 1) and anisotropic resistivity models (columns 2-4) at Canoe Reach South at 3 depth slices from Lee (2020). Anisotropic resistivities are calculated in three axes: N-S (ρ_x), E-W (ρ_y), and vertically (ρ_z). Black dots are MT stations. Line A and Line B correspond to the model sections in Figure 3.5. Numbered isotropic conductors (IC), isotropic resistors (IR), and anisotropic features (AF) are discussed in the text. SRMTF = Southern Rocky Mountain Trench Fault.

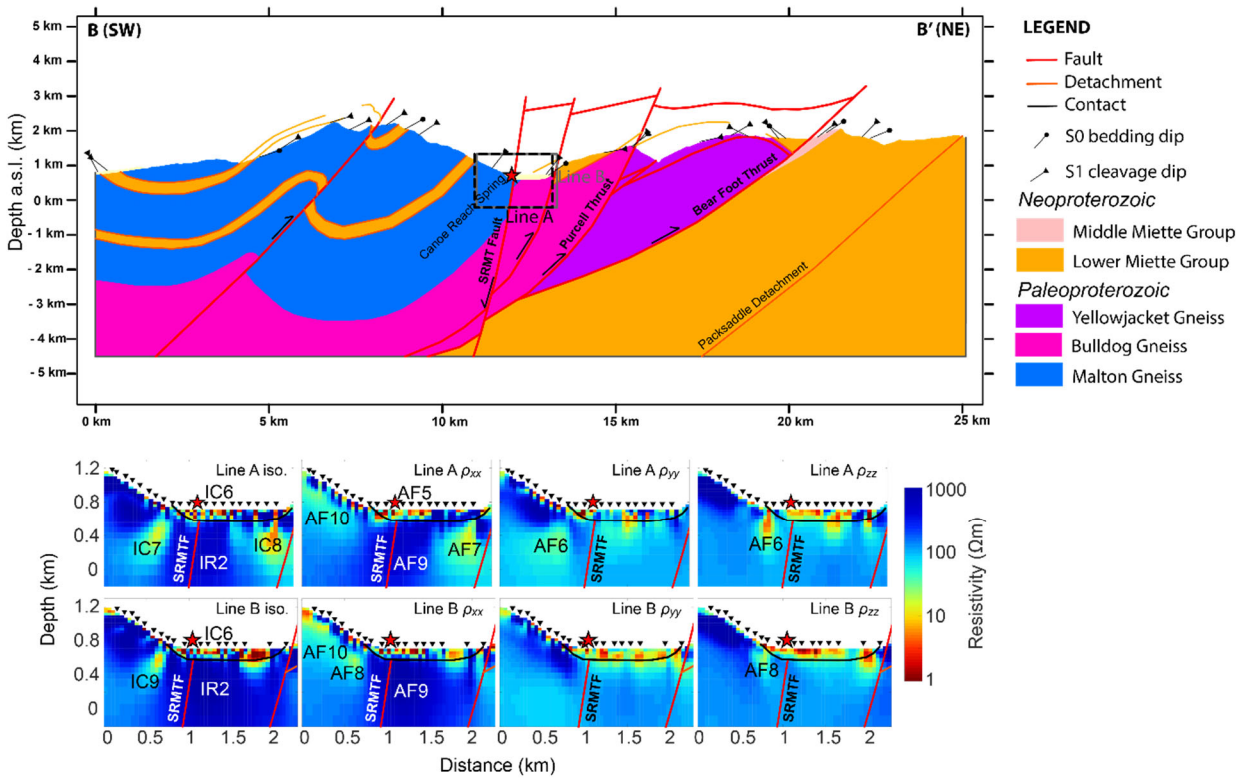

Figure 3.5. Cross Section B compared to MT isotropic (iso.) and anisotropic (ρ_x, ρ_y, and ρ_z) resistivity models at Canoe Reach South from Lee (2020). Black and grey rectangles on the geologic cross-section indicate the alignment of model sections Line A (northern profile) and Line B (southern profile) with the geology.

3.5.1.3 Cross Section C (Canoe Reach South)

Cross Section C (Figure 3.7) corresponds to the two southernmost MT surveys (line C and D; Lee 2020) conducted by Quantec at Canoe Reach South, located approximately 30 km southeast of Valemount. Lee (2020) performed two inversions, one assuming isotropic resistivity, and another assuming anisotropic resistivity. Both models contain features that correspond to geological boundaries in maps and cross sections (Figures 3.6 and 3.7), although the r.m.s. misfit was lower for the anisotropic inversion at all frequencies (Figure 5.11; Lee 2020). For a detailed discussion and interpretation of these features, see section 4.5 of Lee (2020).

A notable anisotropic feature that matches well with the geology is AF12. In map view (Figure 3.6) it is truncated by the trace of the SRMT fault, and in the cross-section (Figure 3.7), it corresponds to a tabular body of the Lower Miette Group. It is conductivity in the vertical direction (ρ_z) and resistive in the horizontal axes (ρ_x and ρ_y). Another notable feature is the highly conductive IC10, which stands out as the largest and most conductive feature in any of the MT models. It may be equivalent to AF11 in the anisotropic models, which is conductive in the horizontal axes (ρ_x and ρ_y) and less so in the vertical. All

these features (AF12, IC10, and AF11) appear to be bound by the SRMT fault, which suggests the fault juxtaposes rocks with different hydrogeological properties.

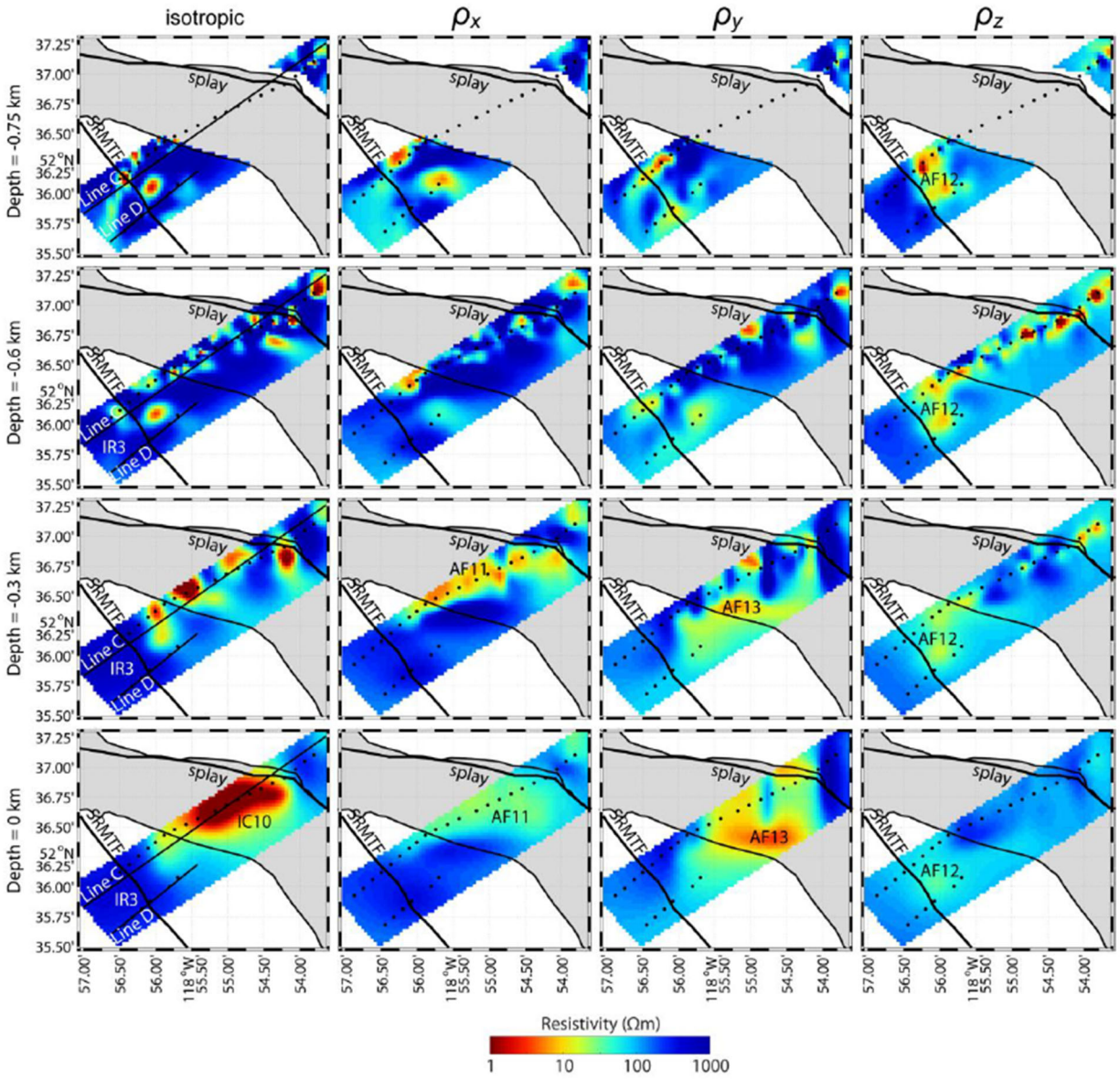

Figure 3.6. Map view of isotropic (column 1) and anisotropic resistivity models (columns 2-4) at Canoe Reach South at 4 depth slices from Lee (2020). Anisotropic resistivities are calculated in three axes: N-S (ρ_x), E-W (ρ_y), and vertically (ρ_z). Black dots are MT stations. Line C and Line D correspond to the model sections in Figure 3.7. Numbered isotropic conductors (IC), isotropic resistors (IR), and anisotropic features (AF) are discussed in the text

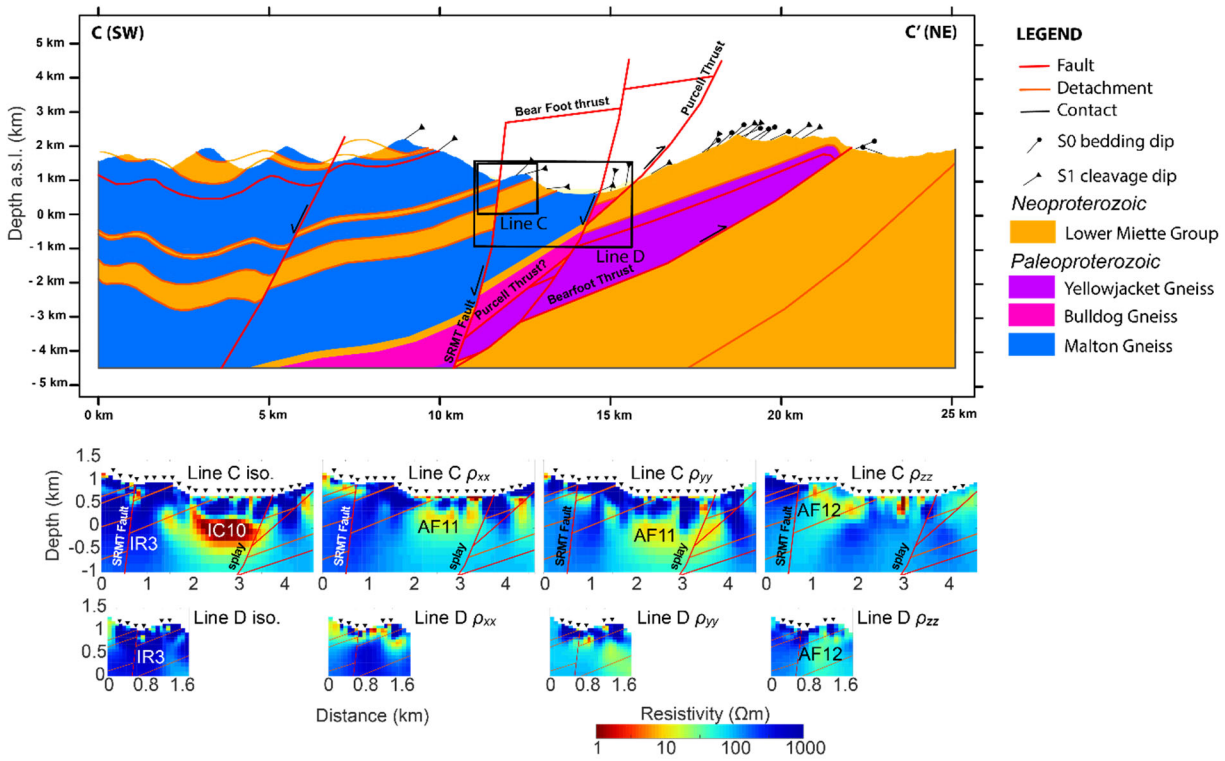

Figure 3.7. Cross Section C compared to MT isotropic (iso.) and anisotropic (ρ_x, ρ_y, and ρ_z) resistivity models at Canoe Reach South from Lee (2020). Black rectangles on the geologic cross-section indicate the alignment of model sections Line C (northern) and Line D (southern) with the geology.

3.5.2 Microscopy

3.5.2.1 Controlling for epoxy

The use of carbon-based epoxy in the sample preparation makes it difficult to ascertain whether a carbon peak in EDS data actually represents graphite. The EDS data in Figure 3.8 show the characteristic spectra for epoxy on the edge of a thin section mount (point 6), and within a discrete fracture that extends inwards from the edge of the thin section (point 5). Carbon concentrations > 50 wt% and an accompanying trace amount of chlorine appear to be indicative of epoxy contamination. This characteristic spectrum is useful when comparing to putative graphite occurrences, which generally have lower carbon peaks (<50%) and no chlorine.

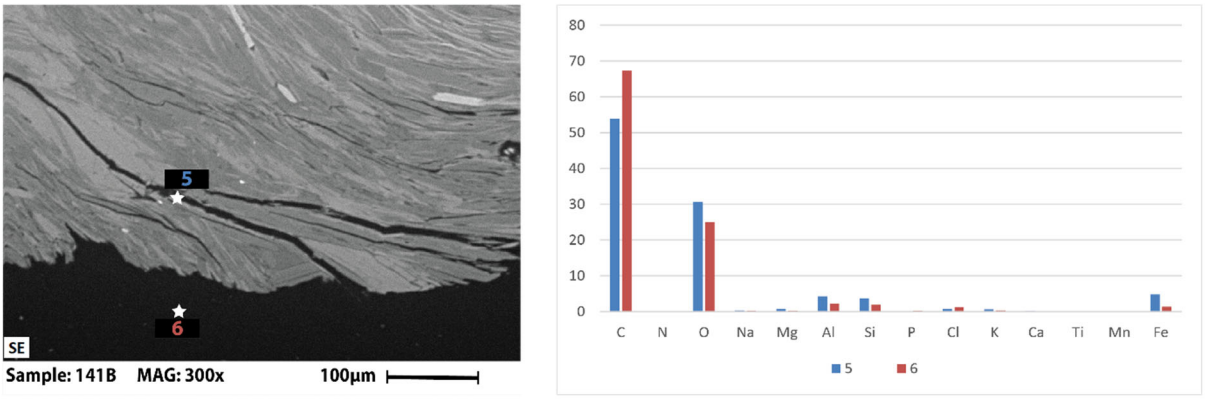

Figure 3.8. SEM image and corresponding EDS data for control point (6) at the edge of a thin section and one point within a discrete fracture (5). The control point is known to be epoxy. The EDS data show a high carbon peak (> 50 wt%) and minor chlorine peak (2 wt%).

3.5.2.2 Sample 113

Sample 113 is a mylonitic orthogneiss collected from an outcrop of Yellowjacket Gneiss 2 km southeast of the Canoe Reach North MT survey, and 15 km southeast of Valemount (Figure 3.1). Thin sections viewed under plane-polarized (PPL), cross-polarized (XPL), and reflected light (RL) (Figure 3.9) reveal that it is dominantly composed of quartz (~50%), plagioclase (~20%), and muscovite (~20%). Quartz crystals are generally equant and less than 200 microns in diameter, and exhibit undulose extinction which is indicative of high strain. Plagioclase porphyroclasts are up to 5mm in diameter and exhibit characteristic polysynthetic twinning. No diagnostic kinematic indicators (e.g., S-C fabrics, delta or sigma porphyroclasts) are observed. Muscovite crystals 500-1000 microns in length are oriented subparallel to the main foliation, but do not provide a sense of shear. Narrow stringers of opaque material visible in PPL and XPL are moderately to highly reflective in RL. In row 2 of Figure 3.9, note that the epoxy visible at the bottom edge of the thin section is transparent in PPL, opaque in XPL, and non-reflective in RL. This is important to note because it is often difficult to distinguish the epoxy from graphitic carbon.

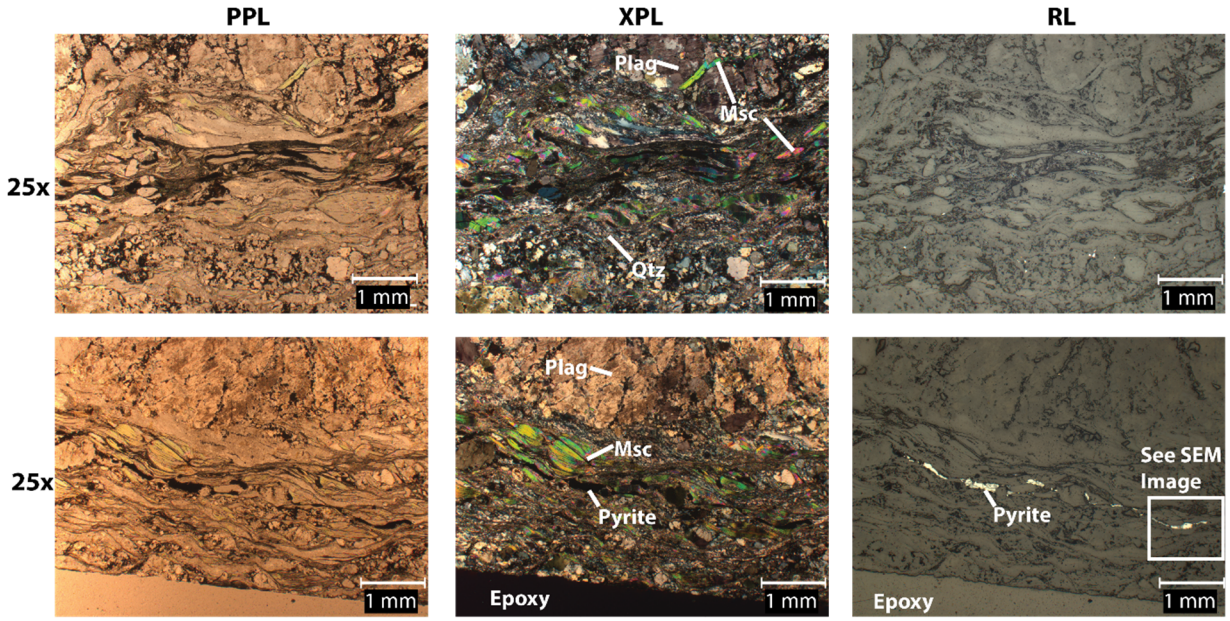

Figure 3.9. Photomicrographs of two perspectives of sample 113 under PPL, XPL, and RL at 25x magnification. Sample location is shown in Figure 3.1. In row 2, note the stringer of opaque (black) material under PPL and XPL that is highly reflective under RL. The white box in RL shows and area that was imaged with the SEM (Figure 3.10), which confirms it is pyrite. Abbreviations: Plag – plagioclase, Msc – Muscovite, Qtz – Quartz.

Of interest to this study is the presence of graphite in the sample. The opaque and reflective stringer observed with the petrographic microscope (Figure 3.9, row 2, column 3) was further investigated using scanning electron microscopy, as graphite is known to be opaque under transmitted light and reflective under reflected light (e.g., Card, 2013). It was evident from the spectra that these reflective minerals were in fact pyrite (FeS_2), as these were the strongest peaks. However, adjacent features too small to be viewed under the petrographic microscope returned anomalously high carbon peaks (Figure 3.10c-f). A complication is that the epoxy adhesive used to prepare the thin sections contains carbon and could be confused as graphite. To circumvent this issue, we also prepared thick sections for examination with the SEM, which were polished deeply to avoid contamination with epoxy. As shown in Figure 3.10d-e, fractures with similar morphology to those in Figure 3.10c, have anomalous carbon peaks, but no chlorine peak, which suggests that these fractures are filled with pure graphite, rather than epoxy.

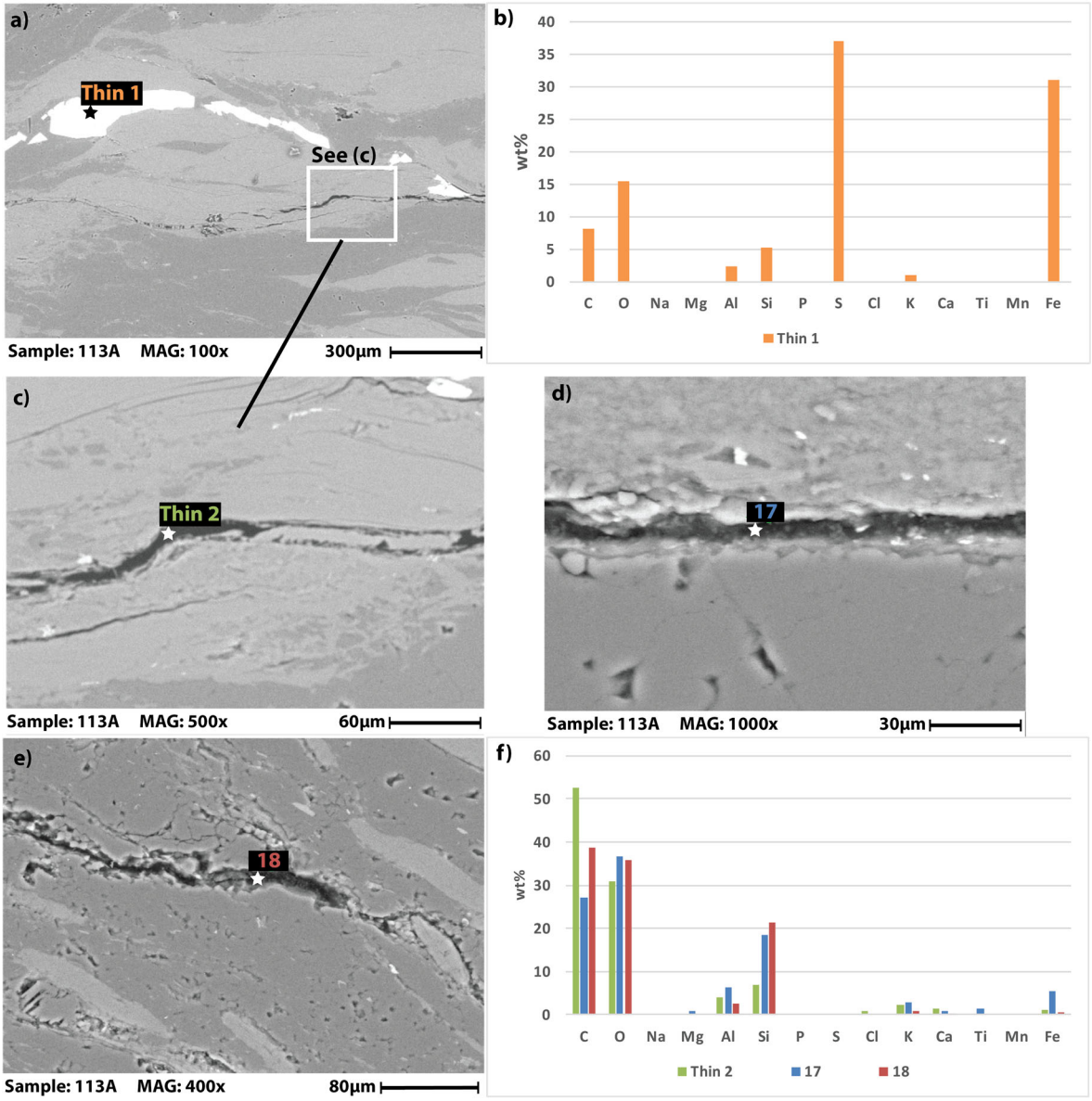

Figure 3.10. SEM images and corresponding EDS data of sample 113. a) Highly reflective pyrite stringer viewed in thin section, and corresponding elemental spectra (b) with high Fe and S peaks. c) Carbon rich fracture in thin section. d) and e) Carbon rich fractures in thick section. f) EDS data for c, d, and e. Note the absence of Cl for points 17 and 18, indicating that carbon represents graphite and not epoxy.

It is apparent from the SEM images that graphite exists in the sample and is partially interconnected parallel to the metamorphic foliation. Moreover, in some places, the graphite is in contact with pyrite stringers that are also parallel to the foliation (Figure 3.10a).

This sample was analyzed with XRD to obtain a modal percentage of the various conductive phases. The XRD was unable to detect a graphite peak, which implies that the graphite is essentially below the limit of detection (1-5 wt%). The XRD did pick out a pyrite peak at the limit of detection.

3.5.2.3 Sample 114

Sample 114 is a mylonitic orthogneiss collected from an outcrop of Yellowjacket Gneiss 3 km southeast of the Canoe Reach North MT survey, and 15 km southeast of Valemount (Figure 3.1). Thin sections viewed under PPL, XPL, and RL reveal that it is dominantly composed of muscovite and quartz. Unlike 113, no feldspar porphyroclasts are present. The mica defines a distinct S-C fabric (Figure 3.11), but because the sample is not oriented to its original position, the sense and direction of shear cannot be deduced from the thin section. Oblong minerals opaque under PPL and XPL and highly reflective under RL, are likely disseminated and highly strained sulfides (pyrite?), which comprise up to 5% of the rock volume.

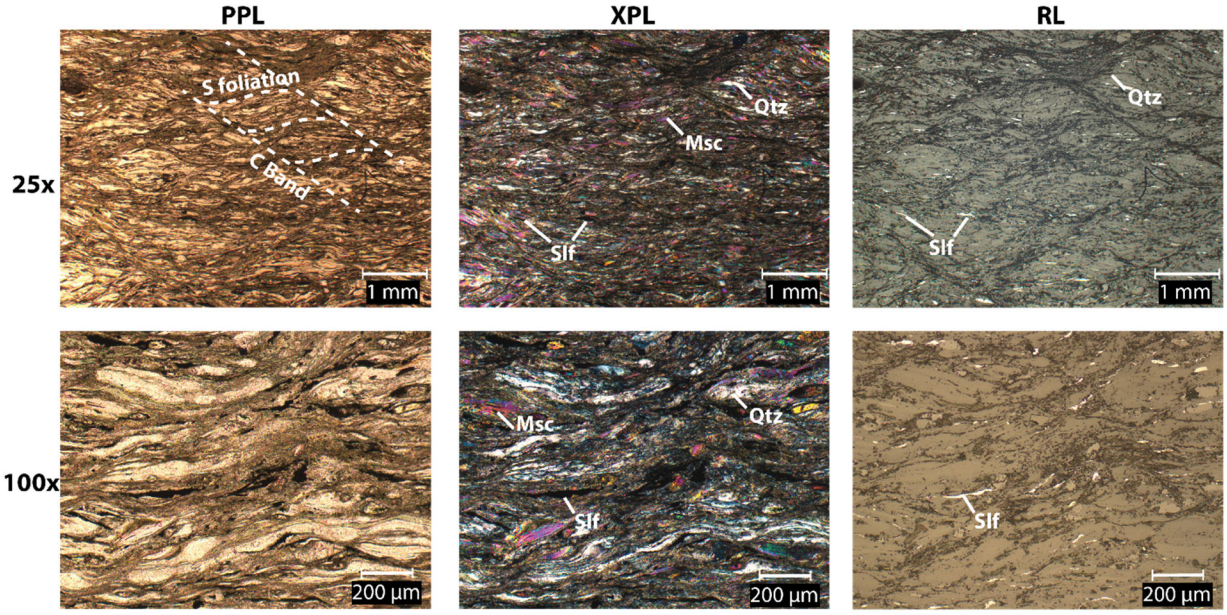

Figure 3.11. Photomicrographs of sample 114 under PPL, XPL, and RL at 25x and 100x magnification. Sample location is shown in Figure 3.1. Note the elongate opaque and reflective sulfide minerals throughout the sample. Abbreviations: Msc – Muscovite, Qtz – Quartz, Slf – Sulfide.

Thick sections of sample 114 examined under SEM (Figure 3.12) display dark grey, amorphous recessive zones, aligned subparallel to the metamorphic foliation. EDS data at points 1-5 (Figure 3.12) do not have chlorine peaks, indicating that the carbon represents graphite. Figure 3.12d is a BSE map showing the distribution of carbon within the fracture imaged in Figure 3.12b. This map demonstrates that the carbon

is not pervasive throughout the sample, and is only present in the dark shaded, recessive fractures. The medium-grey crystal within the fracture has 50 wt% of carbon, and no chlorine peak, indicating that it is graphite.

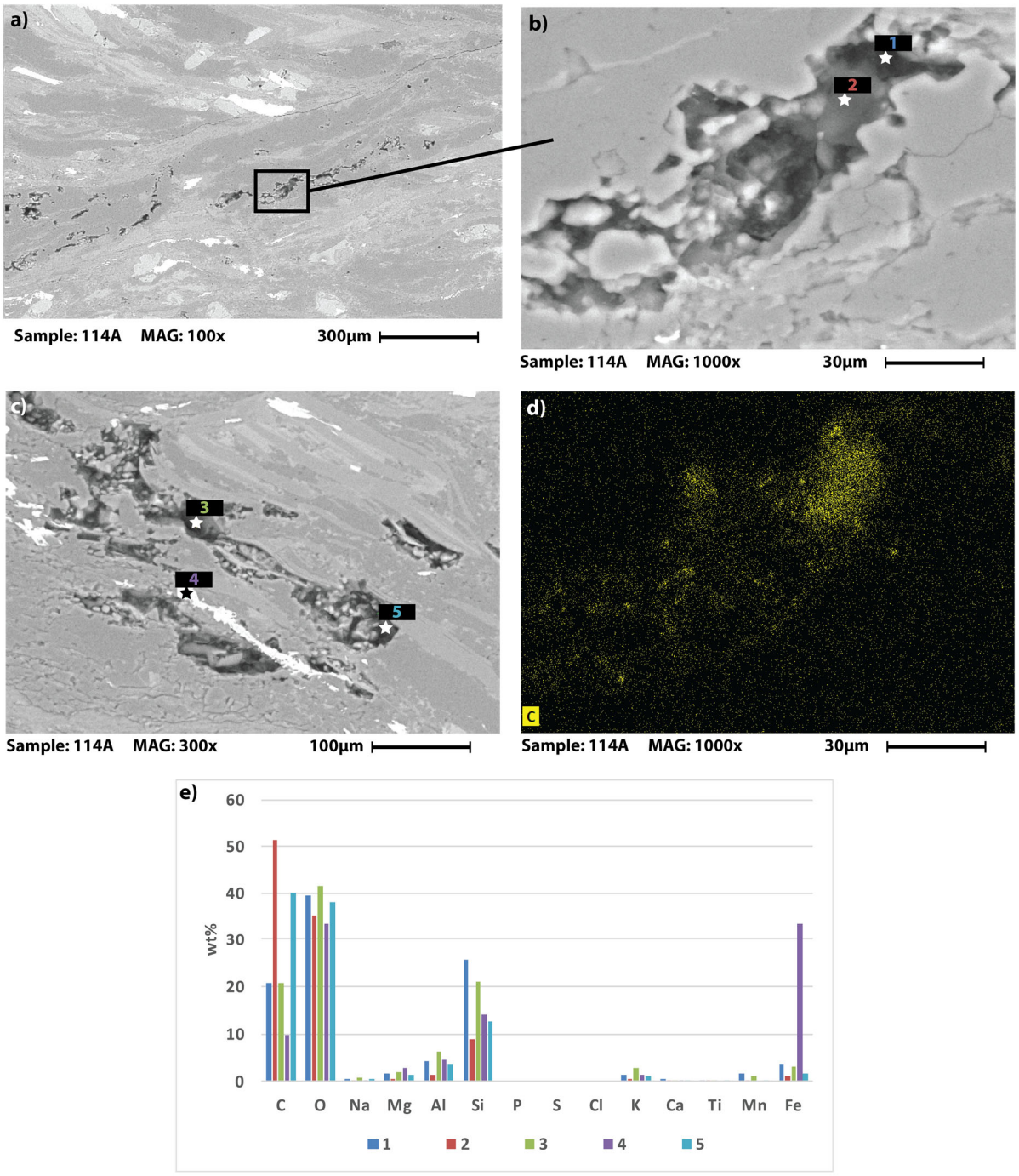

Figure 3.12. SEM images and EDS data for thick section of sample 114. a) recessive regions containing putative graphite aligned along metamorphic foliation. b) close-up view of recessive region from (a), showing

two points (1 and 2) with high carbon peaks (20-50 wt%) and no chlorine peaks. c) Recessive regions with carbon peaks between 20 and 40 wt% (points 3 and 5). White (reflective) mineral (point 4) is an iron oxide with distinct Fe peak seen in (e). d) BSE element map of carbon in same view as (b) demonstrates that carbon is not present throughout entire sample. e) EDS data for a, b, and c.

3.5.2.4 Sample 117

Sample 117 is a quartzose biotite schist collected from an outcrop of the Lower Miette Group 5 km southeast of the Canoe Reach North MT survey, and 17 km southeast of Valemount (Figure 3.1). Thin sections viewed under PPL, XPL, and RL (Figure 3.13) reveal that it is dominantly composed of quartz (80%), and biotite (20%), with a trace amount of sulfide minerals, likely pyrite. The biotite defines a weak foliation between quartzose layers. Sulfides, which are highly reflective under RL, are sub-equant and not as highly strained/lineated as those observed in the Yellowjacket Gneiss (samples 113 and 114).

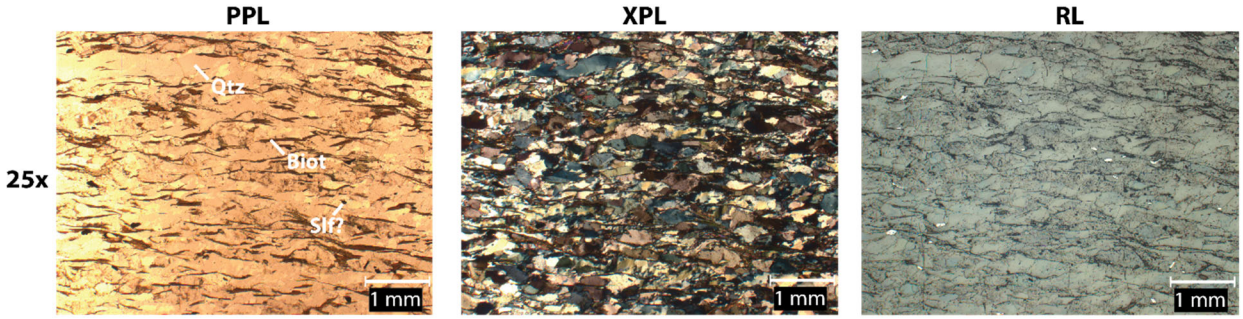

Figure 3.13. Photomicrographs of sample 117 under PPL, XPL, and RL at 25x magnification. Sample location is shown in Figure 3.1. Abbreviations: Qtz – Quartz, Biot – Biotite, Slf – Sulfide.

SEM images of sample TF18-117 reveal minor carbon peaks (5-8 wt%) in fractures and grain boundaries between biotite and quartz (Figure 3.14). Carbon does not appear to be a major constituent of this sample.

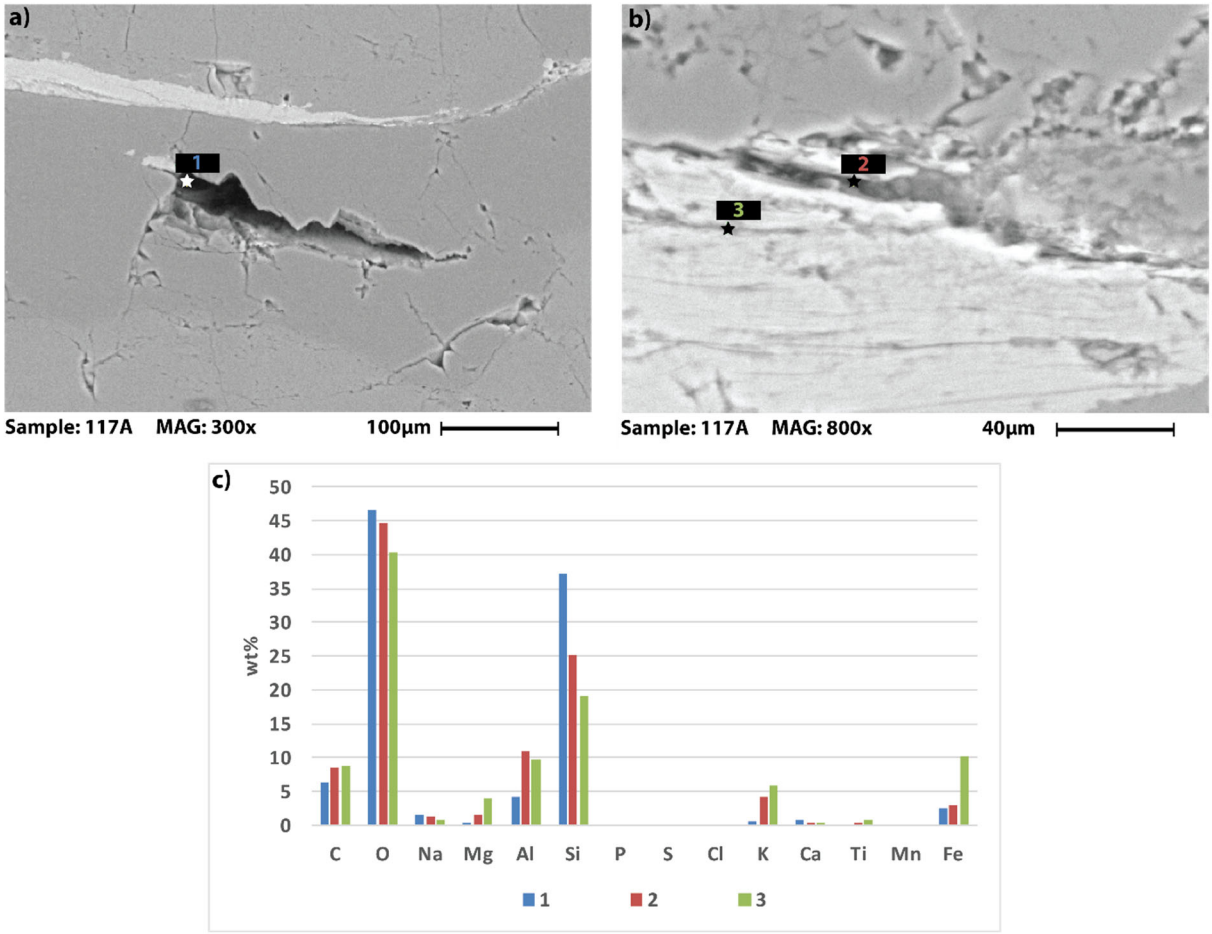

Figure 3.14. SEM images and elemental spectra for sample 117. a) a fracture within dominantly quartz matrix contains a minor carbon peak. b) grain boundaries between quartz and biotite have minor carbon peaks. c) EDS data for points 1-3 in (a) and (b).

3.5.2.5 Sample 138

Sample 138 is a crenulated biotite schist collected 2 km northwest of the Canoe Reach North MT survey, and 10 km southeast of Valemount. It is polydeformed, with a strong primary foliation and secondary crenulation cleavage evident both in hand sample and in thin section (Figure 3.15). The rock is 90% biotite with sparse layers of quartz constituting the remaining 10%. Rare elongate pyrite crystals occur parallel to the primary foliation. Detachment along primary cleavage planes has allowed for void space to open in the hinges of crenulations. This void space is filled with epoxy and an unknown material.

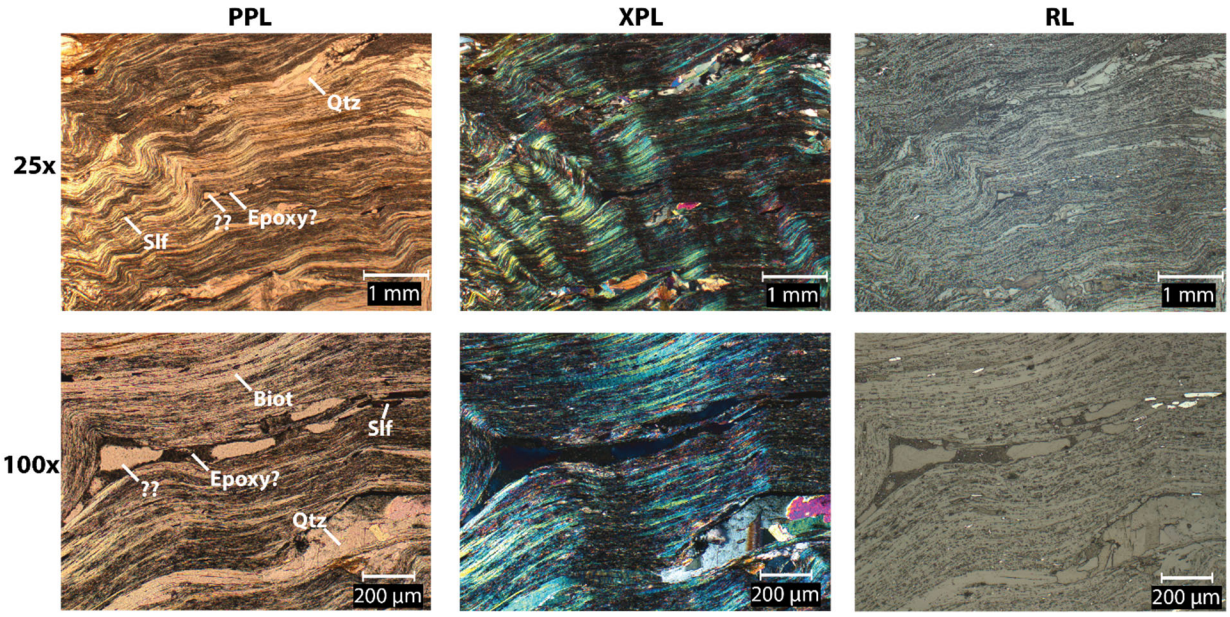

Figure 3.15. Photomicrographs of sample 138 under PPL, XPL, and RL at 25x and 100x magnification. Sample location is shown in Figure 3.1. Abbreviations: Qtz – Quartz, Slf – Sulfide, Msc – Muscovite, ?? – unknown material.

SEM images (Figure 3.16a and b) reveal dark amorphous zones with moderate carbon peaks between 10-35 wt% carbon and no chlorine (points 1-7, 9, 11-13). Brittle fractures (points 8 and 10) show very high carbon peaks (up to 59 wt%) and minor chlorine peaks, suggesting they may be contaminated with epoxy. The fact that carbon weight percentage increases in the presence of chlorine, but the remainder of the spectra remain similar, suggests that both graphite and carbon-based epoxy may be present in the same recessive fractures. BSE mapping (not shown in figure) confirms that carbon is only present in dark recessive regions, and is not pervasive throughout the sample.

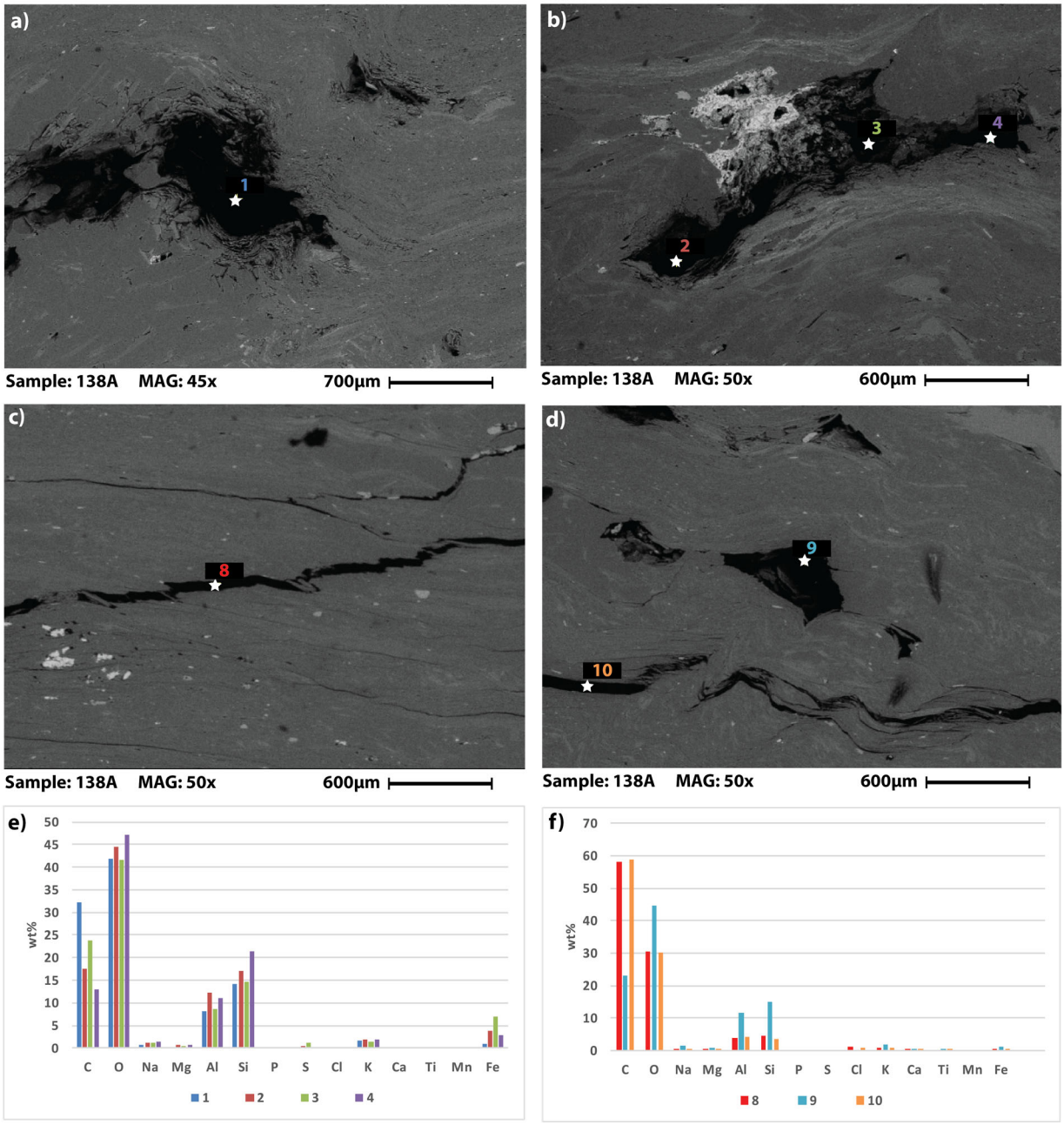

Figure 3.16. SEM images and EDS data for thick section of sample 138. a) and b) discontinuous recessive zones containing carbon peaks (13-32 wt%) with no accompanying chlorine. c) and d) fractures with anomalously high carbon peaks (up to 59 wt%) accompanied by a minor chlorine peak. e) and f) EDS data for a-d.

3.5.2.6 Sample 141

Sample 141 is a crenulated biotite schist collected at the northeast end of the Canoe Reach North MT survey, 14 km southeast of Valemount. It is polydeformed, exhibiting a strong primary foliation and a secondary crenulation cleavage evident in both hand sample and thin section (Figure 3.17). The

crenulation is not as strongly developed as in sample 138, but otherwise these samples are very similar in composition and morphology. The rock is 90% biotite and 10% quartz, with trace amounts of pyrite and amphibole. The pyrite crystals are elongate and occur parallel to the primary foliation.

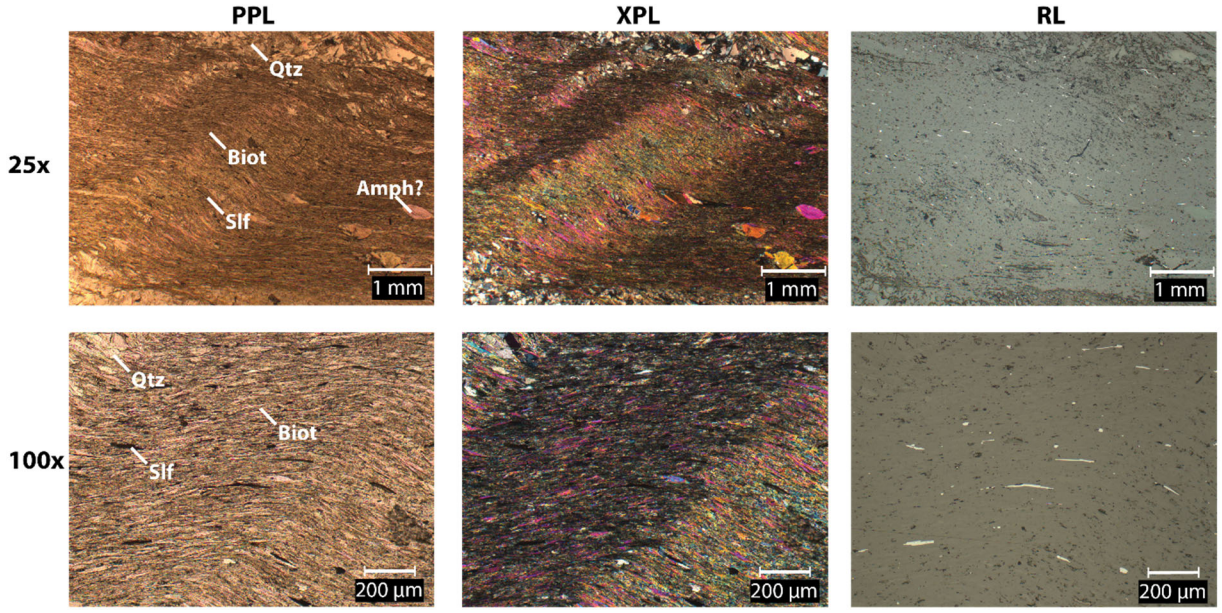

Figure 3.17. Photomicrographs of sample 141 at 25 x and 100x magnification. Sample location is shown in Figure 3.1. Abbreviations: Qtz – Quartz, Slf – Sulfide (pyrite), Biot – Biotite, Amph. - Amphibole.

SEM images of thick sections of sample 141 (Figure 3.18a and b) reveal that zones of carbon (43-52 wt%) occur on grain boundaries between quartz and biotite crystals but these do not appear to be well connected. BSE mapping (not shown in figure) confirms that carbon is only present in dark recessive region, and not pervasive throughout sample. Larger, dark, elongate features (Figure 3.18c and d) have significant carbon peaks (50 wt%), but a trace amount of chlorine suggests they may be contaminated by epoxy. At higher magnification (3000-5000x; Figure 3.19), carbon peaks are observed on thin, dark grey rims surrounding biotite crystals, and no chlorine is present. These rims are likely graphite and are well-connected to facilitate electrical conduction.

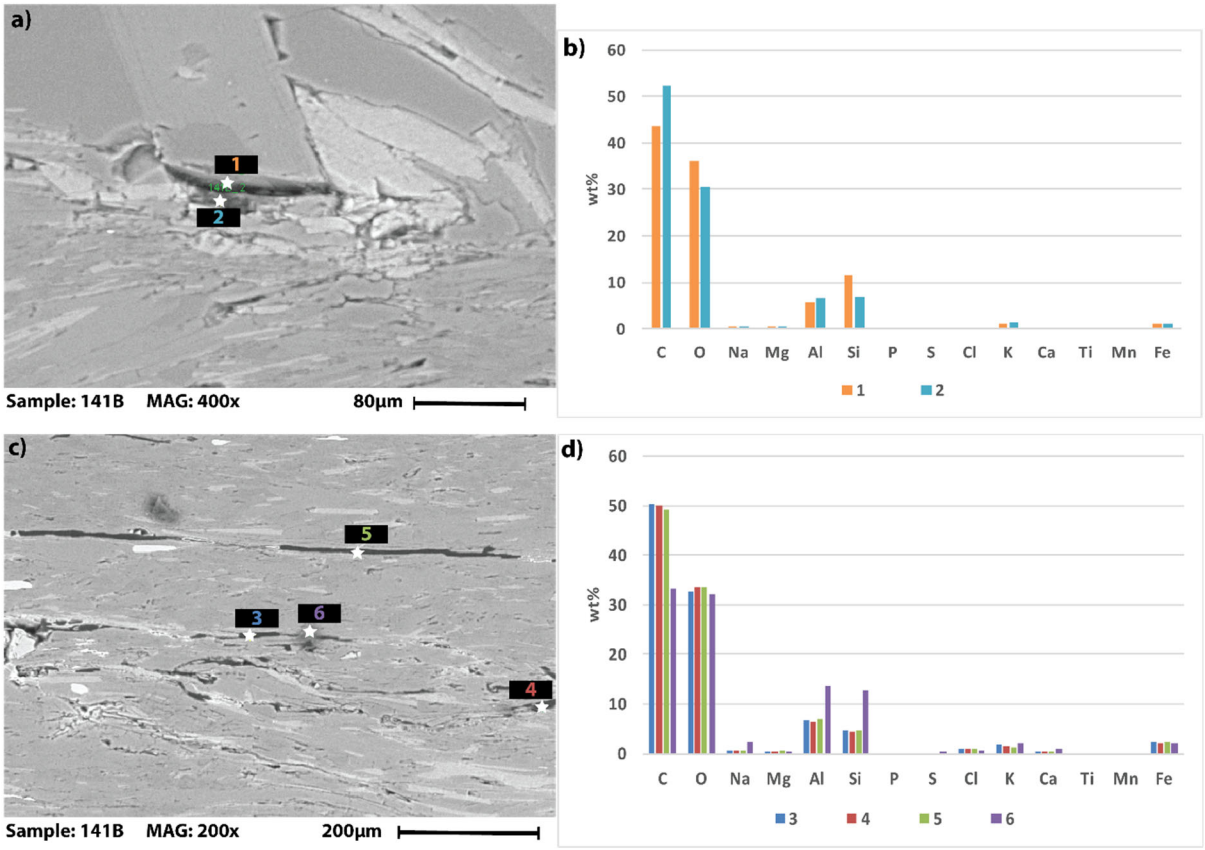

Figure 3.18. SEM images and elemental spectra of thick sections of sample 141. a) and b) image and EDS data for recessive zones between quartz and biotite crystal boundaries. These regions have 43-52 wt% carbon and no chlorine, but are poorly connected. c) and d) image and EDS data for elongate recessive zones with high carbon peaks and minor chlorine peaks.

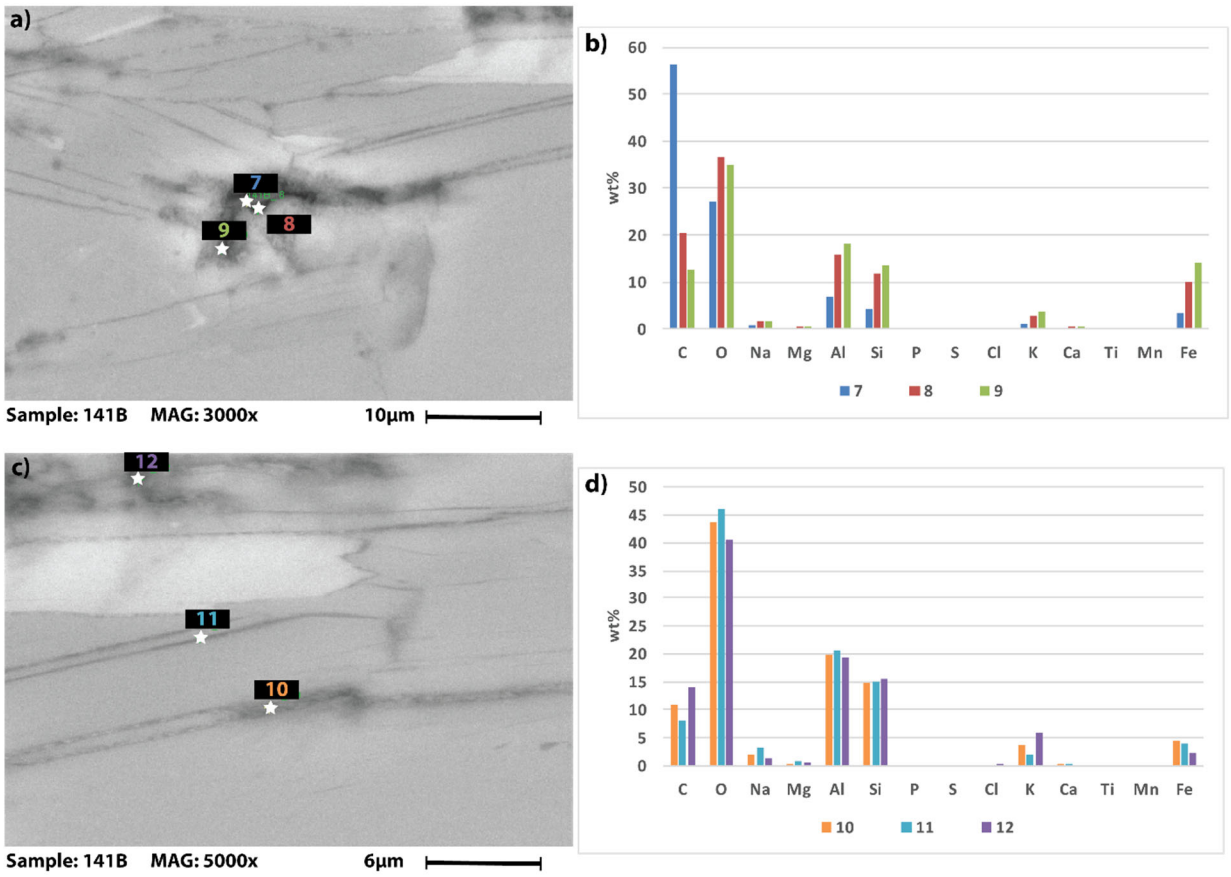

Figure 3.19. High magnification (3000-5000x) SEM images and EDS data for thick section of sample 141. a) and b) image and EDS data for carbon bearing, amorphous zone between biotite crystals. c) and d) image and EDS data for carbon-bearing rims surrounding biotite crystals.

3.5.2.7 Sample 144

Sample 144 is a biotite schist collected from an outcrop of the Lower Miette Group 15 km northwest along-strike from the Canoe Reach North MT survey, immediately northeast of the town of Valemount. The hand sample appeared quite graphitic with a dark grey metallic luster and leaving dark grey smudges on hands. Thin sections revealed that most of the rock is biotite, with minor quartz layering (Figure 3.20). The rock is also weakly crenulated. Minor, highly reflective, subrounded, iron oxides are disseminated throughout (see Figure 3.20 row 2, column 3). The hand sample was friable and required the use of a substantial amount of epoxy during preparation. In row 1 of Figure 3.20, the epoxy on the bottom edge of the thin section shares similar optical properties to the material filling numerous fractures ranging from 50 µm to 1 mm in width, suggesting these fractures are epoxy-filled.

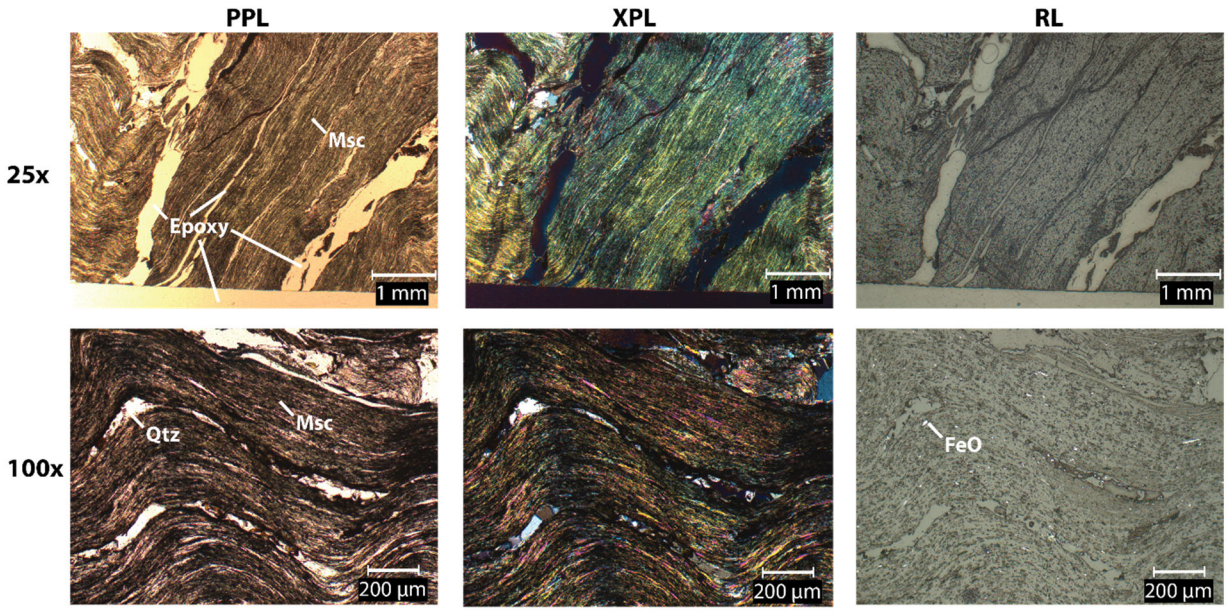

Figure 3.20. Photomicrographs of sample 144 at 25x and 100x magnification. Sample location is shown in Figure 3.1. In row 1, epoxy is shown filling 50µm to 1 mm wide fractures. One such fracture is imaged with the SEM in Figure 3.21a. The optical characteristics of epoxy at the bottom edge of the thin section is shown for comparison to the fracture-filling epoxy. In row 2, minor layers of quartz are shown between muscovite. Abbreviations: Msc – Muscovite, Qtz – Quartz, FeO – Iron Oxide.

Due to the COVID-19 shutdown, no thick sections of sample 144 were imaged with the SEM, however the thin section still provided valuable data. SEM images (Figure 3.21a) of thin sections reveal a 53 wt% carbon peak in a 50 µm wide brittle fracture with similar morphology to the brittle fractures observed with the petrographic microscope in Figure 3.20. However, this peak is accompanied by small chlorine peak, suggesting possible epoxy contamination. EDS data from a 1.5 x 10^5 μm^2 rectangular area shows no detectable carbon, which confirms that carbon is not pervasive throughout the sample and is only a significant constituent in discrete fractures and recessive cavities. At higher magnification (1000x), SEM images (Figure 3.21b) reveal the presence of 15-21 wt% carbon along grain boundaries between biotite with no accompanying chlorine peaks. It is therefore likely these thin films are graphite, and not epoxy. These graphite films appear well connected and may allow for electrical conduction.

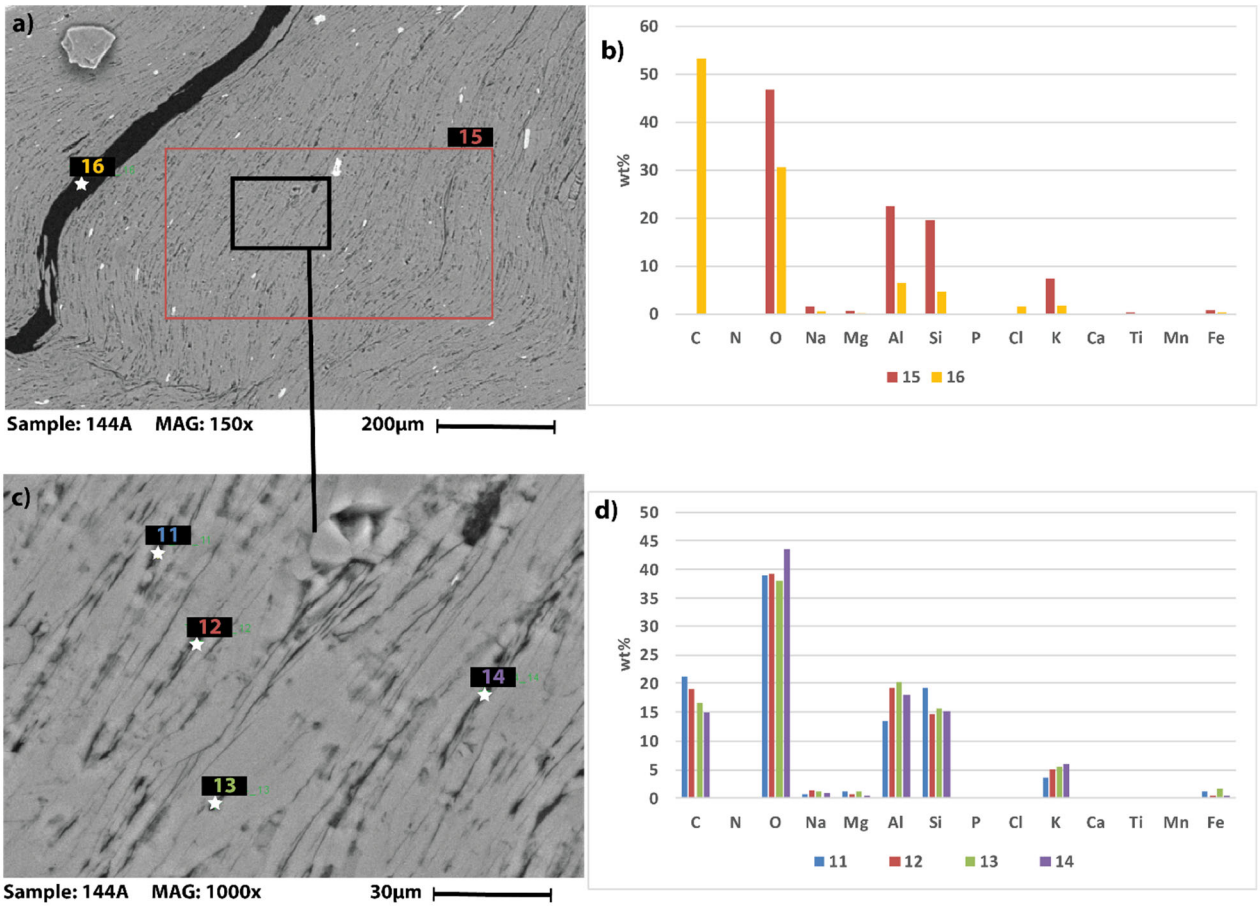

Figure 3.21. SEM images and elemental spectra of sample 144. a) and b) SEM image and EDS data for a 1.5 x 10^5 µm^2 area (15) and a 50-µm-wide fracture (16). Fracture has 53 wt% carbon, but a trace amount of chlorine indicates possible epoxy contamination. Large rectangular area has no detectable carbon. c) and d) show higher magnification image and EDS data for the area within black box in (a); dark regions on muscovite grain boundaries (points 11-14) are carbon rich (15-21 wt%) and do not contain chlorine.

3.6 Discussion

3.6.1 Anisotropy at microscopic and regional scales

The rocks underlying Canoe Reach are polydeformed and record a protracted history of deformation from the Jurassic to the Quaternary. Both the ductile and brittle deformation impart a strong structural fabric on the region. The penetrative and non-penetrative fabrics produced by each phase of deformation are all strike-parallel (NNW-SSE) with each other, collectively enhancing the structural anisotropy. The penetrative ductile fabrics may govern electrical anisotropy at a microscopic scale (µm to mm) due to the alignment of conductive minerals, while the non-penetrative brittle fabrics (faults) may govern electrical anisotropy at regional scale (m to km) due to the enhanced permeability of fault damage zones.

Previous studies have investigated the relationships between conductive mineral phases and conductivity anomalies observed through geophysical means. Nelson and Van Voorhis (1983) showed that concentrations of interconnected sulfides of at least 8 wt% are required to produce low resistivity anomalies of 10 Ωm or less. Frost et al., (1989) showed that thin graphite films (0.1 μm thick) present on mineral grain boundaries could produce low resistivity anomalies in the crust. Such graphite films need only constitute a minor percentage of the rock volume (1-100ppm) to produce conductivity anomalies on the order of 10's of Ωm (Katsube and Mareschal, 1993; Hyndman et al., 1993). Mareschal et al. (1992) found ortho- and paragneiss of the Canadian Shield to have graphite films on grain boundaries. Mathez et al. (1995) described a sample of schist from the Yukon-Tanana Terrane of Alaska that contained a discrete 2 cm long stringer of graphite. Though not anomalously conductive, they demonstrated an increasing conductivity with pressure that was interpreted to represent reconnection of the brittly-fractured graphite. Pelitic schists and gneisses are identified as a common rock type in which grain-boundary graphite might occur, due to precipitation of carbon from CO_2-rich fluids during post-metamorphic cooling (Frost et al., 1989; Hyndman et al., 1993).

Evidence presented in this chapter, including visual inspection of hand samples, petrographic microscopy, SEM imaging, and XRD analyses, all suggest that graphite and sulfide (pyrite) are present in rocks of the Yellowjacket Gneiss and Lower Miette Group in low concentrations. We have not been able to determine exact modal percentages, only that these minerals are present near the detection limit (1-5%) of the XRD instrument. Both the graphite and sulfide mineral phases appear well connected due to their alignment along metamorphic foliations and are present to varying degrees in all rocks we examined. Elongate sulfide minerals are typically observable with the naked eye or petrographic microscope, while the graphite requires SEM imaging. In some cases, graphite appears to fill fractures and voids in the rock, and is observable at magnifications on the order of 10 to 100x. Graphite is also observed at extremely high magnifications up to 5000x, where it is pervasive on grain boundaries. In some cases (e.g., sample 114) graphite and sulfides are in direct contact, which may facilitate conduction of electricity between mineral phases. The combination of 1-5 wt% of sulfide in addition to pervasive graphite filling fractures and coating grain boundaries may together be sufficient to explain some of the conductivity anomalies in the MT inversions conducted by Lee (2020). For example, feature AF3 may be caused by graphite and sulfides aligned along the cleavage of the Yellowjacket Gneiss, and feature AF12 may be related to anisotropic fabrics in the Lower Miette Group.

Brittle fabrics, faults in particular, play a strong role in controlling fluid circulation and therefore may also explain some of the conductivity anomalies. Fluid flow in the subsurface will likely be impeded in the cross-fault direction and enhanced parallel to the fault (Caine et al., 1996). Broad fault damage zones may

act as significant fluid reservoirs due to the permeability of dense fracture networks. Young or active faults are typically more permeable than old ones, as episodic re-fracturing during earthquakes is necessary to prevent mineral precipitate from clogging up fault planes (Curewitz and Karson, 1997).

As described in Section 3.3.3., the Canoe Reach area has a complex structural history with at least five phases of deformation. The first three are represented by ductile shear zones (Yellowjacket detachment, Bear Foot thrust, and Purcell thrust) and folds developed during Jurassic to Cretaceous orogeny, and these are likely not hydrogeologically significant. The latter two are represented by brittle faulting from the Eocene to recent on the SRMT fault. Previous mapping described the evidence for Eocene normal faulting (McDonough and Simony, 1988). Evidence for recent dextral faulting is described in Chapter 2 of this thesis, in which we showed that abundant dextral kinematic indicators (slickenlines) are consistent with the focal mechanism of local earthquakes. It is therefore likely that the SRMT fault is a permeable structure due to its recent activity. At Canoe Reach South in the vicinity of the Canoe River hot spring, several anisotropic conductive features align with the trace of the SRMT fault and are interpreted to be thermal fluids rising along the fault damage zone. For example, feature AF6 may represent fluids rising to the outlet of the Canoe River spring. Faults may also act as hydrogeologic barriers, separating lithologies with different hydrogeological properties. Example of this are the features IC10, AF12, and AF13, all of which appear bounded to the southwest by the SRMT fault.

3.6.2 Geothermal exploration in regions with anisotropic geology

The MT method is commonly used in geothermal exploration around the world. However, until recently, electrical anisotropy has not been included in 3D inversions. Lee (2020) is the first to apply an anisotropic inversion to a geothermal play. He found that the anisotropic inversions had a lower r.m.s. misfit than the isotropic inversion, and that features in the anisotropic model are more readily explained geologically. In this chapter, the cause of this anisotropy is investigated, and found to be due to a combination of subparallel brittle and ductile fabrics at regional to microscopic scales. These results highlight the importance of considering anisotropy when exploring for geothermal resources in highly deformed regions. For example, the features IC4 and IC5 may appear to be promising targets for exploration (possible hydrothermal upwellings), but the anisotropic model reveals that these features are more likely due to conductive minerals aligned along the metamorphic fabric of the Yellowjacket Gneiss. On the other hand, features like AF6, which have high conductivity in the vertical direction, and underly the Canoe River hot spring outlet along the SRMT fault, may be more favourable targets. Furthermore, high resolution anisotropic inversions could be useful in determining the orientation of permeable fractures, an application that would be particularly useful for structurally-controlled geothermal resources and Enhanced Geothermal Systems (e.g., Peacock et al., 2013). As geothermal exploration expands to less-

conventional fault-hosted, plutonic, and orogenic geothermal resources, anisotropic inversions may prove to be very useful.

3.7 Conclusions

This chapter has described how MT surveys in the Valemount area were augmented with geological constraints on structure and lithology. Geological maps and cross-sections created independently of the MT resistivity models helped to identify which inversions produced the best results: anisotropic inversions appeared to match the geological maps and cross-sections better than isotropic inversions did. The anisotropic conductive features in the anisotropic resistivity model could represent non-penetrative structural fabrics such as permeable brittle faults, or they could represent conductive mineral phases (e.g., graphite and/or sulfides) aligned along penetrative metamorphic fabrics.

Microscopic examination (petrographic microscopy, SEM, and XRD) of rocks collected in the vicinity of one of the MT survey lines (Figure 3.1) revealed the presence of graphite and sulfide (pyrite) aligned along cleavage planes of the Yellowjacket Gneiss and Lower Miette Group. The sulfide minerals likely represent less than 5% of the rock and may be insufficient on its own to create the conductivity anomaly. However, in most samples, graphite is pervasive on grain boundaries, and likely exceeds the 1-100 ppm minimum required to create a conductivity anomaly (Katsube and Mareschal, 1993; Hyndman et al., 1993). Some uncertainty still exists due to the potential for contamination of the samples by the carbon-based epoxy. However, in the absence of any other potential cause for the enhanced anisotropic conductivity, it seems most likely that graphite is the main cause.

This study shows that inversions which consider anisotropy are important for geothermal exploration in highly deformed, structurally-controlled geothermal plays, where electrical anisotropy at microscopic and regional scales may be poorly represented by an isotropic MT resistivity model. Electrically anisotropic models will better-resolve the geometry of fluid-filled faults (good exploration targets), as well as the geometry of conductive metamorphic rock (poor exploration targets). As shown in this chapter, geological fieldwork and petrological analyses are necessary to validate the results of the anisotropic inversions.

Chapter 4: Summary and Conclusions

4.1 Summary of thesis

This thesis was motivated by a need to improve the geological understanding of potential geothermal resources in southeastern British Columbia. This region has previously been identified as prospective for geothermal heating and electricity production (Fairbank and Faulkner, 1992; Grasby et al., 2012; Geoscience BC, 2015; Tuya Terra Geo Corp, 2016). Heat flow in this region is high (100mW/m^2), as demonstrated by several existing temperature gradient wells (Lewis et al., 1992), and the presence of numerous hot springs. The notable lack of active volcanism in the vicinity of these hydrothermal systems has led some authors to speculate that the source of the heat is anomalously high radioactive heat generation in Cretaceous and Eocene plutonic suites in the area (Lewis et al., 1992; Grasby et al., 2012). Plutons have been successfully exploited for geothermal energy elsewhere in the world (e.g., Alaska; (Holdmann, 2007; Kolker, 2008), for direct-use heating, traditional hydrothermal electricity generation, as well as Enhanced Geothermal Systems. It is thought that major crustal faults such as the SRMT, Purcell Trench, and Columbia River faults might facilitate the deep (2-5 km) circulation of meteoric water to the heat source (Grasby and Hutcheon, 2001). However, a better understanding of the structural factors that control geothermal upwellings is necessary to encourage further investment and exploration. In Chapter 2 of this thesis, a regional study of the structural and neotectonic controls on these geothermal resources across southeastern BC was presented. In Chapter 3, structural cross-sections and petrological analyses were used to augment geophysical models of a geothermal play near Valemount, BC. The results from Chapter 2 provide a new regional framework to explain and predict the locations of geothermal upwellings in southeastern BC. Chapter 3 is a novel, integrated application of geophysics and geology, that highlights some of the challenges of exploring for geothermal resources in highly deformed regions.

4.1.1 Summary of Chapter 2: Fault Kinematics and Crustal Stress in Southeastern BC

The geothermal resources in southeastern BC are known to be spatially associated with several major faults: the SRMT fault, the Purcell Trench fault, and the Columbia River fault (Grasby and Hutcheon, 2001). What remained unanswered – and thus constitutes the main focus of this thesis – is the specific role these faults play in localizing hydrothermal systems. In other words: what controls the location of hydrothermal systems along the strike of these faults, and can that knowledge be used to identify locations of previously unidentified resources?

Fault zones introduce strong heterogeneity to the permeability of the subsurface. They can act as fluid conduits as well as impermeable barriers (Caine et al., 1996), both of which are important in understanding hydrothermal systems. As conduits, they can permit the rapid movement of geothermal

fluids to the surface, and as barriers they can isolate hydrothermal convection cells, and prevent the diffusion of thermal waters near the surface. There are several factors that influence the permeability structure of fault zones, including: age, maturity, kinematics, and stress orientations. Older faults tend to be less permeable to flow because mineral precipitate from groundwater eventually clogs the open conduit. Young faults, particularly those that are still seismically active in high strain zones, retain their permeability through episodic refracturing. Immature fault zones (i.e., those with little overall displacement) typically are more permeable because strain is distributed across a wide damage zone. As faults mature, strain tends to be localized on discrete fault planes with large impermeable clay gouge zones, and narrow damage zones. While the kinematics of faults (i.e., normal, reverse, or strike-slip) are not known to influence the absolute permeability, it has been shown to influence the directionality of permeability. For example, Sibson (1996) showed that fluid preferentially travels parallel to the medium stress axis (σ_2), which implies that strike-slip faults will be more permeable to vertical flow, and dip-slip faults more permeable to horizontal flow. The orientation of crustal stress fields plays a critical role in fault permeability, as faults oriented parallel or at low angles to the maximum stress direction will dilate or slip, respectively, while those oriented at high angles will tend to clamp shut. This study was designed to better understand these factors for the major faults associated with geothermal systems in southeastern BC.

Field investigations were carried out over a broad area in southeastern BC, with a focus on investigating outcrops in the vicinity of major fault zones. Bedrock outcrop in this part of BC is heavily obscured by extensive glacial deposits and dense vegetation, which has hindered past and current efforts to investigate these faults in detail. Therefore, work was focused on roadcuts, which provided the freshest rock exposures. To constrain fault kinematics, nearly 700 kinematic indicators (slickenlines, mineral lineations, etc) were collected at highway-side outcrops throughout the study area. Careful analysis of this dataset revealed information on the kinematics of slip on these fault zones. The cumulative slip of these faults – a proxy for maturity – was estimated by careful inspection of geological maps for clear piercing points. The age of these faults was more difficult to ascertain, but rare cross cutting relationships provided some indication of relative age. Comparing the kinematics of these faults to regional stress directions and earthquake focal mechanisms showed that they may be active at low levels in the present day, which allows for a new understanding of why hydrothermal systems occur where they do. The most important findings of this chapter are as follows:

1. **The three major fault zones studied in southeastern BC – the SRMT fault, the Purcell Trench fault, and the Columbia River fault – all show evidence of dextral slip.** Field investigations revealed abundant occurrences of diagnostic kinematics indicators such as

slickenlines and mineral fibers on fault planes. Although previous research has speculated or shown that dextral slip has occurred on specific segments of some of these faults (e.g., minor dextral slip on the Columbia River fault (Lane, 1984); minor dextral slip on the SRMT near Valemount (Murphy, 1990)), this is the first study to demonstrate dextral strain is recorded on all major fault zones in southeastern BC, from the U.S. border to Valemount, BC. Most of these faults were previously only considered to be Eocene normal faults (e.g., Clague, 1974; Read and Brown, 1981; van der Velden and Cook, 1996; Doughty and Price, 2000).

2. **Dextral slip on these faults is the most recent phase of slip and is related to the current stress field**. The dextral slickenlines measured in the field represent the most abundant population of kinematic indicators (34%) and are therefore inferred to be the youngest. In some cases, brittle dextral faults cross-cut Eocene ductile fabrics, suggesting that dextral deformation post-dates normal faulting. Finally, the maximum stress direction required for dextral slip on these faults is closely aligned with the current maximum stress direction (NNE-SSW) derived from small crustal earthquakes in the area.
3. **The identification of dextral transpression as the most recent and possibly current mode of deformation in southeast BC allows for the possibility of predictive mapping of geothermal systems in the region**. Known hydrothermal systems, (i.e., thermal springs) occur in locations of enhanced structural complexity and strain concentration (fault tips, intersections, and relays/stepovers) in broad region undergoing dextral transpression. Other blind geothermal systems may occur at identified regions of strain concentration, and be masked by thick glacial overburden
4. **Thermal springs are correlated with zones of seismicity across the Canadian Cordillera**. Although seismicity in the interior of BC is low relative to the active plate margin, there is a correlation between zones with moderate seismicity, and clusters of thermal springs. Areas with no seismicity do not host thermal springs. Thus, active seismicity is an important parameter when assessing the favorability of regions for geothermal exploration.
5. **The dextral kinematics identified on faults in southeast BC fit in the context of diffuse dextral shear identified across the entire North American Cordillera**. From California to Alaska, numerous north-south striking dextral faults have been mapped. The faults in southeast BC have historically been regarded as extensional, with little attention paid to the recent/current tectonism in the area. This study is the first to show that dextral shear is occurring in the southeastern Canadian Cordillera.

4.1.2 Summary of Chapter 3: Geophysical and Geological Investigations of Electrical Anisotropy at Valemount, BC

Over the past 3 decades, the Canoe Reach area has attracted commercial interest as a geothermal play, largely due to the high temperature thermal spring that discharges along the shore of Kinbasket Lake. Recently, Borealis GeoPower Inc. has undertaken an exploration campaign in the area, with the intention of developing a thermal spa, district heating system, and possibly an electrical plant. The hydrothermal system underlying Canoe Reach is thought to be controlled by the SRMT fault, which may facilitate the deep circulation of fluids in the subsurface, and focused discharge at the surface. To better understand the role of the SRMT fault, Lee (2020) applied the MT method, commonly used in geothermal exploration, to image the resistivity structure of the subsurface. He produced two sets of 3-D resistivity models, one assuming electrical isotropy, and the other assuming anisotropy. The anisotropic models appeared to be more geologically-plausible, and had lower r.m.s. errors, however, interpretation of resistivity models derived from MT data is difficult due to the inherent non-uniqueness of the model solutions, and it was determined that geological constraints, in the form of structural cross sections and petrological analyses, would be helpful.

Bedrock mapping was conducted in the vicinity of a geothermal play near Valemount, BC. A primary focus of this mapping was to document the kinematics of the SRMT fault (as documented in Chapter 2), however structural measurements were also made to augment existing 1:50k bedrock maps. Additionally, numerous samples were collected with the goal of investigating the microstructural features that might cause electrical anisotropy. Observations and measurements from fieldwork were used to create detailed geological cross sections to compare with the MT models. Samples we examined with petrographic microscope, SEM, and XRD instruments to determine whether conductive minerals such as graphite or pyrite were present, and whether their morphology and modal percentage was sufficient to create a conductivity anomaly. The most important findings of this chapter are as follows:

1. **Graphite, sulfide minerals, and fluid-filled faults may all contribute to electrical anisotropy in the Valemount region.** The subsurface structure near Valemount BC is highly anisotropic on regional and microscopic scales. On a regional scale, the non-penetrative, brittle fault fabrics contribute to anisotropic resistivity. For example, a vertically-conductive feature in the anisotropic resistivity model aligns with the SRMT fault and the outlet of the Canoe River thermal spring, and probably represents fluid in the SRMT fault. On a microscopic scale, sulfide minerals and graphite aligned along cleavage planes likely play a role in directing electrical currents. The pyrite content is 1-5 wt% in some samples, and graphite is pervasive and well-connected on many grain boundaries and likely exceeds the minimum 1-100 ppm concentration

required to produce a conductivity anomaly. The Yellowjacket Gneiss, which is shown to have connected sulfide minerals and graphite films, aligns well with the most conspicuous feature in the anisotropic MT model.

2. **Structural anisotropy must be considered when using MT to investigate geothermal systems in highly deformed regions**. MT is a commonly used exploration method for geothermal systems. However, we have demonstrated that in highly deformed regions, electrical anisotropy must be considered. Even in the absence of nearby magmatism, not every conductor should be interpreted as hydrothermal fluid. Anisotropic MT models combined with geological mapping and microscopic analyses, can help distinguish between good exploration targets and poor ones.

4.2 Future work

Geothermal exploration in BC is still in its infancy and a tremendous amount of work remains in order for development to progress. This thesis has illustrated that the following research directions would be worthy of pursuit:

4.2.1 Better seismic and geodetic studies of the interior Canadian Cordillera

Seismographs and GNSS instruments are sparse in the southeastern Canadian Cordillera, as the network of stations in Canada is primarily focused on the zones of high seismicity on the Pacific coast. Increasing seismograph station coverage elsewhere in the Cordillera would allow for more accurate determination of focal mechanisms and hypocenter locations. Currently, hypocenter locations are subject to a high degree of uncertainty and it is unclear whether earthquakes align along known faults or not. Focal mechanisms are for the most part unattainable because moment magnitudes are generally less than 4, and high noise-to-signal ratios, due to long travel times between earthquakes and seismographs, prevent reliable P-wave first motion solutions. Increasing GNSS station coverage would allow for identification of subtle strain gradients and the orientation of strain vectors. Currently, there are no GNSS stations in the entire southeastern Cordillera between Kelowna and Calgary, which precludes the observation of subtle changes in strain across structures, and the direction of principle strain throughout the region. Data from additional seismic and GNSS stations would serve as a critical test of some of the conclusions of this thesis: namely that the principle strain axis is oriented NNE-SSW, and that the major fault zones host a low level of seismicity on dextral strike-slip faults.

4.2.2 Testing the hypothesis: do blind geothermal systems exist?

Following the conclusion that strain in the southeastern Cordillera is transpressional, this study suggests thermal springs in the Cordillera occur in zones of strain concentration such as fault intersections, fault tips, and restraining bends. Having identified the structural settings that thermal springs occur in, it may

also be possible to identify zones where blind geothermal systems exist. Several possible locations were identified in Chapter 2. Confirming that such blind systems exist could be difficult, and potentially expensive. Subtle thermal anomalies may be identified using thermal imagery from remote sensing platforms (e.g., Haselwimmer et al., 2013), or perhaps with shallow drilling (e.g., Craig et al., 2017). The ultimate test would be the installation of a full temperature gradient well, but this would come at considerable expense.

4.2.3 More heat generation data from plutons in southeastern BC.

Previous work has identified that several Cretaceous and Eocene intrusive suites in southeastern BC produce anomalously high amounts of radiogenic heat (Lewis and Bentkowski, 1988; Lewis et al., 1992). Given the abundance of high temperature thermal springs, and notable lack of active magmatism in this region, it has been speculated in this thesis, and by other authors, that these rocks provide the heat source for active hydrothermal systems in this region. However, the data that do exist do not provide high spatial resolution, and a number of plutons are not included in the dataset. It may be worthwhile to revisit this dataset and collect new samples in the vicinity of thermal springs. In particular, the Kuskanax batholith would benefit from further study considering that at least five thermal springs occur in its vicinity. Other candidates for further study are the Nelson Batholith (Ainsworth hot spring is nearby) and the Fry Creek Batholith (Dewar Creek hot spring, the hottest in the Cordillera, is nearby). Combining heat generation data with the identification of favourable structural settings would improve predictive mapping efforts. Such data would constitute critical parameters in statistically-robust play-fairway analyses (e.g., Faulds et al., 2015) of potential geothermal sites, which have proven effective at identifying new geothermal systems in the past (Craig et al., 2017).

4.2.4 Better quantification of graphite and sulfide content in rocks near Valemount.

In Chapter 3, attempts are made to identify the presence and volume of graphite and sulfides in rocks collected in the Valemount area. Hand samples from this region appear graphitic, with a dark grey greasy texture that stains the hands black. Abundant carbon-rich zones were imaged using the SEM and may represent conductive graphite, though the possibility of contamination from hydrocarbon-based epoxy casts some uncertainty on this result. If the carbon-rich zones are indeed graphite, then it is likely present in amounts greater than the 1-100 ppm minimum required to create a conductivity anomaly. However, efforts to obtain a precise modal percentage of graphite using a Rietveld Refinement of XRD data were interrupted by the COVID-19 shutdown. Sulfides were also observed in petrographic thin sections, and positively identified via energy dispersive X-ray spectroscopy with the SEM, though their modal percentage is at or below the 1-5 wt% detection limit of the XRD instrument. Future work should focus

on obtaining precise modal percentages of graphite and sulfides via Rietveld Refinement of XRD data, and potentially by employing Raman spectroscopy.

4.2.5 Physical measurements of electrical anisotropy in rocks from Valemount.

MT surveys of the subsurface near Valemount have shown that the rocks of the Lower Miette Group and Yellowjacket Gneiss are electrically conductive and anisotropic. Microscopic analyses presented in Chapter 3 showed that graphite and sulfide may explain some of these conductivity features. An outstanding question is whether these electrical properties can be demonstrated in a lab setting. It is challenging to replicate the natural conditions present in the subsurface that allow for electrical conduction, and it has been shown that graphite films tend to break and lose conductivity as they are exhumed (e.g., Mathez et al., 1995; Yoshino and Noritake, 2011). However, demonstrating via lab experiment that the resistivity structure of these hand samples is anisotropic would be a critical test of our hypothesis, and worth pursuing.

References

Agemar, T., Weber, J., and Schulz, R., 2014, Deep Geothermal Energy Production in Germany: Energies, v. 7, p. 4397–4416, doi:10.3390/en7074397.

Allen, D.M., Grasby, S.E., and Voormeij, D.A., 2006, Determining the circulation depth of thermal springs in the southern Rocky Mountain Trench, south-eastern British Columbia, Canada using geothermometry and borehole temperature logs: Hydrogeology Journal, v. 14, p. 159–172, doi:10.1007/s10040-004-0428-z.

Allis, R., Moore, J., Davatzes, N., Gwynn, M., Hardwick, C., Kirby, S., McClennan, J., Pankow, K., Potter, S., and Simmons, S., 2016, EGS Concept Testing and Development at the Milford, Utah FORGE Site: Proceedings 41st Workshop on Geothermal Reservoir Engineering, p. 13.

Anderson, E.M., 1905, The dynamics of faulting: Transactions of the Edinburgh Geological Society, v. 8, p. 387–402, doi:10.1144/transed.8.3.387.

Archibald, D.A., Glover, J.K., Price, R.A., Farrar, E., and Carmichael, D.M., 1983, Geochronology and tectonic implications of magmatism and metamorphism, southern Kootenay Arc and neighbouring regions, southeastern British Columbia. Part I: Jurassic to mid-Cretaceous: Canadian Journal of Earth Sciences, v. 20, p. 1891–1913, doi:10.1139/e84-062.

Archie, G.E., 1942, The Electrical Resistivity Log as an Aid in Determining Some Reservoir Characteristics: Transactions of the AIME, v. 146, p. 54–62, doi:10.2118/942054-G.

Armstrong, R.L., 1982, Cordilleran Metamorphic Core Complexes – From Arizona to Southern Canada: Annual Review of Earth and Planetary Sciences, v. 10, p. 129–154, doi:10.1146/annurev.ea.10.050182.001021.

Armstrong, R.L., 1988, Mesozoic and early Cenozoic magmatic evolution of the Canadian Cordillera, *in* Geological Society of America Special Papers, Geological Society of America, v. 218, p. 55–92, doi:10.1130/SPE218-p55.

Bachu, S., 1993, Basement heat flow in the Western Canada Sedimentary Basin: Tectonophysics, v. 222, p. 119–133, doi:10.1016/0040-1951(93)90194-O.

Bachu, S., and Burwash, R.A., 1991, Regional-scale analysis of the geothermal regime in the Western Canada Sedimentary Basin: Geothermics, v. 20, p. 387–407, doi:10.1016/0375-6505(91)90028-T.

Banks, J., 2016, Deep-Dive Analysis of the Best Geothermal Reservoirs for Commercial Development in Alberta: Final Report: University of Alberta, 93 p.

Banks, J., and Harris, N.B., 2018, Geothermal potential of Foreland Basins: A case study from the Western Canadian Sedimentary Basin: Geothermics, v. 76, p. 74–92, doi:10.1016/j.geothermics.2018.06.004.

Bao, X., Eaton, D.W., and Guest, B., 2014, Plateau uplift in western Canada caused by lithospheric delamination along a craton edge: Nature Geoscience, v. 7, p. 830–833, doi:10.1038/ngeo2270.

Barbier, E., 2002, Geothermal energy technology and current status: an overview: Renewable and Sustainable Energy Reviews, v. 6, p. 3–65, doi:10.1016/S1364-0321(02)00002-3.

Barton, C.A., Zoback, M.D., and Moos, D., 1995, Fluid flow along potentially active faults in crystalline rock: Geology, v. 23, p. 683–686, doi:10.1130/0091-7613(1995)023<0683:FFAPAF>2.3.CO.

BC Hydro, 2019, BC Hydro Fiscal 2020 to Fiscal 2021 Revenue Requirements Application: Twenty-Year Load Forecast:, https://www.bchydro.com/content/dam/BCHydro/customer-portal/documents/corporate/regulatory-planning-documents/regulatory-filings/rra/00-2019-10-03-bchydro-f20-f21-rra-20-year-load-forecast.pdf (accessed July 2020).

Bedrosian, P.A., 2007, MT+, Integrating Magnetotellurics to Determine Earth Structure, Physical State, and Processes: Surveys in Geophysics, v. 28, p. 121–167, doi:10.1007/s10712-007-9019-6.

Bemis, S.P., Weldon, R.J., and Carver, G.A., 2015, Slip partitioning along a continuously curved fault: Quaternary geologic controls on Denali fault system slip partitioning, growth of the Alaska Range, and the tectonics of south-central Alaska: Lithosphere, v. 7, p. 235–246, doi:10.1130/L352.1.

Bish, D.L., and Post, J.E. (Eds.), 1989, Modern Powder Diffraction: Mineralogical Society of America, 384 p.

Blackwell, D.D., and Richards, M., 2004, Geothermal Map of North America: AAPG Map, https://www.smu.edu/Dedman/Academics/Departments/EarthSciences/Research/GeothermalLab/DataMaps/GeothermalMapofNorthAmerica (accessed July 2019).

Brown, D.A., Doughty, T.P., and Stinson, P., 1994, Preliminary Geology of the Creston Map Area , Southeastern British Columbia (82F / 2):, 135–155 p.

Brown, D.A., and MacLeod, R.I., 2011, Geology, Boswell, British Columbia: Geological Survey of Canada Open File 6310.

Caine, J.S., Evans, J.P., and Forster, C.B., 1996, Fault zone architecture and permeability structure: Geology, v. 24, p. 1025–1028, doi:10.1130/0091-7613(1996)024<1025.

Canadian Geochronology Knowledgebase, 2013, https://www.nrcan.gc.ca/earth-sciences/geography/atlas-canada/canadian-geochronology-knowledgebase/18211#reccit.

Cant, D.J., and Stockmal, G.S., 1989, The Alberta foreland basin: relationship between stratigraphy and Cordilleran terrane-accretion events: Canadian Journal of Earth Sciences, v. 26, p. 1964–1975, doi:10.1139/e89-166.

Card, C., 2013, Altered Pelitic Gneisses and Associated " Quartzite Ridges " Beneath the Southeastern Athabasca Basin: Alteration Facies and their Relationship to Uranium Deposits along the Wollaston-Mudjatik Transition: Summary of Investigations, v. 2.

Caron, M., Grasby, S.E., and Ryan, M.C., 2007, Spring geochemistry: a tool for mineral exploration in the south Nahanni River basin of the Mackenzie Mountains, Northwest Territories: Geological Survey of Canada, v. Open File, p. 31–74.

Carr, S.D., 1992, Tectonic setting and U-Pb geochronology of the Early Tertiary Ladybird Leucogranite Suite, Thor-Odin - Pinnacles Area, Southern Omineca Belt, British Columbia: Tectonics, v. 11, p. 258–278, doi:10.1029/91TC01644.

Carr, S., 1986, The Valkyr Shear Zone and the Slocan Lake Fault: Eocene structures that bound the Valhalla Complex, southeastern British Columbia, doi:10.3102/00346543067001043.

Carr, S.D., Parrish, R.R., and Brown, R.L., 1987, Eocene structural development of the Valhalla Complex, southeastern British Columbia: Tectonics, v. 6, p. 175–196, doi:10.1029/TC006i002p00175.

Cassidy, J.F., Rogers, G.C., and Hyndman, R.D., 2014, An Overview of the 28 October 2012 Mw 7.7 Earthquake in Haida Gwaii, Canada: A Tsunamigenic Thrust Event Along a Predominantly Strike-Slip Margin: Pure and Applied Geophysics, v. 171, p. 3457–3465, doi:10.1007/s00024-014-0775-1.

Chamberlain, V.E., Lambert, R.S.J., and Holland, J.G., 1985, Geochemistry and geochronology of the gneisses east of the Southern Rocky Mountain Trench, near Valemount, British Columbia: Canadian Journal of Earth Sciences, v. 22, p. 980–991, doi:10.1139/e85-103.

Charlesworth, H.A.K., 1959, Some suggestions on the structural development of the Rocky Mountains of Canada: Journal of the Alberta Society of Petroleum Geologists, v. 7.

Chave, A.D., and Jones, A.G., 2012, The Magnetotelluric Method: Theory and Practice: Cambridge University Press, 571 p.

Chen, Y., Gu, Y.J., Currie, C.A., Johnston, S.T., Hung, S.-H., Schaeffer, A.J., and Audet, P., 2019, Seismic evidence for a mantle suture and implications for the origin of the Canadian Cordillera: Nature Communications, v. 10, p. 1–10, doi:10.1038/s41467-019-09804-8.

Clague, J.J., 1974, The St. Eugene Formation and the Development of the Southern Rocky Mountain Trench: Canadian Journal of Earth Sciences, v. 11, p. 916–938, doi:10.1139/e74-091.

Coney, P.J., and Harms, T.A., 1984, Cordilleran metamorphic core complexes: Cenozoic extensional relics of Mesozoic compression: Geology, v. 12, p. 550–554, doi:10.1130/0091-7613(1984)12<550:CMCCCE>2.0.CO;2.

Cook, F. a, Varsek, J.L., Clowes, R.M., Kanasewich, E.R., Spencer, C.S., Parrish, R.R., Brown, R.L., Carr, S.D., and Johnson, B.J., 1992, LITHOPROBE crustal reflection cross section of the southern Canadian Cordillera, 1, Foreland thrust and fold belt to Fraser River Fault: Tectonics, v. 11, p. 12–35.

Coolbaugh, M.F., Raines, G.L., Zehner, R.S.E., Shevenell, L., and Williams, C.F., 2006, Prediction and discovery of new geothermal resources in the Great Basin: Multiple evidence of a large undiscovered resource base, *in* GRC Transactions, v. 30.

Corbett, C.R., and Simony, P.S., 1984, The Champion Lake Fault in the Trail-Castlegar Area of Southeastern British Columbia, *in* Geological Survey of Canada Current Research, Paper 84-1A, p. 103–104.

Craig, J.W., Faulds, J.E., Shevenell, L.A., and Hinz, N.H., 2017, Discovery and Analysis of a Potential Blind Geothermal System in Southern Gabbs Valley, Western Nevada: GRC Transactions, p. 7.

Craw, D., 1978, Metamorphism, structure and stratigraphy in the Southern Park Ranges, British Columbia: Canadian Journal of Earth Sciences, v. 15, p. 86–98, doi:10.1139/e78-008.

Cui, Y., Miller, D., Schiarizza, P., and Diakow, L.J., 2017, British Columbia Digital Geology: British Columbia Geological Survey Open File 2017-8, http://cmscontent.nrs.gov.bc.ca/geoscience/PublicationCatalogue/OpenFile/BCGS_OF2017-08.pdf (accessed July 2019).

Cumming, W., 2009, Geothermal Resource Conceptual Models Using Surface Exploration Data, *in* Proceedings, Thirty-Fourth Workshop on Geothermal Reservoir Engineering, Stanford, California, Stanford University.

Curewitz, D., and Karson, J.A., 1997, Structural settings of hydrothermal outflow: Fracture permeability maintained by fault propagation and interaction: Journal of Volcanology and Geothermal Research, v. 79, p. 149–168, doi:10.1016/S0377-0273(97)00027-9.

Dahlstrom, C.D.A., 1969, Balanced cross sections: Canadian Journal of Earth Sciences, v. 6, p. 743–757, doi:10.1139/e69-069.

Dalrymple, G.B., Grove, M., Lovera, O.M., Harrison, T.M., Hulen, J.B., and Lanphere, M.A., 1999, Age and thermal history of the Geysers plutonic complex (felsite unit), Geysers geothermal field, California: a 40Ar/39Ar and U–Pb study: Earth and Planetary Science Letters, v. 173, p. 285–298, doi:10.1016/S0012-821X(99)00223-X.

Davies, J.H., and Davies, D.R., 2010, Earth's surface heat flux: Solid Earth, v. 1, p. 5–24.

Davis, E.E., and Lewis, T.J., 1984, Heat flow in a back-arc environment: Intermontane and Omineca Crystalline belts, southern Canadian Cordillera: Can. J. Earth Sci., v. 21, p. 715–726.

Desrochers, D.T., 1992, Geothermal feasibility study for the use of hot water near Riondel, British Columbia: Geological Survey of Canada Open File 2502.

DiPippo, R., 2015, Geothermal power plants: Evolution and performance assessments: Geothermics, v. 53, p. 291–307, doi:10.1016/j.geothermics.2014.07.005.

Dobson, P.F., 2016, A Review of Exploration Methods for Discovering Hidden Geothermal Systems, *in* GRC Transactions, v. 40, p. 695–706.

Doughty, P.T., and Price, R.A., 2000, Geology of the Purcell Trench rift valley and Sandpoint Conglomerate: Eocene en echelon normal faulting and synrift sedimentation along the eastern flank of the Priest River metamorphic complex, northern Idaho: GSA Bulletin, v. 112, p. 1356–1374.

Doughty, P.T., and Price, R.A., 1999, Tectonic evolution of the Priest River complex, northern Idaho and Washington: A reappraisal of the Newport fault with new insights on metamorphic core complex formation: Tectonics, v. 18, p. 375–393, doi:10.1029/1998TC900029.

Dresen, G., 1991, Stress distribution and the orientation of Riedel shears: Tectonophysics, v. 188, p. 239–247, doi:10.1016/0040-1951(91)90458-5.

Dye, S.T., 2012, Geoneutrinos and the radioactive power of the Earth: Reviews of Geophysics, v. 50, doi:10.1029/2012RG000400.

East, J.S., 1982, Geothermal investigations at Manley Hot Springs, Alaska: University of Alaska, Fairbanks, https://scholarworks.alaska.edu/bitstream/handle/11122/8392/East_J_1982.pdf?sequence=1 (accessed June 2020).

ECCC, 2016, Pan-Canadian Framework on Clean Growth and Climate Change: Canada's plan to address climate change and grow the economy: Environment and Climate Change Canada, 78 p.

Edwards, R.N., Nobes, D.C., and Gómez-Treviño, E., 1984, Offshore electrical exploration of sedimentary basins: The effects of anisotropy in horizontally isotropic, layered media: GEOPHYSICS, v. 49, p. 566–576, doi:10.1190/1.1441691.

Edwards, B.R., and Russell, J., 2000, Distribution, nature, and origin of Neogene–Quaternary magmatism in the northern Cordilleran volcanic province, Canada: Geological Society of America Bulletin, p. 16.

EIA, 2020, Electric Power Monthly with data for February 2020: U.S. Energy Information Administration, 273 p., https://www.eia.gov/electricity/monthly/.

Evenchick, C., McMechan, M.E., McNicoll, V.J., and Carr, S.D., 2007, A synthesis of the Jurassic–Cretaceous tectonic evolution of the central and southeastern Canadian Cordillera: Exploring links across the orogen: Geological Society of America, v. Special Paper 433, p. 117–145, doi:10.1130/2007.2433(06).For.

Fairbank, B.P., and Faulkner, R.L., 1992, Geothermal Resources of British Columbia: Geological Survey of Canada, http://ftp.geogratis.gc.ca/pub/nrcan_rncan/publications/ess_sst/133/133397/of_2526.pdf (accessed March 2020).

Farquharson, N., Schubert, A., and Steiner, U., 2016, Geothermal Energy in Munich (and Beyond): A Geothermal City Case Study, *in* GRC Transactions, v. 40, p. 189–196.

Faulds, J., and Hinz, N., 2015, Favorable Tectonic and Structural Settings of Geothermal Systems in the Great Basin Region, Western USA: Proxies for Discovering Blind Geothermal Systems: Proceedings World Geothermal Congress, p. 6.

Faulds, J.E., Hinz, N.H., Coolbaugh, M.F., Shevenell, L.A., and Siler, D.L., 2016, The Nevada Play Fairway Project — Phase II: Initial Search for New Viable Geothermal Systems in the Great Basin Region, Western USA, *in* GRC Transactions, Geothermal Resources Council, p. 6.

Faulds, J.E., Hinz, N.H., Coolbaugh, M.F., Shevenell, L.A., Siler, D.L., Wannamaker, P.E., Queen, J.H., and Visser, C.F., 2015, Integrated Geologic and Geophysical Approach for Establishing Geothermal Play Fairways and Discovering Blind Geothermal Systems in the Great Basin Region, Western USA: A Progress Report: GRC Transactions, v. 39, p. 10.

Ferguson, G., and Grasby, S.E., 2011, Thermal springs and heat flow in North America: Geofluids, v. 11, p. 294–301, doi:10.1111/j.1468-8123.2011.00339.x.

Ferguson, G., and Ufondu, L., 2017, Geothermal energy potential of the Western Canada Sedimentary Basin: Clues from coproduced and injected water: Environmental Geosciences, v. 24, p. 113–121, doi:10.1306/eg.0206171600917003.

Foo, W.K., 1979, Evolution of Transverse Structures Linking the Purcell Anticlinorium to the Western Rocky Mountains Near Canal Flats, British Columbia: Queens University.

Fossen, H., and Cavalcante, G.C.G., 2017, Shear zones – A review: Earth-Science Reviews, v. 171, p. 434–455, doi:10.1016/j.earscirev.2017.05.002.

Fraser, T.A., Grasby, S.E., Witter, J.B., Colpron, M., and Relf, C., 2018, Geothermal Studies in Yukon – Collaborative Efforts to Understand Ground Temperature in the Canadian North: GRC Transactions, v. 42, p. 20.

Frost, B.R., Fyfe, W.S., Tazaki, K., and Chan, T., 1989, Grain-boundary graphite in rocks and implications for high electrical conductivity in the lower crust: Nature, v. 340, p. 134–136, doi:10.1038/340134a0.

Gabrielse, H., 1985, Major dextral transcurrent displacements along the Northern Rocky Mountain Trench and related lineaments in north-central British Columbia: Bulletin of the Geological Society of America, v. 96, p. 1–14, doi:10.1130/0016-7606(1985)96<1:MDTDAT>2.0.CO;2.

Gabrielse, H., Monger, J.W.H., Wheeler, J.O., and Yorath, C.J., 1991, Tectonic Framework, Part A: Morphogeological belts, tectonic assemblages and terranes, *in* Geology of the Cordilleran Orogen in Canada, Geological Survey of Canada, v. 4, p. 15–28.

Gabrielse, H., and Yorath, C.J., 1991, Tectonic Synthesis, *in* Geology of the Cordilleran orogen in Canada, Geological Survey of Canada, v. 4, p. 680–705.

Gal, L.P., and Ghent, E.D., 1990, Metamorphism in the Solitude Range , southwestern Rocky Mountains , British Columbia : comparison with adjacent Omineca Belt rocks and tectonometamorphic implications for the Purcell Thrust:

Geoscience BC, 2015, An Assessment of the Economic Viability of Selected Geothermal Resources in British Columbia. Geoscience BC Report 2015-11:, http://www.geosciencebc.com/i/project_data/GBCReport2015-11/GBC2015-11_KWL_Geothermal Economics_Project_Report_27Sep16.pdf.

Ghomshei, M.M., 2007, Qualifying report on: A high-grade geothermal resource in the Canadian Rockies; Canoe Hot Springs, Valemount, British Columbia: Comstock Energy Inc.

Ghomshei, M.M., Kimball, S.J., and Porkial, S., 2009, Geochemical Evidence of a Geothermal Power Resource in the Canadian Rockies: Canoe Hot Springs, British Columbia: GRC Transactions, v. 33, p. 6.

Goldstein, B.A. et al., 2011, Great Expectations for Geothermal Energy to 2100, *in* Proceedings, Thirty-Sixth Workshop on Geothermal Reservoir Engineering, Stanford University, Stanford, California, p. 8.

Goldstein, J.I., Newbury, D.E., Michael, J.R., Ritchie, N.W.M., Scott, J.H.J., and Joy, D.C., 2018, Scanning Electron Microscopy and X-Ray Microanalysis: New York, NY, Springer New York, doi:10.1007/978-1-4939-6676-9.

Grasby, S.E. et al., 2020, Garibaldi Geothermal Energy Project; Mount Meager 2019 Field Report: Geoscience BC Geoscience BC Report 2020-09, 153 p.,

http://www.geosciencebc.com/i/project_data/GBCReport2020-09/GeoscienceBC%20Report%202020-09.pdf (accessed May 2020).

Grasby, S.E. et al., 2012, Geothermal Energy Resource Potential of Canada: 6914, 322–322 p.

Grasby, S.E., and Hutcheon, I., 2001, Controls on the distribution of thermal springs in the southern Canadian Cordillera: Canadian Journal of Earth Sciences, v. 38, p. 427–440, doi:10.1139/e00-091.

Grasby, S.E., Hutcheon, I., and Krouse, H.R., 2000, The influence of water-rock interaction on the chemistry of thermal springs in western Canada: Applied Geochemistry, v. 15, p. 439–454.

Grasby, S.E., and Lepitzki, D.A.W., 2002, Physical and chemical properties of the Sulphur Mountain thermal springs, Banff National Park, and implications for endangered snails: Canadian Journal of Earth Sciences, v. 39, p. 1349–1361, doi:10.1139/e02-056.

Green, N.L., Armstrong, R.L., Harakal, J.E., Souther, J.G., and Read, P.B., 1988, Eruptive history and K-Ar geochronology of the late Cenozoic Garibaldi volcanic belt, southwestern British Columbia: GSA Bulletin, v. 100, p. 563–579, doi:10.1130/0016-7606(1988)100<0563:EHAKAG>2.3.CO;2.

Grose, L., Ailleres, L., Laurent, G., Armit, R., and Jessell, M., 2019, Inversion of geological knowledge for fold geometry: Journal of Structural Geology, v. 119, p. 1–14, doi:10.1016/j.jsg.2018.11.010.

Haselwimmer, C., Prakash, A., and Holdmann, G., 2013, Quantifying the heat flux and outflow rate of hot springs using airborne thermal imagery: Case study from Pilgrim Hot Springs, Alaska: Remote Sensing of Environment, doi:10.1016/j.rse.2013.04.008.

Heidbach, O., Rajabi, M., Reiter, K., and Ziegler, M., 2016, World Stress Map: GFZ Data Service, doi:10.5880/WSM.2016.001.0.

Heise, W., Caldwell, T.G., Bertrand, E.A., Hill, G.J., Bennie, S.L., and Palmer, N.G., 2016, Imaging the deep source of the Rotorua and Waimangu geothermal fields, Taupo Volcanic Zone, New Zealand: Journal of Volcanology and Geothermal Research, v. 314, p. 39–48, doi:10.1016/j.jvolgeores.2015.10.017.

Heise, W., Caldwell, T.G., Bibby, H.M., and Bannister, S.C., 2008, Three-dimensional modelling of magnetotelluric data from the Rotokawa geothermal field, Taupo Volcanic Zone, New Zealand: Geophysical Journal International, v. 173, p. 740–750, doi:10.1111/j.1365-246X.2008.03737.x.

Henderson, G.G.L., 1954, Geology of the Stanford Range of the Rocky Mountains: British Columbia Department of Mines Bulletin, v. 35, p. 93.

Hitchon, B., 1984, Geothermal Gradients, Hydrodynamics, and Hydrocarbon Occurrences, Alberta, Canada.: American Association of Petroleum Geologists Bulletin, v. 68, p. 713–743.

Hofmann, H., Weides, S., Babadagli, T., Zimmermann, G., Moeck, I., Majorowicz, J., and Unsworth, M., 2014, Potential for enhanced geothermal systems in Alberta, Canada: Energy, v. 69, p. 578–591, doi:10.1016/j.energy.2014.03.053.

Holdmann, G., 2007, Chena Power Geothermal Power Plant: Chena Power Company, 37–37 p.

Höy, T., British Columbia, and Geological Survey Branch, 1993, Geology of the Purcell Supergroup in the Fernie west-half map area, southeastern British Columbia: Victoria, B.C., British Columbia, Ministry of Energy, Mines and Petroleum Resources.

Huang, K., Thompson, A., and Kent, A., 2018, An Overview of Borealis GeoPower Projects and Community Engagement: GRC Transactions, v. 42, p. 9.

Hudson, T., Plaſker, G., and Dixon, K., 1980, Horizontal offset history of the Chatham Strait fault: The United States Geological Survey in Alaska: Accomplishments during 1980, v. Geological Survey Circular 844, p. 5.

Huttrer, G., 2020, Geothermal Power Generation in the World 2015-2020 Update Report: Proceedings World Geothermal Congress 2020, p. 17.

Hyndman, D.W., 1968, Petrology and structure of Nakusp map area, British Columbia: 161, doi:10.4095/102320.

Hyndman, R., and Currie, C., 2011, Why is the North America Cordillera high? Hot backarcs, thermal isostasy, and mountain belts: Geology, v. 39, p. 783–786, doi:10.1130/G31998.1.

Hyndman, R.D., Currie, C.A., and Mazzotti, S.P., 2005, Subduction zone backarcs, mobile belts, and orogenic heat: GSA Today, v. 15, p. 4–10, doi:10.1130/1052-5173(2005)015<4:SZBMBA>2.0.CO;2.

Hyndman, R.D., and Lewis, T.J., 1995, Review: The thermal regime along the southern Canadian Cordillera Lithoprobe corridor: Canadian Journal of Earth Sciences, v. 32, p. 1611–1617, doi:10.1139/e95-129.

Hyndman, R.D., Vanyan, L.L., Marquis, G., and Law, L.K., 1993, The origin of electrically conductive lower continental crust: saline water or graphite? Physics of the Earth and Planetary Interiors, v. 81, p. 325–345, doi:10.1016/0031-9201(93)90139-Z.

IEA, 2019, World Energy Outlook 2019: International Energy Agency, https://www.iea.org/reports/world-energy-outlook-2019.

IPCC, 2013, Climate Change 2013: The Physical Science Basis. Contribution of Working Group I to the Fifth Assessment Report of the Intergovernmental Panel on Climate Change: Cambridge University Press, 1535 p.

IPCC, 2014a, Climate Change 2014: Impacts, Adaptation, and Vulnerability. Part A: Global and Sectoral Aspects. Contribution of Working Group II to the Fifth Assessment Report of the Intergovernmental Panel on Climate Change: Cambridge University Press AR5, 1132 p.

IPCC, 2014b, Climate Change 2014: Mitigation of Climate Change. Contribution of Working Group III to the Fifth Assessment Report of the Intergovernmental Panel on Climate Change: Cambridge University Press AR5, 1967 p.

Jessop, A.M., Ghomshei, M.M., and Drury, M.J., 1991, Geothermal Energy in Canada: Geothermics, v. 20, p. 369–385.

Johnston, S.T., 1999, Large-scale coast-parallel displacements in the Cordillera: a granitic resolution to a paleomagnetic dilemma: Journal of Structural Geology, v. 21, p. 1103–1108, doi:10.1016/S0191-8141(99)00015-2.

Jolie, E., Klinkmueller, M., and Moeck, I., 2015, Diffuse surface emanations as indicator of structural permeability in fault-controlled geothermal systems: Journal of Volcanology and Geothermal Research, v. 290, p. 97–113, doi:10.1016/j.jvolgeores.2014.11.003.

Journeay, J.M., and Csontos, L., 1989, Preliminary Report On the Structural Setting Along the Southeast Flank of the Coast Belt, British Columbia: 89–1E, 89–1E p., doi:10.4095/127480.

Journeay, J.M., and van Ulden, J., 1998, Neogene structural elements of northern Cascadia, British Columbia: 1998-A/B, 1998-A/B p., doi:10.4095/209503.

Katsube, T.J., and Mareschal, M., 1993, Petrophysical model of deep electrical conductors: Graphite lining as a source and its disconnection due to uplift: Journal of Geophysical Research: Solid Earth, v. 98, p. 8019–8030, doi:10.1029/92JB02864.

Kelbert, A., Meqbel, N., Egbert, G.D., and Tandon, K., 2014, ModEM: A modular system for inversion of electromagnetic geophysical data: Computers & Geosciences, v. 66, p. 40–53, doi:10.1016/j.cageo.2014.01.010.

Kimball, S., 2010, Favourability Map of British Columbia Geothermal Resources: The University of British Columbia, http://pics.uvic.ca/sites/default/files/uploads/publications/kimball_thesis_2010.pdf.

Klepeis, K.A., Crawford, M.L., and Gehrels, G., 1998, Structural history of the crustal-scale Coast shear zone north of Portland Canal, southeast Alaska and British Columbia: Journal of Structural Geology, v. 20, p. 883–904, doi:10.1016/S0191-8141(98)00020-0.

Kolker, A.M., 2008, Geologic Setting of the Central Alaskan Hot Springs Belt: Implications for Geothermal Resource Capacity and Sustainable Energy Production.

Kong, W., Lin, C., Unsworth, M.J., Tan, H., Lee, B., Peng, M., Wang, M., and Tong, T., 2020, Three-dimensional inversion of magnetotelluric data for a resistivity model with arbitrary anisotropy [manuscript submitted for publication]:

Kraft, J.L., 2013, Stratigraphy, paleogeography and tectonic evolution of early Paleozoic to Triassic pericratonic strata in the northern Kootenay Arc, southeastern Canadian Cordillera, British Columbia: ERA, doi:10.7939/R3KD89.

Kraft, J.L., Thompson, R.I., and Dhesi, P., 2011, Geology, Beaton, British Columbia: Geological Survey of Canada Open File 6574.

Kreemer, C., Blewitt, G., and Klein, E.C., 2014, A geodetic plate motion and Global Strain Rate Model: Geochemistry, Geophysics, Geosystems, v. 15, p. 3849–3889, doi:10.1002/2014GC005407.

Kristmannsdóttir, H., and Ármannsson, H., 2003, Environmental aspects of geothermal energy utilization: Geothermics, v. 32, p. 451–461, doi:10.1016/S0375-6505(03)00052-X.

Kubli, T.E., and Simony, P.S., 1994, The Dogtooth duplex, a model for the structural development of the northern Purcell Mountains: Canadian Journal of Earth Sciences, v. 31, p. 1672–1686.

Lane, L.S., 1984, Brittle deformation in the Columbia River fault zone near Revelstoke, southeastern British Columbia: Canadian Journal of Earth Sciences, v. 21, p. 584–598, doi:10.1139/e84-063.

Lanphere, M.A., 1978, Displacement history of the Denali fault system, Alaska and Canada: Canadian Journal of Earth Sciences, v. 15, p. 817–822, doi:10.1139/e78-086.

Lavigne, C., Guthjonsdottir, M., and Banks, J., 2020, Heat or Power - Proposing Geothermal Development on the Basis of Fossil Fuel Displacement.pdf: Proceedings World Geothermal Congress 2020, p. 13.

Lee, B.M., 2020, Improving exploration for geothermal resources with the magnetotelluric method [PhD Thesis]: University of Alberta, 371 p.

Leitch, A., Haley, B., and Hastings-Simon, S., 2019, Can the oil and gas sector enable geothermal technologies? Socio-technical opportunities and complementarity failures in Alberta, Canada: Energy Policy, v. 125, p. 384–395, doi:10.1016/j.enpol.2018.10.046.

Lemieux, Y., Thompson, R.I., and Erdmer, P., 2003, Stratigraphy and structure of the Upper Arrow Lake area, southeastern British Columbia: new perspectives for the Columbia River Fault Zone: Geological Survey of Canada Current Research 2003-A7,.

Lewis, T.J., and Bentkowski, W.H., 1988, Potassium, Uranium and Thorium concentrations of crustal rocks: a data file: Geological Survey of Canada Open File 1744 Open File 1744, http://ftp.geogratis.gc.ca/pub/nrcan_rncan/publications/ess_sst/130/130475/of_1744.pdf (accessed May 2020).

Lewis, T.J., Bentkowski, W.H., and Hyndman, R.D., 1992, Crustal temperatures near the Lithoprobe Southern Canadian Cordillera Transect: Canadian Journal of Earth Sciences, v. 29, p. 1197–1214, doi:10.1139/e92-096.

Liddell, M., Unsworth, M., and Pek, J., 2016, Magnetotelluric imaging of anisotropic crust near Fort McMurray, Alberta: implications for engineered geothermal system development: Geophysical Journal International, v. 205, p. 1365–1381, doi:10.1093/gji/ggw089.

Lund, J.W., and Toth, A., 2020, Direct Utilization of Geothermal Energy 2020 Worldwide Review: Proceedings World Geothermal Congress 2020, p. 39.

MacKenzie, W.S., and Adams, A.E., 1994, Rocks and Minerals in Thin Section: A Colour Atlas: London, CRC Press, 192 p.

Majorowicz, J., and Grasby, S.E., 2010, Heat flow, depth–temperature variations and stored thermal energy for enhanced geothermal systems in Canada: Journal of Geophysics and Engineering, v. 7, p. 232–241, doi:10.1088/1742-2132/7/3/002.

Majorowicz, J., and Moore, M., 2014, The feasibility and potential of geothermal heat in the deep Alberta foreland basin-Canada for CO2 savings: Renewable Energy, v. 66, p. 541–549, doi:10.1016/j.renene.2013.12.044.

Majorowicz, J., Unsworth, M., Chacko, T., Gray, A., Heaman, L., Potter, D.K., Schmitt, D.R., and Babadagli, T., 2013, Geothermal Energy as a Source of Heat for Oil Sands Processing in Northern Alberta, Canada, *in* Hein, F.J., Leckie, D., Larter, S., and Suter, J.R. eds., Heavy-oil and oil-sand petroleum systems in Alberta and beyond: AAPG studies in Geology, p. 22.

Mandl, G., 1987, Tectonic deformation by rotating parallel faults: the "bookshelf" mechanism: Tectonophysics, v. 141, p. 277–316, doi:10.1016/0040-1951(87)90205-8.

Mareschal, M., Fyfe, W.S., Percival, J., and Chan, T., 1992, Grain-boundary graphite in Kapuskasing gneisses and implications for lower-crustal conductivity: Nature, v. 357, p. 674–676, doi:10.1038/357674a0.

Martin, N., 2018, Hot Commodity: Geothermal Electricity in Alberta: Canada West Foundation, 32 p.

Mathez, E.A., Duba, A.G., Peach, C.L., Léger, A., Shankland, T.J., and Plafker, G., 1995, Electrical conductivity and carbon in metamorphic rocks of the Yukon-Tanana Terrane, Alaska: Journal of Geophysical Research: Solid Earth, v. 100, p. 10187–10196, doi:10.1029/95JB00615.

McDonough, M.R., and Morrison, M.L., 1990, Ptarmigan Creek West Half, British Columbia (83D/10): Geological Survey of Canada Open File 2305.

McDonough, M.R., Morrison, M.L., Currie, L.D., Walker, R.T., Pell, J., and Murphy, D.C., 1991, Canoe Mountain, British Columbia (83D/11): Geological Survey of Canada Open File 2511.

McDonough, M.R., and Mountjoy, E.W., 1990, Lucerne West-half, British Columbia (83D/15): Geological Survey of Canada Open File 2260.

McDonough, M.R., and Murphy, D.C., 1994, Geology, Valemount, West of the Sixth Meridian British Columbia (83D/14): Geological Survey of Canada "A" Series Map 1843A.

McDonough, M.R., and Parrish, R.R., 1991, Proterozoic gneisses of the Malton Complex, near Valemount, British Columbia: U–Pb ages and Nd isotopic signatures: Canadian Journal of Earth Sciences, v. 28, p. 1202–1216, doi:10.1139/e91-108.

McDonough, M.R., and Simony, P.S., 1988, Structural evolution of basement gneisses and Hadrynian cover, Bulldog Creek area, Rocky Mountains, British Columbia: Canadian Journal of Earth Sciences, v. 25, p. 1687–1702, doi:10.1139/e88-159.

McDonough, M.R., and Simony, P.S., 1989, Valemount strain zone: a dextral oblique-slip thrust system linking the Rocky Mountain and Omineca belts of the southeastern Canadian Cordillera: Geology, v. 17, p. 237–240, doi:10.1130/0091-7613(1989)017<0237:VSZADO>2.3.CO;2.

McMechan, M.E., 2000, Walker Creek fault zone, central Rocky Mountains, British Columbia-southern continuation of the Northern Rocky Mountain Trench fault zone: Canadian Journal of Earth Sciences, v. 37, p. 1259–1273, doi:10.1139/e00-038.

Meixner, J., Schill, E., Grimmer, J.C., Gaucher, E., Kohl, T., and Klingler, P., 2016, Structural control of geothermal reservoirs in extensional tectonic settings: An example from the Upper Rhine Graben: Journal of Structural Geology, v. 82, p. 1–15, doi:10.1016/j.jsg.2015.11.003.

Moeck, I.S., 2014, Catalog of geothermal play types based on geologic controls: Renewable and Sustainable Energy Reviews, v. 37, p. 867–882, doi:10.1016/j.rser.2014.05.032.

Moreno, D., Lopez-Sanchez, J., Blessent, D., and Raymond, J., 2018, Fault characterization and heat-transfer modeling to the Northwest of Nevado del Ruiz Volcano: Journal of South American Earth Sciences, v. 88, p. 50–63, doi:10.1016/j.jsames.2018.08.008.

Moynihan, D., and Pattison, D.R.M., 2008, Origin of the Kootenay Lake Metamorphic High , Southeastern British Columbia: British Columbia Geological Survey Geological Fieldwork 2008–1, 147–158 p.

Muller, J.E., Cameron, B.E.B., and Northcote, K.E., 1981, Geology and mineral deposits of the Nootka Sound map-area (92E) Vancouver Island, British Columbia.: , p. 59.

Muñoz, G., 2014, Exploring for Geothermal Resources with Electromagnetic Methods: Surveys in Geophysics, v. 35, p. 101–122, doi:10.1007/s10712-013-9236-0.

Murphy, D.C., 1990, Direct evidence for dextral strike-slip displacement from mylonites in the southern Rocky Mountain Trench near Valemount, British Columbia: Geological Survey of Canada Current Research, Paper 90-1E,.

Murphy, D.C., Walker, R.T., and Parrish, R.R., 1991, Age and geological setting of Gold Creek gneiss, crystalline basement of the Windermere Supergroup, Cariboo Mountains, British Columbia: Canadian Journal of Earth Sciences, v. 28, p. 1217–1231, doi:10.1139/e91-109.

NASA/METI/AIST/Japan Spacesystems, and U.S./Japan ASTER Science Team, 2019, ASTER Global Digital Elevation Model V003 [Data set]: NASA EOSDIS Land Processes DAAC, https://doi.org/10.5067/ASTER/ASTGTM.003.

Nelson, P.H., and Van Voorhis, G.D., 1983, Estimation of sulfide content from induced polarization data: Geophysics, v. 48, p. 62–75.

North, F.K., and Henderson, G.G.L., 1954a, Summary of the Geology of the Southern Rocky Mountains of Canada: Guide Book Fourth Annual Field Conference Banff-Golden-Radium, p. 15–81.

North, F.K., and Henderson, G.G.L., 1954b, The Rocky Mountain Trench: Canadian Society of Petroleum Geologists,.

Parrish, R.R., 1981, Geology of the Nemo Lakes belt, northern Valhalla Range, southeast British Columbia: Canadian Journal of Earth Sciences, v. 18, p. 944–958, doi:10.1139/e81-091.

Parrish, R.R., Carr, S.D., and Parkinson, D.L., 1988, Eocene extensional tectonics and geochronology of the Southern Omineca Belt, British Columbia and Washington: Tectonics, v. 7, p. 181–212, doi:10.1029/TC007i002p00181.

Parrish, R.R., and Wheeler, J.O., 1983, A U–Pb zircon age from the Kuskanax batholith, southeastern British Columbia: Canadian Journal of Earth Sciences, v. 20, p. 1751–1756, doi:10.1139/e83-165.

Peacock, J.R., Thiel, S., Heinson, G.S., and Reid, P., 2013, Time-lapse magnetotelluric monitoring of an enhanced geothermal system: GEOPHYSICS, v. 78, p. B121–B130, doi:10.1190/geo2012-0275.1.

Petit, J.P., 1987, Criteria for the sense of movement on fault surfaces in brittle rocks: Journal of Structural Geology, v. 9, p. 597–608, doi:10.1016/0191-8141(87)90145-3.

Piteau Associates Engineering Ltd., 1994, Preliminary assessment of Canoe Hot springs near Valemount, British Columbia.:

Pommier, A., and Le-Trong, E., 2011, "SIGMELTS": A web portal for electrical conductivity calculations in geosciences: Computers & Geosciences, v. 37, p. 1450–1459, doi:10.1016/j.cageo.2011.01.002.

Pope, M.C., and Sears, J.W., 1997, Cassiar platform, north-central British Columbia: A miogeoclinal fragment from Idaho: , p. 4.

Poulton, T.P., and Simony, P.S., 1980, Stratigraphy, sedimentology, and regional correlation of the Horsethief Creek Group (Hadrynian, Late Precambrian) in the northern Purcell and Selkirk Mountains, British Columbia: Canadian Journal of Earth Sciences, v. 17, p. 1708–1724, doi:10.1139/e80-179.

Price, R.A., and Carmichael, D.M., 1986, Geometric test for Late Cretaceous-Paleogene intracontinental transform faulting in the Canadian Cordillera: Geology, v. 14, p. 468–471, doi:10.1130/0091-7613(1986)14<468:GTFLCI>2.0.CO;2.

Read, P., 1990, Mount Meager Complex, Garibaldi Belt, Southwestern British Columbia: Geoscience Canada, v. 17, p. 167–170.

Read, B., and Brown, R.L., 1981, Columbia River fault zone: southeastern margin of the Shuswap and Monashee complexes, southern British Columbia: v. 1145, p. 1127–1145.

Reed, B.L., and Miller, T.P., 1980, Uranium and Thorium content of some Tertiary granitic rocks in the southern Alaska Range: United States Geological Survey Open-File Report 80-1052 Open-File Report.

Reyes, A.G., 2015, Low-temperature geothermal reserves in New Zealand: Geothermics, v. 56, p. 138–161, doi:10.1016/j.geothermics.2015.04.004.

Reyes, A.G., Christenson, B.W., and Faure, K., 2010, Sources of solutes and heat in low-enthalpy mineral waters and their relation to tectonic setting, New Zealand: Journal of Volcanology and Geothermal Research, v. 192, p. 117–141, doi:10.1016/j.jvolgeores.2010.02.015.

Rietveld, H.M., 1969, A profile refinement method for nuclear and magnetic structures: Journal of Applied Crystallography, v. 2, p. 65–71, doi:10.1107/S0021889869006558.

Ristau, J., Rogers, G.C., and Cassidy, J.F., 2007, Stress in western Canada from regional moment tensor analysis: Canadian Journal of Earth Sciences, v. 44, p. 127–148, doi:10.1139/e06-057.

Roddick, J.A., 1967, Tintina Trench: Journal of Geology, v. 75, p. 23–33.

Rogers, G.C., Ellis, R.M., and Hasegawa, H.S., 1980, The McNaughton Lake Earthquake of May 14, 1978: Bulletin of the Seismological Society of America, v. 70, p. 1771–1786.

Rohr, K.M.M., Scheidhauer, M., and Trehu, A.M., 2000, Transpression between two warm mafic plates: The Queen Charlotte Fault revisited: Journal of Geophysical Research: Solid Earth, v. 105, p. 8147–8172, doi:10.1029/1999JB900403.

Ross, J.V., and Kellerhals, P., 1968, Evolution of the Slocan Syncline in south-central British Columbia: Canadian Journal of Earth Sciences, v. 5, p. 851–872, doi:10.1139/e68-082.

Rotstein, Y., and Schaming, M., 2011, The Upper Rhine Graben (URG) revisited: Miocene transtension and transpression account for the observed first-order structures: Tectonics, v. 30, p. 1–14, doi:10.1029/2010TC002767.

Rusmore, M.E., Gehrels, G., and Woodsworth, G.J., 2001, Southern continuation of the Coast shear zone and Paleocene strain partitioning in British Columbia–southeast Alaska: GSA Bulletin, v. 113, p. 961–975, doi:10.1130/0016-7606(2001)113<0961:SCOTCS>2.0.CO;2.

Sadlier-Brown, T.L., and May, B., 2009, A report on a geophysical survey of the Hot Spring Gold and BMAYS mineral claims, Valemount - Kinbasket Lake area, British Columbia (NTS: 083D/10):, 120 p.

Shipton, Z.K., Soden, A.M., Kirkpatrick, J.D., Bright, A.M., and Lunn, R.J., 2006, How thick is a fault? Fault displacement-thickness scaling revisited, *in* Abercrombie, R., McGarr, A., Kanamori, H., and Di Toro, G. eds., Geophysical Monograph Series, Washington, D. C., American Geophysical Union, v. 170, p. 193–198, doi:10.1029/170GM19.

Sibson, H., 1996, Structural permeability of fluid-driven fault-fracture meshes: Journal of Structural Geology, v. 18, p. 1–12, doi:10.1016/0191-8141(96)00032-6.

Siripunvaraporn, W., Egbert, G., and Uyeshima, M., 2005, Interpretation of two-dimensional magnetotelluric profile data with three-dimensional inversion: synthetic examples: Geophysical Journal International, v. 160, p. 804–814, doi:10.1111/j.1365-246X.2005.02527.x.

Smart, K.J., Pavlis, T.L., Sisson, V.B., Roeske, S.M., and Snee, L.W., 1996, The Border Ranges fault system in Glacier Bay National Park, Alaska: evidence for major early Cenozoic dextral strike-slip motion: Canadian Journal of Earth Sciences, v. 33, p. 1268–1282, doi:10.1139/e96-096.

Stanton, R.J., 1966, The Solution Brecciation Process: GSA Bulletin, v. 77, p. 843–848, doi:10.1130/0016-7606(1966)77[843:TSBP]2.0.CO;2.

Statistics Canada, 2017, 2016 Census of Population: Data products, 2016 Census, https://www12.statcan.gc.ca/census-recensement/2016/dp-pd/index-eng.cfm (accessed July 2020).

Stefansson, V., 2000, The renewability of geothermal energy: Proceedings World Geothermal Congress 2000, p. 6.

Steno, N., 1669, De Solido intra Solidum Naturaliter contento Dissertationis Prodromus: Florentiae, https://www.jonathanahill.com/pages/books/2536/nicolaus-steno/de-solido-intra-solidum-naturaliter-contento-dissertationis-prodromus (accessed June 2020).

Stumpf, C., 2019, Parameter Optimization of a Low Temperature Difference Gamma-Type Stirling Engine to Maximize Shaft Power: University of Alberta, doi:10.7939/r3-jb09-7t31.

Sutherland, R. et al., 2017, Extreme hydrothermal conditions at an active plate-bounding fault: Nature, v. 546, p. 137–140, doi:10.1038/nature22355.

Taylor, M.A., 2007, The State of Geothermal Technology: Geothermal Energy Association, 80 p.

Thompson, R.I., and Dhesi, P., 2009, Geology, Rosebery, British Columbia: Geological Survey of Canada.

Thompson, R.I., Glombick, P., and Lemieux, Y., 2004a, Geology, Eureka Mountain, British Columbia: Geological Survey of Canada.

Thompson, R.I., Glombick, P., and Lemieux, Y., 2004b, Geology: Mount Fosthall: Geological Survey of Canada Open File 4377.

Thompson, R.I., Lemieux, Y., Glombick, P., and Dhesi, P., 2009a, Geology, Nakusp, British Columbia: Geological Survey of Canada.

Thompson, R.I., Lemieux, Y., Glombick, P., and Dhesi, P., 2009b, Geology, St. Leon, British Columbia: Geological Survey of Canada Open File 6185.

Thordarson, T., and Larsen, G., 2007, Volcanism in Iceland in historical time: Volcano types, eruption styles and eruptive history: Journal of Geodynamics, v. 43, p. 118–152, doi:10.1016/j.jog.2006.09.005.

Tuya Terra Geo Corp, 2016, Direct-use Geothermal Resources in British Columbia:, http://cdn.geosciencebc.com/project_data/GBCReport2016-07/GBC%20Report2016-07_SectionA_Summary.pdf (accessed March 2020).

Vanderhaeghe, O., and Teyssier, C., 1997, Formation of the Shuswap metamorphic core complex during late-orogenic collapse of the Canadian Cordillera: Role of ductile thinning and partial melting of the mid-to lower crust: Geodinamica Acta, v. 10, p. 41–58, doi:10.1080/09853111.1997.11105292.

van der Velden, A.J., and Cook, F.A., 1996, Structure and tectonic development of the southern Rocky Mountain trench: Tectonics, v. 15, p. 517–544, doi:10.1029/95TC03288.

Village of Valemount, 2012, Canoe Reach geothermal generation downstream economic development and district energy pre-feasibility study:, http://www.valemount.ca/sites/default/files/docs/EDO/MMM%20Summary%20Report%201.pdf (accessed March 2020).

Villamor, P., Nicol, A., Seebeck, H., Rowland, J., Townsend, D., Massiot, C., McNamara, D.D., Milicich, S.D., Ries, W., and Alcatraz, S., 2017, Tectonic structure and permeability in the Taupo Rift: New insights from analysis of LIDAR derived DEMs: Proceedings 39th New Zealand Geothermal Workshop,.

Vollmer, F., 2019, Orient: Spherical Projection and Orientation Data Analysis Software User Manual:, https://www.frederickvollmer.com/orient/download/Orient_User_Manual.pdf (accessed July 2019).

Wallace, L.M., Beavan, J., McCaffrey, R., and Darby, D., 2004, Subduction zone coupling and tectonic block rotations in the North Island, New Zealand: Journal of Geophysical Research: Solid Earth, v. 109, doi:10.1029/2004JB003241.

Weber, J., Ganz, B., Schellschmidt, R., Sanner, B., and Schulz, R., 2015, Geothermal Energy Use in Germany: Proceedings World Geothermal Congress, p. 19–25, doi:10.2307/1565994.

Williams, J.H., and Johnson, C.D., 2004, Acoustic and optical borehole-wall imaging for fractured-rock aquifer studies: Journal of Applied Geophysics, v. 55, p. 151–159, doi:10.1016/j.jappgeo.2003.06.009.

Witter, J., 2019, South Meager Geothermal Project: New perspectives from recently unearthed data: Geoscience BC Report 2019-07, http://www.geosciencebc.com/i/pdf/Report-2019-07-Innovate-Geothermal.pdf (accessed June 2020).

Witter, J.B., Trainor-Guitton, W.J., and Siler, D.L., 2019, Uncertainty and risk evaluation during the exploration stage of geothermal development: A review: Geothermics, v. 78, p. 233–242, doi:10.1016/j.geothermics.2018.12.011.

Woodsworth, G., and Woodsworth, D., 2014, Hot Springs of Western Canada: A Complete Guide: Gordon Soules Book Publishers, 303 p.

Yekini Suberu, M., Wazir Mustafa, M., and Bashir, N., 2014, Energy storage systems for renewable energy power sector integration and mitigation of intermittency: Renewable and Sustainable Energy Reviews, v. 35, p. 499–514, doi:10.1016/j.rser.2014.04.009.

Yoshino, T., and Noritake, F., 2011, Unstable graphite films on grain boundaries in crustal rocks: Earth and Planetary Science Letters, v. 306, p. 186–192, doi:10.1016/j.epsl.2011.04.003.

Zarrouk, S.J., and Moon, H., 2014, Efficiency of geothermal power plants: A worldwide review: Geothermics, v. 51, p. 142–153, doi:10.1016/j.geothermics.2013.11.001.

Appendices

Appendix A – Blog posts from the Hugh C. Morris Fellowship

In 2018 I was awarded an inaugural Hugh C. Morris Fellowship, funded by the Kimberley Foundation. The Morris fellowship provides generous funding for travel and experiential learning for Canadian graduate students seeking to expand their educational experience on topics broadly related to global sustainability. As Canada currently has no installed geothermal energy capacity and only a handful of experts, I proposed that I stood to benefit from travel to countries with active geothermal energy industries. Over a period of 5 months I travelled to Iceland, the US, Germany, and New Zealand, and met with geothermal experts at academic institution, government organizations, and private companies. I shared my ongoing research, participated in field studies, and learned about the cutting-edge scientific techniques being used to explore for, develop, and monitor geothermal energy resources. This experience served to broaden my horizons as a researcher and provided much needed global context for my work in Canada. The fundamental knowledge that I gained as part of this experiential learning program contributed to my fundamental understanding of geothermal energy resources, thereby bolstering the introductory chapter (Chapter 1) of this thesis. Furthermore, many suggestions from researchers I met during my travels have been incorporated into the methods and interpretations of my research in Chapters 2 and 3. I documented my travels in several blog posts aimed towards a broad audience. These blogs are reproduced here.

A Summer Spent in the Trenches (August 2018)

It has been a busy, busy summer! Since early May, I think I have spent a grand total of 4 weeks at home in Edmonton, and for the rest I've been occupied with TA'ing field school, attending a conference, visiting family, and conducting field work for my thesis. It has certainly been tiring, but also extremely engaging and fun, reaffirming my passion for field geology.

When I say the summer was spent in the "trenches", I don't mean those of warfare, nor the metaphorical trenches of hard work (though there was some of that), nor a paleoseismological trench excavated across an active fault, nor a tectonic trench at a plate boundary; I am referring to "morphogeological trenches", a fancy name for several of the large valleys in British Columbia whose shape, and perhaps very existence, can be attributed to large fault zones that run along their floors. Because fault zones comprise of highly fractured rock, they tend to be more easily eroded by rivers and glaciers, and therefore promote the growth of large valleys. It is rare to find big faults on mountain tops! The unfortunate consequence for geologists, is that the faults themselves are often obscured by glacial and fluvial sediments that fill the valley bottoms, and direct observation of the faults is rare.

The largest and most well-known of the trenches is the Southern Rocky Mountain Trench, which runs along the western flank of the Rocky Mountains, and contains the towns of Invermere, Golden, and Valemount. Beyond Prince George it becomes known as the Northern Rocky Mountain Trench, and beyond the Yukon border it is called the Tintina Trench. Together these trenches form an incredibly linear feature that stretches for thousands of kilometers from Montana to Alaska. The northern two segments of this trench system are thought to host upwards of 400 km of right-lateral strike-slip motion - that is, the west side has moved 400 km north relative to the east side. Strangely, this significant amount of displacement seems to disappear in the southern segment, which is instead thought to contain a normal fault, on which the west side has moved several kilometers downwards relative to the east.

Moving west, the next big trench is the Purcell Trench, which forms the boundary between the Purcell and Selkirk mountain ranges. It runs from northern Idaho up towards Rogers Pass where it merges with the Southern Rocky Mountain Trench, and contains Kootenay Lake, and the towns of Creston and Kaslo. Most of the literature on the Purcell Trench concerns the southernmost portion near the international border, where a normal fault is thought to have moved the east side down relative to the west. Further north, a mix of normal faults and thrust faults are believed to run along or near the valley floor.

West of the Purcell Trench is the Columbia River Valley, which runs from Castlegar up past Nakusp and Revelstoke before merging with the Southern Rocky Mountain Trench near BC Hydro's Mica Dam site. While not officially recognized as a "trench" in literature, it seems to fit the bill: a large valley containing

a large fault. In this case, the Columbia River Fault is thought to have moved the east side down several 10s of kilometers relative to the west.

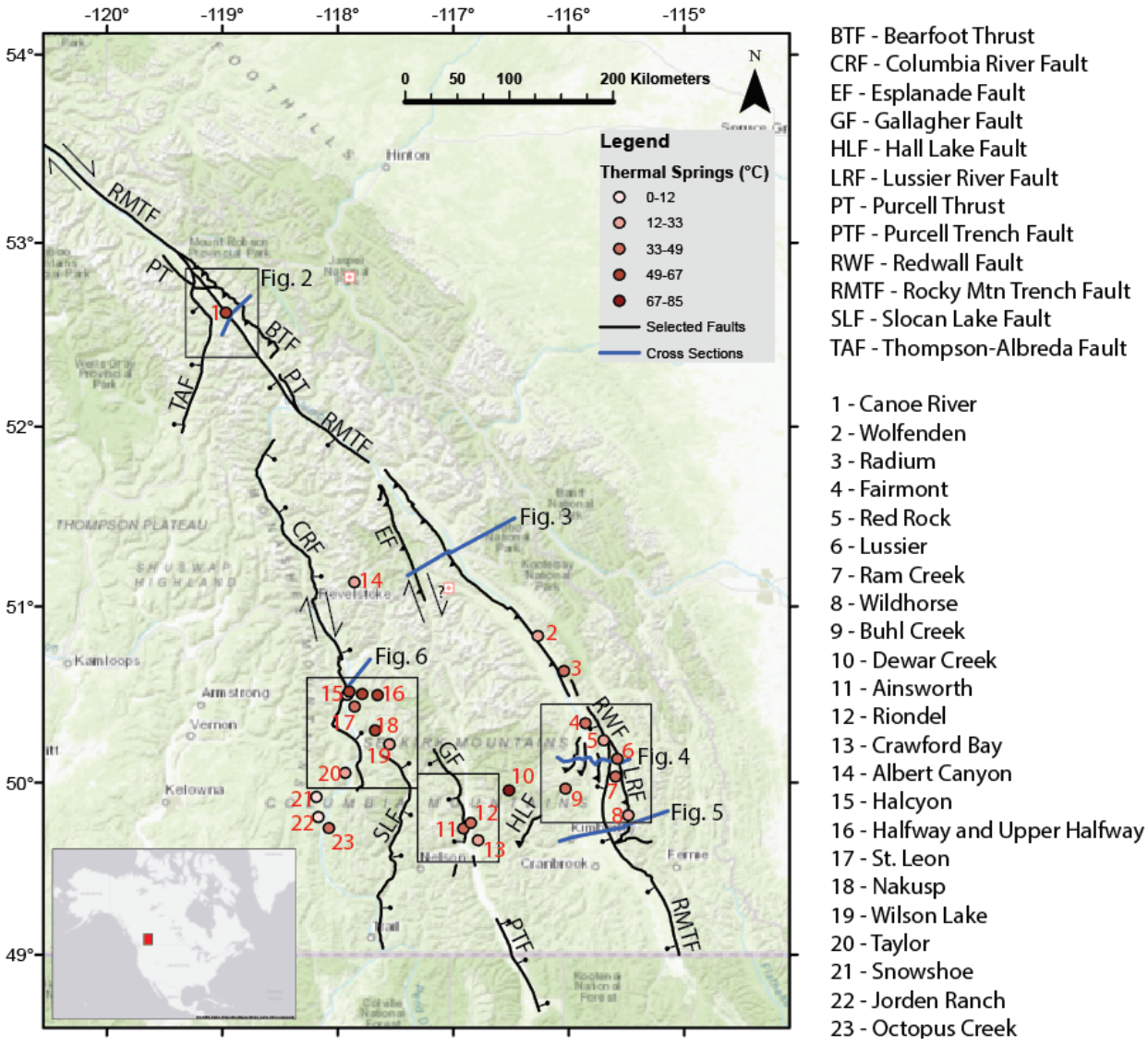

BTF - Bearfoot Thrust
CRF - Columbia River Fault
EF - Esplanade Fault
GF - Gallagher Fault
HLF - Hall Lake Fault
LRF - Lussier River Fault
PT - Purcell Thrust
PTF - Purcell Trench Fault
RWF - Redwall Fault
RMTF - Rocky Mtn Trench Fault
SLF - Slocan Lake Fault
TAF - Thompson-Albreda Fault

1 - Canoe River
2 - Wolfenden
3 - Radium
4 - Fairmont
5 - Red Rock
6 - Lussier
7 - Ram Creek
8 - Wildhorse
9 - Buhl Creek
10 - Dewar Creek
11 - Ainsworth
12 - Riondel
13 - Crawford Bay
14 - Albert Canyon
15 - Halcyon
16 - Halfway and Upper Halfway
17 - St. Leon
18 - Nakusp
19 - Wilson Lake
20 - Taylor
21 - Snowshoe
22 - Jorden Ranch
23 - Octopus Creek

Figure A.1. A map of major faults and hot springs in BC.

Figure A.2. Looking northwest in the Southern Rocky Mountain Trench near Valemount, BC.

Figure A.3. Looking north in the Purcell Trench near Kaslo, BC

Figure A.4. Looking southwest in the Columbia River Valley near Nakusp.

These trenches are interesting from a tectonic perspective because they represent major boundaries between different groups and types of rocks. The amount of displacement on the faults within them is debated, as are the kinematics (i.e., which way they moved). Again, because the faults themselves are rarely observed directly, geologists must rely on correlating geological units across the trenches in order to estimate the amount and direction of offset. Similarly, the age of the faults is only constrained indirectly by documenting which geologic units are offset by the fault, and which units lie undisturbed across it. In our case, the trenches are broadly thought to have been active as recently as the Eocene (56-34 million years ago), after the cessation of mountain building in the Jurassic and Cretaceous.

The trenches are also interesting from a geothermal energy perspective, because they appear to at least partially control the distribution of hot springs in British Columbia. The basic theory is that fault zones create highly permeable pathways that allow ground and surface water to circulate to great depths where it becomes heated before returning to the surface. Though the occurrence of hot springs doesn't guarantee the viability of a geothermal energy resource, it can be a good place to start. Thus, the main focus of my thesis has been to investigate these large faults in greater detail than before, particularly in the vicinity of hot springs, but also in the trench segments where there are no hot springs, to determine what dictates the occurrence of hot springs in some places but not others.

So, I have spent my summer in the trenches, getting up close and personal with the faults than run along their floors. I focused my efforts on looking for direct evidence of faulting, such as slickenlines, which are essentially mineral growths that form lines in the direction of fault movement. Many hot days were spent

Figure A.5. Inside a large strike-slip fault with a wide gouge zone. Slickenlines are also faintly visible on the right hand side, above Noah's head.

alongside highways where rock is well exposed in road cuts, measuring the orientations of fault planes and the slickenlines on them. Ultimately I measured almost 500 fault planes, which should allow for an

improved understanding of past fault movements, and how they might influence spring distribution. I also spent a significant amount of time looking for fault gouge - when faults are large enough they create what is known as a "gouge zone". Fault gouge is comprised of tiny clay minerals (mica) that form under the heat and pressure of faulting. Recently, an innovative method has been developed for dating these clay minerals, and we may make use of this to improve the age constraints on the faults. So, whenever I came across a gouge zone, I took a sample, which usually involved wedging myself into crevices armed with a hammer and Ziplock bag. Ultimately I will have to decide which of about 50 samples I want to obtain an age for, and then cross my fingers that the method works!

Data analysis will be a slow process over the coming months, especially as I begin my travels as part of the Hugh Morris Fellowship. Stay tuned for my next post, which should be from Alaska!

Staying Warm in Alaska (September 2018)

The first leg of my fellowship travels is now complete, and I write this enroute to Iceland, with the gorgeous Brooks Range, and Canadian Arctic Archipelago passing underneath. My visit to Alaska was jam-packed and I am glad to have the opportunity to write and reflect on all I have learned in Fairbanks.

When selecting destinations to visit for this fellowship, Alaska was an obvious choice. While geothermal energy does not represent a significant portion of the electricity production in the state, the resources they do have are, geologically, quite similar to those in Canada. I wanted to learn why Alaska has been successful in developing the resource, while we still lag behind in Canada. More specifically, I wondered if there were subtle geological differences that I was missing, or whether the answer was more to do with economics.

One of the most basic indicators of a geothermal resource is the occurrence of hot springs. Especially in places like British Columbia, where geothermal exploration is still in its infancy, hot springs are really all we have to start with. Some have argued that using hot springs as an exploration tool may be overly simplistic, likening it to hunting for oil seeps in the early days of petroleum exploration. Nevertheless, hot springs are a place to start. Alaska is home to around 100 hot springs, and the handful of geothermal energy projects in the state are centered around a few of these springs: Chena Hot Springs, Manley Hot Springs, and Pilgrim Hot Springs.

These three springs occur within what is known as the Central Alaska Hot Springs Belt (CAHSB), which is a diffuse zone of ~30 moderate-temperature springs that runs east to west across the state, from the Beaufort Sea to the Yukon border. Unlike the numerous springs in the Aleutians and Wrangells, which are likely heated by volcanic activity, the heat source of the CAHSB is more elusive. The springs occur in rough conjunction with a belt of Cretaceous-aged plutons, and while these magma bodies cooled long-ago, they tend to contain elevated levels of Uranium and Thorium, which may heat the groundwater via radioactive decay. Furthermore, these plutons seem to be affected by strike-slip faulting, which probably allows for the permeability that allows for groundwater to percolate to great depths. The fractured, radioactive plutons act like gigantic heat exchangers, slowly heating groundwater before it rises to the surface.

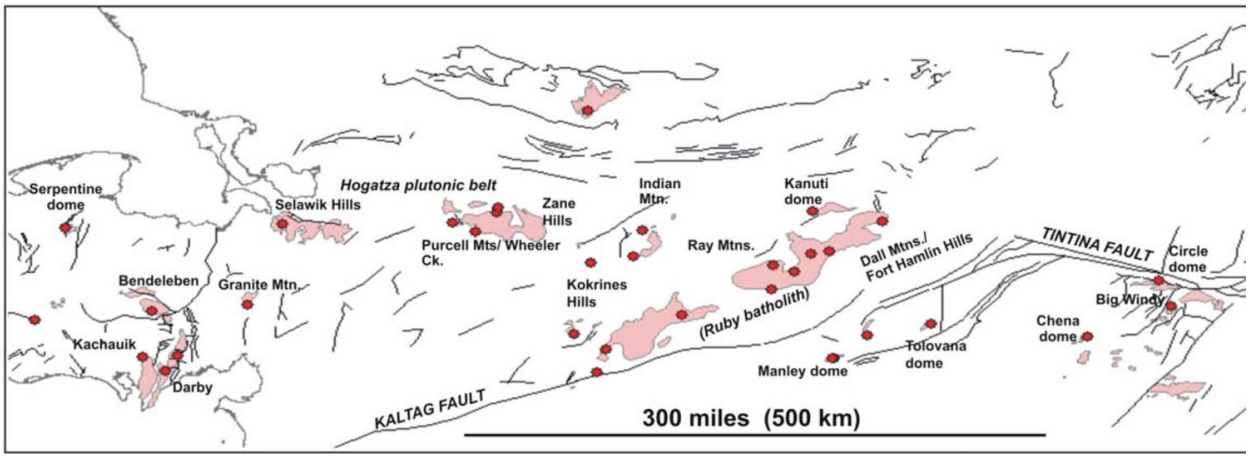

Figure A.6. The Central Alaska Hot Springs Belt, and associated plutons. Chena and Manley are in the bottom right. (Kolker, 2008). The Cretaceous plutons often form the core of "domes", which are basically just rounded hills.

Figure A.7. Chena Hot Springs Pluton. Not enough radioactivity to be dangerous, but enough radioactivity to heat groundwater!

Chena Hot Springs (73 C)

One of the biggest geothermal success stories in Alaska is found at Chena Hot Springs, approximately 100km east of Fairbanks. It began as a typical hot spring resort, with tourists coming purely for the novelty of soaking in the naturally heated water. However in recent years it has been developed into a renewable energy showcase in its own right. In fact, it holds the distinction of being the world's lowest-temperature electricity-producing geothermal resource. Water emanates from the spring at about 73 °C, well below boiling. It is then run through a heat exchanger in which its thermal energy is transferred to an organic compound known as R-134A (1,1,1,2-Tetrafluoroethane), a refrigerant which has a boiling point of -26.3 °C. The R-134A flashes to vapour, causing a rise in pressure sufficient to turn a turbine and generate electricity. Cold creek water or cold winter air is used to cool the refrigerant before it is cycled back through the system. The refrigerant is contained in a closed loop, and never mixes with groundwater. This type of power plant is known as an Organic Rankine Cycle engine, and is quite commonly used in low to medium temperature geothermal resources, where the formation water itself is not hot enough to generate steam.

The "waste" water from the power plant is piped to a hot pool for tourists' enjoyment, before being reinjected into the ground several hundred meters from the production (i.e., extraction) well. The reinjection stage is critical for the longevity of the geothermal resource. If not handled properly, the hot aquifer will lose heat over time.

In addition to electricity, the hot water is used to directly heat buildings at the resort. Especially in cold climates where heating constitutes a large portion of an electrical bill, direct heating makes economic sense. Rather than wasting energy by converting from thermal, to electrical, and back to thermal, it makes far more sense to use the heat from the water directly.

A major issue that Alaskans face is food security, due to their geographic isolation from the continental US. While farming in the north can be relatively successful due to the long summer days, the growing season is quite short. At Chena Hot Springs, geothermal water is used to heat greenhouses year-round, allowing for a 12-month growing season! Hydroponic systems provide nutrients to plants, and efficient LEDs (powered by geothermal electricity) provide the necessary light. Several varieties of lettuce and tomatoes are grown and used in the resort kitchen, and I am told there is usually a surplus of produce. I made sure to sample the goods in the restaurant, and found the tomatoes to be especially delicious.

Another use of hot water at Chena is, counterintuitively, refrigeration. Using some serious thermodynamic trickery, the geothermal water is used to drive an absorption chiller (look it up - there are

YouTube videos that can explain it better than me), in order to keep an ice sculpture museum cold throughout the summer months. While this use may seem like a bit of a novelty, the first thing that came to my mind was: ice rinks. There are certainly many of these in Canada that need to be kept cool year round!

Figure A.8. The power plant at Chena Hot Springs along with an assortment of older machinery. Three Organic Rankine Cycle (ORC) engines are installed, producing approx. 400kWh.

Figure A.9. The tomato greenhouse at Chena Hot Springs.

Figure A.10. Chena Hot Springs pool.

Figure A.11. The Ice Museum at Chena Hot Springs, kept cold year-round with a geothermally powered absorption chiller.

Manley Hot Springs (59 C)

As the crow flies, Manley Hot Springs is quite close to Fairbanks, but by road, the route is circuitous, and takes about 4 hours to drive, and about 250km on gravel. Despite this isolation, Manley Hot Springs was actually home to the first ever Organic Rankine Engine used for a geothermal energy application. There is no longer any electrical power produced at Manley (ironically, it is back on diesel), however there is a farming operation that uses geothermal heat to extend the growing season for tomatoes, beans, eggplants, and a variety of other vegetables. The geothermal anomaly at Manley occurs over a broad area surrounding the town, punching a hole in the permafrost and allowing for more lush vegetation to grow locally. The naturally-occurring springs are used to heat a rustic bath-house/greenhouse, while the heat for the farm is extracted from a separate well several hundred meters away from the spring. I spoke with the owner of the farm, and he said the largest problem he faced was finding enough people to help him pick all the produce!

Figure A.12. Geothermally assisted eggplant!

Figure A.13. Geothermal well used for heating the greenhouses. Solar panels power the down-hole pump.

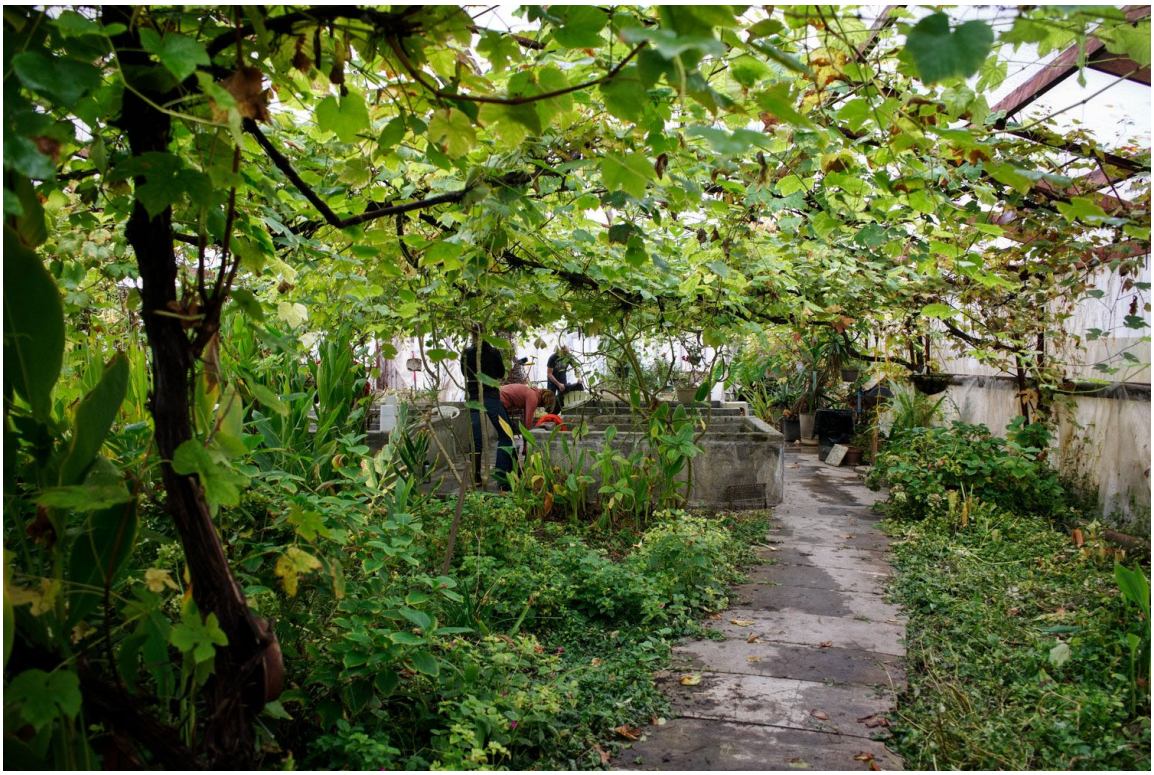

Figure A.14. Manley bath house, with grapevines and other plants that would otherwise not survive at 65 degrees north.

Pilgrim Hot Springs (90 C)

Though I never had the chance to visit it, I spoke with several researchers at the Alaska Center for Energy and Power, and the University of Alaska Fairbanks, about their work at Pilgrim Hot Springs, which is located north of Nome, on the Seward Peninsula in western Alaska. This site has seen a lot of recent exploration activity, with the intention of providing Nome with electricity, and possibly growing produce in a similar fashion to Chena and Manley. Unlike Chena and Manley, the source of heat for this hot spring may be recent volcanism. The geothermal reservoir occurs in the upper 300m of unconsolidated sediment, but water is thought to emanate from a deeper reservoir along an active fault that cuts through the bedrock at depth.

Innovative techniques in remote sensing and groundwater modelling have been applied here. Airborne Thermal Infra-Red (TIR) imaging was used to provide a more comprehensive map of where hot water is reaching the surface. In a setting like Pilgrim, where the spring outlets are diffuse, this was very useful in providing a more accurate estimate of heat flux than could be achieved with measurements on the ground.

When assessing a geothermal resource, it is critical to understand just how much energy you have, and TIR is a relatively inexpensive way of doing this.

Information from TIR imagery can be combined with other parameters to produce models of the spring's "plumbing systems" at depth. A common software package used for this application is COMSOL Multiphysics, which, given a set of boundary conditions, can model the transport of mass and heat underground. In the case of Pilgrim, researchers essentially asked: "given a regional heat flow, and the local groundwater flow regime, how do we end up with the spring distribution highlighted by the TIR imagery". This combination of techniques makes for a very powerful first-pass model of the geothermal system, which can then be followed up with targeted geophysics and drilling. Efforts are underway to pinpoint the exact location of the fault from which the hot water is emanating, with the hope of tapping into a hotter reservoir.

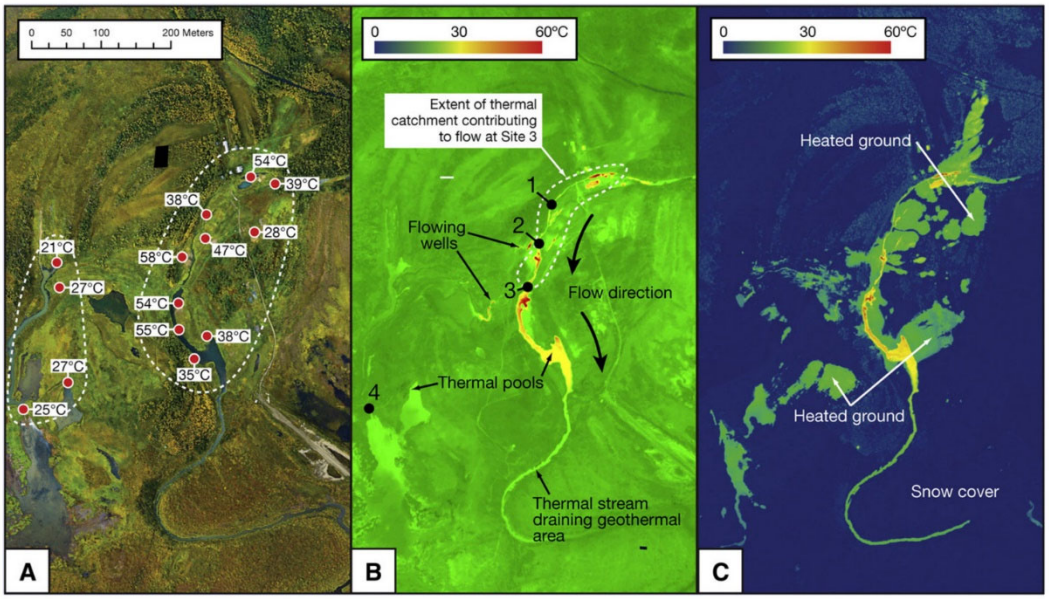

Figure A.15. Optical and TIR imagery of Pilgrim Hot Springs. (Haselwimmer et al., 2013)

Comparison to Canada

Considering the modest success of these geothermal resources in Alaska, it is worth asking what is preventing further development of similar resources in Canada. I won't go into great depth here, and I sure there is much more nuance than I can convey in a blog post, but here are some of my initial thoughts...

First: the geology. Generally, it seems quite similar: hot springs are roughly associated with fault systems that allow for deep circulation of meteoric water. In many cases the hot springs in Canada are also situated within Cretaceous plutons, though it has not yet been established whether or not these plutons

have elevated radioactivity, as they do in Alaska. The springs in Alaska are on the high end of the temperature scale when compared to Canada, though there are some that have comparable outlet temperatures. The geothermal reservoirs that are being utilized in Alaska are all within several 100 meters of the surface, though there are thought to be hotter reservoirs at greater depths. In Canada, we tend to only discuss the use of deep reservoirs, several kilometers down, which are obviously much more expensive to tap into. Perhaps shallow reservoirs should be considered, however there is a valid concern that this would disrupt the natural flow of hot springs, which nobody wants. In Alaska, disturbing the springs seems to be less of a concern because they are so remote and fewer tourists and locals visit them.

Second: economic factors. I believe these may be more important controls on our respective levels of geothermal development. To start with, there are numerous communities in Alaska that are completely off-grid, and rely on diesel generators to provide power. This electricity comes at a premium, and is not subsidized by the government (as it is in Canada), so the residents of these communities have a strong incentive to push for alternative sources of power. The energy market itself is diverse, with numerous companies competing for business, unlike British Columbia, which has essentially one option: BC Hydro. Furthermore, most communities in BC are already connected to the power grid, which provides cheap electricity from hydro dams, so there isn't an economic or environmental incentive to change things. Only remote, off-grid communities in Canada's northern territories might have reason to push for geothermal energy development, but again, because their power is partially subsidized, the desire isn't as strong as it is in Alaska. In BC, there may be more interest in direct use geothermal applications, e.g., heating a greenhouse to extend a growing season, or heating a house through the winter to offset electricity bills.

This is perhaps a discouraging note to end on, but on the bright side, I think that Alaska is proof that low-temperature geothermal developments can be successful. Perhaps in the face of growing population and electricity demands, the economics will change in western Canada, and the demand for geothermal energy will grow. To brighten the mood, I'll leave you with a picture of Denali, which I had the rare opportunity to see on a clear day, with fall colours in full force!

My sincere thanks go to all those who I met with in Fairbanks, who generously shared their research and ideas with me: Gwen Holdmann, Ronnie Daanen, Anupma Prakash, Santosh Panda, and John Dart.

Figure A.16. The tall one, Denali

Iceland, a Geothermal Hotspot (September 2018)

When you think of geothermal energy, Iceland immediately comes to mind. Situated on a segment of mid-ocean ridge fortuitously intersected by a mantle plume, the heat flow is very high, and geothermal resources are abundant. Compared to other countries, Iceland doesn't produce the most megawatts of geothermal power - that distinction belongs to the US. However, in terms of percentage of national power generation, Iceland ranks the highest, with ~27% of their electricity coming from geothermal power plants, and the rest from hydro. Geologically, Iceland is quite different from western Canada, perhaps even polar opposite, the former being at a divergent plate boundary, and the latter at a convergent boundary. Nevertheless, there are plenty of parallels that can be drawn between the two, and lots to be learned from the experts there.

My visit was hosted by the Iceland GeoSurvey (aka. ISOR: Islenkar Orkurannsoknir = Icelandic Energy Research), a state-owned institution that receives its funding only through project contracts with various companies and organizations. Their focus is on geothermal energy exploration, but they consult on other geoscience topics as well. Headquartered in Reykjavik, they have a small branch in the northern town of Akureyri, which is where I spent most of my time.

Geothermal resources in Iceland are typically divided into two categories: low-temperature (<150°C at 1 km depth) and high-temperature (>200°C at 1km depth). The range in between doesn't apply to many systems in Iceland. The low temperature resources are certainly more relevant to Canada and were the focus of my visit, but I made to sure to visit and learn about the high temperature resources as well because Iceland is a world-class example.

High Temperature Resources

The high temperature resources occur in the volcanically active regions in the immediate vicinity of the active rift zone that zig-zags from north to south across the island. These are the geothermal resources that Iceland is famous for, with big power plants situated in dramatic volcanic landscapes. The heat for these systems comes from still-molten magma chambers that occur along the spreading center. Groundwater percolates down along the active normal faults and gets heated up in proximity to these magma bodies, becoming partially if not totally vapourized. Boreholes are drilled to depths of ~1-3 kilometers to bring this steam to the surface. Unlike the binary fluid Organic Rankine Cycle engines used in low and medium temperature resources elsewhere in the world (see previous blog post about Alaska), this steam can be used directly to turn turbines and generate electricity, rather than requiring a second fluid to flash to vapour. In some cases, in addition to generating electricity, the heat from the steam is used to heat fresh groundwater, which is then piped into Reykjavik and other towns to provide direct heating for homes and

businesses. The fresh groundwater is used for this purpose because it causes less scaling and corrosion issues than the hydrothermal fluid

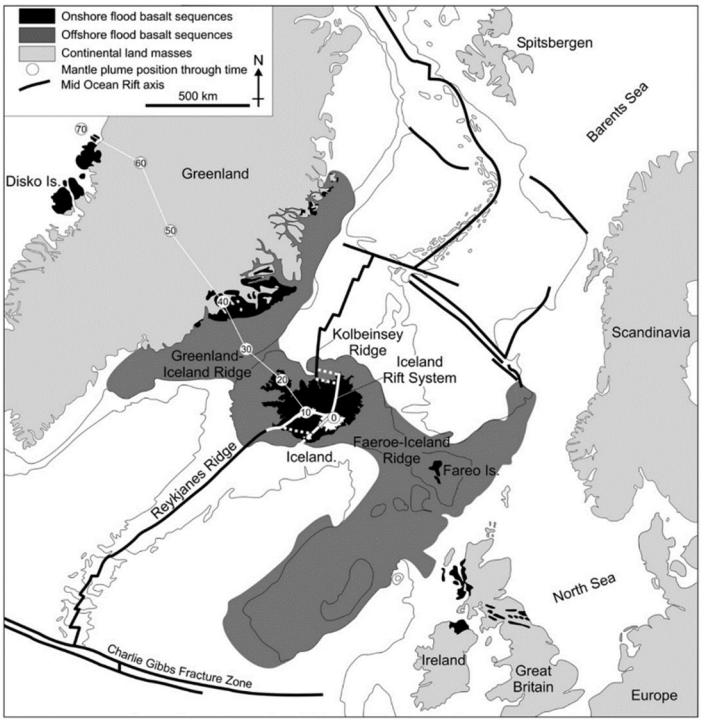

Figure A.17. Tectonic setting of Iceland in the northern Atlantic. Note how the Iceland Rift System steps out east from the trend of the submarine Reykjanes and Kolbeinsey Ridges. Circled numbers indicate the location of the mantle plume over the past 70 million years. Source: Thordarson and Larsen (2007).

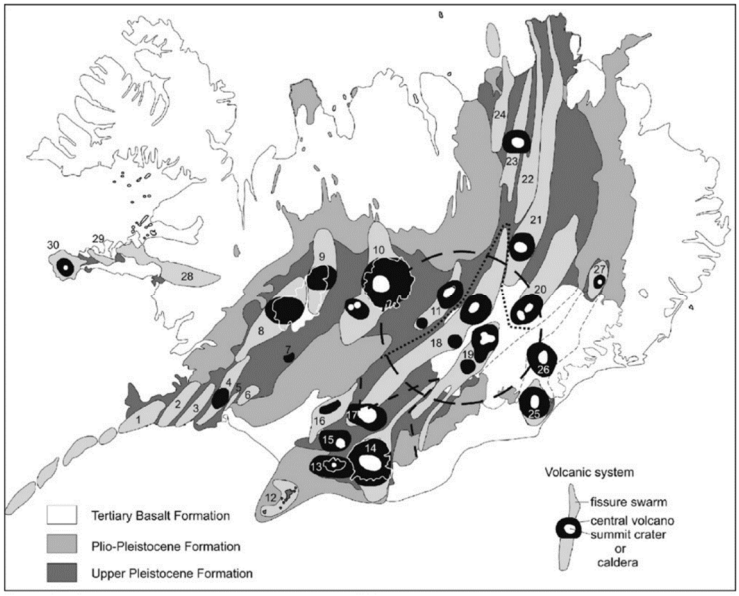

Figure A.18. Map of active volcanic systems in Iceland. Reykjanes-Svartsengi (1), Hengill (4), Krafla (23), and Theistareykir (24) all host high temperature geothermal power plants. Source: Thordarson and Larsen (2007).

A number of volcanic centers occur along the spreading center, and geothermal power plants are situated near these volcanoes. Near the Keflavik International Airport, are the Svartsengi (76MW) and Reykjanes (100MW) power plants. The waste water from Svartsengi is piped into the pool known as the Blue Lagoon, famous among tourists. The entire Reykjanes peninsula is very tectonically active, and when I first arrived I was struck first by the slight scent of sulfur in the air, and second by how barren the area is, with fresh basalt flows stretching in all directions. Nearer to Reykjavik, the Nesjavellir (120MW) and Hellisheidi (303MW) geothermal power plants sit on the flanks of Hengill volcano, which most recently erupted in 150 CE.

Figure A.19. Nesjavellir Power Plant, situated on the northern flank of Hengill Volcano.

Three more power plants exist on the north side of the island. Krafla power plant (60MW) and nearby Bjarnaflag (3MW), are located just to the northeast of the famous Lake Myvatn, and are two of the older power plants on the island. Coincidentally, while Krafla was being constructed, nearby fissures opened up and spewed lava intermittently for about a decade, an event known as the Krafla Fires. The power plant still operates today, though heat and water levels in the production wells have decreased over time, as is

inevitable with any geothermal system. While the geothermal power companies are under no regulatory obligation to sustain their fields for certain amounts of time, it is in their best interest to manage the reservoir sustainably.

Krafla is also home to the first Iceland Deep Drilling Project (IDDP-1) borehole, which was supposed to be drilled to a depth of 4-5km in an attempt to reach supercritical steam. The enthalpy of supercritical fluid is much higher than standard liquid and vapour dominated systems, potentially dwarfing previous power plant outputs. The project hit a major snag when the borehole unexpectedly intersected a small pocket of rhyolite magma at 2100m. A second attempt on a deviated hole hit a second pocket of magma. As you might expect, the drilling equipment was ruined by this, and the borehole was abandoned. All that remains is an inconspicuous wellhead - the well itself is now filled in with concrete. A second, more successful IDDP well has since been drilled on the Reykjanes Peninsula, reaching temperatures of 427C and pressures of 340 bars at a depth of 4659m! The well is still undergoing extensive testing to see better understand the resource, and explore the possibility of using it for electrical generation.

The final, and newest geothermal power plant is Theistareykir (90MW), which I didn't have the opportunity to visit. Because geothermal power is so abundant and cheap Iceland actually attracts businesses from around the world who wish to save money on energy intensive steps in manufacturing, while simultaneously reducing their carbon footprint. There are a number of aluminum smelters in Iceland that take advantage of geothermal power, and Theistareykir will primarily power a silicon metal plant owned by a German company.

One aspect of geothermal energy that tends to deter investors is the initial uncertainty of how many megawatts the plant will be able to produce. Unlike hydro dams, where the production can modelled fairly accurately beforehand, the output of geothermal plants can't really be determined until the plant is operating. Even then, there is uncertainty about how much water and heat can be extracted before it become unsustainable, and this can take several years of operation to determine. A balance must be struck between keeping investors happy in the short term, and keeping the geothermal field sustainable in the long term.

Figure A.20. Cooling towers at the Krafla Power Plant

Figure A.21. The inconspicuous IDDP-1 wellhead near Krafla Power Plant. Now sealed with concrete, this borehole encountered liquid rhyolite magma at ~2km depth.

Low Temperature Resources

I spent the bulk of my time in Akureyri, which is Iceland's second-largest town and unofficial capital of the north, situated on the western shores of Eyjafjordur. Unlike Reykjavik, Akureyri is a few hundred kilometers west of the axis of the spreading ridge. The surrounding region is characterized by deep fjords cut through Neogene (old, by Icelandic standards) layer-cake basalt flows. This area is not considered prospective for high temperature geothermal resources, but there is enough residual heat to provide district heating for Akureyri and surrounding towns (pop. ~20,000).

Much of the historical settlement of the area was based upon the locations of hot and warm springs, which were an important resource in the cold climate. Thermals waters were used in limited capacity for direct heating for much of the 20th century, but it wasn't until the oil crisis of the 1970s that a major push was made towards a district-wide geothermal heating system. As Akureyri grew, this system became more and more stressed, and there was barely enough heat to keep the town warm in the winter, with electric boilers taking up the slack during the coldest periods. A major breakthrough was finally made in 1999 with the discovery of a high temperature anomaly in shallow groundwater wells at Hjalteyri, north of Akureyri. A production well was drilled, which now produces more than half of Akureyri's heating needs, with plenty of capacity to spare. However, Akureyri continues to grow, so the search for new direct use geothermal resources continues.

Figure A.22. One of two wellheads at the highly successful Hjalteyri field on the east shore of Eyjafjordur. Hot water is carried via buried pipeline to heat buildings in Akureyri, ~20km south. Such a small spatial footprint!

One aspect of ISOR's research activities is baseline geological mapping. Given Iceland's small size, I was surprised to learn that a significant portion of the country has not been mapped in high detail. In particular, the "old" basalt flows have not been given as much attention as the more exciting active volcanic areas. Having good maps is critical in understanding the reservoirs in which hot water circulates. During my visit I tagged along with ISOR staff member, Sigurveig, to do some mapping in her PhD study area, an old volcanic center. The weather in September in Iceland is hardly conducive to geological mapping, and we were almost blown off the mountain several times, but it was a great opportunity to get out and look at some volcanic rocks, which I don't have a lot of experience with.

The basalt itself is not a great reservoir, as most void space has been plugged with alteration minerals. Hot groundwater is instead hosted in fault and fracture systems that have high permeability. Who knew there would be something for a structural geologist to look at in Iceland!? The permeability of these fault zones is maintained by earthquake activity, which breaks through precipitated minerals, essentially "unclogging" the fault zones. Interestingly, recent investigations have indicated that the fault systems that these fluids are hosted in, are not on the same orientation as normal faults that would be expected in a rift system. Instead the fluids seems to be in north-south striking strike-slip faults, interpreted to have arisen from ongoing transform motion on the Tjornes Fracture Zone (TFZ), offshore to the north. The TFZ is an east-west striking, dextral fault zone that transfers extensional strain from the Iceland Rift System to the Kolbeinsey Ridge. The north-south striking fractures in Eyafjordur may be behaving according to a "bookshelf" faulting model, which would predict left-lateral slip on these fractures. On a brief field excursion I observed this for myself, and measured several roughly north-striking fractures with horizontal slickenlines.

Figure A.23. Mapping Torfufell, a Neogene volcanic center, which is likely the source of much of the extensive basalt flows in the region.

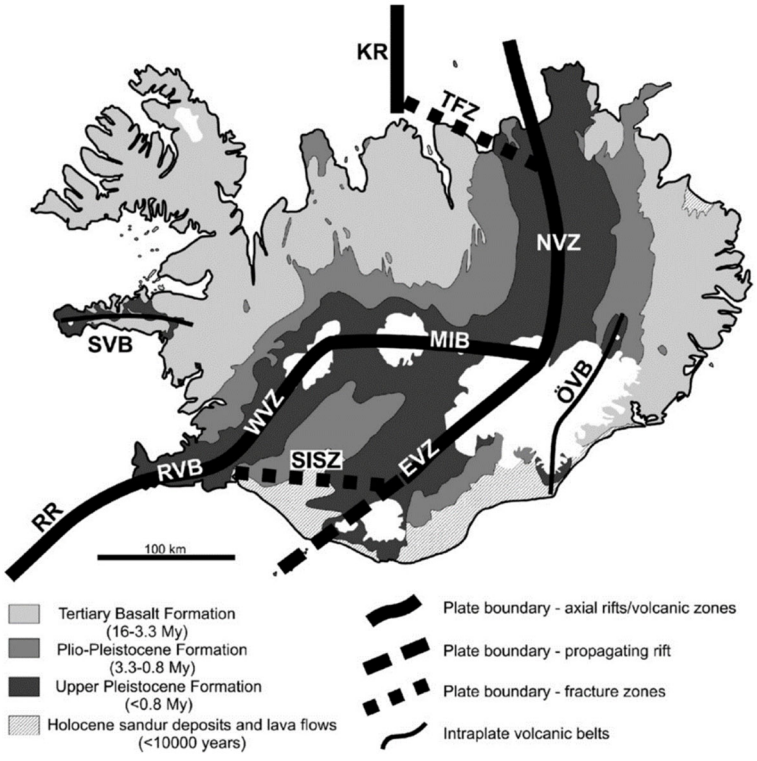

Figure A.24. Major crustal boundaries in Iceland. Note the Tjornes Fracture Zone (TFZ) offshore to the north of the north-south orientated Eyjafjordur. North-south oriented faults in Eyjafjordur may be the hosts of hydrothermal reservoirs. Source: Thordarson and Larsen (2007)

Figure A.25. Mapping north-south oriented fractures near Ytri-Vik. Red iron-staining suggests hydrothermal fluid circulation.

Some of these faults are observed at the surface, but they can also be mapped out at depth using a variety of well-logging techniques. A commonly used tool is an acoustic televiewer, which uses reflected sound waves to image the walls of boreholes. The acoustic waves are attenuated by fractured rock, and the fractures will appear as sinusoids of varying amplitude, depending on the angle at which the fracture intersects the borehole. The amplitude of the returned acoustic waves can also be used to estimate whether the fractures are open, or closed (clogged with mineral precipitate). When all the fracture data is amalgamated from a borehole, estimates of local stress directions can be obtained, which help determine which fracture orientations might be most permeable.

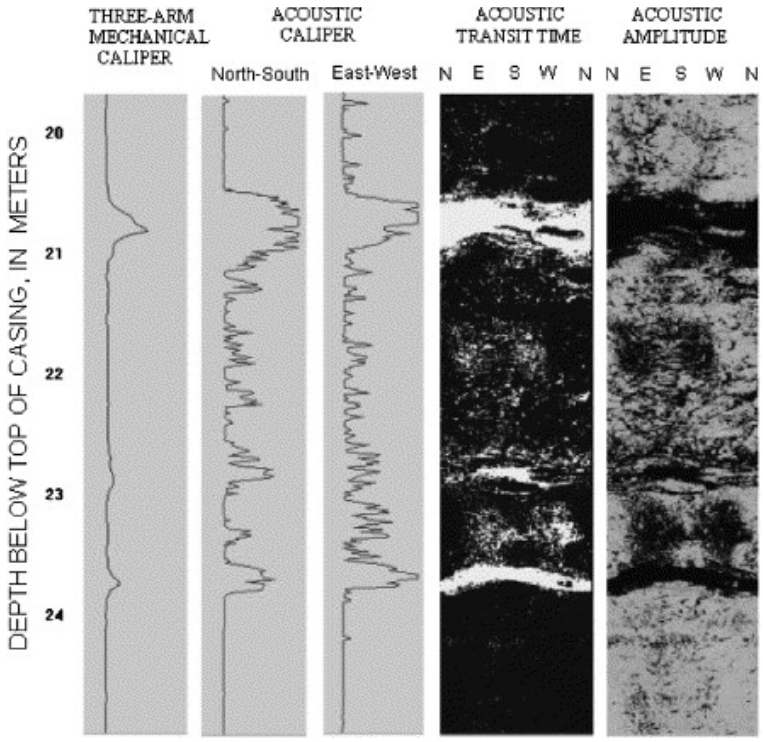

Figure A.26. Example of acoustic televiewer data displaying dipping fractures in a borehole. Zones with intense fracturing may act as conduits for hydrothermal waters. Source: Williams and Johnson (2004)

Conclusions

My visit to Iceland was fantastic and I learned a ton about geothermal energy from my hosts at ISOR. Perhaps one of my favourite parts of visiting Iceland was how geologically aware the public is. It's no surprise really, since their lives are so directly influenced by so many geological factors. Not only does the earth provide heat and electricity, it presents serious hazards in the forms of earthquakes, volcanic eruptions, and glacial outburst floods. I was impressed by the number of geological museums, and the abundance of interpretative signage around the island. Every tourist stop (waterfalls, beaches, mountains, glaciers, geysers, etc.) had detailed explanations of the geological phenomena at play, which made my drive to and from Akureyri from Reykjavik all the more interesting! I know I'll be back soon… but now on to warmer temperatures and desert climates in the southwestern US!

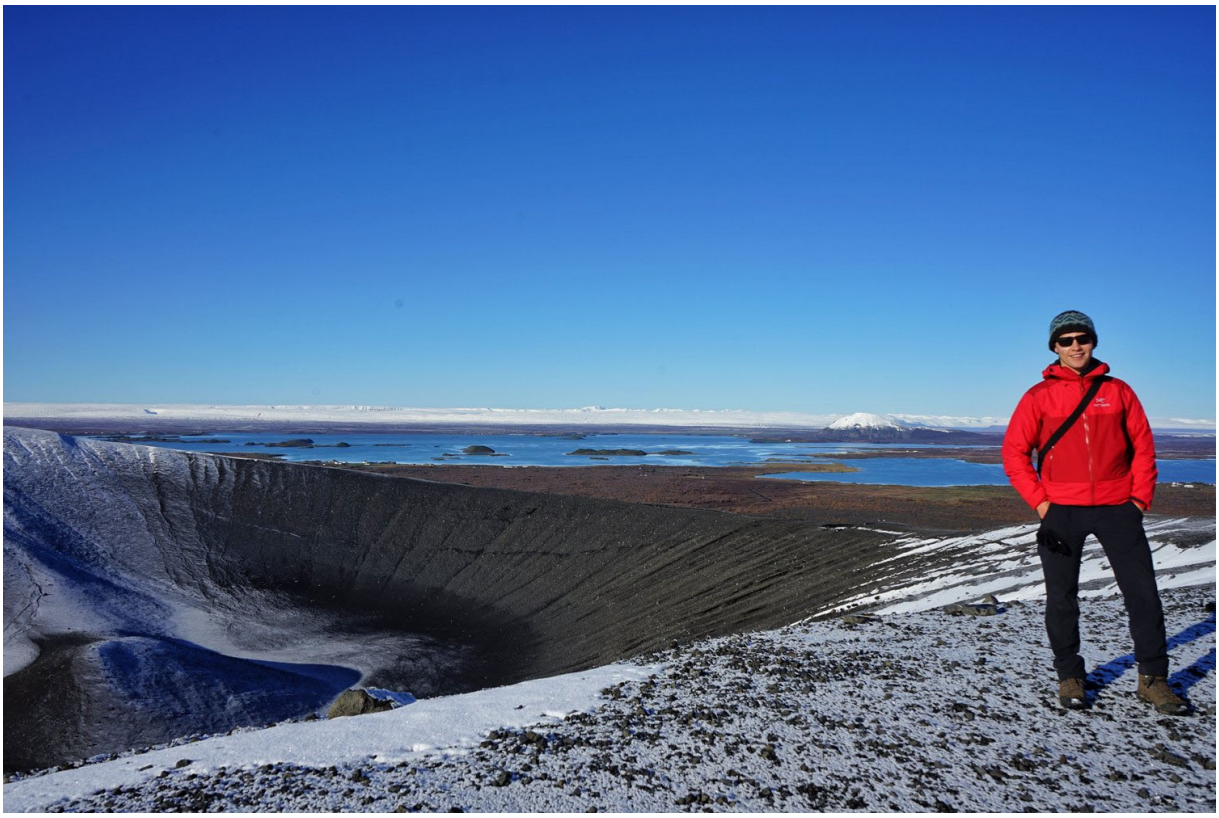

Figure A.27. Exploring Hverfjall, a tephra cone near Krafla Power Plant

A geothermal transect in the western US (October 2018)

Time is flying and another leg of my journey is now complete. I think the past 4 weeks in the central-western US have been the busiest so far, packed full of meetings, conferences, tours, and field trips. My brain is feeling pretty saturated, and hopefully there is some room for more knowledge in Germany, my next destination.

The United States produces the most geothermal electricity in the world, and the majority of the resources are in the states of California, Nevada, and Utah. Minor resources are also found in Washington, Oregon, and Idaho. The abundance of geothermal resources in this part of the world is largely due to combination of young volcanism and active faulting; there is plenty of heat in the shallow crust, and plenty of permeability to allow groundwater to heat up.

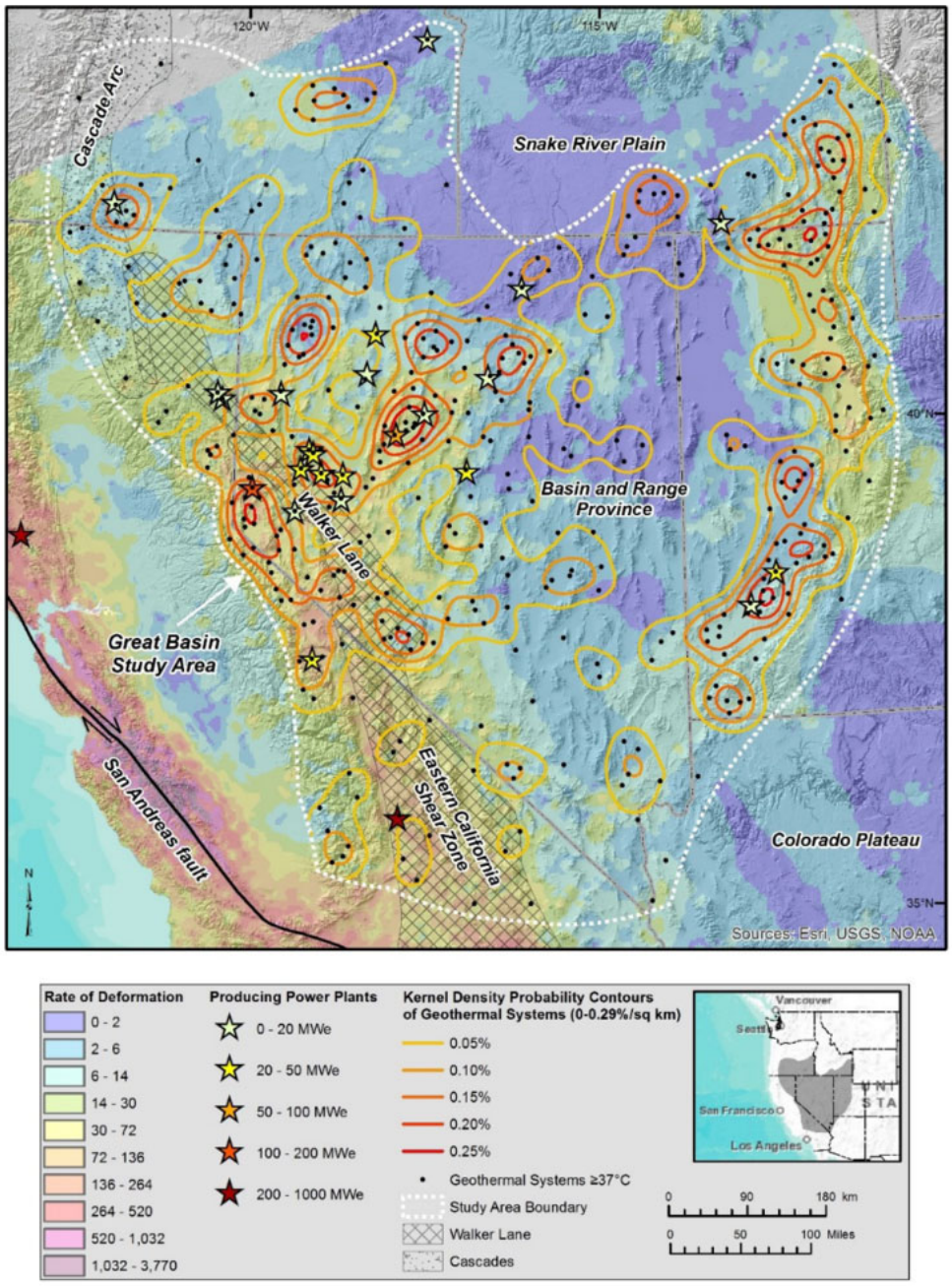

Figure A.28. Geothermal systems and regional tectonic setting of the central-western United States. The Basin and Range geologic province is characterized by north-south trending horsts (ranges) and grabens (basins). The majority of dextral shear strain between the Pacific and North American plates is accommodated on or near the San Andreas fault, with a minor component on the Eastern California Shear Zone and Walker Lane. Note that Nevada hosts the greatest number of geothermal power plants, but the largest power producers are in California. Source: Faulds and Hinz (2015)

My visit began in Reno, NV, which is probably known more widely for its casinos than its geothermal resources. However, it is actually one of the major centers of geothermal exploration in the US. Situated on the eastern flank of the lofty Sierra Nevada, the city itself sits in a fault controlled valley that is part of the Walker Lane shear zone. This NW-SE-striking shear zone takes up roughly 20% of the right-lateral shear strain between the Pacific and North American plates, the remainder of which is mostly accommodated by the San Andreas fault. Moving east of Reno, the dextral transtension of the Walker Lane transitions to pure extension in the Basin and Range geologic province. This is an area characterized by north-south trending ridges (horsts) and valleys (grabens). The horsts typically have a normal fault on one or both of their flanks, and many are host to regular seismicity.

The geothermal resources in the Basin and Range are considered "amagmatic", meaning that there is no shallow magma body providing heat. Instead, because of the active extension, the earth's crust is quite thin, and the geothermal gradient and heat flow are consequently high. The active faulting provides abundant permeable pathways for fluid to percolate downwards, and it doesn't have to go far before it passes the boiling point.

I spent the first few days of my visit with researchers at the Great Basin Center for Geothermal Energy, a branch of the Nevada Bureau of Mines and Geology, situated on the University of Nevada, Reno, campus. This visit was of special interest to me because of the work done at the GBCGE on amagmatic, fault hosted geothermal resources, which are in some ways analogous to my field area in southeastern British Columbia.

Favourable Structural Settings

Nevada is a great place to do structural geology. Unlike the lush forests of British Columbia, the dry climate and sparse vegetation do not act to obscure structural features in the landscape. Because of ongoing extension, many of these faults still have conspicuous scarps that betray their exact location, which makes them mappable for many kilometers along strike. The abundance of structural data has allowed researchers at the GBCGE to identify the most favourable structural settings for geothermal resources, i.e., those locations that have the highest permeability. It turns out that zones of high structural complexity and localized extension seem to host the greatest number of known geothermal systems in Nevada. I hope to identify similar localities in my own study area.

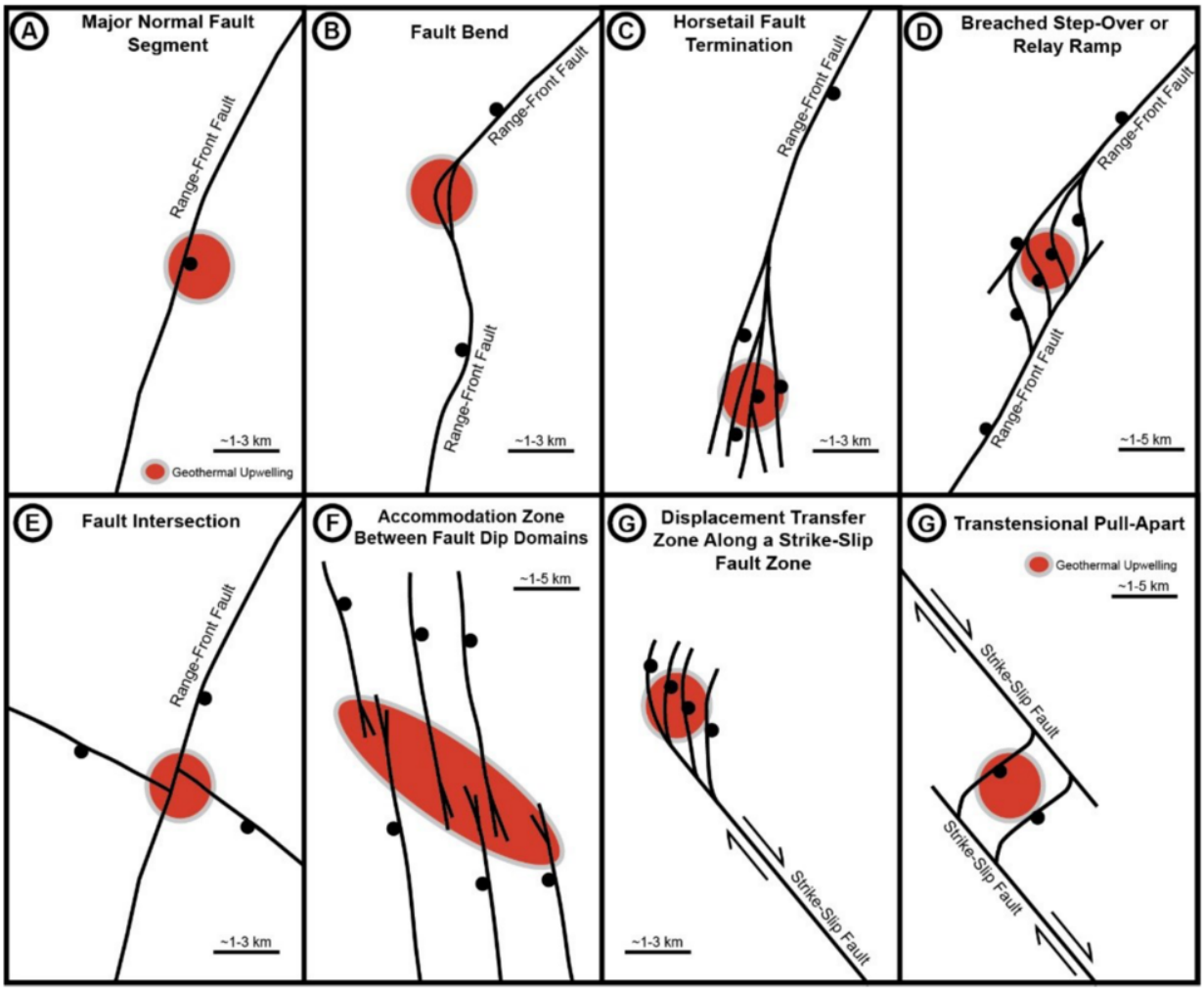

Figure A.29. Favourable structural settings for hydrothermal systems in Nevada. The highest percentage of geothermal systems in Nevada occur on fault terminations (C), fault step-overs (D), and fault intersections (E). Source: Faulds and Hinz (2015)

Play-Fairway Analysis

Researchers at the GBCGE have developed an geothermal exploration method dubbed "Play-Fairway" analysis. This is a term borrowed from the oil industry, and it essentially refers to a regional statistical assessment of a number of factors that might control the presence or absence of a resource, including heat flow, fault activity, crustal stress, and the orientation of faults. The key of course, is assigning a proper weight to each parameter such that the map you produce is actually useful; put too much weight on a single parameter, and you might end up with a bunch of false negatives and positives. The method is calibrated by comparing the results to previously known geothermal system, as well as ground-truthing the predictions through ground temperature measurements.

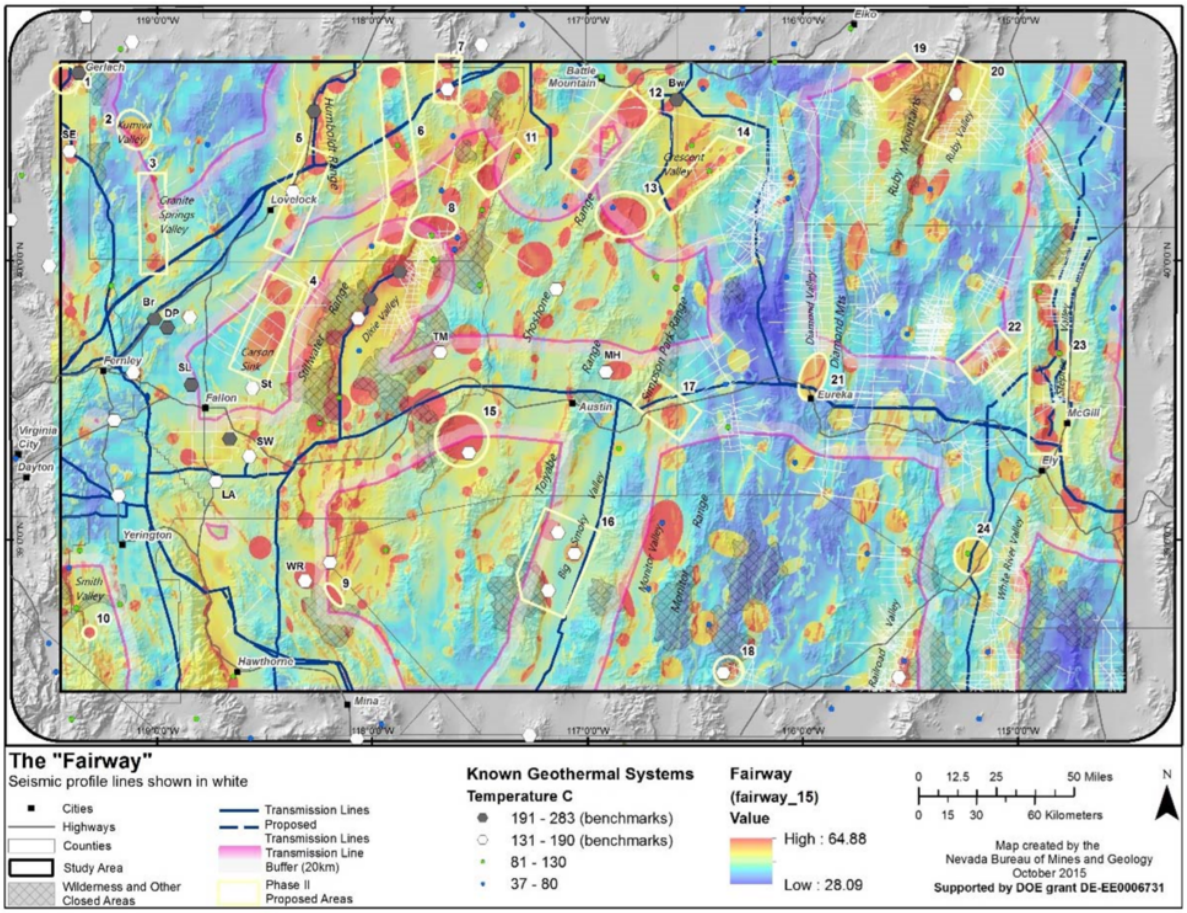

Figure A.30. Final product of the Play-Fairway analysis of the Great Basin. Most favourable areas for new geothermal development are highlighted in bright red, based on a statistical analysis of numerous layers of data. Source: (Faulds et al., 2016).

Blind geothermal systems and Gabbs Valley

Interestingly, the assessment of structural settings and Play-Fairway analysis has pointed to regions in Nevada that did not previously appear to host geothermal systems. These are known as “blind” geothermal systems, because there is no surface manifestation (e.g., hot spring, fumarole) to indicate their presence. There are a few reasons these systems are hidden, including a low, cold water table that blocks hot water up-flows from reaching the surface, and/or a permeable upper layer of sediment that might cause hot up-flows to diffuse before reaching the surface. It is estimated that ~75% of geothermal systems in Nevada are “blind”, which makes approaches like Play-Fairway very powerful.

A great example of a blind geothermal system is found in Gabbs Valley, to the east of Reno, on the western boundary of the Walker Lane shear zone. Structural mapping and Play Fairway analysis predicted that this area might host a geothermal system, and an array of shallow (2 m) temperature probes

confirmed a positive temperature anomaly right at the intersection of a dextral fault and a normal fault, i.e., a zone of local extension and structural complexity. A more comprehensive temperature gradient hole drilling program was completed this past summer, and temperatures of 152°C water within 117 m of the surface! Perhaps there will be a new power plant here in the future.

Figure A.31. A temperature gradient hole well head in Gabbs Valley. You wouldn't know it from the surface, but 117 m down this well, water temperatures reach 152 C!

Geothermal Resources Council Meeting

My visit to Reno also coincided with the annual meeting of the Geothermal Resources Council. This conference brings people from all parts of the geothermal industry together, including geoscientists, drillers, engineers, and entrepreneurs. It was a busy few days with many, many interesting talks on geothermal projects occurring around the world. It would be impossible to summarize all of the talks and conversations here, but suffice to say, my eyes were widened. It seemed to me that one of the major focuses of the conference was on Enhanced Geothermal Systems, and the complex reservoir engineering required to make them a reality… more on them below. The conference was held at the Peppermill Resort and Casino, chosen in part because it actually gets all of its heat from geothermal wells drilled on the property! The project came at a cost of $9.7 million, but with annual savings of $2.2 million previously spent on natural gas, the return on investment was fast!

Long Valley Caldera

As part of the Geothermal Resources Council meeting, I participated in a 3-day field trip to the Long Valley Caldera in central-eastern California. The Long Valley Caldera, once home to a massive eruption second only to Yellowstone, has a complex volcanic and tectonic history, spanning the last 4 million years. The caldera itself, which covers roughly 500km2, formed around 770,000 years ago with the eruption of the famous Bishop Tuff. It sits in a right-stepover between the right-lateral Eastern California Shear Zone and Walker Lane, resulting in localized crustal extension that probably controls both the volcanism and hydrothermal systems. Geothermal exploration has occurred here since the 1960s, and one power plant produces ~40 MW. Initial exploration focused on the center of the caldera, under the assumption that the source of the heat would be at the center of the volcanism. More recent investigations have shown that the main source of hot water comes up along the southwestern edge of the caldera, and is likely fault-controlled (surprise!).

Figure A.32. Hot Creek thermal springs in the Long Valley Caldera. The gap in solid bedrock outcrop on the far stream bank corresponds to a fault zone, in which damaged rocks are more susceptible to weathering. The spring, which appear to emanate from this fault zone, has fluctuated in temperature and flow rate over the years due to volcanic unrest. Don't go swimming in this one unless you want to end up like that couple in Dante's Peak!

Salt Lake City and the Wasatch Front

I then took the Amtrak train from Reno east to Salt Lake City and was treated to a stunning sunset in the desert, passing basin after range, horst after graben. I think I'll take the train every change I get from now on! I woke up in Salt Lake City and took the weekend to explore the area. Salt Lake City and the adjacent urban areas are collectively known as the Wasatch Front, as they are located along the north-trending Wasatch Range, which is controlled by the Wasatch Normal Fault on its western flank. This is an active fault and is due for a rupture in the near future. There are several thermal springs along the Wasatch Front, and these seem to occur in association with deviations (aka salients) in the strike of the fault, possibly because of high structural complexity and permeability at these locations.

Figure A.33. Looking south along the Wasatch Front. An active normal fault at the base of the Wasatch Mountains drops the west (right) side down every ~350 years. The segments of the fault near major population centers like Salt Lake City are considered at high risk for another earthquake. Thermal springs seem to occur in conjunction with bends in the Wasatch Fault, where there is perhaps more structural complexity and permeability.

The Milford FORGE Site and EGS

Many consider the future of geothermal energy to lie in Enhanced or Engineered Geothermal Systems (EGS). There is heat to be found in earth's crust all around the world, but the trick is finding heat within shallow enough depths, and with enough permeability to allow water to circulate. Lack of permeability truly restricts wide adoption of geothermal energy. The idea behind EGS is to create the necessary permeability by way of hydraulic fracking or shearing, i.e., pressurized injection of water in order to cause fractures to open or slip.

While promising in theory, EGS projects have had limited success. In an attempt to stimulate research on the topic, the US Department of Energy has funded a program known as the Frontier Observatory for Geothermal Energy (FORGE). Groups in Idaho, Washington, Idaho, and Nevada competed for the final funding, and ultimately Utah was selected. My visit to Salt Lake was hosted by the Energy and Geoscience Institute at the University of Utah, who lead the charge on the FORGE project in Utah. I was

fortunate to have the opportunity to visit the future site of the FORGE site near the town of Milford. It is situated near an existing geothermal power plant, and the wells from this plant were instrumental in understanding the hydrogeology of the area.

Two full size wells will be drilled into an impermeable granite pluton in the subsurface. One or both will be used to stimulate the reservoir, by injecting water at several intervals along the borehole in hopes of creating connected pathways between the wells. The trick is getting the fracture size and density just right so that water can pass through fast enough to maintain flow, but slow enough to pick up sufficient heat from the surrounding rock. If fracking is successful, water will be injected into the lower well, from which it will flow upwards due to buoyancy, and exit via the upper well, at that point hopefully hot enough to generate electricity. The success of this project will probably be hugely influential in the future of EGS, so this is certainly one to watch.

Figure A.34. The Milford Renewable Energy Corridor, looking WNW. In the foreground, the Blundell Geothermal Power Plant produces 34 MW of power from a hydrothermal system that appears to be bounded by a steep fault that roughly corresponds to the treed hillside behind the plant. The Milford FORGE site will be between the rows of wind turbines on the right side of the image. Across the valley, a large solar farm also produces electricity.

Homestead Crater

On my last day in SLC, we visited Homestead Crater, near Park City up in the mountains. At first glance this tourist destination is simply a mound of travertine (carbonate), but when you climb to the top, you can peer down a hole into the hollow center filled with warm water. A shaft has been tunneled into the side of the crater, and a local lodge runs SCUBA courses in the cavern. The question is: why is the travertine mound hollow, and why is the water level only halfway up the inside? It seems that this phenomena might provide insight into the paleohydrogeology of the region. The head (level of the water table) must have been higher at the spring outlet in the past in order to construct the full height of the travertine mound. At some point the spring water must have become undersaturated in carbonate, leading to the dissolution and hollowing-out of the crater.

Figure A.35. The Homestead Crater, a dome of travertine with a deep pool of warm water inside.

California and the Geysers

The last stop was Berkeley, California. My primary destination was the Lawrence Berkeley National Lab, which is home to a geothermal research group. The Bay Area is also home to a number of geothermal consulting companies, and was fortunate enough to have informative meetings with geoscientists at

Geologica, GeothermEx, and ThermoChem, about the work they do, and which techniques they find most useful in geothermal exploration.

One of the highlights of my visit was a tour of the massive Geysers geothermal field near Santa Rose, California. Situated about 2 hours north of Berkeley, this is the largest geothermal field in the world. Over 300 wells collect steam over an area of approximately 115 km2, producing around 735 MW, or power enough for 735,000 homes! The geothermal potential of the Geysers was first identified back in the early 1900s, but it wasn't fully developed until the 1970s. At that time, very little was known about reservoir sustainability, and steam was extracted at an enormous rate, producing upwards of 2000 MW! Eventually it became apparent that the field was in decline, as too much heat and pressure was being removed. A win-win solution was reached with local communities who were looking for somewhere to dispose of their treated waste water, which could not be put back in local creeks; water from Santa Rosa and Lake County was pumped up to the Geysers and injected into the wells. Since the beginning of this program, the production at the Geysers has stabilized.

The heat source of the Geysers is believed to be a ~1 million year old felsic intrusion about 1000 m below the surface, as well as some possible smaller younger intrusions. These intrusions are still young enough that they have residual heat, rather than radioactive heat like the plutons in Alaska. This region is also heavily influenced by the transform motion between the pacific Plate and the North America plate. While the San Andreas fault takes up most of this strain, a portion is distributed among smaller parallel faults, a few of which run through the Geysers field.

While the major faults in the Geysers area are easily identified with surficial mineral deposits and topographic manifestations (i.e., linear valleys), many smaller faults have only recently been identified using 3D mapping of micro-seismicity. The continuous extraction and reinjection of fluids into the subsurface induces many small earthquakes beneath the Geysers area. These are monitored closely with a dense network of seismometers. When their precise locations are plotted in three dimensions, distinct fault planes are illuminated. The team at the Geysers takes public outreach very seriously, and are very transparent with their operations and the resulting seismicity. As a result, local communities are very supportive and trustworthy of their operations, despite the occasional microseismic events. This is certainly a model future geothermal projects should follow!

I'd better end this blog (novel) here because it's getting way too long. My sincere thanks go to everyone who hosted me during my transect of Utah, Nevada, and California!

Figure A.36. One of the many power plants at the Geysers geothermal field, the world's largest geothermal power producer. In the background, numerous steam pipes from various wells are visible.

Geothermal in Germany (November 2018)

It may seem surprising that I chose Germany as a stop on a world tour of geothermal resources. The country certainly doesn't top the list of geothermal producers worldwide, generating only 40 MW of power (for comparison, the US generates ~3500 MW). However, for several reasons, the sector is poised to grow, and they are leading the way in a lot of research. Germany does not possess the attention-grabbing high-temperature geothermal resources like those in Iceland, the United States, or New Zealand. There is no active volcanism and the country is not directly situated on an active plate boundary. However, geothermal potential does exist, and there are several geological similarities with Canada, particularly between the sedimentary basins, that make it worthy of a visit.

There is an appetite for renewable energy in Europe, and in the wake of the 2011 nuclear meltdown at Fukushima, Germany has opted to phase-out nuclear power plants. Other renewable energy sources are required to fill the void, geothermal among them. The German federal government has incentivized geothermal development with a "feed-in tariff", which makes geothermal development more economically feasible and attractive. This subsidy will theoretically decrease over time as the cost of the technology decreases and better knowledge of the resource reduces the initial risk of investment.

Geothermal resources in Germany are generally found in three regions: the North German Basin, which stretches across most of the northern quarter of the country; the Molasse Basin, which lies at the front of the Alps, surrounding Munich; and the Upper Rhine Graben, a major fault-controlled valley in the southwest. My visit to Germany took me to research institutions and geothermal companies located in all three regions. My goal at each place was to learn about groundbreaking geothermal research, get a broad understanding of the regional geology, and draw comparisons with Canada.

My visit began with a short conference in Berlin, called Shaping the Future of Energy, held at the Canadian Embassy as part of Berlin Science Week. The conference was organized by the Future Energy Systems program at the University of Alberta, and was designed to showcase some of our work on renewable energy, and to discuss collaboration with German institutions. I presented a poster with some of my preliminary results from last summer's field work, and watched several talks and a panel discussion on various renewable energy topics. It was a great learning experience overall.

From Berlin I travelled to the Karlsruhe Institute of Technology (KIT), located in the southwest corner of Germany. Karlsruhe is located in the Upper Rhine Graben, a NNE-SSW trending rift valley that extends from the foothills of the Alps (Jura Mountains) near Basel, Switzerland, to the city of Frankfurt. The Rhine Graben has a complex history. It's underlying structure is controlled by pre-existing (~300 Myr old) weaknesses in the crust that were reactivated ~30 million years ago (Eocene) during the continental

collision that gave rise to the Alps. Initially, the stress regime favoured pure E-W extension, later shifting to left-lateral transpression and transtension (See figure below). Some authors have argued for an even more complicated stress history. The geothermal reservoirs in the Rhine Graben are heavily influenced by the main boundary faults (i.e., the faults that form the edges of the rift), and it is thus quite important to understand the full tectonic history of these features.

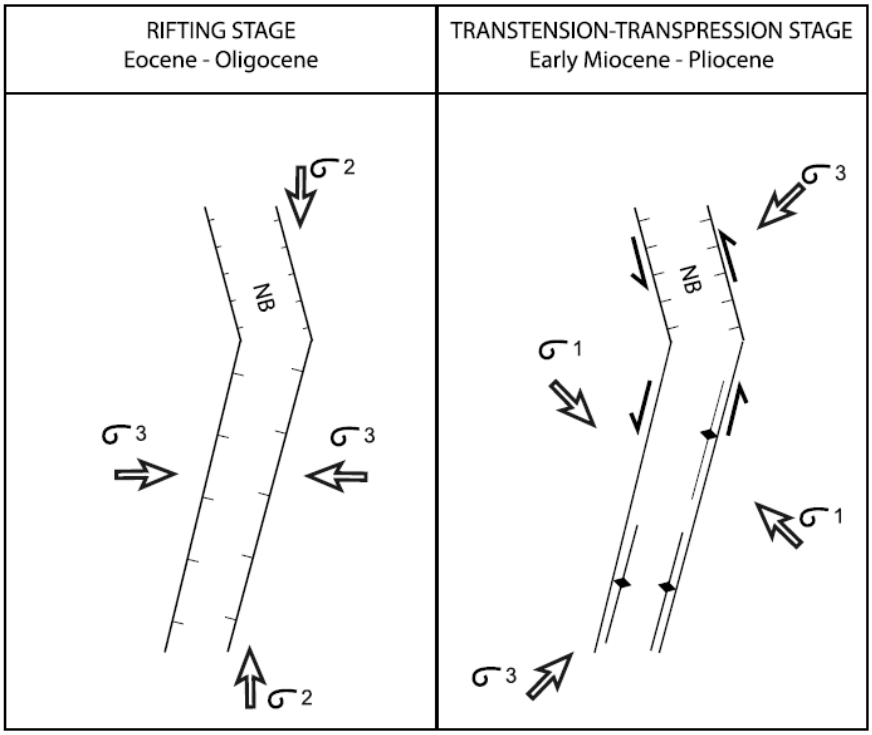

Figure A.37. Simplified stress history of the Upper Rhine Graben. Extension in the Eocene to Oligocene took advantage of pre-existing crustal weakness. This was followed by a transition to left-lateral transpression and transtension in the Miocene to Pliocene. Source: Rotstein and Schaming (2011).

Not only is the stress history important to understand - so is the current stress regime, and the influence it has on pre-existing fault planes. Faults that have been recently active tend to be more permeable than those that have had time to get clogged with mineral precipitate. One method we discussed while at KIT is known as “Slip and Dilation Tendency Analysis”, in which a modeled stress regime is applied to a 3D fault model. Faults are considered likely to slip if the effective shear stress is equal or greater than the frictional resistance to sliding; the resistance to sliding depends on the normal stress acting on the fault plane (anyone else having flashbacks from highschool physics?). The likelihood of a fault to dilate is determined based on the relative magnitude of the maximum compressive stress and the normal stress acting on a fault plane; the greater the difference, the more the fault will dilate, allowing fluid to flow.

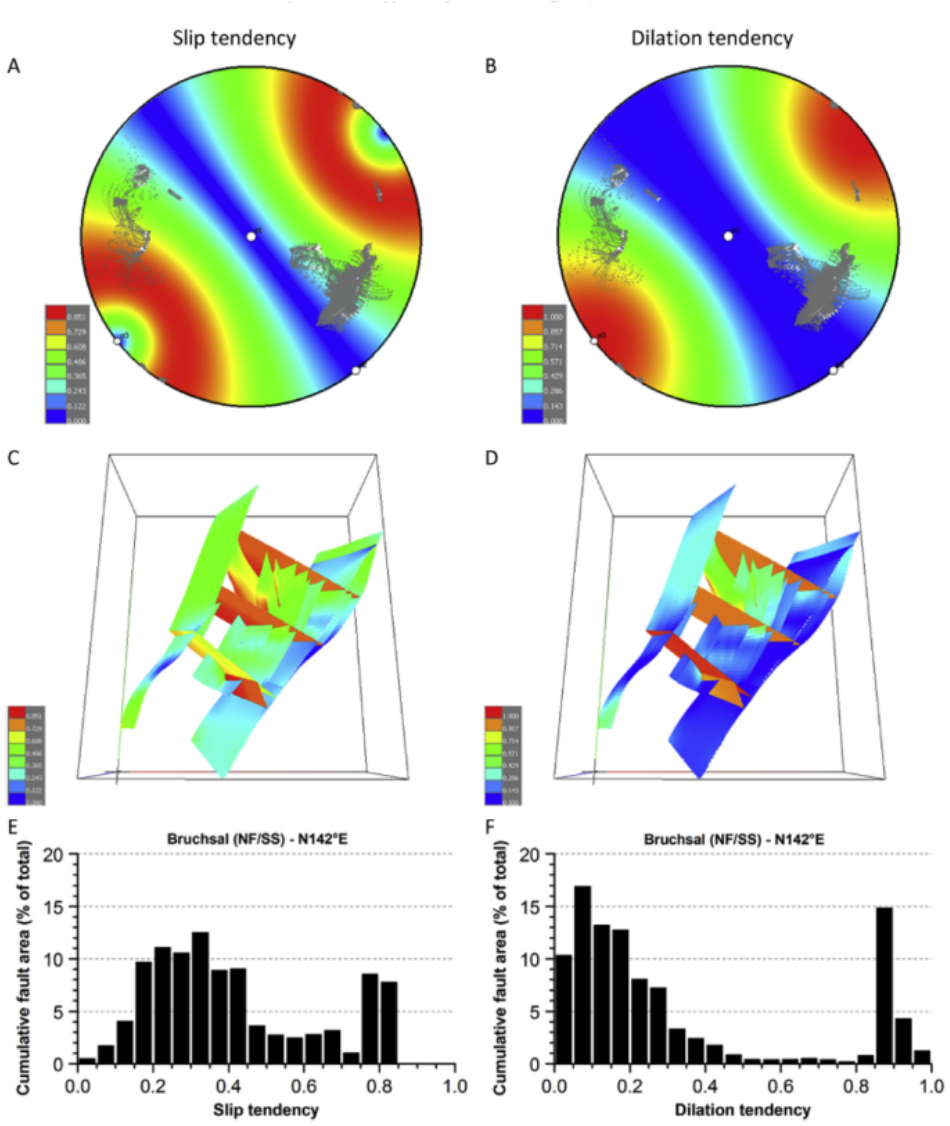

Figure A.38. Results from a Slip and Dilation Tendency Analysis performed by Meixner et al. (2016) on 3D fault model of the Bruchsal geothermal system near Karlsruhe. You can see that the WNW-ESE oriented faults are much more likely to slip and dilate, indicating that they may be more favourable fluid paths.

While at KIT, I had the opportunity to visit an engineering lab that has been working on a technology that could have significant impact in the geothermal energy industry. Generally, geothermal reservoirs need to be at or above 100˚C to be used for electricity generation via a steam turbine, but there are a few exceptions to this. In some cases, like at Chena Hotsprings in Alaska, a heat exchanger is used to transfer heat from the sub-boiling water (~73˚C) to a working fluid with a lower boiling point (haloalkane refrigerant R-134a) which goes through the turbine. At the University of Alberta, there is ongoing research into the application of Stirling engines to geothermal electricity production at low temperatures

(https://sites.ualberta.ca/~dnobes/research_1.html). Particularly in geologic settings like the Western Canada Sedimentary Basin, Molasse Basin, and North German Basin, there are a great deal of hot water reservoirs that don't quite reach the boiling point. It would therefore allow for much wider development of geothermal energy if we could generate electricity from such reservoirs.

Known as an "entropy wheel" (image below), the machine at KIT consists of an inner and outer wheel held apart by numerous small springs that are made of a special material that shrinks when it is heated (see: http://www.itcp.kit.edu/wilhelm/entropierad.php). As the wheel passes through hot water at the bottom of its cycle, the springs contract, and then expand again when they pass by the cooling fans mounted above the wheel. This variable expansion and contraction causes the center of mass of the outer wheel to be slightly offset from the inner wheel, which drives continuous rotation. This device has the potential to generate electricity from geothermal water well below boiling.

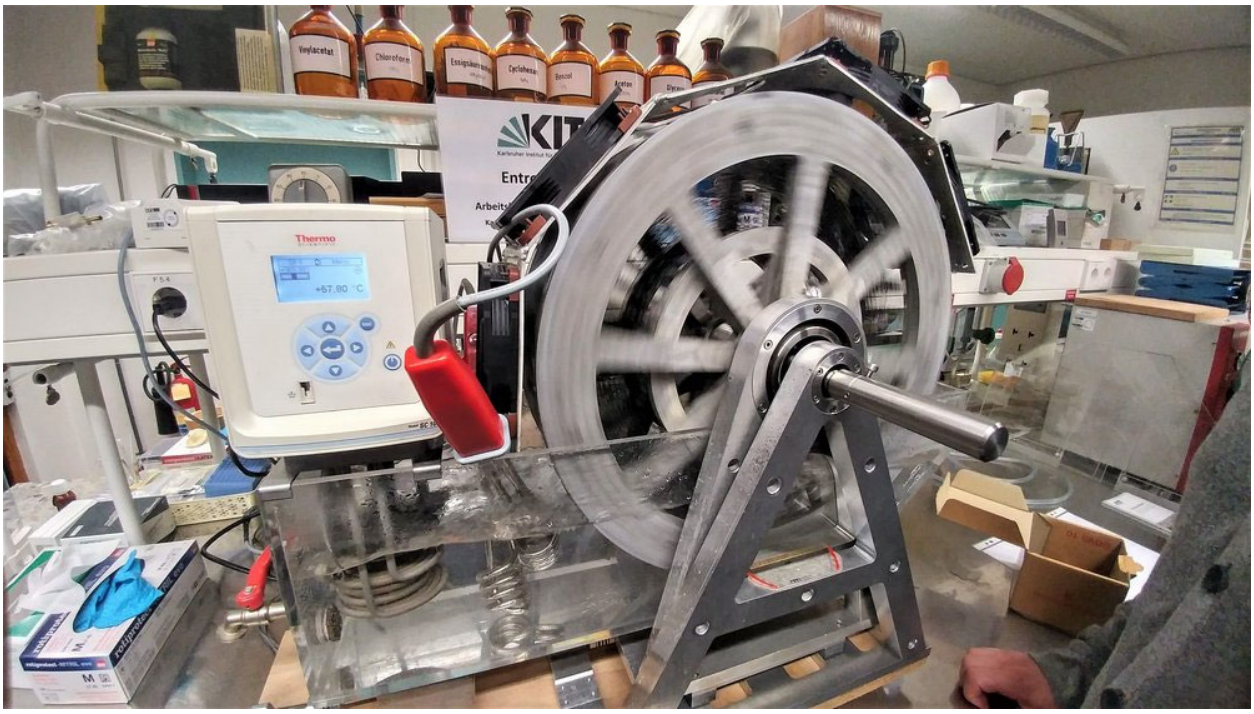

Figure A.39. Entropy wheel at KIT. In this image the wheel is rotating clockwise. The axis of the outer wheel is offset above and to the right of the inner wheel, driving continuous rotation. Note that the water temperature is <60˚C!

My next stop was in the city of Munich, which is located in the southeast corner of Germany, in the state of Bavaria. Munich is located north of the Alps, and sits atop the Molasse Basin, which is comparable in many ways to the Western Canada Sedimentary Basin east of the Rockies. During and following the rise

of the Alps in the late Cretaceous to Eocene, up to 6 km of sediments eroded from the mountains were deposited in this basin. In geology, the term “molasse basin” is often broadly applied to a sedimentary basin comprised of mostly terrestrial or shallow-marine river deposits of sandstone and conglomerate shed from a rising mountain range, with the Alpine Molasse Basin being the reference case.

Before the development of the Alps, the area was covered by the shallow northern extent of the Tethys Ocean, an ancient sea that separated the supercontinents of Laurasia (now North America and most of Eurasia) and Gondwana (now South America, Africa, India, Australia…). In the late Jurassic (~150 million years ago) a carbonate reef system now known as the Malm Formation covered the sea floor, in places reaching up to 600 m thick. Now deeply buried beneath the Molasse Basin, this geological unit makes for an excellent aquifer, as it has good natural porosity which has been enhanced by the dolomitization process, in which Calcium atoms are replaced with Magnesium, resulting in shrinking of the crystal structure and increase in void space. Below Munich the temperature of groundwater in the Malm exceeds boiling, and only increases with depth to the south.

From a sedimentological point of view, the Malm is much more complex than the figure below conveys. Throughout the history of the reef system, varying amounts of clastic sedimentation would have controlled the growth and connectedness of the reef. When sedimentation rate is higher, individual segments of the reef will be more isolated; when lower, the reef would expand laterally and become more connected. In terms of geothermal energy exploration it is preferable to find a large, well-connected part of the reservoir, simply because there is more hot water to access, and less chance of depletion. In general, the Malm is an excellent geothermal reservoir. It is highly permeable, laterally extensive, and has low mineral content, which means that corrosion and scaling is less of a concern when constructing power and heating plants.

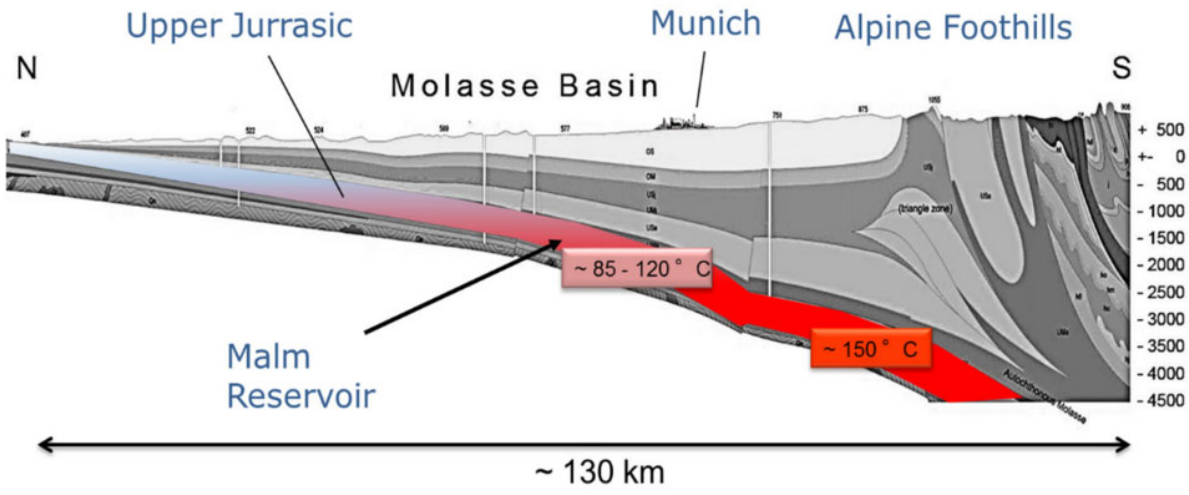

Figure A.40. Simplified cross-section of the Alpine foothills and foreland near Munich. The Jurassic Malm formation contains a significant volume of hot water, increasing in temperature to the south. Source: Farquharson et al. (2016).

Facing pressure to transition to renewable energy, Munich City Utilities (Stadwerke Munchen) and the municipalities in the surrounding region have been investing heavily in geothermal projects. Many of these cities and towns have historically used district distribution systems to carry hot water/steam heated in centralized gas plants to commercial and residential buildings for space heating. These systems can be adapted to carry geothermally-heated water, and Munich has set the ambitious goal of transitioning to 100% geothermal district heating by 2040, which they seem to be well on their way toward. Centralized district heating systems are rare in Canada, as many people heat their homes with individual gas or electric furnaces, or electric or water baseboard heaters. While the Western Canada Sedimentary Basin appears to possess similar hot water aquifers, a major challenge would be developing comparable district heating systems from scratch.

While in Munich, I was hosted by Erdwerk GmbH, a consulting company heavily involved in the exploration and development of many of the geothermal resources in the region. I learned a lot about the local geology from them, and had the opportunity to visit two geothermal sites under development. The first was an active drilling operation just outside the Munich city center, on the site of an operating gas-powered district heating plant (https://www.erdwerk.com/en/schaftlarnstrasse). They have drilled to a depth of ~3 km to access water at about ~100˚C, and plan to connect the new geothermal system into the existing gas-powered district heating system. Having never been on an active drill site before, this visit was very informative for me, as I learned a lot about the drilling process, how progress of the borehole is tracked from the surface, and how the well is tested for its productivity.

Figure A.41. The Schaftlarnstrasse geothermal drilling operation near the Munich city center. Electronics had to be turned off while on the drill rig, so this is the best photo I've got!

The second geothermal project I got a tour of was south of Munich in the town of Holzkirchen (https://www.erdwerk.com/en/holzkirchen). As can be seen in the cross section above, the temperature of the reservoir increases significantly to the south, but the reservoir also gets a lot deeper. The well itself reaches depths of ~5.1 km, making it the deepest in the Molasse Basin, and of its kind in Europe! Because of the higher temperatures, the Holzkirchen project will actually provide both hot water for district heating and a modest amount of electricity. I was fortunate enough to get a tour of the facility, which was a hive of activity as they prepared for its first test operation, which occurred in December.

Figure A.42. Cooling towers at Holzkirchen. Working fluid must be cooled to create a pressure differential to drive the turbines.

To round out my time in Munich I took a day trip by train to the Bavarian Alps, about an hour south of the city, accompanied by a few Erdwerk employees. Once above the valley fog, we were treated to stunning views of the front ranges. I was immediately struck by how geologically similar these mountains and associated foreland basin are to the front ranges of the Canadian Rockies, which I have spent a fair bit of time in. It certainly made me think that if they can do geothermal here, we can probably do it in Alberta.

Figure A.43. View northwest from Bischof peak in the Bavarian Prealps. Munich is in the distance on the right, hidden beneath the fog. The geology, morphology, and vegetation of these mountains were very reminiscent of the front ranges of the Canadian Rockies.

The final stop on my tour of Germany was at the GeoForschungZentrum (GFZ), a geological research institute in Potsdam, just outside of Berlin. Potsdam is located on the southern edge of the North German Basin (NGB), a large, deep (2-10 km), and complex basin with a protracted tectonic history spanning from the Permian to Cenozoic (330 million years ago to recent). The earliest origin of the basin is attributed to the downward flexure of the crust due to the Variscan orogeny, an ancient mountain building event that occurred in the Carboniferous Period (~330 million years ago). Following initial subsidence, the basin was affected by several phases of rifting and strike slip tectonics that caused many episodes of uplift and subsidence and the development of numerous sub-basins. Compressive stress from the Alpine orogeny in the Cretaceous (150-60 mya) caused widespread uplift of the basin. Complicating matters is a 250 million year old layer of evaporite (salt), which has significantly deformed overlying layers via salt-tectonic processes.

The NGB has a lot of potential for geothermal development, but is considered to be underutilized. Much of the geothermal resource is considered to be “petrothermal” as opposed to “hydrothermal”, which means that hydraulic fracking or shearing is required to create a geothermal reservoir in the otherwise impermeable hot rock. This type of geothermal project is known as an Enhanced Geothermal System (EGS), and I wrote a little about it in my previous blog post. A large part of the work conducted by the

geothermal group at the GFZ is focused on improving reservoir stimulation methods, and a key factor in this is constraining the mechanical properties of rocks, for which they have a large laboratory. Understanding the stress state at which a rock will shear or fracture is critical in engineering a geothermal reservoir, in which a balance must be struck between too little and too much connectivity between the injection and production well; too little and the water won't flow, too much and it will flow too fast to heat up sufficiently.

Figure A.44. Rock Mechanics Test System at the GFZ, used for determining behaviour of potential geothermal reservoir rock under stress.

The expertise of my hosts at the GFZ lay in understanding the thermal properties of the lithosphere, including thermal conductivity of rock and the resulting heat flow. Understanding these factors is critical in assessing the amount of geothermal energy in a potential reservoir. Thermal properties of individual minerals are well known, but in a rock comprised of numerous minerals, the bulk thermal conductivity reflects a mix of conductivities, and therefore must be measured directly. Typically, thermal conductivity is measured directly by applying heat to a solid rock sample, via various methods, and measuring its response in a transient (while heating) or steady (once heated) state. Researchers at GFZ have tested a new approach wherein thermal conductivity of plutonic rocks is estimated based on the relative percentages of minerals present in a rock sample, and have shown that the results are consistent with traditional methods (see Fuchs et al., 2018). This method is exciting because it may allow for the

estimation of thermal properties even when only drill cuttings (chips and fragments) exist. It is far cheaper, and thus more common, to obtain drill cuttings rather than intact cores, so this method has the potential to improve understanding of the subsurface temperature field dramatically.

Another interesting area of research I learned about while at the GFZ, was the use of gas emissions as a geothermal exploration method. Researchers at the GFZ have demonstrated that elevated surface concentrations of carbon dioxide, hydrogen sulfide, radon, thoron, and gamma radiation correspond spatially to permeable fault zones through which geothermal fluids may also flow (see Jolie et al., 2015). Thus far, this has only been attempted in Nevada, where fault zones are known to be very active, and hot water and gas is very close to the surface. I would be curious to see if such a method would yield any noteworthy results in my thesis area in British Columbia.

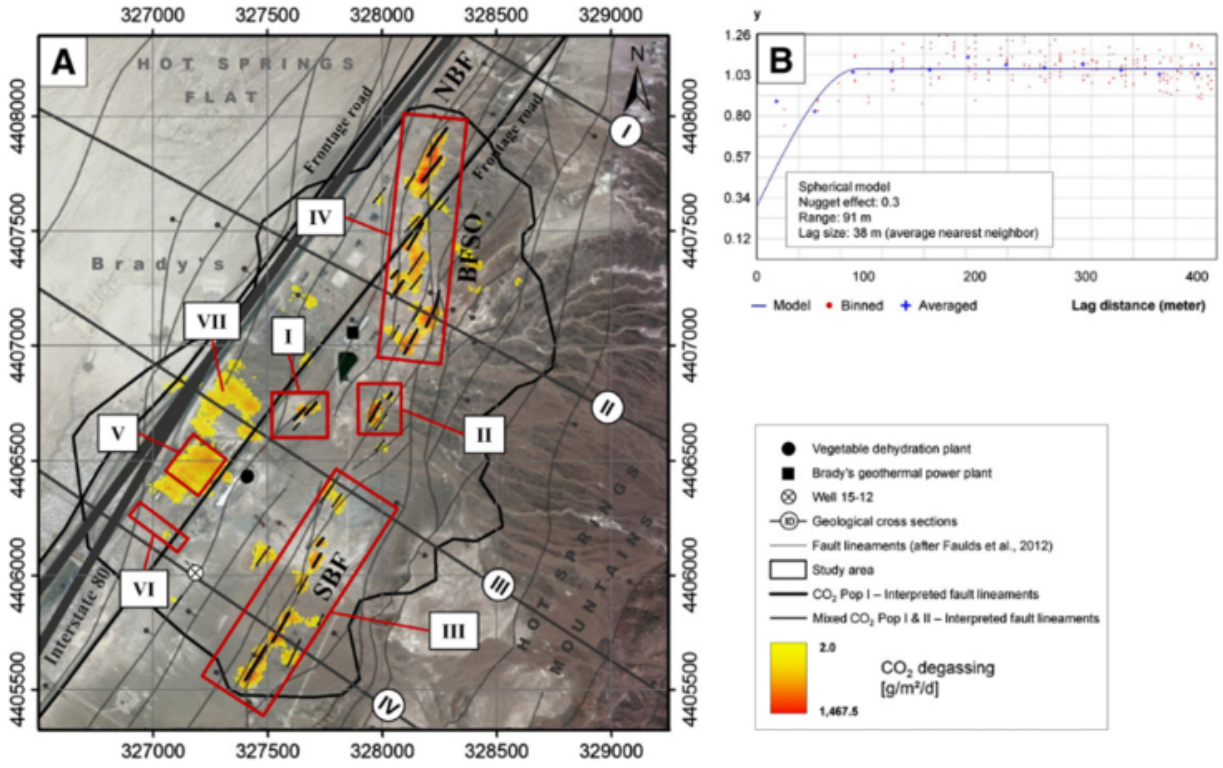

Figure A.45. Map of CO2 emissions near the Brady's geothermal system in Nevada. Note how closely the anomalies match mapped fault traces. Source: Jolie et al. (2015).

That wraps up my visit to Germany. Sincere thanks go to my hosts and everyone I met at KIT, Erdwerk, and GFZ! I am currently back in Edmonton, taking a break from travels before embarking on the final leg to New Zealand in March! More to come…

New Zealand: a natural lab for volcano-tectono-hydrothermal interactions (March 2019)

New Zealand, Aotearoa, has long been a place I've wanted to visit. It owes its incredible and diverse landscapes to a fascinating combination of tectonic and volcanic processes, and there is plenty to keep a geologist excited. Built on the mostly-submerged ancient continental crust of Zealandia, the present-day New Zealand rises above the ocean thanks to the collision between the Pacific and Australian tectonic plates. On the north island, the Pacific Plate dips westward beneath the Australian plate at the Hikurangi subduction zone off the east coast. At the southernmost end of the South Island, the polarity of the collision is reversed, and the Australian plate dips eastward beneath the Pacific Plate at the Puysegur Subduction Zone. It is the transition between eastward- and westward-dipping subduction that gives New Zealand some of its most unique geological features and geothermal resources. During my visit, I had the opportunity to explore nearly the entire length of the onshore plate boundary, from subduction zone to subduction zone, stopping along the way at the Taupo Volcanic Zone, Marlborough Fault System, and Alpine Fault. My visit was hosted by GNS Science, a government-owned research institute responsible for a wide range of geoscience research in New Zealand. In this blog I will share some of what I learned from these fantastic scientists.

North Island

As with many other subduction zones around the world, there is a chain of volcanoes on the North Island that runs parallel to the trench. At a certain depth, water is released from hydrous minerals the subducting plate, inducing partial melting of the mantle, which ultimately leads to volcanism. This particular volcanic chain is known as the Taupo Volcanic Zone, and includes famous volcanoes and calderas like Ruapehu, Ngauruhoe (Mt. Doom from LOTR), Tongariro, Taupo, and Okataina.

Figure A.46. Mt. Ruapehu, the southernmost volcano in the Taupo Volcanic Zone

Where the Hikurangi Subduction Zone merges with the Marlborough Fault System near Cook Strait, the subduction interface is locked (not slipping). To the north however, it becomes unlocked, and the subducting slab is rolling back (eastward) into the mantle. Because of this along-strike change in locking, the entire forearc region (area between the inland volcanic chain and the oceanic trench) is rotating clockwise around an axis in Cook Strait. The consequence of this rotation is crustal extension in the Australian Plate in an area known as the Taupo Rift, which begins near Mt. Ruapehu and widens towards the north to the Bay of Plenty. Offshore, rifting continues in the Kermadec-Tonga Trough. The Taupo Rift overlaps almost completely with the Taupo Volcanic Zone, making the Taupo Volcanic Zones a rare example of a rifted volcanic arc.

The combination of active volcanism (Taupo Volcanic Zone) and active crustal extension (Taupo Rift) creates the perfect setting for high enthalpy geothermal resources, as there is an abundance of heat in the shallow crust, and plenty of fracture permeability to allow the circulation of geothermal fluids. There are 23 high temperature geothermal fields in New Zealand, mostly centered around the touristy towns of Taupo and Rotorua. Some of these fields are preserved for their natural appeal, while others are host to power plants. Currently, geothermal energy contributes about 17% of the national electricity production,

with a capacity of just over 1000 MW. The majority (59%) of New Zealand's power comes from hydro dams, but 16% still comes from fossil fuels (coal, diesel, and natural gas). New Zealand's government has committed to have net zero emissions by 2050, and, geothermal energy may be part of the solution – but, doubling geothermal power output is no easy task, especially when many of the known fields are already developed.

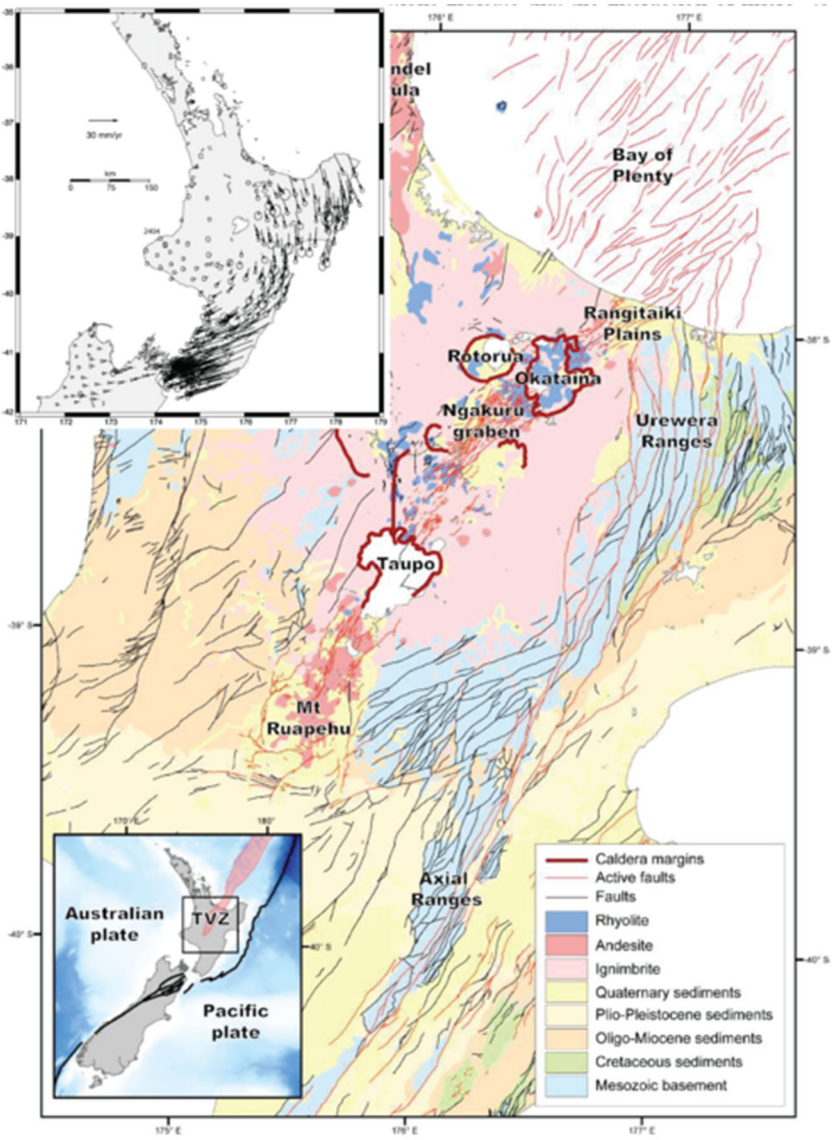

Figure A.47. Geologic map of the North Island, including the volcanoes and calderas of the Taupo Volcanic Zone, and extensional faults of the overlapping Taupo Rift (Villamor et al., 2017) . Upper left inset shows crustal velocities of the Pacific Plate relative to the Australian plate (Wallace et al., 2004). Note the clockwise rotation of the forearc, resulting in extension at the Taupo Rift, and transpression towards the south.

Figure A.48. The champagne pool at Wai-O-Tapu geothermal area near Rotorua. This is one of the 23 high-temperature geothermal areas on the North Island, but it is not used to generate electricity.

With most of the obvious geothermal fields already developed, researchers are looking towards more unconventional sources. There is considerable interest among scientists to explore the possibility of supercritical geothermal resources, much like those being explored in Iceland. Supercritical fluid (beyond the critical point of ~377°C and 217 atmospheres) contains about 10x more thermal energy than conventional fluids and would therefore be a massive power source if tapped into. The trick with exploring for supercritical fluids is to find a zone where the crust is still brittle, not molten. Iceland's first attempt at this ran into problems when they struck an unexpected zone of molten magma. Furthermore, for fluids to circulate, brittle fractures must exist, and these do not exist below the brittle-ductile transition.

An interesting direction of geothermal research in New Zealand seeks to determine what the natural life span of geothermal resources is. Geothermal resources are typically considered renewable, and if managed properly they can certainly produce energy for long periods of time. However, particularly in such a volcanically and tectonically active region as the Taupo Volcanic Zone/Taupo Rift, natural events such as earthquakes and volcanic eruptions can drastically change the "plumbing" of earth's crust. It is therefore important to understand the triggering mechanisms and recurrence intervals of these events not

only from a public safety point of view, but also from an economic one – i.e., would such an event mean the end of a geothermal system. Indeed, there is evidence for extinct geothermal systems in the form of fossil sinter (siliceous precipitate from old hot springs) hinting at the ephemeral nature of the geothermal upwellings.

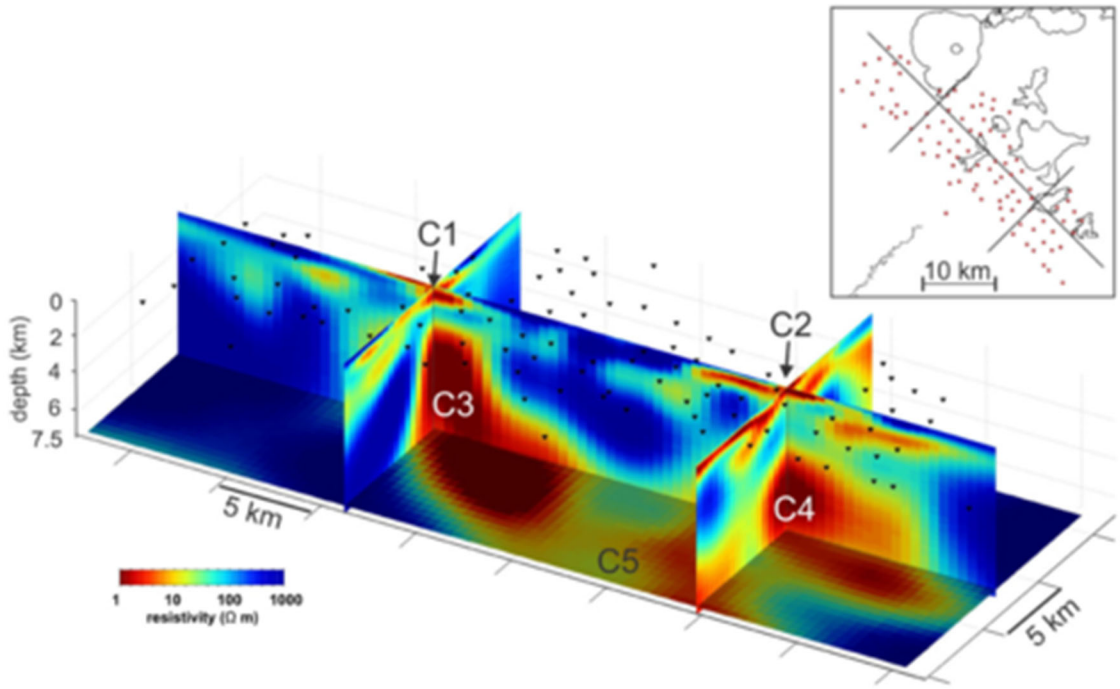

Figure A.49. Magnetotelluric resistivity model of the Taupo Volcanic Zone, showing the deep roots of the hydrothermal system (Heise et al., 2016). Models like this are useful for locating potential supercritical geothermal resources, as well as understanding the long term evolution of the earth's plumbing system.

My initial plan in New Zealand was to participate in the excavation of a paleoseismic trench in north end of the Taupo Rift, in search of evidence for the inter-relation between volcanism, tectonics, and hydrothermal systems. Sadly the trenching had to be postponed due to unforeseen issues with land use permissions, but I still learned a lot while in the area. Paleoseismic trenches are commonly used to establish the rupture history of young faults based on observed offsets in young, typically unconsolidated sedimentary layers. An excavator is used to dig a trench, several meters deep, and 10s of meters long across the surface trace of a known fault. The walls of the trench are mapped in detail and then graphics software is used to virtually restore each successive offset. In the Taupo Volcanic Zone, trenches can provide exceptionally detailed earthquake rupture histories thanks to a distinct and easily-dated succession of volcaniclastic deposits from past volcanic eruptions. Some trenches also include fossil

sinter layers, indicating past geothermal fluid up-flow. Thus, by reconstructing the relative timing of volcanic eruptions, faulting, and fluid flow, one can start to piece together a very detailed history, possibly showing whether tectonism triggered volcanism or vice versa, and if tectonism or volcanism triggered, blocked, or diverted hydrothermal fluid flow.

Figure A.50. An excellent cross-section of volcaniclastic strata exposed in a water pipeline corridor near Rotorua. Unfortunately there were no faults to investigate here - if there were, this would have made for a fantastic paleoseismic trench.

Of course, there are more complications to understanding the location of geothermal systems, number one being that topography also plays a large role in the location of upwellings – and this is something that is difficult to decipher in a paleoseismic trench. It has been shown in the Taupo Volcanic Zone, despite extremely high heat flow and subdued topographic relief, that geothermal upwellings are mostly found in topographic lows. This means that landscape evolution and erosion (which of course, are intimately tied to climate and tectonics), may play a role in the long term evolution of subsurface hydrothermal systems.

South Island

For many decades there has been interest in the possibility of developing lower-enthalpy geothermal resources on the South Island, which does not possess a high-enthalpy resource like the Taupo Volcanic Zone. Much like in western Canada, the Southern Alps have a number of thermal springs that are suggestive of a possible geothermal resource. These thermal springs are closely spatially associated with the hanging wall (eastern side) of the Alpine Fault.

Motion on the Alpine Fault is ~75% right-lateral and ~25% reverse (thrust), and over its ~25 million year life-span, the eastern side has shifted almost 460 km southward relative to the western side. This immense amount of displacement was first recognized thanks to a distinct belt of ultramafic rocks known as the Dun Mountain ophiolite, which were cut in two by the fault, and now outcrop on the west side of the fault near the town of Nelson, and on the east side way down south near Mt. Aspiring. The average strike-slip rate of the Alpine Fault is estimated to be ~20-30 mm/year, although it is currently locked and much of this strain will likely be released as a large earthquake in the future. The 25% of reverse slip on the Alpine Fault is responsible for the growth of the Southern Alps, which reach elevations as high as 3724 m at Mt. Cook. As the Pacific Plate is thrust skyward, erosion is outpaced by uplift, allowing the mountains to grow.

Uplift is so rapid in fact, that cooling isn't keeping pace with exhumation. This was confirmed recently as part of the Deep Fault Drilling Project (DFDP) conducted near the town of Whataroa. The primary aim of the DFDP was to observed the physical properties of the Alpine Fault and install an in-situ observatory to improve earthquake hazard monitoring. To everyone's surprise, they found extremely hot temperatures at shallow depths, with an astounding geothermal gradient of 130C/km! This discovery has re-stoked hopes that geothermal resources could be developed on the South Island.

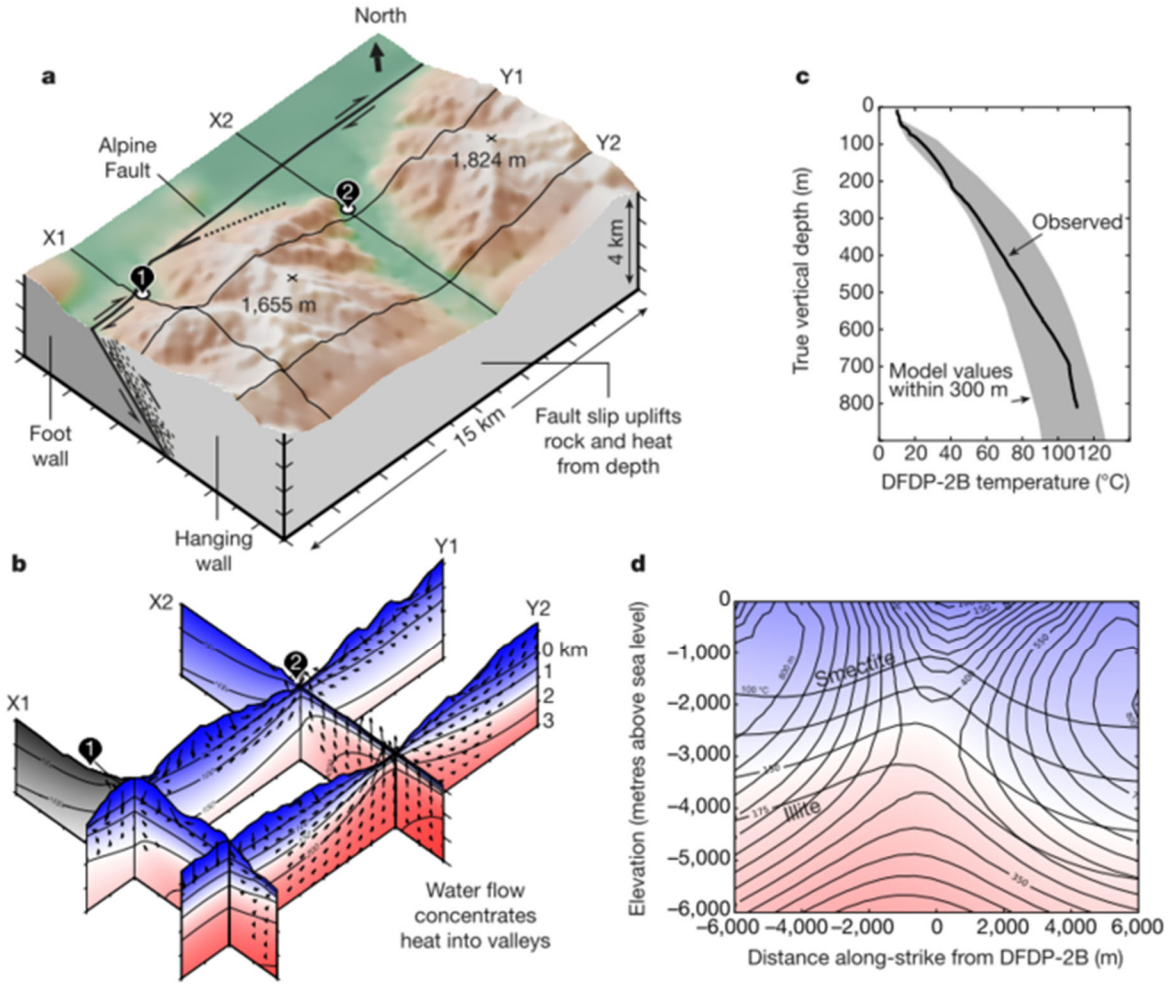

Figure A.51. a) Location map of DFDP-1 and DFDP-2 boreholes along the Alpine Fault near Whataroa. b) Temperature contours and fluid flow in the vicinity of the boreholes. c) temperature profile at DFDP-2, indicating a thermal gradient of ~130C/km. d) Fluid pressure and temperature on the Alpine Fault plane. (Sutherland et al., 2017).

Researchers have undertaken preliminary studies to learn more about the potential resources in this region. In doing so they have also found possible geothermal resources in the footwall (western side) of the Alpine Fault, which while not uplifting at the same rate, is undergoing active deformation. A set of anticlines and synclines in the vicinity of Greymouth are actively bending, and as a result, the geothermal gradient in the anticline cores are elevated. Targeted drilling on the peaks of these anticlinal structures may yield low-enthalpy geothermal resources suitable for direct use heating. Ironically, this sort of exploration strategy is very similar to old-school oil exploration, where the peaks of anticlines were targeted as structural traps of buoyant hydrocarbons. Historically, the economy of Greymouth and

surrounding towns on the west coast have been based on coal mining. Coal is still produced here and many homes and industrial facilities still use coal for heating. Naturally there is excitement among locals to develop direct use geothermal systems to replace coal heating.

The thermal springs in the Southern Alps share many similarities with the thermal springs in the Canadian Cordillera including similar outlet temperatures, maximum temperature estimates (from aqueous geothermometry), topographic relief, and climate. It is therefore tempting to wonder if similar resources exist in Canada. The main difference is the lack of major active uplift on a major fault structure like the Alpine Fault. The Canadian Cordillera is home to many large fault systems, however none are the main plate boundary fault, and none have been shown to have such active uplift rates. That said, GPS data is sparse in the Canadian Cordillera, as is thermochronological and borehole data. At this point I would say that it is too early to tell if a similar tectonically-induced geothermal anomaly might exist in Canada.

The discovery of a geothermal anomaly on the Alpine Fault could represent a whole new kind of geothermal resource, as of yet undeveloped worldwide. It certainly begs the question of whether other highly active transpressional fault systems have similar geothermal gradients. The Alaska Range, home to the rapidly rising Denali (formerly Mt. McKinley) comes to mind. I also wonder what the thermal regime might be in active compressional mountain belts like the Andes and Himalaya, though I suspect that the geometry of these systems may not be as conducive to high geothermal gradients as more vertical strike slip systems. These would make for some exciting research projects!

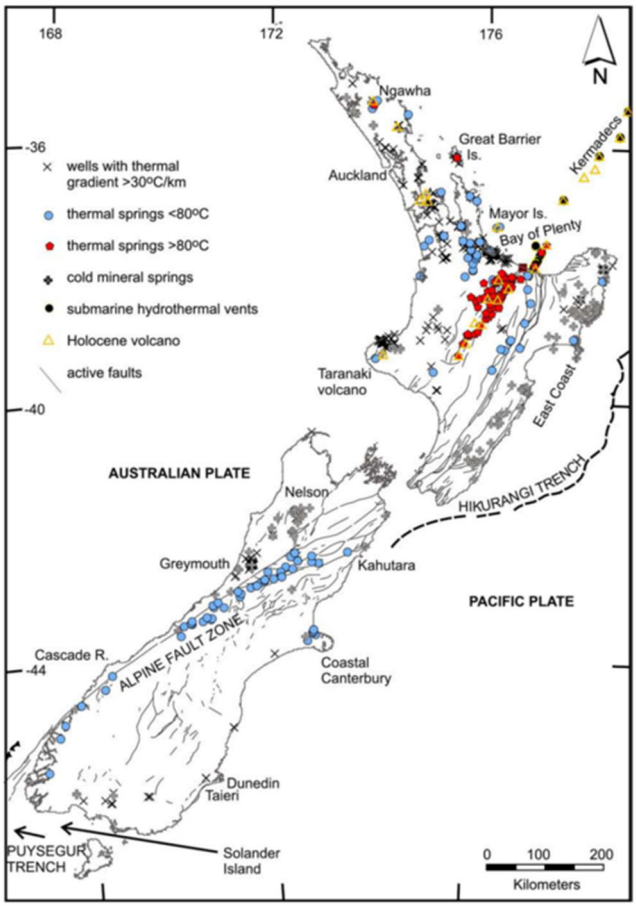

Figure A.52. Thermal and cold mineral springs, and wells with elevated thermal gradients in New Zealand (Reyes et al., 2010). Note the concentration of springs along the Alpine Fault, and the wells with elevated geothermal gradients near Greymouth.

Figure A.53. Looking east at New Zealand's Southern Alps near Fox Glacier. The Alpine Fault runs along the base of the mountains, which rise up to 3724 m at Mount Cook, here obscured by cloud. Rapid active uplift of these mountains has led to an elevated geothermal gradient on the eastern side.

Appendix B – Chapter 2 supplemental data

Table of kinematic indicators. Regions are abbreviated as follows: CRF = Columbia River fault, PTF = Purcell Trench fault, SLF = Slocan Lake fault, SRMT = Southern Rocky Mountain Trench, CR = Canoe Reach.

Region	*Station*	*Lat.*	*Long.*	*Group*	*Strike*	*Dip*	*Trend*	*Plunge*	*Error*	*Kinematics*	*Conf.*	*Notes*
CRF	TF18-199	50.5991	-117.8948	Albert Point	319	77	93	74	1.32	Normal	3	
CRF	TF18-200	50.5978	-117.9003	Albert Point	110	60	161	44	7.86	Sinistral-normal	3	
CRF	TF18-200	50.5977	-117.8999	Albert Point	300	73	60	66	4	Normal	3	
CRF	TF18-200	50.5978	-117.8997	Albert Point	155	84	82	84	11.73	Normal	3	
CRF	TF18-200	50.5978	-117.8995	Albert Point	174	86	190	32	11.32	Dextral	3	
CRF	TF18-201	50.5950	-117.9061	Albert Point	205	82	284	81	0.84	Normal	3	
CRF	TF18-201	50.5950	-117.9061	Albert Point	246	88	254	32	5.71	Sinistral	3	
CRF	TF18-201	50.5950	-117.9061	Albert Point	208	88	217	42	5.33	Sinistral	3	
CRF	TF18-202	50.5936	-117.9070	Albert Point	166	72	179	31	1.39	Sinistral	3	
CRF	TF18-202	50.5936	-117.9070	Albert Point	106	83	251	76	1.12	Normal	3	
CRF	TF18-202	50.5936	-117.9070	Albert Point	176	58	197	11	11.37	Sinistral	3	
CRF	TF18-202	50.5938	-117.9070	Albert Point	180	72	226	64	1.27	Sinistral-normal	3	
CRF	TF18-202	50.5942	-117.9064	Albert Point	138	82	313	32	0.03	Sinistral	3	
CRF	TF18-202	50.5944	-117.9064	Albert Point	170	67	193	41	0.87	Sinistral-normal	3	
CRF	TF18-203	50.5923	-117.9074	Albert Point	39	73	59	47	0.53	Sinistral-normal	3	
CRF	TF18-203	50.5923	-117.9076	Albert Point	39	75	43	18	0.91	Dextral	3	
CRF	TF18-204	50.5896	-117.9068	Albert Point	156	88	165	72	0.87	Normal	3	
CRF	TF18-205	50.5873	-117.9064	Albert Point	220	86	250	73	4.54	Normal	3	
CRF	TF18-205	50.5874	-117.9064	Albert Point	215	58	256	55	6.6	Normal	3	
CRF	TF18-205	50.5874	-117.9064	Albert Point	172	48	216	39	1.14	Normal	3	
CRF	TF18-205	50.5875	-117.9064	Albert Point	212	80	240	65	2.18	Normal	3	
CRF	TF18-206	50.5852	-117.9065	Albert Point	340	60	116	56	4.48	Normal	3	
CRF	TF18-206	50.5853	-117.9064	Albert Point	179	76	185	21	0.46	Sinistral	3	
CRF	TF18-206	50.5855	-117.9064	Albert Point	333	70	91	52	13.96	Normal	3	
CRF	TF18-206	50.5857	-117.9064	Albert Point	13	82	10	25	6.07	Sinistral	3	
CRF	TF18-207	50.5819	-117.9062	Albert Point	119	59	170	57	3.96	Normal	1	

CRF	TF18-207	50.5820	-117.9064	Albert Point	340	80	130	71	0.22	Reverse	3	
CRF	TF18-209	50.5776	-117.9042	Albert Point	10	25	25	25	16.49	Sinistral	3	
CRF	TF18-209	50.5777	-117.9041	Albert Point	186	80	220	70	1.44	Normal	3	Overprinted by dextral slickenlines
CRF	TF18-209	50.5777	-117.9041	Albert Point	186	80	3	38	3.8	Dextral	3	Overprint normal slickelines
CRF	TF18-209	50.5778	-117.9040	Albert Point	140	84	312	44	1.54	Dextral	3	
CRF	TF18-210	50.5744	-117.9044	Albert Point	313	82	29	75	6.56	Normal	3	
CRF	TF18-211	50.5736	-117.9017	Albert Point	184	65	243	61	0.4	Normal	3	
CRF	TF18-211	50.5736	-117.9017	Albert Point	180	58	249	52	4.01	Normal	3	
CRF	TF18-211	50.5737	-117.9018	Albert Point	174	57	231	44	7.33	Normal	3	
CRF	TF18-212	50.5659	-117.8949	Albert Point	339	42	94	37	2.13	Normal	3	
CRF	TF18-212	50.5660	-117.8951	Albert Point	0	55	156	30	0.1	Dextral	2	
CRF	TF18-212	50.5661	-117.8951	Albert Point	7	82	186	10	0.41	Dextral	3	
CRF	TF18-212	50.5663	-117.8949	Albert Point	201	60	240	42	4.04	Normal	3	
CRF	TF18-213	50.5552	-117.8961	Albert Point	170	86	171	15	0.07	Dextral	2	
CRF	TF18-213	50.5553	-117.8961	Albert Point	210	79	217	1	6.68	Dextral	2	
CRF	TF18-213	50.5554	-117.8961	Albert Point	192	61	8	31	11.38	Dextral	2	
CRF	TF18-213	50.5560	-117.8962	Albert Point	212	66	237	34	5.32	Sinistral	3	
CRF	TF18-213	50.5561	-117.8961	Albert Point	214	57	270	50	1.7	Normal	3	
CRF	TF18-213	50.5564	-117.8961	Albert Point	185	79	185	17	3.2	Sinistral	3	
CRF	TF18-213	50.5564	-117.8961	Albert Point	187	43	193	10	3.26	Sinistral	3	
CRF	TF18-213	50.5564	-117.8962	Albert Point	145	77	240	75	1.94	Normal	3	
CRF	TF18-214	50.5536	-117.8965	Albert Point	215	68	312	68	0.15	Normal	3	
CRF	TF18-214	50.5539	-117.8964	Albert Point	198	72	228	53	2.26	Normal	3	
CRF	TF18-215	50.5419	-117.9010	Albert Point	199	84	286	87	3	Normal	3	
CRF	TF18-224	50.3467	-118.0384	Arrow Park Lower	218	66	234	35	1.55	Sinistral	3	
CRF	TF18-224	50.3467	-118.0384	Arrow Park Lower	316	71	80	57	8.85	Normal	3	
CRF	TF18-224	50.3467	-118.0384	Arrow Park Lower	220	83	240	60	3.68	Normal	3	
CRF	TF18-224	50.3467	-118.0384	Arrow Park Lower	220	83	224	17	1.75	Sinistral	3	
CRF	TF18-224	50.3467	-118.0384	Arrow Park Lower	0	54	80	50	3.55	Normal	3	

CRF	TF18-224	50.3467	-118.0384	Arrow Park Lower	213	50	276	51	4.01	Normal	3	
CRF	TF18-224	50.3467	-118.0383	Arrow Park Lower	238	34	237	6	5.53	Sinistral	3	
CRF	TF18-224	50.3467	-118.0383	Arrow Park Lower	222	60	229	1	5.55	Sinistral	3	
CRF	TF18-224	50.3467	-118.0383	Arrow Park Lower	331	41	114	33	4.58	Dextral-normal	3	
CRF	TF18-224	50.3467	-118.0383	Arrow Park Lower	352	78	7	69	5.93	Normal	3	
CRF	TF18-224	50.3467	-118.0383	Arrow Park Lower	299	68	359	67	1.78	Normal	3	
CRF	TF18-224	50.3467	-118.0382	Arrow Park Lower	228	38	48	2	1.58	Sinistral	3	
CRF	TF18-239	50.3415	-118.0381	Arrow Park Upper North	4	85	181	49	1.81	Dextral-reverse	1	
CRF	TF18-239	50.3415	-118.0381	Arrow Park Upper North	204	83	221	33	10.2	Dextral	2	
CRF	TF18-239	50.3416	-118.0381	Arrow Park Upper North	210	80	243	38	18.41	Dextral	2	
CRF	TF18-239	50.3416	-118.0380	Arrow Park Upper North	228	86	230	49	1.71	Dextral	2	
CRF	TF18-239	50.3416	-118.0379	Arrow Park Upper North	201	79	230	61	3.66	Dextral-reverse	3	
CRF	TF18-240	50.3407	-118.0392	Arrow Park Upper South	305	40	50	38	1.01	Reverse	3	
CRF	TF18-240	50.3410	-118.0388	Arrow Park Upper South	94	81	178	55	25.8	Reverse	2	
CRF	TF18-241	50.3400	-118.0403	Arrow Park Upper South	153	67	303	40	5.82	Dextral-normal	3	
CRF	TF18-241	50.3401	-118.0402	Arrow Park Upper South	150	48	305	42	12.38	Dextral-normal	3	
CRF	TF18-241	50.3401	-118.0402	Arrow Park Upper South	126	44	235	35	7.21	Reverse	3	Overprinted by dextral slickenlines
CRF	TF18-241	50.3401	-118.0402	Arrow Park Upper South	126	44	115	9	14.09	Dextral	3	Overprint reverse slickenlines
CRF	TF18-241	50.3401	-118.0401	Arrow Park Upper South	96	26	105	1	3.03	Dextral	3	
CRF	TF18-241	50.3402	-118.0401	Arrow Park Upper South	195	74	20	1	5.08	Dextral	3	
CRF	TF18-241	50.3403	-118.0400	Arrow Park Upper South	38	45	47	12	2.22	Dextral	3	
CRF	TF18-170	51.9020	-118.5640	Birch Ck.	30	86	210	60	3.46	Sinistral-normal	3	
CRF	TF18-170	51.9025	-118.5635	Birch Ck.	199	79	215	57	0.73	Sinistral-normal	3	
CRF	TF18-170	51.9033	-118.5631	Birch Ck.	55	53	88	30	4.35	Normal	3	

CRF	TF18-170	51.9034	-118.5631	Birch Ck.	75	70	198	57	8.19	Reverse	3
CRF	TF18-354	49.9163	-117.8935	Burton Ck.	212	50	237	26	0.53	Dextral	3
CRF	TF18-354	49.9161	-117.8936	Burton Ck.	232	62	245	33	5.11	Dextral	3
CRF	TF18-353	50.0649	-117.9095	Burton North	159	60	324	24	0.08	Dextral	3
CRF	TF18-356	49.7799	-118.1364	Edgewood	355	79	44	78	1.87	Reverse	2
CRF	TF18-356	49.7801	-118.1368	Edgewood	349	79	81	46	32.97	Reverse	2
CRF	TF18-357	49.7843	-118.1399	Edgewood	172	88	180	60	2.25	Sinistral-normal	2
CRF	TF18-357	49.7844	-118.1399	Edgewood	196	68	229	67	8.48	Sinistral-normal	2
CRF	TF18-358	49.7908	-118.1402	Edgewood	5	65	151	54	2.52	Dextral-normal	3
CRF	TF18-358	49.7908	-118.1403	Edgewood	324	75	93	64	5.53	Dextral-normal	3
CRF	TF18-358	49.7909	-118.1403	Edgewood	190	89	11	69	1.29	Dextral-normal	3
CRF	TF18-358	49.7909	-118.1404	Edgewood	311	68	345	55	0.54	Normal	3
CRF	TF18-358	49.7910	-118.1404	Edgewood	163	87	341	24	0.6	Dextral	3
CRF	TF18-358	49.7910	-118.1404	Edgewood	328	70	105	59	2.11	Dextral-normal	3
CRF	TF18-358	49.7911	-118.1405	Edgewood	170	89	165	57	3.56	Dextral-reverse	3
CRF	TF18-358	49.7911	-118.1405	Edgewood	166	90	343	4	2.99	Dextral	3
CRF	TF18-358	49.7912	-118.1405	Edgewood	173	43	316	36	5.61	Dextral-normal	3
CRF	TF18-358	49.7914	-118.1405	Edgewood	202	52	274	51	0.39	Normal	3
CRF	TF18-358	49.7915	-118.1405	Edgewood	345	75	35	73	1.79	Reverse	3
CRF	TF18-220	50.5329	-117.8903	Halcyon Mountain	34	69	42	18	0.74	Sinistral	3
CRF	TF18-220	50.5330	-117.8903	Halcyon Mountain	199	57	292	50	6.96	Normal	3
CRF	TF18-220	50.5330	-117.8903	Halcyon Mountain	225	78	46	9	2.83	Sinistral	3
CRF	TF18-220	50.5330	-117.8903	Halcyon Mountain	196	65	3	20	2.7	Dextral	3
CRF	TF18-220	50.5330	-117.8904	Halcyon Mountain	222	59	27	34	5.97	Sinistral	3
CRF	TF18-220	50.5330	-117.8904	Halcyon Mountain	9	77	2	25	11.69	Sinistral	3
CRF	TF18-220	50.5330	-117.8904	Halcyon Mountain	193	83	308	74	7.52	Normal	3
CRF	TF18-220	50.5331	-117.8904	Halcyon Mountain	189	61	306	60	1.73	Normal	3
CRF	TF18-220	50.5331	-117.8904	Halcyon Mountain	209	57	307	54	2.72	Normal	3

CRF	TF18-220	50.5335	-117.8904	Halcyon Mountain	192	63	307	57	3.39	Normal	3	
CRF	TF18-220	50.5335	-117.8905	Halcyon Mountain	227	43	293	40	0.41	Normal	3	
CRF	TF18-218	50.5209	-117.8994	Halcyon Point	354	87	350	18	4.73	Dextral	3	
CRF	TF18-218	50.5212	-117.8995	Halcyon Point	0	80	175	2	4.57	Dextral	3	
CRF	TF18-218	50.5214	-117.8996	Halcyon Point	232	85	346	66	16.89	Reverse	3	
CRF	TF18-218	50.5216	-117.8997	Halcyon Point	215	82	245	75	0.36	Normal	3	
CRF	TF18-218	50.5217	-117.8997	Halcyon Point	221	76	229	10	5.22	Dextral	3	
CRF	TF18-218	50.5217	-117.8997	Halcyon Point	218	64	221	10	1.71	Dextral	3	Large fault, with 1m wide damage zone
CRF	TF18-218	50.5216	-117.8999	Halcyon Point	53	89	235	11	2.15	Dextral	3	Large fault, with 1m wide damage zone
CRF	TF18-218	50.5215	-117.8997	Halcyon Point	185	76	~	~		No Indicators	1	
CRF	TF18-218	50.5217	-117.9000	Halcyon Point	171	79	~	~		No Indicators	1	
CRF	TF18-218	50.5217	-117.9000	Halcyon Point	169	69	325	50	1.74	Sinistral-reverse	3	
CRF	TF18-218	50.5217	-117.9000	Halcyon Point	169	69	190	34	4.41	Dextral-reverse	3	
CRF	TF18-218	50.5218	-117.9001	Halcyon Point	135	76	~	~		No Indicators	1	
CRF	TF18-218	50.5219	-117.9001	Halcyon Point	307	84	~	~		No Indicators	1	
CRF	TF18-218	50.5219	-117.8999	Halcyon Point	344	30	48	30	2.51	Normal	3	
CRF	TF18-218	50.5219	-117.8999	Halcyon Point	218	84	298	85	1.08	Reverse	3	
CRF	TF18-218	50.5220	-117.9000	Halcyon Point	184	67	~	~		No Indicators	1	
CRF	TF18-218	50.5222	-117.9001	Halcyon Point	182	59	344	28	0.45	Dextral-normal	3	
CRF	TF18-218	50.5222	-117.9003	Halcyon Point	155	75	324	38	0.81	Dextral-normal	3	
CRF	TF18-219	50.5212	-117.8997	Halcyon Point	357	84	174	5	2.45	Sinistral	3	
CRF	TF18-221	50.5066	-117.8995	Halcyon South	10	68	6	14	8.82	Sinistral	3	
CRF	TF18-221	50.5069	-117.8993	Halcyon South	26	81	21	5	5.7	Sinistral	3	

CRF	TF18-221	50.5072	-117.8989	Halcyon South	357	87	354	12	3.55	Sinistral	3
CRF	TF18-151	51.2082	-118.2026	Hathaway Ck.	167	77	330	44	2.79	Sinistral-reverse	3
CRF	TF18-190	50.6933	-117.7625	Hill Ck.	245	53	245	54	29.14	Sinistral-normal	3
CRF	TF18-191	50.6917	-117.7722	Hill Ck.	330	60	123	37	0.75	Dextral	3
CRF	TF19-052	50.2841	-117.7376	Kuskanax South	186	81	222	80	3.05	Dextral-normal	1
CRF	TF19-052	50.2841	-117.7372	Kuskanax South	203	73	208	33	5.13	Dextral-reverse	3
CRF	TF19-052	50.2841	-117.7369	Kuskanax South	192	70	13	90	20	Dextral-reverse	1
CRF	TF19-052	50.2841	-117.7367	Kuskanax South	20	82	190	69	3.92	Dextral-normal	3
CRF	TF19-052	50.2842	-117.7364	Kuskanax South	55	45	198	47	13.12	Ambiguous	1
CRF	TF19-052	50.2849	-117.7343	Kuskanax South	20	90	202	50	1.29	Dextral-normal	3
CRF	TF19-053	50.2950	-117.7051	Kuskanax South	25	81	43	31	10.43	Ambiguous	1
CRF	TF19-053	50.2951	-117.7047	Kuskanax South	348	55	55	52	0.7	Ambiguous	1
CRF	TF18-168	52.0127	-118.5673	Mica Ck.	355	60	174	19	8.54	Dextral	3
CRF	TF18-168	52.0129	-118.5672	Mica Ck.	135	77	130	6	6.2	Dextral	3
CRF	TF18-168	52.0134	-118.5673	Mica Ck.	35	62	55	31	0.98	Sinistral	3
CRF	TF18-168	52.0135	-118.5674	Mica Ck.	2	84	169	32	7.72	Dextral	3
CRF	TF18-153	52.0797	-118.5587	Mica Dam	218	70	315	70	0.14	Normal	3
CRF	TF18-153	52.0798	-118.5587	Mica Dam	140	46	188	39	1.24	Normal	3
CRF	TF18-154	52.0927	-118.5263	Mica Dam	222	58	342	50	3.79	Normal	2
CRF	TF18-155	52.0997	-118.5071	Mica Dam	91	83	165	80	2.62	Normal	2
CRF	TF18-166	52.0707	-118.5591	Mica Dam	229	39	315	43	4.06	Normal	3
CRF	TF18-166	52.0707	-118.5592	Mica Dam	43	49	101	34	9.42	Normal	3
CRF	TF18-166	52.0709	-118.5591	Mica Dam	235	41	329	41	0.07	Normal	3
CRF	TF18-166	52.0709	-118.5591	Mica Dam	54	24	115	25	3.65	Normal	3
CRF	TF18-166	52.0710	-118.5591	Mica Dam	60	41	120	48	10.41	Normal	3
CRF	TF18-166	52.0711	-118.5592	Mica Dam	243	42	324	39	2.63	Normal	2
CRF	TF18-167	52.0486	-118.5918	Nagle Ck.	60	82	65	29	0.46	Sinistral	3
CRF	TF18-167	52.0489	-118.5916	Nagle Ck.	0	81	175	4	4.3	Dextral	3

CRF	TF18-176	51.3888	-118.4210	Northcap Rec Site	162	55	191	37	1.61	Normal	3	
CRF	TF18-176	51.3884	-118.4206	Northcap Rec Site	144	38	195	34	2.52	Normal	3	
CRF	TF18-169	51.9696	-118.5596	Pitt Ck.	13	88	193	45	1.41	Sinistral	3	
CRF	TF18-169	51.9709	-118.5600	Pitt Ck.	190	89	192	2	1.96	Sinistral	2	
CRF	TF18-169	51.9712	-118.5600	Pitt Ck.	197	82	194	27	6.28	Sinistral	3	
CRF	TF18-150	51.0484	-118.1902	Revelstoke Dam	240	88	248	44	4.35	Dextral	3	Large, 50cm gouge zone reinforced with rebar
CRF	TF18-150	51.0485	-118.1902	Revelstoke Dam	205	72	260	68	0.31	Normal	3	
CRF	TF18-150	51.0487	-118.1900	Revelstoke Dam	60	58	180	67	11.59	Normal	3	
CRF	TF18-150	51.0490	-118.1898	Revelstoke Dam	188	65	296	58	5.64	Normal	3	
CRF	TF18-150	51.0491	-118.1895	Revelstoke Dam	110	44	248	46	11.22	Normal	3	
CRF	TF19-037	50.2914	-117.9109	Saddle Mountain	175	70	192	45	2.73	Sinistral-normal	3	
CRF	TF19-039	50.2869	-117.9244	Saddle Mountain	280	67	86	20	4.34	Dextral	3	
CRF	TF19-040	50.2897	-117.9332	Saddle Mountain	298	49	91	19	6.34	Dextral	2	
CRF	TF19-040	50.2896	-117.9330	Saddle Mountain	288	47	95	14	0.31	Dextral	2	
CRF	TF19-040	50.2896	-117.9329	Saddle Mountain	294	60	105	18	1.47	Dextral	2	
CRF	TF19-044	50.2923	-117.9371	Saddle Mountain	268	52	0	50	1.98	Reverse	3	Major gouge zone. Slip vector based on folds in the footwall
CRF	TF19-044	50.2911	-117.9375	Saddle Mountain	235	70	242	24	1.98	Dextral	3	
CRF	TF18-179	50.6324	-117.9373	Shelter Bay	357	85	185	2	8.14	Dextral	3	Large fault with gouge zone
CRF	TF18-179	50.6324	-117.9372	Shelter Bay	40	88	219	72	1.59	Reverse	2	
CRF	TF18-179	50.6324	-117.9371	Shelter Bay	216	67	281	69	3.77	Normal	3	
CRF	TF18-179	50.6324	-117.9369	Shelter Bay	49	54	231	2	2.79	Sinistral	3	
CRF	TF18-179	50.6327	-117.9360	Shelter Bay	29	60	50	45	7.71	Sinistral	3	
CRF	TF18-178	50.6873	-117.9758	Shelter Bay North	312	80	355	70	3.82	Normal	3	
CRF	TF18-178	50.6873	-117.9758	Shelter Bay North	220	72	218	12	5.55	Dextral	3	
CRF	TF18-178	50.6873	-117.9758	Shelter Bay North	314	80	341	71	1.07	Reverse	2	

CRF	TF18-178	50.6874	-117.9759	Shelter Bay North	329	62	42	58	2.83	Normal	3	
CRF	TF18-178	50.6876	-117.9761	Shelter Bay North	335	52	45	50	0.25	Normal	3	
CRF	TF18-178	50.6876	-117.9761	Shelter Bay North	50	84	212	50	6.75	Sinistral-reverse	3	
CRF	TF18-178	50.6876	-117.9762	Shelter Bay North	306	64	41	61	2.9	Normal	3	
CRF	TF18-178	50.6877	-117.9762	Shelter Bay North	178	65	268	62	3	Normal	3	Crosscut by dextral fault
CRF	TF18-178	50.6877	-117.9762	Shelter Bay North	178	65	168	20	17	Dextral	3	Crosscuts normal fault
CRF	TF18-178	50.6877	-117.9762	Shelter Bay North	55	80	238	5	3.81	Sinistral	3	
CRF	TF18-178	50.6877	-117.9762	Shelter Bay North	233	79	231	21	5.76	Sinistral	3	
CRF	TF18-178	50.6878	-117.9764	Shelter Bay North	220	88	218	47	2.83	Sinistral	3	
CRF	TF18-178	50.6879	-117.9765	Shelter Bay North	48	88	225	36	1.25	Sinistral	3	Crosscuts normal fault
CRF	TF18-180	50.6149	-117.9428	Shelter Bay South	44	86	227	29	4.56	Dextral	2	
CRF	TF18-181	50.5974	-117.9535	Shelter Bay South	345	72	358	32	1.01	Dextral	3	
CRF	TF18-181	50.5973	-117.9535	Shelter Bay South	74	61	68	8	9.09	Sinistral	3	
CRF	TF18-181	50.5973	-117.9537	Shelter Bay South	96	80	166	82	2.47	Reverse	3	
CRF	TF18-182	50.5909	-117.9518	Shelter Bay South	342	88	157	34	3.02	Dextral	3	
CRF	TF18-182	50.5907	-117.9520	Shelter Bay South	181	86	180	34	3.06	Dextral	3	
CRF	TF18-183	50.5858	-117.9544	Shelter Bay South	184	55	204	39	8.23	Sinistral	3	
CRF	TF18-184	50.6536	-117.9879	Shelter Bay West	355	48	107	40	5.61	Normal	3	
CRF	TF18-185	50.6529	-117.9989	Shelter Bay West	346	38	76	38	0	Normal	3	
CRF	TF18-187	50.6294	-117.9859	Shelter Bay West	355	41	138	26	1.38	Normal	3	
CRF	TF18-187	50.6298	-117.9872	Shelter Bay West	315	34	66	26	6.07	Normal	3	
CRF	TF18-159	52.0998	-118.4795	Sprague Bay	111	66	134	70	15.08	Normal	3	
CRF	TF18-159	52.0998	-118.4795	Sprague Bay	111	66	281	21	0.13	Normal	3	
CRF	TF18-159	52.0998	-118.4794	Sprague Bay	116	67	220	65	1.34	Normal	3	

CRF	TF18-188	50.6793	-117.8467	Storm Pt.	29	50	180	28	1.5	Dextral-normal	3	
CRF	TF18-188	50.6793	-117.8467	Storm Pt.	29	50	144	46	1.14	Normal	3	
CRF	TF18-188	50.6793	-117.8467	Storm Pt.	50	49	124	50	2.08	Normal	3	
CRF	TF18-188	50.6793	-117.8467	Storm Pt.	57	62	229	8	3.23	Sinistral	3	
CRF	TF18-188	50.6793	-117.8468	Storm Pt.	5	89	195	40	8.29	Sinistral-normal	3	
CRF	TF18-188	50.6792	-117.8468	Storm Pt.	62	48	104	38	1.15	Sinistral-normal	3	
CRF	TF18-188	50.6792	-117.8469	Storm Pt.	64	59	77	25	2.46	Sinistral-normal	3	
CRF	TF18-188	50.6791	-117.8471	Storm Pt.	59	58	85	45	6.42	Sinistral-normal	3	
CRF	TF18-189	50.6806	-117.8349	Storm Pt.	55	61	168	48	10.28	Normal	1	
CRF	TF18-189	50.6806	-117.8350	Storm Pt.	64	54	75	18	2	Sinistral	3	
CRF	TF18-189	50.6806	-117.8352	Storm Pt.	71	48	92	21	0.51	Sinistral	3	
CRF	TF18-189	50.6806	-117.8353	Storm Pt.	66	51	80	14	1.73	Sinistral	3	
CRF	TF18-189	50.6806	-117.8355	Storm Pt.	69	47	75	7	0.41	Sinistral	3	
CRF	TF18-189	50.6806	-117.8361	Storm Pt.	66	72	225	41	3.12	Dextral	3	
CRF	TF18-189	50.6806	-117.8366	Storm Pt.	60	58	199	52	4.3	Sinistral-normal	3	
CRF	TF18-360	49.8913	-118.1227	Whatshan South	356	76	10	35	3.07	Dextral	3	
CRF	TF18-360	49.8910	-118.1226	Whatshan South	164	69	275	68	0.33	Normal	3	
CRF	TF18-360	49.8909	-118.1225	Whatshan South	354	70	5	32	1.67	Dextral	3	
CRF	TF18-361	49.8860	-118.1208	Whatshan South	186	88	2	28	2.59	Dextral	3	Large, cuts across entire outcrop
CRF	TF18-361	49.8849	-118.1197	Whatshan South	334	76	158	8	5.78	Dextral	3	
CRF	TF18-361	49.8848	-118.1196	Whatshan South	339	76	141	50	0.42	Dextral	3	
CRF	TF18-362	49.8739	-118.1038	Whatshan South	173	74	182	45	5.08	Dextral	3	
CRF	TF19-048	49.9008	-118.1230	Whatshan South	208	89	28	7	0.12	Dextral	2	
PTF	TF18-297	49.7391	-116.9113	Ainsworth	357	60	11	20	1.48	Sinistral	3	Large fault plane, 10cm wide brecciated zone
PTF	TF18-297	49.7392	-116.9114	Ainsworth	350	58	1	18	0.56	Sinistral	3	Large fault plane, 10cm wide brecciated zone
PTF	TF18-297	49.7392	-116.9114	Ainsworth	350	58	77	66	8.03	Normal	3	Large fault plane, 10cm wide brecciated zone. Overprints sinistral slickenlines.
PTF	TF18-297	49.7398	-116.9115	Ainsworth	155	46	221	44	0.56	Normal	3	

PTF	TF18-297	49.7401	-116.9116	Ainsworth	145	73	184	69	3.28	Normal	2	
PTF	TF18-298	49.7427	-116.9132	Ainsworth	5	62	60	64	6.02	Normal	3	1m-wide brecciated zone
PTF	TF18-298	49.7432	-116.9133	Ainsworth	166	56	151	10	17.96	Sinistral	3	Wide 20mx20m fault plane exposed
PTF	TF18-277	49.4284	-116.7553	Akokli Ck.	187	54	263	52	1.15	Normal	3	
PTF	TF18-277	49.4284	-116.7553	Akokli Ck.	285	33	289	29	21.92	Dextral	2	
PTF	TF18-312	50.1845	-116.9282	Argenta	165	89	175	62	3.79	Dextral	3	
PTF	TF18-313	50.1565	-116.9197	Argenta	174	63	171	5	4.93	Dextral	3	
PTF	TF18-314	50.1550	-116.9199	Argenta	349	68	159	5	7.34	Dextral	3	
PTF	TF18-314	50.1550	-116.9199	Argenta	334	72	155	16	5.8	Dextral	3	
PTF	TF18-315	50.1535	-116.9195	Argenta	345	78	353	2	7.4	Dextral	3	
PTF	TF18-284	49.8703	-116.8574	Bernard Ck. Gp. 1	345	70	167	50	16.44	Dextral	2	
PTF	TF18-284	49.8704	-116.8575	Bernard Ck. Gp. 1	191	89	184	40	6	Dextral	3	
PTF	TF18-284	49.8705	-116.8576	Bernard Ck. Gp. 1	60	84	65	31	1.17	Sinistral	3	
PTF	TF18-284	49.8705	-116.8576	Bernard Ck. Gp. 1	265	50	~	~		No Indicators	1	
PTF	TF18-284	49.8712	-116.8576	Bernard Ck. Gp. 1	152	87	337	58	5.19	Dextral	3	
PTF	TF18-284	49.8713	-116.8577	Bernard Ck. Gp. 1	268	31	269	2	1.2	Sinistral	3	
PTF	TF18-284	49.8714	-116.8579	Bernard Ck. Gp. 1	150	85	332	8	2.67	Dextral	3	
PTF	TF18-284	49.8718	-116.8578	Bernard Ck. Gp. 1	266	30	89	1	2.37	Sinistral	3	
PTF	TF18-284	49.8722	-116.8577	Bernard Ck. Gp. 1	170	53	245	53	0.94	Normal	3	
PTF	TF18-284	49.8723	-116.8577	Bernard Ck. Gp. 1	196	78	231	67	1.59	Normal	3	
PTF	TF18-284	49.8723	-116.8577	Bernard Ck. Gp. 1	163	85	194	74	3.3	Normal	3	
PTF	TF18-285	49.8727	-116.8577	Bernard Ck. Gp. 1	175	89	181	31	4.62	Dextral	3	
PTF	TF18-285	49.8728	-116.8577	Bernard Ck. Gp. 1	329	21	325	1	2.37	Sinistral	3	4cm offset of pegmatite dyke
PTF	TF18-285	49.8728	-116.8577	Bernard Ck. Gp. 1	254	35	297	20	5.02	Sinistral	3	
PTF	TF18-285	49.8728	-116.8577	Bernard Ck. Gp. 1	216	86	214	16	3.02	Sinistral	3	
PTF	TF18-292	49.8761	-116.8564	Bernard Ck. Gp. 2	49	79	68	64	1.8	Sinistral-normal	3	

PTF	TF18-292	49.8762	-116.8564	Bernard Ck. Gp. 2	62	74	85	45	4.05	Sinistral-normal	3	
PTF	TF18-292	49.8763	-116.8564	Bernard Ck. Gp. 2	58	70	98	56	3.11	Sinistral-normal	3	
PTF	TF18-292	49.8764	-116.8563	Bernard Ck. Gp. 2	60	58	109	62	9.64	Normal	3	
PTF	TF18-292	49.8765	-116.8563	Bernard Ck. Gp. 2	2	80	15	59	1.99	Sinistral	3	
PTF	TF18-292	49.8765	-116.8563	Bernard Ck. Gp. 2	83	75	95	41	1.04	Sinistral-normal	3	
PTF	TF18-292	49.8766	-116.8563	Bernard Ck. Gp. 2	190	80	200	26	4.45	Sinistral	3	
PTF	TF18-292	49.8766	-116.8562	Bernard Ck. Gp. 2	253	30	270	6	3.14	Sinistral	3	
PTF	TF18-292	49.8767	-116.8562	Bernard Ck. Gp. 2	46	53	111	51	0.7	Normal	3	
PTF	TF18-291	49.8777	-116.8561	Bernard Ck. Gp. 3	186	80	355	37	2.61	Dextral	3	Large fault plane
PTF	TF18-291	49.8778	-116.8561	Bernard Ck. Gp. 3	203	84	21	28	1.06	Sinistral	3	
PTF	TF18-291	49.8779	-116.8561	Bernard Ck. Gp. 3	168	64	263	63	0.91	Reverse	3	
PTF	TF18-291	49.8779	-116.8562	Bernard Ck. Gp. 3	304	87	305	8	0.57	Dextral	3	
PTF	TF18-291	49.8781	-116.8562	Bernard Ck. Gp. 3	354	81	169	38	1.63	Dextral	3	
PTF	TF18-291	49.8783	-116.8563	Bernard Ck. Gp. 3	170	88	166	32	4.45	Dextral	3	
PTF	TF18-291	49.8783	-116.8559	Bernard Ck. Gp. 3	179	69	347	24	1.81	Dextral	3	
PTF	TF18-287	49.9039	-116.8600	Clute Lk.	197	83	8	18	6.32	Dextral	3	
PTF	TF18-287	49.9039	-116.8600	Clute Lk.	197	83	197	68	6.49	Normal	3	
PTF	TF18-287	49.9039	-116.8601	Clute Lk.	6	88	100	82	5.98	Reverse	3	
PTF	TF18-288	49.8971	-116.8561	Clute Lk.	38	81	29	29	12.18	Sinistral	2	
PTF	TF18-339	50.5643	-117.0001	Cockle Ck.	224	87	44	15	0.78	Dextral	3	
PTF	TF18-339	50.5643	-117.0001	Cockle Ck.	122	78	128	10	3.7	Sinistral	3	
PTF	TF18-339	50.5644	-117.0001	Cockle Ck.	206	70	16	16	3.59	Dextral	3	
PTF	TF18-339	50.5644	-117.0001	Cockle Ck.	99	60	113	15	4.18	Sinistral	3	Crosscut by dextral faults
PTF	TF18-339	50.5644	-117.0001	Cockle Ck.	112	40	123	7	1.63	Sinistral	3	
PTF	TF18-339	50.5645	-117.0001	Cockle Ck.	169	82	188	76	3.27	Dextral-reverse	3	
PTF	TF18-339	50.5645	-117.0001	Cockle Ck.	98	81	95	1	3.12	Sinistral	3	

PTF	TF18-293	49.6976	-116.9153	Coffee Ck. Lower	68	75	223	52	2.72	Dextral-normal	3	
PTF	TF18-293	49.6976	-116.9155	Coffee Ck. Lower	113	65	234	61	0.4	Normal	3	
PTF	TF18-293	49.6975	-116.9156	Coffee Ck. Lower	56	73	215	48	0.69	Dextral-normal	3	
PTF	TF18-293	49.6974	-116.9161	Coffee Ck. Lower	57	72	219	57	5.69	Dextral-normal	3	
PTF	TF18-294	49.6983	-116.9459	Coffee Ck. Upper	220	73	230	28	0.54	Dextral	3	
PTF	TF18-294	49.6982	-116.9459	Coffee Ck. Upper	230	57	346	47	6.65	Dextral	3	
PTF	TF18-294	49.6982	-116.9461	Coffee Ck. Upper	253	78	192	73	26.68	Dextral-normal	3	
PTF	TF18-294	49.6983	-116.9465	Coffee Ck. Upper	245	55	345	54	0.58	Normal	3	
PTF	TF18-296	49.6988	-116.9358	Coffee Ck. Upper	223	39	314	36	3	Normal	3	
PTF	TF18-296	49.6987	-116.9359	Coffee Ck. Upper	84	63	257	16	1.19	Dextral	3	
PTF	TF18-296	49.6987	-116.9360	Coffee Ck. Upper	194	79	239	66	6.2	Normal	3	
PTF	TF18-296	49.6986	-116.9362	Coffee Ck. Upper	81	65	250	15	3.31	Sinistral	3	
PTF	TF18-296	49.6986	-116.9362	Coffee Ck. Upper	81	65	238	37	1.63	Dextral	3	
PTF	TF18-280	49.6597	-116.8048	Crawford Bay	335	41	85	36	3.16	Reverse	3	
PTF	TF18-280	49.6598	-116.8048	Crawford Bay	340	75	108	74	2.23	Normal	3	1m wide fault zone
PTF	TF18-280	49.6599	-116.8048	Crawford Bay	337	57	38	51	2.2	Dextral-reverse	3	1m wide fault zone
PTF	TF18-280	49.6599	-116.8049	Crawford Bay	165	89	165	44	0.69	Dextral-reverse	3	1m wide fault zone
PTF	TF18-281	49.6546	-116.8031	Crawford Bay	9	87	9	17	0.88	Dextral	3	
PTF	TF18-281	49.6548	-116.8032	Crawford Bay	182	84	356	20	3.55	Dextral	2	
PTF	TF18-272	49.1275	-116.5238	Creston North	154	88	325	62	2.44	Dextral	3	
PTF	TF18-258	49.0492	-116.5134	Creston South	213	65	221	14	1.15	Dextral	2	Large 1m wide fault zone
PTF	TF18-263	49.0546	-116.5151	Creston South	17	60	61	54	2.92	Reverse	3	
PTF	TF18-263	49.0550	-116.5154	Creston South	12	81	189	38	3.19	Dextral	3	

PTF	TF18-263	49.0554	-116.5153	Creston South	188	87	190	40	0.4	Dextral	3	Large oxidized fault plane
PTF	TF18-263	49.0555	-116.5153	Creston South	12	88	175	4	16.8	Dextral	3	
PTF	TF18-250	49.1387	-116.6411	Creston Summit Ck.	355	84	0	7	4.2	Sinistral	2	
PTF	TF18-250	49.1387	-116.6412	Creston Summit Ck.	336	40	100	39	3.9	Normal	3	
PTF	TF18-250	49.1390	-116.6416	Creston Summit Ck.	186	55	244	56	4.99	Normal	3	
PTF	TF18-250	49.1392	-116.6419	Creston Summit Ck.	24	89	199	1	4.98	Dextral	3	2m wide breccia zone. Crosscuts normal fault
PTF	TF18-250	49.1392	-116.6420	Creston Summit Ck.	331	68	119	43	5.96	Normal	2	Crosscut by dextral fault
PTF	TF18-250	49.1396	-116.6425	Creston Summit Ck.	15	66	198	4	4.36	Dextral	3	2m wide breccia zone
PTF	TF18-250	49.1397	-116.6426	Creston Summit Ck.	328	70	326	2	2.56	Dextral	3	
PTF	TF18-250	49.1402	-116.6432	Creston Summit Ck.	182	89	190	4	7.91	Sinistral	2	5mm breccia zone
PTF	TF18-250	49.1402	-116.6432	Creston Summit Ck.	338	74	157	7	0.97	Sinistral	2	
PTF	TF18-251	49.1407	-116.6443	Creston Summit Ck.	324	74	41	69	4.49	Normal	3	
PTF	TF18-252	49.1411	-116.6453	Creston Summit Ck.	181	79	292	77	1.16	Normal	3	
PTF	TF18-265	49.1217	-116.6356	Creston West	20	57	114	61	4.06	Normal	2	
PTF	TF18-265	49.1215	-116.6358	Creston West	0	65	~	~		No Indicators	1	
PTF	TF18-266	49.1298	-116.6348	Creston West	185	89	286	89	0.02	Reverse	2	
PTF	TF18-266	49.1303	-116.6352	Creston West	140	76	~	~		No Indicators	1	
PTF	TF18-266	49.1317	-116.6355	Creston West	142	47	~	~		No Indicators	1	
PTF	TF18-267	49.1354	-116.6369	Creston West	171	52	197	22	5.14	Dextral-reverse	2	
PTF	TF18-267	49.1359	-116.6375	Creston West	126	41	293	10	0.82	Dextral-normal	3	
PTF	TF18-267	49.1361	-116.6377	Creston West	134	62	304	20	0.95	Dextral	3	
PTF	TF18-338	50.5403	-116.9829	Duncan Clancy Ck.	194	89	16	15	2.19	Dextral	3	
PTF	TF18-338	50.5410	-116.9833	Duncan Clancy Ck.	212	86	19	23	10.33	Dextral	3	

PTF	TF18-330	50.6315	-117.0375	Duncan Lk. North	193	59	277	58	0.86	Normal	3	
PTF	TF18-330	50.6319	-117.0375	Duncan Lk. North	224	86	240	69	1.91	Normal	3	
PTF	TF18-340	50.6013	-117.0239	Duncan Lk. North	122	88	295	44	3.63	Dextral-normal	3	
PTF	TF18-332	50.4158	-116.9600	Duncan Lk. Right Step	292	71	301	10	5.11	Dextral	3	
PTF	TF18-332	50.4163	-116.9593	Duncan Lk. Right Step	165	73	169	20	2.14	Dextral	3	
PTF	TF18-332	50.4163	-116.9592	Duncan Lk. Right Step	155	81	310	60	4.2	Dextral	3	
PTF	TF18-332	50.4164	-116.9591	Duncan Lk. Right Step	184	78	3	3	0.35	Dextral	3	
PTF	TF18-332	50.4168	-116.9586	Duncan Lk. Right Step	139	89	140	40	0.12	Dextral	3	
PTF	TF18-333	50.4170	-116.9583	Duncan Lk. Right Step	328	80	332	21	0.11	Dextral	3	
PTF	TF18-335	50.4226	-116.9498	Duncan Lk. Right Step	45	71	115	66	3.67	Reverse	3	
PTF	TF18-335	50.4226	-116.9496	Duncan Lk. Right Step	148	70	326	40	11.23	Dextral	3	
PTF	TF18-336	50.4264	-116.9313	Duncan Lk. Right Step	320	85	333	51	4.2	Sinistral	2	
PTF	TF18-337	50.4458	-116.9127	Duncan Lk. Right Step	337	82	339	18	0.58	Dextral	3	
PTF	TF18-337	50.4458	-116.9127	Duncan Lk. Right Step	349	89	345	19	4.11	Dextral	3	
PTF	TF18-341	50.6740	-117.0714	Duncan River	152	53	270	50	0.44	Normal	3	Overprints dextral slickenlines
PTF	TF18-341	50.6740	-117.0714	Duncan River	152	53	335	23	15.88	Dextral	3	Overprinted by normal slickenlines
PTF	TF18-341	50.6741	-117.0714	Duncan River	174	43	291	54	13.56	Normal	3	Overprints dextral slickenlines
PTF	TF18-341	50.6741	-117.0714	Duncan River	174	43	330	26	4.09	Dextral	3	Overprinted by normal slickenlines
PTF	TF18-342	50.6867	-117.0855	Duncan River	144	85	261	72	11.03	Dextral-normal	3	
PTF	TF18-343	50.6958	-117.1008	Duncan River	145	81	347	12	23.23	Dextral	3	Large 20m wide limonitic fault plane
PTF	TF18-344	50.7209	-117.1261	Duncan River	156	67	302	38	9.5	Dextral-normal	3	
PTF	TF18-344	50.7210	-117.1263	Duncan River	4	74	41	70	3.51	Normal	3	
PTF	TF18-344	50.7211	-117.1264	Duncan River	24	54	54	28	4.66	Sinistral	3	
PTF	TF18-310	49.9075	-116.9367	Kaslo	96	70	239	53	3.85	Normal	3	

PTF	TF18-310	49.9075	-116.9367	Kaslo	96	70	275	1	0.6	Normal	3	
PTF	TF19-068	49.9098	-116.9272	Kaslo	56	79	234	20	1.9	Dextral	2	
PTF	TF18-268	49.2954	-116.6573	Kootenay Lk. South	135	80	278	67	4.11	Normal	3	
PTF	TF18-268	49.2954	-116.6574	Kootenay Lk. South	139	80	308	22	6.27	Dextral	3	
PTF	TF18-268	49.2955	-116.6574	Kootenay Lk. South	131	80	288	64	0.72	Dextral-normal	3	
PTF	TF18-269	49.2819	-116.6532	Kootenay Lk. South	319	65	114	43	0.46	Dextral-reverse	2	
PTF	TF18-270	49.2777	-116.6517	Kootenay Lk. South	334	78	~	~		No Indicators	1	
PTF	TF18-270	49.2777	-116.6517	Kootenay Lk. South	151	83	~	~		No Indicators	1	
PTF	TF18-271	49.2541	-116.6319	Kootenay Lk. South	297	58	319	29	1.2	Sinistral	3	
PTF	TF18-273	49.2983	-116.6588	Kootenay Lk. South	150	83	164	25	9.56	Dextral	3	
PTF	TF18-273	49.2984	-116.6589	Kootenay Lk. South	144	87	146	8	1.56	Dextral	3	
PTF	TF18-273	49.2984	-116.6590	Kootenay Lk. South	139	84	141	25	0.73	Dextral	3	
PTF	TF18-302	50.1658	-116.9576	Lardeau	92	80	101	12	6.58	Sinistral	3	
PTF	TF18-304	50.1155	-116.9464	Ledge Ck. North	169	86	351	9	2.6	Dextral	2	
PTF	TF18-304	50.1158	-116.9466	Ledge Ck. North	332	71	142	26	0.28	Dextral	3	large oxidized fault plane 20m wide
PTF	TF18-304	50.1158	-116.9466	Ledge Ck. North	332	71	335	6	0.87	Dextral	3	
PTF	TF18-304	50.1162	-116.9467	Ledge Ck. North	348	88	173	39	5.14	Dextral	3	
PTF	TF18-304	50.1162	-116.9467	Ledge Ck. North	348	88	157	76	0.7	Dextral-normal	3	
PTF	TF18-304	50.1164	-116.9468	Ledge Ck. North	355	76	146	60	1.47	Dextral	3	
PTF	TF18-304	50.1164	-116.9468	Ledge Ck. North	355	76	150	45	6.83	Dextral	3	
PTF	TF18-305	50.0936	-116.9358	Ledge Ck. South	313	60	82	50	2.84	Normal	3	
PTF	TF18-305	50.0936	-116.9358	Ledge Ck. South	30	87	251	77	11.44	Dextral-normal	3	
PTF	TF18-305	50.0936	-116.9358	Ledge Ck. South	336	45	66	45	0	Normal	3	
PTF	TF18-305	50.0937	-116.9358	Ledge Ck. South	344	59	53	57	0.22	Normal	3	

PTF	TF18-305	50.0938	-116.9358	Ledge Ck. South	321	86	143	57	4.44	Dextral-normal	3	
PTF	TF18-305	50.0938	-116.9359	Ledge Ck. South	334	51	100	52	6.25	Dextral-normal	3	
PTF	TF18-305	50.0938	-116.9359	Ledge Ck. South	321	71	115	45	3.6	Dextral-normal	3	
PTF	TF18-305	50.0938	-116.9359	Ledge Ck. South	306	86	134	66	6.9	Normal	3	
PTF	TF18-305	50.0939	-116.9359	Ledge Ck. South	183	50	215	22	7.79	Sinistral-normal	2	
PTF	TF18-317	50.2514	-116.9654	Marblehead	342	89	155	75	0.84	Normal	3	
PTF	TF18-317	50.2515	-116.9655	Marblehead	162	71	332	22	1.73	Dextral	3	
PTF	TF18-282	49.5948	-116.7983	McFarlane Ck.	341	61	56	60	0.15	Normal	2	
PTF	TF18-282	49.5948	-116.7983	McFarlane Ck.	341	61	356	50	13.05	Dextral-reverse	3	
PTF	TF18-301	49.8516	-116.9046	Mirror Lk.	59	84	235	50	2.03	Dextral-normal	3	
PTF	TF18-301	49.8518	-116.9043	Mirror Lk.	306	78	307	20	3.16	Sinistral	3	
PTF	TF18-301	49.8519	-116.9042	Mirror Lk.	69	88	243	68	0.39	Dextral-normal	3	
PTF	TF18-301	49.8519	-116.9042	Mirror Lk.	69	88	242	57	2.12	Dextral-normal	3	
PTF	TF18-301	49.8523	-116.9033	Mirror Lk.	23	81	178	62	3.32	Reverse	3	
PTF	TF18-301	49.8524	-116.9032	Mirror Lk.	5	63	5	1	0.92	Dextral	3	Major, well constrained fault, 40cm oxidized zone, and 2cm gouge layer
PTF	TF18-301	49.8534	-116.9026	Mirror Lk.	299	77	310	24	4.49	Sinistral	2	
PTF	TF18-192	50.7025	-117.7095	North Adit	345	85	150	14	13.24	Dextral	3	Large fault plane
PTF	TF18-289	49.8914	-116.8583	Powder Ck.	314	81	113	53	5.05	Dextral-normal	3	
PTF	TF18-289	49.8914	-116.8584	Powder Ck.	355	81	0	1	4.78	Dextral	3	Large fault plane with 15cm gouge.
PTF	TF18-289	49.8915	-116.8586	Powder Ck.	162	78	340	26	3.47	Dextral	2	Large fault zone, 3cm gouge
PTF	TF18-289	49.8917	-116.8590	Powder Ck.	237	24	295	23	2.26	Sinistral-normal	3	
PTF	TF18-289	49.8916	-116.8591	Powder Ck.	321	58	56	59	1.1	Normal	3	
PTF	TF18-289	49.8917	-116.8591	Powder Ck.	329	86	59	81	5	Reverse	3	
PTF	TF18-289	49.8917	-116.8591	Powder Ck.	327	55	319	5	9.41	Sinistral	3	Overprinted by dextral-normal slickenlines
PTF	TF18-289	49.8917	-116.8591	Powder Ck.	327	55	111	45	3.73	Dextral-normal	3	Overprint sinistral slickenlines
PTF	TF18-289	49.8917	-116.8591	Powder Ck.	327	55	356	50	10.61	Sinistral-normal	3	
PTF	TF18-290	49.8905	-116.8599	Powder Ck.	156	82	320	70	2.14	Reverse	3	
PTF	TF18-290	49.8907	-116.8596	Powder Ck.	323	61	0	48	0.46	Sinistral-normal	3	

PTF	TF18-290	49.8907	-116.8594	Powder Ck.	136	68	291	45	0.7	Dextral-normal	3	3m-wide breccia and gouge zone
PTF	TF18-290	49.8907	-116.8594	Powder Ck.	136	68	310	10	1.74	Sinistral	3	Minor phase overprinting dextral slickenlines in major fault zone
PTF	TF18-290	49.8907	-116.8594	Powder Ck.	173	78	340	54	2.23	Dextral-normal	3	Large fault zone
PTF	TF18-290	49.8908	-116.8588	Powder Ck.	265	31	287	13	0.28	Sinistral-normal	3	
PTF	TF18-290	49.8908	-116.8587	Powder Ck.	79	75	107	57	1.71	Sinistral-normal	3	
PTF	TF18-290	49.8908	-116.8586	Powder Ck.	144	66	144	1	0.41	Dextral	3	Large fault plane
PTF	TF18-290	49.8908	-116.8585	Powder Ck.	62	73	58	35	12.85	Sinistral	3	
PTF	TF18-290	49.8909	-116.8584	Powder Ck.	119	54	261	37	2.52	Dextral-normal	3	
PTF	TF18-290	49.8909	-116.8584	Powder Ck.	149	55	288	48	3.82	Dextral-normal	3	
PTF	TF18-259	49.0027	-116.5007	Rykerts	15	89	193	1	1.98	Dextral	3	50cm wide breccia and gouge
PTF	TF18-259	49.0028	-116.5008	Rykerts	199	89	204	26	4.05	Dextral	3	
PTF	TF18-259	49.0029	-116.5008	Rykerts	5	75	1	10	6.39	Dextral	2	
PTF	TF18-260	49.0093	-116.5034	Rykerts	181	71	199	38	1.71	Dextral	3	
PTF	TF18-260	49.0094	-116.5034	Rykerts	192	72	1	41	3.77	Dextral-normal	2	
PTF	TF18-260	49.0095	-116.5034	Rykerts	186	86	190	9	3.31	Dextral	3	
PTF	TF18-276	49.3653	-116.7271	Sanca Ck.	342	52	348	20	7.65	Dextral	3	
PTF	TF18-276	49.3654	-116.7271	Sanca Ck.	335	66	350	22	3.83	Dextral	3	
PTF	TF18-276	49.3656	-116.7271	Sanca Ck.	51	30	74	16	2.92	Sinistral-normal	3	
PTF	TF18-276	49.3657	-116.7271	Sanca Ck.	324	48	1	33	0.61	Dextral-reverse	3	Overprinted by sinistral-reverse slickenlines
PTF	TF18-276	49.3657	-116.7271	Sanca Ck.	324	48	109	29	2.77	Sinistral-reverse	3	Overprints dextral-reverse slickenlines
PTF	TF18-276	49.3659	-116.7271	Sanca Ck.	332	65	0	29	9.63	Dextral	3	
PTF	TF18-276	49.3666	-116.7271	Sanca Ck.	321	53	331	14	0.63	Dextral	3	
PTF	TF18-276	49.3672	-116.7272	Sanca Ck.	341	63	149	20	1.08	Dextral	3	
PTF	TF18-306	50.0485	-116.9125	Schroeder Pt.	152	48	251	59	11.28	Normal	2	
PTF	TF18-307	50.0647	-116.9143	Schroeder Pt.	356	84	355	33	4.1	Dextral	3	
PTF	TF18-307	50.0653	-116.9144	Schroeder Pt.	336	76	94	75	0.68	Normal	3	
PTF	TF18-307	50.0655	-116.9143	Schroeder Pt.	338	88	355	76	2.11	Sinistral-normal	3	
PTF	TF18-255	49.1520	-116.6449	Topaz Ck. FSR	51	87	54	17	1.99	Sinistral	3	

PTF	TF18-257	49.1641	-116.6438	Topaz Ck. FSR	205	81	295	81	0	Normal	3	
PTF	TF18-257	49.1642	-116.6438	Topaz Ck. FSR	224	84	215	10	9.87	Sinistral	3	
PTF	TF18-319	50.4504	-117.1836	Trout River	319	63	119	27	3.75	Dextral	3	
PTF	TF18-320	50.4926	-117.2535	Trout River	302	81	320	37	8.6	Dextral	3	
PTF	TF18-274	49.3307	-116.7067	Twin Bays Ck	332	38	93	29	4.56	Normal	3	
PTF	TF18-274	49.3308	-116.7067	Twin Bays Ck	333	47	105	31	6.58	Normal	3	
PTF	TF18-274	49.3308	-116.7068	Twin Bays Ck	322	60	86	53	1.88	Reverse	3	
PTF	TF18-274	49.3309	-116.7069	Twin Bays Ck	164	72	166	7	0.27	Sinistral	3	
PTF	TF18-274	49.3309	-116.7070	Twin Bays Ck	279	36	82	11	0.82	Reverse	2	
PTF	TF18-274	49.3324	-116.7085	Twin Bays Ck	290	82	105	38	1.01	Sinistral	3	
PTF	TF18-274	49.3327	-116.7089	Twin Bays Ck	313	64	107	34	4.68	Dextral	3	
PTF	TF18-299	49.7974	-116.9199	Woodbury Ck.	310	66	155	38	33.69	Sinistral-normal	3	
PTF	TF18-299	49.7975	-116.9206	Woodbury Ck.	286	65	250	61	38.9	Normal	3	
PTF	TF18-299	49.7990	-116.9235	Woodbury Ck.	277	71	287	19	2.82	Sinistral	2	
PTF	TF18-300	49.7938	-116.9162	Woodbury Ck.	181	69	315	71	6.9	Normal	2	
PTF	TF18-300	49.7939	-116.9163	Woodbury Ck.	190	79	~	~		No Indicators	1	
PTF	TF18-300	49.7938	-116.9164	Woodbury Ck.	194	49	~	~		No Indicators	1	1-2m wide gouge zone
PTF	TF18-300	49.7938	-116.9166	Woodbury Ck.	305	81	315	6	8.87	Sinistral	3	
SLF	TF19-082	50.0351	-117.4197	Rosebery	339	85	349	11	8.81	Dextral	3	
SLF	TF19-083	50.0352	-117.4201	Rosebery	210	56	218	19	4.18	Dextral	3	3m wide brecciated zone through Cretaceous granitoid
SLF	TF19-084	50.0353	-117.4203	Rosebery	15	90	197	20	1.88	Dextral	3	
SLF	TF19-085	50.0358	-117.4213	Rosebery	187	59	280	56	2.96	Dextral	3	
SLF	TF19-086	50.0699	-117.4441	Rosebery	333	73	348	28	4.66	Dextral	3	
SLF	TF19-087	50.0346	-117.4168	Rosebery	27	72	125	67	4.79	Normal	3	
SLF	TF19-094	49.8192	-117.4529	Slocan Lk. South	180	88	0	3	0.1	Dextral	3	
SLF	TF19-095	49.8189	-117.4548	Slocan Lk. South	191	60	195	9	1.06	Dextral	3	
SLF	TF19-096	49.8190	-117.4605	Slocan Lk. South	4	84	184	2	0.21	Dextral	3	

SLF	TF19-097	49.8100	-117.4650	Slocan Lk. South	183	90	15	18	11.4	Dextral	2	
SLF	TF19-098	49.8189	-117.4550	Slocan Lk. South	172	74	~	~		No Indicators	1	Wide fault zone cutting Valkyr Shear Zone
SLF	TF19-099	49.8189	-117.4551	Slocan Lk. South	171	73	~	~		No Indicators	1	Wide fault zone cutting Valkyr Shear Zone
SLF	TF19-088	49.9003	-117.3867	Slocan Lookout	142	85	346	38	21.9	Dextral	2	
SLF	TF19-089	49.9011	-117.3865	Slocan Lookout	197	77	5	20	6.51	Dextral	2	
SLF	TF19-090	49.9020	-117.3857	Slocan Lookout	188	76	6	19	2.68	Dextral	3	
SLF	TF19-091	49.9024	-117.3853	Slocan Lookout	62	83	60	6	2.7	Dextral	3	
SLF	TF19-092	49.9020	-117.3858	Slocan Lookout	295	40	332	25	1.54	Dextral-reverse	2	20cm gouge zone
SLF	TF19-093	49.9022	-117.3855	Slocan Lookout	15	79	~	~		No Indicators	1	8 cm gouge zone
SLF	TF19-100	50.1105	-117.3769	Wilson Ck.	81	73	140	72	1.42	Reverse	3	
SLF	TF19-101	50.1105	-117.3769	Wilson Ck.	90	76	153	75	0.57	Reverse	3	
SLF	TF19-102	50.0651	-117.3884	Wilson Ck.	218	58	262	48	0.02	Sinistral-normal	3	
SLF	TF19-103	50.0652	-117.3885	Wilson Ck.	205	67	236	47	2.15	Sinistral-normal	3	
SLF	TF19-104	50.0652	-117.3885	Wilson Ck.	221	47	257	33	0.63	Sinistral-normal	3	
SRMT	TF19-003	51.2351	-116.6538	Beaverfoot	312	72	326	44	2.82	Dextral	3	
SRMT	TF19-003	51.2350	-116.6537	Beaverfoot	324	84	135	23	5.88	Dextral	3	Overprints normal slickenlines
SRMT	TF19-003	51.2350	-116.6537	Beaverfoot	324	84	86	80	2.49	Normal	3	Overprinted by dextral slickenlines
SRMT	TF19-007	51.6373	-117.4188	Blackwater Lk.	168	77	345	12	0.18	Dextral	2	
SRMT	TF19-007	51.6376	-117.4191	Blackwater Lk.	162	76	160	1	2.18	Dextral	3	Large fault plane with abundant slickenlines
SRMT	TF19-110	50.4962	-115.9145	Invermere	346	64	146	32	1.63	Dextral	3	
SRMT	TF19-111	50.4962	-115.9146	Invermere	311	50	122	13	1.59	Dextral	3	
SRMT	TF19-112	50.4959	-115.9141	Invermere	215	46	17	17	0.54	Dextral	2	
SRMT	TF19-113	50.1346	-115.5866	Lussier	75	84	91	67	0.62	Reverse	3	
SRMT	TF19-114	50.1345	-115.5871	Lussier	75	88	228	85	0.27	Reverse	3	
SRMT	TF19-128	50.1022	-115.6481	Lussier West	175	86	168	27	8.05	Dextral	3	
SRMT	TF19-129	50.1023	-115.6482	Lussier West	180	84	353	33	2.56	Dextral-normal	3	
SRMT	TF19-130	50.1025	-115.6483	Lussier West	181	81	336	61	3.76	Normal	3	

SRMT	TF19-131	50.1028	-115.6485	Lussier West	357	69	114	71	3.9	Normal	3
SRMT	TF19-132	50.1020	-115.6478	Lussier West	174	81	327	77	2.96	Reverse	2
SRMT	TF19-133	50.1025	-115.6483	Lussier West	175	87	353	32	0.1	Sinistral	2
SRMT	TF19-134	50.1025	-115.6483	Lussier West	175	87	342	58	4.28	Sinistral-reverse	2
SRMT	TF19-015	50.6355	-116.0356	Radium	153	63	189	45	2.83	Sinistral-normal	3
SRMT	TF19-015	50.6356	-116.0361	Radium	342	65	350	10	2.91	Dextral	2
SRMT	TF19-015	50.6356	-116.0362	Radium	325	64	330	22	5.25	Dextral	2
SRMT	TF19-015	50.6356	-116.0369	Radium	168	64	~	~		No Indicators	1
SRMT	TF19-015	50.6356	-116.0369	Radium	174	59	178	9	1.23	Dextral	2
SRMT	TF19-015	50.6356	-116.0371	Radium	185	48	~	~		No Indicators	1
SRMT	TF19-015	50.6356	-116.0372	Radium	304	86	119	30	2.32	Dextral	3
SRMT	TF19-016	50.6357	-116.0324	Radium	325	71	308	22	22.23	Dextral	2
SRMT	TF19-016	50.6359	-116.0327	Radium	328	83	~	~		No Indicators	1
SRMT	TF19-113	50.6191	-116.0147	Radium	140	79	323	42	9.55	Dextral	3
SRMT	TF19-125	50.2404	-115.6977	RedRock	358	81	0	22	1.53	Dextral	3
SRMT	TF19-126	50.2388	-115.6965	RedRock	347	63	153	19	3.21	Dextral	2
SRMT	TF19-127	50.2387	-115.6964	RedRock	345	80	17	70	0.88	Sinistral-normal	2
SRMT	TF19-135	49.7177	-115.5456	Wildhorse	200	88	16	14	3.39	Dextral	2
SRMT	TF19-136	49.7177	-115.5456	Wildhorse	200	88	217	25	14.48	Dextral	3
CR	TF18-124	52.7640	-119.0599	Bear Foot	281	35	60	23	1.51	Reverse	3
CR	TF18-125	52.7647	-119.0595	Bear Foot	145	79	156	48	0.94	Reverse	3
CR	TF18-012	52.6288	-118.9575	Bulldog Ck.	118	41	~	~		No indicators	1
CR	TF18-068	52.6286	-118.9571	Bulldog Ck.	136	64	136	18	7.79	Dextral	3
CR	TF18-069	52.6297	-118.9598	Bulldog Ck.	177	48	235	34	8.53	Normal	3
CR	TF18-069	52.6299	-118.9600	Bulldog Ck.	145	83	156	15	8.71	Dextral	3
CR	TF18-069	52.6300	-118.9602	Bulldog Ck.	131	85	132	15	0.33	Dextral	3
CR	TF18-069	52.6301	-118.9606	Bulldog Ck.	119	71	145	50	0.98	Dextral-reverse	3
CR	TF18-070	52.6310	-118.9626	Bulldog Ck.	149	72	159	16	4.22	Dextral	3
CR	TF18-070	52.6311	-118.9628	Bulldog Ck.	157	45	159	10	5.65	Dextral	3
CR	TF18-071	52.6335	-118.9662	Bulldog Ck.	136	85	137	5	0.56	Dextral	3

CR	TF18-071	52.6338	-118.9664	Bulldog Ck.	130	50	140	15	2.17	Dextral	3	
CR	TF18-072	52.6370	-118.9697	Bulldog Ck.	112	72	196	62	9.86	Normal	2	
CR	TF18-072	52.6371	-118.9699	Bulldog Ck.	111	90	115	8	3.96	Dextral	2	
CR	TF18-072	52.6372	-118.9702	Bulldog Ck.	97	88	175	85	2.89	Normal	2	
CR	TF18-072	52.6377	-118.9716	Bulldog Ck.	120	64	149	35	6.06	Dextral-reverse	3	
CR	TF18-074	52.6411	-118.9758	Bulldog Ck.	139	84	143	15	2.29	Dextral	3	
CR	TF18-075	52.6442	-118.9799	Bulldog Ck.	152	77	166	50	1.19	Dextral	3	
CR	TF18-076	52.6466	-118.9857	Bulldog Ck.	100	75	90	30	15.94	Sinistral	3	
CR	TF18-077	52.6493	-118.9892	Bulldog Ck.	134	59	136	8	2.41	Dextral	3	Overprinted by normal slickenlines
CR	TF18-077	52.6493	-118.9892	Bulldog Ck.	134	59	180	48	1.71	Normal	3	Overprinted by dextral slickenlines
CR	TF18-078	52.6552	-118.9925	Bulldog Ck.	150	85	339	32	10.27	Dextral	3	
CR	TF18-079	52.6588	-118.9971	Bulldog Ck. North	134	63	184	65	7.07	Normal	2	
CR	TF18-080	52.6613	-118.9999	Bulldog Ck. North	125	76	132	35	2.4	Dextral	3	Overprinted by normal slickenlines
CR	TF18-080	52.6614	-118.9999	Bulldog Ck. North	134	63	228	67	4.05	Normal	3	Overprints dextral slickenlines
CR	TF18-080	52.6614	-119.0001	Bulldog Ck. North	130	66	254	57	4.09	Normal	3	
CR	TF18-080	52.6615	-119.0004	Bulldog Ck. North	124	57	233	57	1.43	Normal	2	
CR	TF18-081	52.6644	-119.0040	Bulldog Ck. North	112	61	242	60	4.87	Normal	2	
CR	TF18-082	52.6660	-119.0056	Bulldog Ck. North	122	74	175	65	4.28	Normal	2	
CR	TF18-083	52.6667	-119.0065	Bulldog Ck. North	152	72	154	32	7.79	Dextral	2	
CR	TF18-083	52.6669	-119.0066	Bulldog Ck. North	171	81	351	50	6.88	Dextral	2	
CR	TF18-083	52.6672	-119.0069	Bulldog Ck. North	114	86	295	12	1.81	Dextral	3	
CR	TF18-083	52.6672	-119.0069	Bulldog Ck. North	114	86	154	64	12.61	Normal	3	
CR	TF18-084	52.6679	-119.0081	Bulldog Ck. North	136	58	184	47	2.42	Normal	3	
CR	SJ18-005	52.7306	-119.0812	Dave Henry Ck.	134	48	199	42	3.03	Reverse	3	
CR	SJ18-006	52.7307	-119.0813	Dave Henry Ck.	166	52	261	53	1.1	Normal	3	
CR	SJ18-007	52.7398	-119.0923	Dave Henry Ck.	20	41	92	37	2.53	Reverse	2	

CR	SJ18-008	52.7389	-119.0913	Dave Henry Ck.	313	33	65	34	2.88	Reverse	2	
CR	TF18-107	52.7315	-119.0800	Dave Henry Ck.	330	68	135	32	0.29	Dextral	3	
CR	TF18-107	52.7317	-119.0808	Dave Henry Ck.	273	75	265	18	12	Sinistral	3	
CR	TF18-108	52.7303	-119.0800	Dave Henry Ck.	185	31	198	4	3.2	Sinistral	3	
CR	TF18-108	52.7303	-119.0800	Dave Henry Ck.	185	31	268	57	26.13	Normal	3	
CR	TF18-123	52.7644	-119.0727	Dave Henry Ck.	151	59	174	33	0.02	Normal	3	
CR	TF18-132	52.7375	-119.0890	Dave Henry Ck.	63	88	236	61	1.63	Sinistral-reverse	3	
CR	TF18-132	52.7375	-119.0891	Dave Henry Ck.	127	62	174	56	1.61	Dextral-reverse	3	
CR	TF18-132	52.7375	-119.0891	Dave Henry Ck.	210	81	348	65	7.9	Reverse	2	
CR	TF18-009	52.7185	-119.0638	East Shore "crush zone"	180	50	223	49	8.18	Normal	3	
CR	TF18-058	52.7242	-119.0740	East Shore "crush zone"	338	65	22	74	13.46	Normal	3	
CR	TF18-103	52.7170	-119.0612	East Shore "crush zone"	344	74	348	40	7.23	Dextral-reverse	3	
CR	TF18-103	52.7170	-119.0613	East Shore "crush zone"	300	73	304	23	3.03	Sinistral	3	
CR	TF18-103	52.7170	-119.0613	East Shore "crush zone"	300	73	70	66	1.77	Reverse	3	
CR	TF18-104	52.7206	-119.0661	East Shore "crush zone"	323	76	145	19	6.36	Dextral	3	
CR	TF18-104	52.7208	-119.0663	East Shore "crush zone"	319	79	124	58	1.56	Normal	3	
CR	TF18-105	52.7229	-119.0705	East Shore "crush zone"	312	77	93	70	0.1	Dextral-normal	3	
CR	TF18-109	52.7242	-119.0740	East Shore "crush zone"	338	65	122	51	0.39	Dextral-normal	3	Overprints reverse slickenlines
CR	TF18-109	52.7242	-119.0743	East Shore "crush zone"	176	47	274	44	2.71	Normal	3	
CR	TF18-109	52.7245	-119.0742	East Shore "crush zone"	312	60	82	66	10.77	Normal	3	
CR	TF18-109	52.7245	-119.0742	East Shore "crush zone"	122	72	225	70	1.52	Normal	3	
CR	TF18-109	52.7250	-119.0749	East Shore "crush zone"	122	63	232	66	4.25	Normal	2	
CR	TF18-109	52.7251	-119.0749	East Shore "crush zone"	130	76	193	68	5.71	Normal	3	

CR	TF18-109	52.7255	-119.0757	East Shore "crush zone"	158	66	257	58	7.66	Normal	3
CR	TF18-109	52.7256	-119.0757	East Shore "crush zone"	176	44	245	40	1.97	Normal	3
CR	TF18-109	52.7258	-119.0759	East Shore "crush zone"	172	72	230	62	6.07	Normal	3
CR	TF18-109	52.7258	-119.0759	East Shore "crush zone"	180	48	255	48	0.97	Normal	3
CR	TF18-109	52.7259	-119.0759	East Shore "crush zone"	356	66	60	64	0.32	Normal	3
CR	TF18-109	52.7259	-119.0759	East Shore "crush zone"	356	66	151	43	0.28	Normal	3
CR	TF18-109	52.7264	-119.0751	East Shore "crush zone"	161	62	240	59	2.52	Normal	3
CR	TF18-109	52.7262	-119.0765	East Shore "crush zone"	132	76	184	69	2.76	Normal	3
CR	TF18-110	52.7265	-119.0767	East Shore "crush zone"	160	44	252	42	1.98	Normal	3
CR	TF18-111	52.7268	-119.0768	East Shore "crush zone"	277	40	28	28	9.8	Normal	3
CR	TF18-111	52.7267	-119.0769	East Shore "crush zone"	288	61	60	56	2.2	Reverse	3
CR	TF18-129	52.7278	-119.0781	East Shore "crush zone"	184	64	248	56	5.07	Normal	3
CR	TF18-129	52.7279	-119.0782	East Shore "crush zone"	292	35	18	27	7.93	Reverse	3
CR	TF18-129	52.7279	-119.0783	East Shore "crush zone"	172	80	252	74	5.76	Normal	3
CR	TF18-129	52.7280	-119.0784	East Shore "crush zone"	284	42	296	6	3.48	Dextral	3
CR	TF18-129	52.7283	-119.0783	East Shore "crush zone"	306	31	25	62	31.3	Normal	3
CR	TF18-129	52.7283	-119.0785	East Shore "crush zone"	342	70	162	0	0	Dextral	3
CR	TF18-085	52.6687	-119.0092	Horse Ck.	120	84	137	62	2.53	Dextral-reverse	3
CR	TF18-085	52.6688	-119.0096	Horse Ck.	115	60	130	26	1.02	Dextral	3
CR	TF18-085	52.6689	-119.0097	Horse Ck.	154	72	299	54	4.05	Normal	3
CR	TF18-085	52.6690	-119.0099	Horse Ck.	146	81	141	13	6.84	Dextral	3
CR	TF18-087	52.6733	-119.0169	Horse Ck.	129	74	164	66	1.58	Dextral-reverse	3
CR	TF18-087	52.6734	-119.0170	Horse Ck.	126	89	299	30	5.55	Dextral-reverse	2
CR	TF18-024	52.6621	-119.0299	Kinbasket West	318	89	320	40	0.89	Ambiguous	1
CR	TF18-036	52.6101	-118.9605	Kinbasket West	140	75	322	26	8.27	Dextral-normal	3

CR	TF18-127	52.6095	-118.9407	Kinbasket West	159	42	320	13	2.58	Dextral-normal	2	
CR	TF18-127	52.6095	-118.9403	Kinbasket West	285	64	327	48	4.4	Dextral	2	
CR	TF19-036	52.6101	-118.9605	Kinbasket West	140	75	322	64	14.32	Dextral-normal	3	
CR	TF18-051	52.6228	-118.9473	Left-Step Bend	133	60	170	44	1.58	Dextral-reverse	3	
CR	TF18-051	52.6231	-118.9482	Left-Step Bend	150	70	174	46	1.12	Dextral-reverse	3	
CR	TF18-051	52.6241	-118.9499	Left-Step Bend	139	53	170	32	1.71	Dextral-reverse	3	
CR	TF18-051	52.6241	-118.9499	Left-Step Bend	139	53	321	1	2.2	Dextral	3	
CR	TF18-052	52.6213	-118.9453	Left-Step Bend	137	63	185	53	2.06	Dextral-reverse	3	
CR	TF18-052	52.6223	-118.9468	Left-Step Bend	138	68	310	10	3.56	Dextral	3	
CR	TF18-052	52.6223	-118.9468	Left-Step Bend	138	68	162	38	3.82	Dextral-reverse	3	
CR	TF18-052	52.6227	-118.9470	Left-Step Bend	102	67	198	66	0.88	Normal	3	
CR	TF18-053	52.6205	-118.9437	Left-Step Bend	110	55	158	48	1.08	Dextral-reverse	3	
CR	TF18-054	52.6201	-118.9423	Left-Step Bend	170	54	333	15	4.38	Dextral	3	
CR	TF18-056	52.6191	-118.9366	Left-Step Bend	123	67	146	39	1.93	Dextral-reverse	3	
CR	TF18-057	52.6185	-118.9291	Left-Step Bend	106	70	147	58	2.1	Normal	2	
CR	TF18-057	52.6185	-118.9292	Left-Step Bend	195	50	224	22	5.94	Sinistral	3	
CR	TF18-057	52.6185	-118.9292	Left-Step Bend	126	63	165	65	10.05	Dextral-reverse	3	
CR	TF18-057	52.6185	-118.9292	Left-Step Bend	240	86	232	28	8.94	Sinistral	3	
CR	TF18-057	52.6185	-118.9295	Left-Step Bend	125	68	216	64	4	Reverse	3	
CR	TF18-058	52.6182	-118.9192	Left-Step Bend	136	84	~	~		No Indicators	1	
CR	TF18-060	52.6168	-118.9051	Left-Step Bend	150	58	163	20	0.11	Dextral	3	
CR	TF18-109	52.6182	-118.9187	Left-Step Bend	338	65	106	78	15.36	Reverse	3	Overprinted by dextral slickenlines
CR	TF18-044	52.5784	-118.8491	Ptarmigan Ck.	77	72	70	8	9.08	Sinistral	3	

CR	TF18-047	52.5820	-118.8432	Ptarmigan Ck.	115	65	202	62	2.97	Reverse	3	Crosscut by dextral fault
CR	TF18-047	52.5819	-118.8427	Ptarmigan Ck.	128	70	132	12	0.4	Dextral	3	
CR	TF18-048	52.5813	-118.8376	Ptarmigan Ck.	242	78	62	13	2.68	Sinistral	3	
CR	TF18-048	52.5813	-118.8376	Ptarmigan Ck.	242	78	82	32	23.2	Sinistral	3	
CR	TF18-048	52.5815	-118.8367	Ptarmigan Ck.	98	88	96	40	2.82	Sinistral	3	
CR	TF18-048	52.5815	-118.8361	Ptarmigan Ck.	105	85	108	55	2.38	Sinistral	3	
CR	TF18-048	52.5815	-118.8354	Ptarmigan Ck.	276	70	72	43	2.65	Sinistral	3	
CR	TF18-048	52.5817	-118.8342	Ptarmigan Ck.	255	78	55	48	3.98	Sinistral	3	
CR	TF18-049	52.5829	-118.8274	Ptarmigan Ck.	46	88	43	12	3.35	Sinistral	3	
CR	TF18-050	52.5840	-118.8398	Ptarmigan Ck.	257	57	63	33	7.27	Sinistral	3	
CR	TF18-013	52.5927	-118.8679	Ptarmigan Ck. South	126	66	150	45	1.42	Dextral-reverse	3	
CR	TF18-019	52.5773	-118.8492	Ptarmigan Ck. South	110	86	120	52	2.96	Normal	3	
CR	TF18-019	52.5773	-118.8492	Ptarmigan Ck. South	110	86	274	18	13.88	Dextral	1	
CR	TF18-039	52.5691	-118.8420	Ptarmigan Ck. South	168	63	192	19	11.24	Dextral-reverse	3	
CR	TF18-039	52.5692	-118.8421	Ptarmigan Ck. South	356	86	~	~		No Indicators	1	
CR	TF18-039	52.5693	-118.8421	Ptarmigan Ck. South	228	83	229	42	3.94	Ambiguous	1	
CR	TF18-039	52.5694	-118.8422	Ptarmigan Ck. South	217	78	224	32	0.52	Sinistral-normal	2	
CR	TF18-040	52.5714	-118.8439	Ptarmigan Ck. South	153	87	325	9	7.42	Dextral	1	
CR	TF18-041	52.5730	-118.8459	Ptarmigan Ck. South	127	64	162	44	3.8	Dextral-reverse	3	
CR	TF18-042	52.5752	-118.8479	Ptarmigan Ck. South	161	56	206	49	2.15	Dextral-reverse	3	Large fault plane
CR	TF18-043	52.5779	-118.8494	Ptarmigan Ck. South	183	63	330	47	0.06	Dextral-normal	2	
CR	TF18-043	52.5778	-118.8495	Ptarmigan Ck. South	155	61	175	32	0.18	Ambiguous	1	
CR	TF18-043	52.5778	-118.8495	Ptarmigan Ck. South	155	61	305	40	1.34	Ambiguous	1	

CR	TF18-046	52.5809	-118.8484	Ptarmigan Ck. South	180	52	343	27	4.26	Dextral-normal	3	
CR	TF18-064	52.5912	-118.8664	Ptarmigan Ck. South	338	57	143	25	1.92	Dextral-reverse	3	
CR	TF18-064	52.5914	-118.8665	Ptarmigan Ck. South	124	78	133	37	0.17	Dextral-reverse	3	
CR	TF18-064	52.5916	-118.8665	Ptarmigan Ck. South	162	84	342	0	0	Dextral	3	
CR	TF18-064	52.5918	-118.8667	Ptarmigan Ck. South	175	87	0	1	5.04	Dextral	3	
CR	TF18-095	52.7163	-119.0218	Yellowjacket Ck.	118	56	130	24	4.01	Dextral	3	Overprinted by reverse slickenlines
CR	TF18-095	52.7163	-119.0218	Yellowjacket Ck.	118	56	220	75	19.28	Reverse	3	Overprints dextral slickenlines
CR	TF18-095	52.7163	-119.0216	Yellowjacket Ck.	100	56	157	42	8.19	Reverse	3	
CR	TF18-096	52.7167	-119.0208	Yellowjacket Ck.	172	85	170	25	3.92	Dextral	3	
CR	TF18-096	52.7168	-119.0208	Yellowjacket Ck.	311	80	31	68	11.67	Normal	3	
CR	TF18-096	52.7169	-119.0207	Yellowjacket Ck.	164	89	170	8	5.8	Dextral	3	
CR	TF18-096	52.7171	-119.0203	Yellowjacket Ck.	62	70	65	0	2.82	Sinistral	3	
CR	TF18-097	52.7181	-119.0150	Yellowjacket Ck.	152	68	330	26	7.77	Dextral	3	
CR	TF18-099	52.7216	-119.0003	Yellowjacket Ck.	313	75	150	15	19.86	Dextral	3	
CR	TF18-100	52.7198	-119.0050	Yellowjacket Ck.	31	89	33	34	1.1	Sinistral	3	
CR	TF18-100	52.7200	-119.0044	Yellowjacket Ck.	298	61	112	26	7.49	Sinistral	3	
CR	TF18-101	52.7185	-119.0095	Yellowjacket Ck.	221	73	45	6	5.56	Sinistral	3	
CR	TF18-101	52.7186	-119.0094	Yellowjacket Ck.	117	60	121	25	9.01	Dextral	3	
CR	TF18-102	52.7183	-119.0121	Yellowjacket Ck.	115	72	128	30	1.76	Sinistral	3	
CR	TF18-118	52.7375	-119.0349	Yellowjacket Ck.	240	89	46	26	12.11	Sinistral	3	
CR	TF18-118	52.7375	-119.0349	Yellowjacket Ck.	221	61	40	7	2.52	Sinistral	3	